External sulfate attack of cement-based materials under complex environmental actions : experiments and modelling

Bo Ran

Université Gustave Eiffel

ÉCOLE DOCTORALE
SCIENCES, INGENIERIE et ENVIRONNEMENT

Thèse préparée dans le cadre d'une cotutelle internationale pour obtenir le grade de
DOCTEUR de l'Université Gustave Eiffel

Spécialité : GÉNIE CIVIL

Présentée par
Bo RAN

Attaque sulfatique externe des matériaux cimentaires sous actions environnementales complexes : expérimentations et modélisation

Thèse présentée et soutenue à Tsinghua University, Beijing, China,

le 07 décembre 2022

Composition du Jury

Rapporteur :	M. Qiang ZENG	Professeur Associé, Zhejiang University
Rapporteur :	M. Antonin FABBRI	Directeur de Recherche, École Nationale des Travaux Publics de l'État
Examinateur :	M. Xiaohui CHENG	Professeur Associé, Tsinghua University
Invité :	M. Patrick DANGLA	Ingénieur Divisionnaire des Travaux Publics de l'État, École Nationale des Ponts et Chaussées - Université Gustave Eiffel
Co-encadrant de Thèse :	M. Othman OMIKRINE-METALSSI	Chargé de Recherche (HDR), Université Gustave Eiffel
Co-directeur de Thèse :	M. Kefei LI	Professeur, Tsinghua University
Directeur de Thèse :	M. Teddy FEN-CHONG	Directeur de recherche, Université Gustave Eiffel

ACKNOWLEDGEMENTS

I am really grateful to the four teachers of the Thesis Supervision Committee. Thanks to Professor Kefei Li and Doctor Teddy Fen-Chong for giving me the chance to do research and for advising me on research ideas and methodology. Thanks to Doctor Othamn Omikrine Metalssi for his guidance on experimental work and to Doctor Patrick Dangla for his teaching on modelling work. Besides, I would like to thank Dr. Haiyun Yang (Analysis Center of Tsinghua University) for his guidance in the NMR measurement and thank Dr. Baraka Mohamed (UMR-MCD, Université Gustave Eiffel) for her help in the ICP tests.

I owe deep thanks to to all the researchers and students at Université Gustave Eiffel's UMR-MCD and Tsinghua University's building materials laboratory. I would like to thank Jean-François, Pauline Huart, Tony Pont, Baptiste Luzu, Mike Jabbour, and Marie Sereng for their help in experiments and life when I was in France. I would like to thank Dongdong Zhang, Wei Jing, Qi Yang, Fuyao Zhao, Meijie Xie, Zhen Wang, and Lei Xu for having discussions with me and providing me helpful messages.

Lastly, I like to express my thankfulness to my wife for her unwavering support and everlasting love.

This research is supported by China National Science Foundation Grant No. 52038004.

Résumé

L'attaque sulfatique externe (ASE) est l'une des principales préoccupations concernant la durabilité des matériaux cimentaires soumis à des sulfates environnementaux. L'ASE est généralement accompagnée d'autres actions agressives, telles que celle par les chlorures et la lixiviation, dans l'environnement naturel, ce qui entraîne des endommagements plus complexes que celui provoqué uniquement par l'ASE. Ce travail a pour but d'étudier les mécanismes d'endommagement des matériaux cimentaires sous l'effet de l'ASE avec et sans action(s) combinée(s), et de proposer des modèles scientifiques adaptés aux applications d'ingénierie.

Dans cette étude, les échantillons de poudre préparés à partir de pâte de ciment ont été immergés dans différentes solutions de sulfate ; la teneur en ettringite (AFt) a ensuite été quantifiée à un temps d'exposition donné pour étudier la cinétique de formation d'AFt. Ensuite, des tranches d'échantillons de 2mm d'épaisseur ont été exposées à différentes solutions de sulfate ; les évolutions de la teneur en AFt, de la structure des pores, de la diffusivité de la vapeur, et de l'expansion du matériau ont été mesurées pour étudier le processus de cristallisation de l'AFt dans les pores et son effet sur les propriétés de transport et mécaniques du matériau. Enfin, des échantillons sous forme de disque ont été immergés dans différentes solutions de sulfate ; les profils de sulfate, le transfert de masse, et la caractéristique de la fissuration ont été examinés à différents temps d'exposition pour étudier l'endommagement de matériaux cimentaires sous ASE. À l'aide des résultats expérimentaux, un modèle chimio-poromécanique a été proposé pour prédire les endommagements causés par l'action combinée de l'ASE et des chlorures. Un modèle de taux d'écaillage pour prédire l'écaillage du matériau cimentaire sous l'action combinée de l'ASE et de la lixiviation a aussi été élaboré.

Les résultats clés de cette étude sont les suivants. (1) Pour la production de l'AFt, une concentration élevée de sulfate couplée à la réaction sulfatique interne (RSI) l'accélèrent, mais les chlorures la ralentissent. Une relation exponentielle entre le taux de formation d'AFt et sa sursaturation a été adoptée avec un exposant à environ 1,90. (2) Les cristaux d'AFt formés dans les micropores (5-40nm) ferment puis rouvrent le col des pores de type "bouteille d'encre", ce qui entraîne une réduction puis une augmentation de la diffusivité de la vapeur, respectivement. Les chlorures atténuent la cristallisation des pores mais la RSI l'accélère. (3) L'endommagement des matériaux cimentaires sous les actions combinées de l'ASE et de la lixiviation se présente sous forme d'écaillage et du gypse s'est formé spécifiquement sous l'action de ces actions combinées. Les chlorures et la RSI, respectivement, atténuent et accélèrent la pénétration des sulfates, l'expansion du matériau, et sa fissuration. (4) Les dilatations simulées de l'ASE par le modèle chimio-poromécanique montrent un bon accord avec les mesures expérimentales. Ce modèle interprète les effets des concentrations en chlorure et sulfate sur le taux d'expansion de l'ASE comme la variation de la sursaturation en AFt et de la pression de cristallisation. (5) À travers le modèle de taux d'écaillage, une relation proportionnelle entre la profondeur d'écaillage et la racine carrée du temps d'exposition est prédite et validée par les mesures de la profondeur de fissuration. Une analyse paramétrique montre l'impact primordial de la teneur en aluminate et de la diffusivité du sulfate sur le taux d'endommagement. Le modèle donne des prédictions conservatives, ce qui reste très utile pour les dimensionnements de durabilité en ingénierie.

Mots clés: Attaque sulfate; Actions combinées; Cinétique; Cristallisation des pores; Écaillage

ABSTRACT

External sulfate attack (ESA) is one of the major concerns for the durability of cement-based material (CBM) subjected to the sulfate-bearing conditions. The ESA is usually accompanied by other aggressive actions, such as chlorides and leaching, in natural environment, resulting in a complicated damage mechanism than that of a single ESA. This work aims to study the mechanisms of the damage of CBM under ESA with and without the combined actions, and to propose scientific models for engineering applications.

In this study, powder samples prepared from cement paste were immersed into different sulfate solutions, and the ettringite (AFt) content was then quantified at given exposure time to investigate the kinetics of ettringite formation. Then, 2mm thickness slice specimens were exposed to different sulfate solutions, and the evolutions of AFt content, pore structure, vapour diffusivity and material expansion were measured to investigate the pore AFt crystallization process and its effect on transport property and material expansion. Finally, disk specimens were immersed into different sulfate solutions, and the sulfates profiles, the mass transfer and cracking pattern were examined at different exposure time to investigate the damage pattern of CBM under ESA. Based on the results of these experimental research, a chemo-poromechanical model to predict the expansion damage of CBM under the combined ESA and chlorides actions, and a spalling rate model to predict the spalling damage of CBM under the combined ESA and leaching actions were proposed.

The key findings based on the above studies include: (1) For the AFt formation, high sulfate concentration and DEF accelerate it but the chlorides decelerate it. An exponential relation between the AFt formation rate and the AFt supersaturation was adopted and the exponential order was fitted as 1.90. (2) The AFt crystals formed in micropores (5-40nm) close and then reopen the neck-part of ”ink-bottle” pores, resulting in a reduction and a subsequent increase in the vapour diffusivity, respectively. The chlorides mitigate the pore crystallization process but DEF accelerate it. (3) The damage pattern of CBM under the combined ESA and leaching actions was found to be a spalling pattern and gypsum is found to be a special product in this combined actions. The chlorides and DEF respectively mitigate and accelerate the sulfate ingress, material expansion and cracking.

(4) The simulated ESA expansions through the chemo-poromechanical model show good agreement with the experimental measurements in this study and literature. This model interprets the effects of chlorides and sulfate concentration on ESA expansion rate as the variation of the AFt supersaturation and the crystallization pressure. (5) In the spalling rate model, a proportional relation between the spalling depth and the square root of the exposure time is predicted and validated through the measurements of cracking depth in this study and literature. A parametric analysis shows the foremost impact of the aluminate content and the sulfate diffusivity on the damage rate. The main assumptions in models lead to conservative predictions, but yet the model results are meaningful for engineering use.

Keywords: Sulfate attack; Combined actions; Kinetics; Pore crystallization; Spalling

TABLE OF CONTENTS

LIST OF FIGURES AND TABLES

LIST OF SYMBOLS AND ACRONYMS

ESA	External sulfate attack
DEF	Delayed ettringite formation
CBM	Cement-based materials
SCMs	Supplementary cementitious materials
OPC	Ordinary Portland cement
HSR	High-sulfate-resistant
C_3S	Tricalcium silicate
C_2S	Dicalcium silicate
C_3A	Tricalcium aluminate
C_4AF	Tetracalcium aluminoferrite
$C\overline{S}H_2$	Gypsum
$C_4A_3\overline{S}$	Calcium sulphoaluminate
CA	Equivalent grouping of aluminum phases
AFt	$Al_2O_3 - Fe_2O_3$ – tri hydrate, ettringite
AFm	$Al_2O_3 - Fe_2O_3$ – mono hydrates
CSH	Calcium silicate hydrate
CH	Portlandite, calcium hydroxide
MH	Magnesium hydroxide
$C_6A\overline{S}H_{32}$	Ettringite
$C_4A\overline{S}H_{12}$	Monosulfoaluminate
C_4AH_{13}	Hydroxy-AFm
$C_3ACaCl_2H_{10}$	Friedel’s salt
ITZ	Interfacial transition zone
PSD	Pore size distributi
DSC	Differential scanning calorimetry
DVS	Dynamic vapour sorption
EDS	Energy Dispersive Spectroscopy
EDXRD	Energy dispersive X-ray diffraction
ICP	Inductively coupled plasma
NMR	Nuclear magnetic resonance
microCT	X-ray microtomography
MIP	Mercury intrusion porosimetry

SEM	Scanning electron microscopy
XRD	X-ray diffraction
n_i	Molar content of solid phases or oxides per liter of CBM
c_i	Concentration of ion species *i*
a_i	Activity of ion species *i*
β_i	Supersaturation index of phase *i*
K_i	Solubility constant of phase *i*
P_J	Pressure of phase J (crystal or liquid phase)
S_J	Saturation of phase J
ϕ_J	Partial porosity of phase J
b_J	Biot coefficient of phase J
μ_J	Chemical potential of phase J
n_J	Molar concentration of phase J
s_J	Volumetric density of entropy of phase J

CHAPTER 1 GENERAL INTRODUCTION

Cement-based materials (CBM) are known as the most widely used engineering materials in the world. In 2021, the world's global clinker production capacity and cement production were about 3.7 and 4.4 billion tons, respectively[1]. Due to such a huge annual consumption, the durability of CBM has an immense influence on the economic development and environmental sustainability[2-3]. Improved material durability can lower construction cement consumption and building maintenance costs by reducing the frequency of repairs, which is favorable for the environment and the economy.

The durability problems of CBM are attributable to the physical-chemical actions from environments and service conditions. These actions lead to degradation of CBM, such as the corrosion of reinforcement caused by chloride ingress and carbonation, the cracking and expansion caused by alkali-silica reaction, freeze-thaw and external sulfate attack (ESA), and the strength loss by calcium leaching. Among these common causes

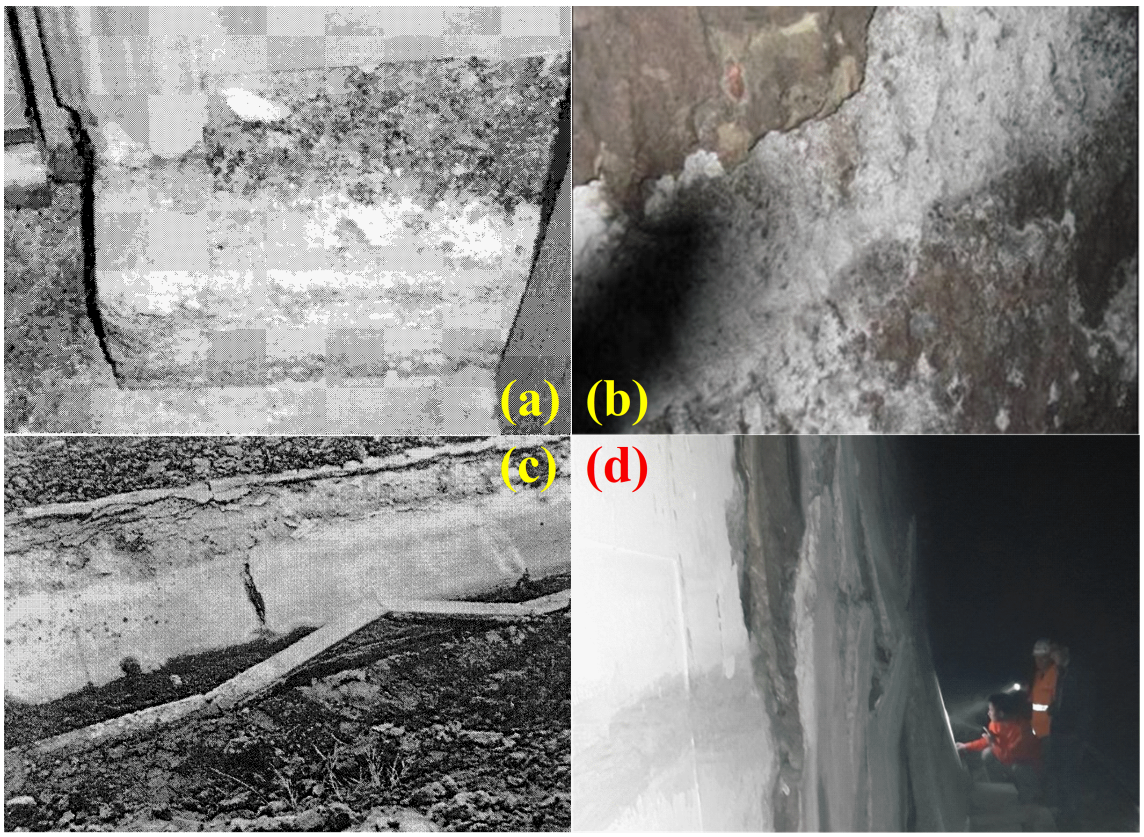

Figure 1.1 Various degradation of concretes exposed to ESA observed in civil engineering. (a) are adopted from Skalny et al., 2002[2], (b) from Lei et al., 2013[4], (c) from Harboe, 1982[5] and (d) from a tunnel in western China.

of durability problems, ESA can be an important process compromising the durability of CBM.

ESA damage is a concrete degradation process caused by the expansion reaction between sulfate ions coming from an external source and the aluminum phases in the hardened cement paste. The engineering cases and laboratory studies on CBM subject to the ESA have a lengthy history: the first report of sulfate attack dates back to 1818, and the expansive product was firstly identified as ettringite (AFt) in 1892[6]. Figure 1.1 presents several engineering cases for ESA damage, illustrating that the ESA damage manifests as expansion (Figure 1.1c) and spalling (Figures 1.1a, b and d). Figures 1.1a and c depict the damage to a house footing by sulfate ions in the ground water and to a concrete lining of an irrigation ditch by sulfate ions in water, respectively. Figures 1.1b and d show the damage to the tunnel concrete linings in different railways by sulfate ions in groundwater. The ESA is regional, dependent on the sulfate distribution in water and soil environments. And it mainly occurs in sulfate-bearing environments, such as saline soil and some groundwater.

Extensive laboratory studies reveal that the ESA is a chemical-physical-mechanical process involving ions diffusion (mainly sulfate ions), chemical reactions between the penetrating sulfate ions and aluminum phases (AFt and gypsum formation) and deformation induced by expansive products (expansion and cracking behavior), cf. Figure 1.2. What's more, the ESA is usually coupled with other actions in the natural sulfate-bearing environments, as shown in Table 1.1: the low pH solutions are related to leaching; other

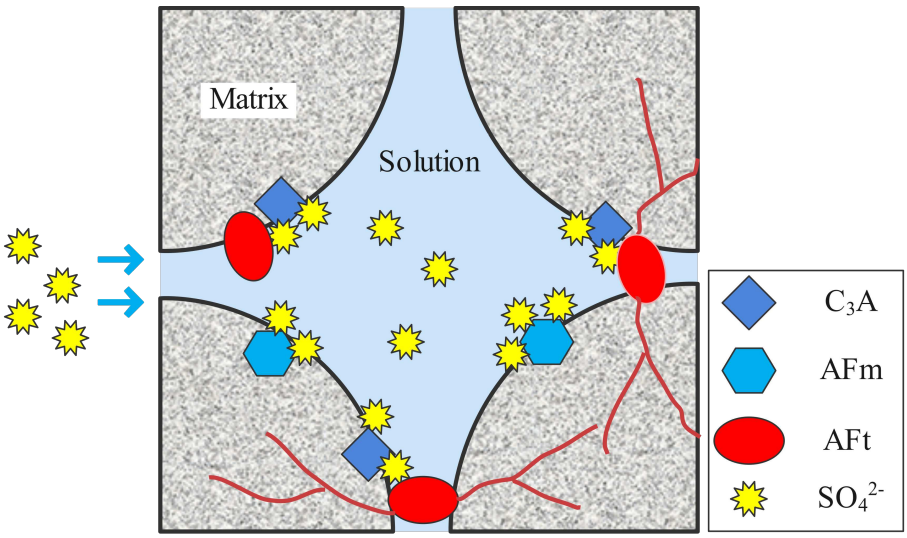

Figure 1.2 Scheme of ESA damage, the blue arrows stands for diffusion process, and the red lines represents cracks.

aggressive ions, such as chlorides and magnesium, are present together with the sulfate ions. Therefore, the mechanisms of ESA damage in complex environments involve multiple processes. In this chapter, the mechanism of the pure ESA is reviewed firstly, followed by the coupled actions.

Table 1.1 Typical values for ion concentration and pH in sulfate-bearing environments.

Environment	SO_4^{2-} content	Cl^- content	Mg^{2+} content	pH value (-)
Saline soil[7]	35.70 g/L	67.20 g/L	1.62 g/L	7.36
Groundwater[8]	1.47 g/L	4.34 g/L	0.235 g/L	7.53
Seawater[9]	1.70 g/L	14.65 g/L	1.01 g/L	7.64

1.1 Mechanism of external sulfate attack

1.1.1 Ettringite formation and its kinetics

The mechanism of ESA damage on the CBM includes ion diffusion, chemical reactions and mechanical response: the sulfates from the external environments disturb the initial solid phases-liquid solution equilibria in the pore space, resulting in the formation of gypsum($C\overline{S}H_2$) and AFt[10-11]; the formed expansive products (mainly AFt) refine the pore structure[12-13], and meanwhile accumulate internal stress to degrade the mechanical resistance[14-15]. As the main source of expansive stress, AFt ($C_6A\overline{S}_3H_{32}$) originates from the chemical reactions between the sulfate ions and the aluminum phases in hardened cement paste in the presence of portlandite (CH). The aluminum phases in hardened cement paste include unhydrated aluminum phases containing C_3A and C_4AF (two main minerals of cement clinker), and hydrated aluminum phases (AFm phases) including hydroxy-AFm (C_4AH_{13}) and monosulfoaluminate ($C_4A\overline{S}H_{12}$). The chemical reactions between these aluminum phases and the sulfate ions write[16],

$$\begin{cases} C_3A + 3CH + 3SO_4^{2-} \longrightarrow C_6A\overline{S}_3H_{32} + 6OH^- \\ 3C_4AF + 12CH + 12SO_4^{2-} \longrightarrow 4C_6A\overline{S}_3H_{32} + 2[(A,F)H_3] + 24OH^- \\ C_4AH_{13} + 3CH + 3SO_4^{2-} \longrightarrow C_6A\overline{S}_3H_{32} + 6OH^- \\ C_4A\overline{S}H_{12} + 2CH + 2SO_4^{2-} \longrightarrow C_6A\overline{S}_3H_{32} + 4OH^- \end{cases} \tag{1.1}$$

To simplify, these reactions for ettringite formation in Eq. (1.1) are lumped into a single

expression[17-18],

$$\mathrm{CA} + q\mathrm{CH} + q\mathrm{SO_4^{2-}} \longrightarrow \mathrm{AFt} + q\mathrm{OH^-} \tag{1.2}$$

where CA represents an equivalent grouping of aluminum phases, and q is the weighted stoichiometric coefficient based on chemical reactions in Eq. (1.1). These two terms are expressed as,

$$\begin{cases} \mathrm{CA} = \gamma_1 \mathrm{C_3A} + \gamma_2 \mathrm{C_4AF} + \gamma_3 \mathrm{C_4AH_{13}} + \gamma_4 \mathrm{C_4A\overline{S}H_{12}} \\ q = 3\gamma_1 + 4\gamma_2 + 3\gamma_3 + 2\gamma_4 \end{cases} \tag{1.3}$$

The term γ_i is the fraction of each aluminate phase in the total aluminate content, $\gamma_i = C_i \left(\sum_{i=1}^{4} C_i \right)^{-1}$, with C_i representing the molar value of clinker mineral i in unit mass of cement paste.

The chemical mechanism for AFt formation has been well investigated as shown in Eq. (1.1) and (1.2). Aluminum phases, portlandite and sulfate ions are consumed with the formation of AFt. However, to predict the service life and to assess the durability of CBM exposed to ESA conditions, the estimation of the AFt amount at a given time, i.e., the kinetics of AFt formation, is essential. Unfortunately, the kinetics of AFt formation is still unclear in the literature.

The small AFt content in CBM, less than 10% of the hardened cement paste in mass, necessitates the use of high-precision instruments. Few tests have been conducted to quantitatively measure the AFt amount. Santhannam et al.[19-20] used differential scanning calorimetry (DSC) to measure the variation of AFt concentration in cement mortar specimens immersed in sulfate solution with time. Although the AFt amount measured in [19-20] show a rational increase trend with exposure time, the measurement principle is questionable. Typically, the decomposition temperature of AFt (about 100°C[21]) falls within the dehydration temperature range (90-120°C[16]) of calcium silicate hydrate (CSH, the main hydrate in cement paste). As a result, the peaks representing AFt and CSH overlap in the DSC curve, making it difficult to separate these two peaks for quantitative analysis. The X-ray diffraction (XRD) using the Rietveld refinement technique is another conventional method for quantifying mineral phases in hydrated cement paste. Müllauer et al.[22] measured the kinetic process of AFt formation in cement mortar specimens exposed to 30g/L SO_4^{2-} solution, and found the increase of AFt content with time. However, the accuracy of this quantitative approach is dependent on operator[21] and the accuracy

of the determination of AFt content in CBM needs to be confirmed[23]. Recently, the ^{27}Al Nuclear Magnetic Resonance (NMR) spectroscopy has recently attracted increased attention as a new technique in civil engineering due to its high precision[24]. Ragoug et al.[25] used this technique to measure the change of AFt amount in cement paste after 2-month exposure to a sulfate solution, and found that almost all the AFm phases are transformed into AFt. But the kinetic process within 2 months was not measured.

Regardless of the lack of experimentally measured kinetic data for AFt formation, several classical kinetic laws have been employed in the numerical simulation works[17-18,26-32]. And the kinetic rate constants in the used kinetic laws were calibrated using the experimental expansion data. The most common law in literature is the second order reaction[17-18,26-29],

$$\frac{\mathrm{d}n_{\mathrm{CA}}}{\mathrm{d}t} = -k_{\mathrm{eq}} n_{\mathrm{CA}} c_{\mathrm{S}} \tag{1.4}$$

where n_{CA} stands for the content of CA in unit volume of CBM, c_{S} for the concentration of the sulfate ions in the pore solution of CBM, and k_{eq} for rate constant in the second-order law. The rate constant, k_{eq}, is calibrated as 1×10^{-7} m^3/(mol·s) in [17,26] and 1.22×10^{-9} m^3/(mol·s) in [18,27-28]. However, the proportional relation between the AFt formation

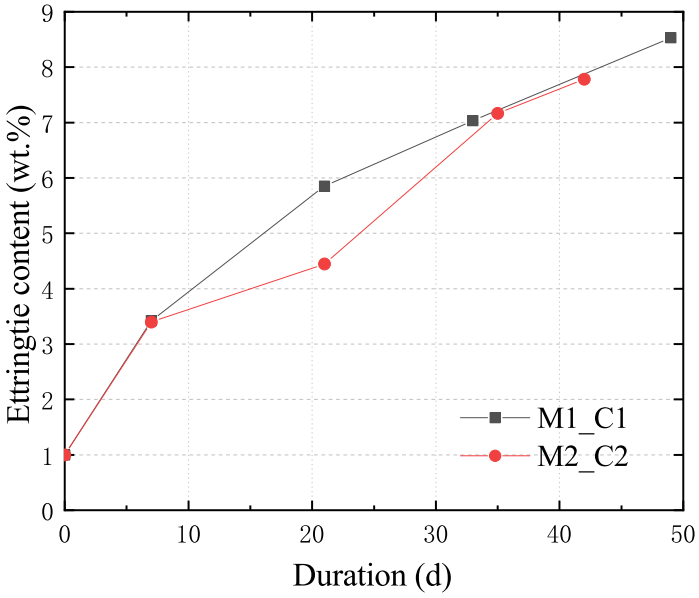

Figure 1.3 AFt contents, measured by XRD and Rietveld refinement method, in two kinds of mortar specimens exposed to 30 g/L SO_4^{2-} solution at different ages. M1-C1 is cast from cement with a high C_3A content (11.7%), and M2-C2 is cast from cement with a low C_3A content (7.6%). The data is adopted from Mullauer et al.[22].

rate $-\mathrm{d}n_{\mathrm{CA}}/\mathrm{d}t$ and the equivalent aluminum phases content n_{CA} in Eq. (1.4) is unreasonable because the solid concentration in aqueous chemical reaction is usually regarded as 1. Hence, Eq. (1.4) should be reduced to a first order form,

$$\frac{\mathrm{d}n_{\mathrm{CA}}}{\mathrm{d}t} = -k_{\mathrm{eq}}c_{\mathrm{S}} \tag{1.5}$$

The experimentally measured AFt amounts in [22], as shown in Figure 1.3, confirmed that the formation rate of AFt is independent of the content of aluminum phases. The AFt amounts in high C_3A cement mortar and low C_3A cement mortar at a given time seem to be the same.

Other studies[30-32] considered that the AFt formation as a crystallization process, and the crystallization rate should be related to the chemical potential difference between the AFt crystal and the aqueous solute, $\Delta\mu$, which is the driving force for AFt crystallization. The difference in chemical potential $\Delta\mu$ can be expressed through the supersaturation degree of AFt β_{AFt}[33],

$$\Delta\mu = -RT\ln(\beta_{\mathrm{AFt}}) \tag{1.6}$$

The AFt crystallization rate as a function of AFt supersaturation β_{AFt} applied in the literature is different. Bary[30] took a simplified kinetic law,

$$\frac{\mathrm{d}n_{\mathrm{AFt}}}{\mathrm{d}t} = k_{\mathrm{cry}}\left(\beta_{\mathrm{AFt}} - 1\right) \tag{1.7}$$

where n_{AFt} stands for the content of AFt in unit volume of CBM, and k_{cry} is the rate constant in the supersaturated-controlled law. The rate constant is fitted as 10^{-9} mol/m^3/s in [30].

Gu[31] considered an interface-controlled crystallization process in the pores of the cement matrix, where the growth rate of AFt crystals is controlled by the active surface area of the crystal/liquid interface,

$$\frac{\mathrm{d}n_{\mathrm{AFt}}}{\mathrm{d}t} = A_{\mathrm{AFt}}\left(1 - \frac{1}{\beta_{\mathrm{AFt}}}\right) \tag{1.8}$$

Here the term A_{AFt} is a rate constant proportional to the active surface area of AFt/liquid interface, which was calibrated as 0.97-2.72×10^{-5} mol/m^3/s in [31].

Soive and Tran[32] took a kinetic law taking the influence of the AFt supersaturation

β_{AFt} and the surface of AFt/liquid interface a_{AFt} into consideration,

$$\frac{\mathrm{d}n_{\mathrm{AFt}}}{\mathrm{d}t} = k_{\mathrm{AFt}} a_{\mathrm{AFt}} \left(\beta_{\mathrm{AFt}} - 1\right) \tag{1.9}$$

The kinetic constant k_{AFt} is taken as 7.08×10^{-13} mol/(m^2·s) in [34].

Table 1.2 lists the kinetic laws for AFt formation in the literature. The major difference among these kinetic laws in Eqs. (1.4), (1.7), (1.8) and (1.9) is the dependence of kinetic rate on sulfate concentration c_{S}. In Eqs. (1.4) and (1.9), the formation rate is proportional to c_{S}, and in Eq. (1.7), the formation rate is positively related to c_{S}, but in Eq. (1.8) it is inversely proportional to the third powder of of c_{S} (β_{AFt}). Therefore, the formation rate is most sensitive to c_{S} in Eq. (1.7), and least sensitive to c_{S} in Eq. (1.8).

Table 1.2 Kinetic laws and constants used in literature.

Kinetic law	Kinetic expression	Kinetic constant
Second order	$k_{\mathrm{eq}} n_{\mathrm{CA}} c_{\mathrm{S}}$	k_{eq}=10^{-7} m^3/(mol·s)[17,26], 1.22×10^{-9} m^3/(mol·s)[18,27-28]
Supersaturation-controlled	$k_{\mathrm{cry}}\left(\beta_{\mathrm{AFt}} - 1\right)$	k_{cry}=10^{-9} mol/m^3/s[30]
Interface-controlled	$A_{\mathrm{AFt}}\left(1 - \frac{1}{\beta_{\mathrm{AFt}}}\right)$	A_{AFt}=0.97-2.72×10^{-5} mol/m^3/s[31]
Integrated	$k_{\mathrm{AFt}} a_{\mathrm{AFt}} \left(\beta_{\mathrm{AFt}} - 1\right)$	k_{AFt}=7.08×10^{-13} mol/(m^2·s)[34]

1.1.2 Diffusion of sulfates

The transport of sulfates in CBM is driven by diffusion under a concentration gradient and by immobilization through chemical reactions in Eq. (1.2). The mass conservation of sulfates in CBM writes,

$$\frac{\partial C_{\mathrm{S}}}{\partial t} = \frac{\partial}{\partial x}\left(D_{\mathrm{S}}^{e} \frac{\partial c_{\mathrm{S}}}{\partial x}\right) - q\frac{\partial n_{\mathrm{AFt}}}{\partial t} \quad \text{with} \quad n_{\mathrm{S}} = \phi c_{\mathrm{S}} + 3n_{\mathrm{AFt}} \tag{1.10}$$

where C_{S} represents the total sulfates content in unit volume of CBM, which is the sum of the free sulfates in pore solution ϕc_{S} and the bound sulfates in AFt crystal $3n_{\mathrm{AFt}}$, D_{S}^{e} denotes the effective sulfate diffusivity, and ϕ is the porosity of CBM. Eq. (1.10) can be rewritten using aqueous sulfate concentration c_{S} and AFt content n_{AFt} as basic variables,

$$\frac{\partial c_{\mathrm{S}}}{\partial t} = \frac{\partial}{\partial x}\left(D_{\mathrm{S}} \frac{\partial c_{\mathrm{S}}}{\partial x}\right) - \frac{q+3}{\phi}\frac{\partial n_{\mathrm{AFt}}}{\partial t} \quad \text{with} \quad D_{\mathrm{S}} = \frac{D_{\mathrm{S}}^{e}}{\phi} \tag{1.11}$$

Here D_S stands for the apparent sulfate diffusivity (m^2/s). Two variables, c_S and n_{AFt} are contained in Eq. (1.11), thus another equation is required to solve the equation. The supplementary equation can be provided by the kinetic laws in Eqs. (1.4), (1.7-1.9).

The immobilization of sulfate ions will diminish the sulfate flux across CBM, resulting in a reduction in apparent diffusivity, D_S, over time. The decrease in apparent diffusivity is observed in literature[35-37]. Tumidajski[35] and Ragoug[36] respectively measured the sulfate profiles in cement concrete specimens and cement paste specimens exposed to sulfate solutions, and both found that the penetration rate decreased with time. Naik[37] measured the distribution of the relative AFt content with exposure depth in cement paste and confirmed the decline in the apparent sulfate diffusivity. The decline in D_S is also called *self-deceleration of sulfate ingress* in [36]. In addition, the self-deceleration of sulfate ingress can also be attributed to the pore-filling effect induced by AFt formation[38-40]. Several models have been developed to quantify the effect of pore refinement on the diffusion coefficient. One model was proposed by Idiart[18,27],

$$D = D_m + (D_0 - D_m)\frac{\exp(-\beta_D)\boldsymbol{\Phi}}{1 + (\exp(-\beta_D) - 1)\boldsymbol{\Phi}} \quad \text{with} \quad \boldsymbol{\Phi} = \frac{\phi}{\phi_0} \tag{1.12}$$

where ϕ and D are the updated (current) porosity and diffusivity after the pore-filling of AFt, ϕ_0 and D_0 are the initial porosity and diffusivity before any pore-filling, β_D is a shape factor, and D_m is the minimum diffusivity when $\phi/\phi_0 = 0$ with the diffusion path provided by the gel nanopores. Another model was proposed by Samson[41-42],

$$\frac{D}{D_0} = \frac{\exp(4.3\phi/V_P)}{\exp(4.3\phi_0/V_P)} \tag{1.13}$$

where V_P is the cement paste volume in unit volume of CBM.

Besides the pore-filling effect, the cracking effect on sulfate transport during ESA is also taken into consideration in literature[17-18,27,42-43]. The most commonly used model describing the cracking effect in literature writes[44],

$$\frac{D}{D_0} = 1 + \frac{32}{9}C_d + \frac{[\max(0, C_d - C_{de})]^2}{C_{dec} - C_d} \tag{1.14}$$

where C_d represents the cracking density, C_{de} and C_{dec} are two percolation thresholds. The density of cracks is low when C_d is smaller than the conduction percolation threshold C_{de}, and C_{dec} is the rigidity percolation threshold at which the cluster of cracks percolates

the volume. The crack density C_d is estimated through the following equation in [45],

$$C_d = k\left(1 - \frac{\epsilon_{sh}}{\epsilon}\right)^m \tag{1.15}$$

where ϵ denotes the strain, ϵ_{th} denotes the threshold strain at which the microcracks start forming, and k and m denote model parameters calibrated from the experimental stress–strain diagram.

The preceding review shows that the diffusion process of sulfates is complicated due to the unclear kinetic law of sulfate immobilization (AFt formation) and the complex change in diffusivity with the evolution of pore structure. A successful simulation of sulfate transport requires a precise mathematical description of the underlying physical process and an efficient numerical method for solving the associated mathematical equations. Sarkar[43] and Soive[32] simulated the sulfate transport in cement paste and mortar specimens, respectively. In Sarkar's work[43], the kinetics of AFt formation was reduced to an equilibrium movement in Eq. (1.1) or Eq. (1.2), and the variation of diffusivity resulting from AFt formation was simulated using Eqs. (1.13) and (1.14). In Soive's work[32], a multi-ions surface complexation model was developed to estimate the adsorbed sulfates on the CSH surface, and the kinetic law used is given in Eq. (1.9). The findings of Soive's simulation suggest that the difference in adsorbed sulfates is the primary source of the change in total sulfate content with exposure depth. Both Sarkar's work and Soive's work successfully simulated the distribution of total sulfates but using different kinetic laws for the AFt formation. Additional experimental investigation, such as the measurement of adsorbed sulfates, is necessary to validate their hypotheses.

1.1.3 Damage of CBM

Most of the ESA damage observations on CBM originate from laboratory tests, and the ESA damage manifests as the expansion of specimens. The expansion curves of cement-based specimens subjected to sulfate solution typically occur in two stages[46-49], as shown in Figure 1.4. The first stage, with a slow rate of expansion, is called the "induction stage". Yu et al.[50] ascribed the slow expansion stage to the AFt formation in large pores, in which AFt crystals grow unconstrained and do not exert stress on the pore walls prior to reaching the pore wall. Gu et al.[31] used a two-stage damage model[51] to explain the two-stage expansion. The slow expansion during the induction stage rate is attributed to the high elastic modulus of the undamaged CBM. In the second stage, the

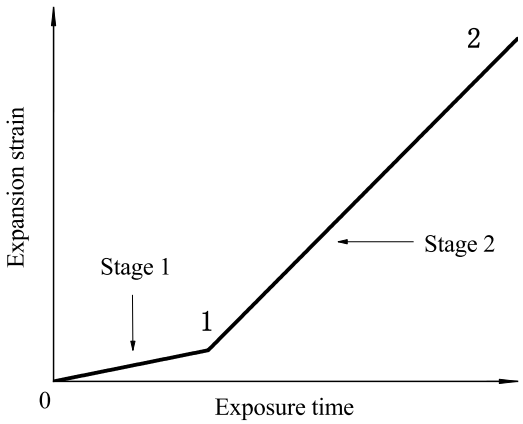

Figure 1.4 Typical two stage expansion strain-exposure time curve of cement-based materials exposed to sulfate solution.

accumulated stress exceeds the tensile strength and cracks appear in the CBM, resulting in a rapid decrease in elastic modulus. The decrease in elastic modulus in the second stage causes the rapid expansion rate.

However, the ESA damage manifests as a spalling pattern in engineering cases, as seen in Figures 1.1a,b and d. There are two interpretations of the spalling damage pattern in the literature. One attributes the spalling pattern to the development of cracks, which accompanies the two-stage expansion of CBM. The cracking originates at the surface of CBM and gradually evolves towards the center of the CBM[52-55,55-56]. At later stages of damage, severe cracks appear and lead to the delamination and exfoliation of CBM[57-58]. Naik[37] proposed that the spalling damage pattern is due to a double-layer near the surface of CBM. The double layer consists of an outer zone of gypsum and an inner zone of AFt. In addition, AFt rather than gypsum is usually considered to contribute to ESA expansion[31,37,50]. Based on the finding of a double layer and the different contributions of AFt and gypsum to expansion, Naik[37] suggested that the appearance of the cracks occurs at the interface of the AFt and gypsum zones, leading to the separation of the outer gypsum layer from the inner AFt layer.

The expansion behaviors of CBM have been well-established, but the expansion mechanism remains contentious. Several expansion theories have been developed to explain the expansion: swelling theory[60], topochemical reaction theory[59,61], volume increase theory[62] and crystallization pressure theory[63-64].

(a) Swelling and topochemical reaction theories

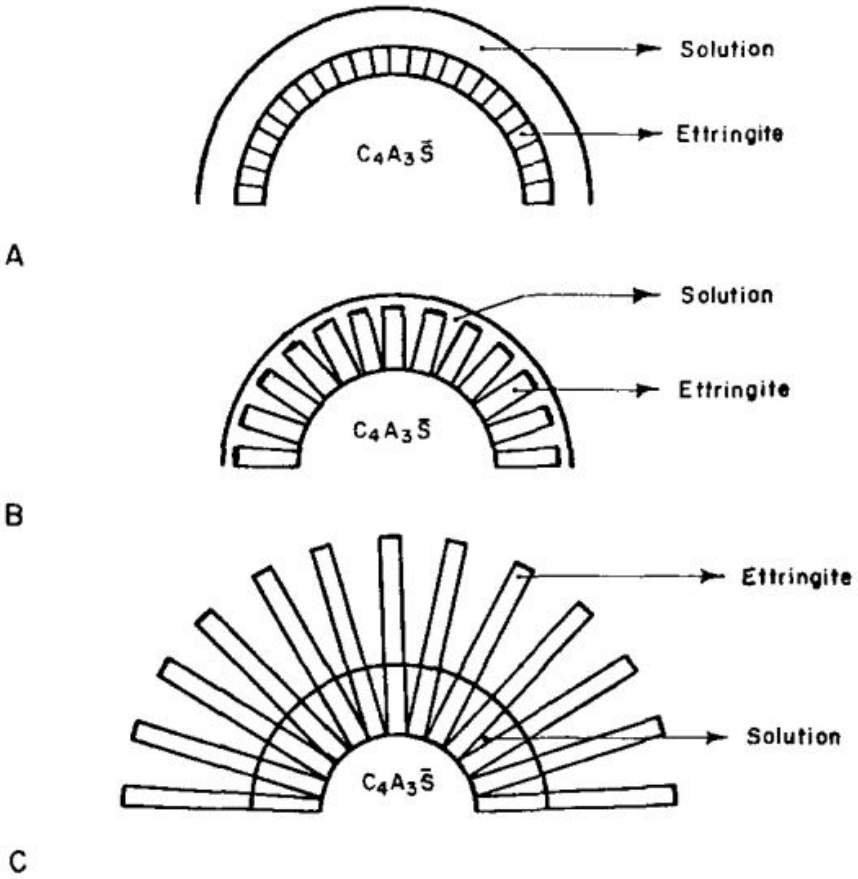

Figure 1.5 Topochemical growth of ettringite crystals and its expansion mechanism. In stage A, immediate formation of ettringite crystals on the surface of reactant particle. In stage B, the anisotropic continuous growth of the ettringite crystals increases its length but not its width and thickness. In stage C, ettringite crystals reach the surface of another particle and exert pressure on it. After Cohen[59].

Mehta[60,65] observed the morphology of ettringite during the hydration of $C_4A_3\bar{S}$-$C\bar{S}H_2$ paste and found that the ettringite is poorly crystallized in the presence of lime and low water-to-cement (w/c) ratio. Besides, the wet-cured paste expanded much more than the dry-cured paste. Based on these two findings, Mehta[60] postulated that the poorly crystalline ettringite is colloidal, and the colloidal ettringite with a high specific surface can absorb lots of water molecules and generate inter-particle repulsion in the presence of water. The repulsion between cement hydrated particles leads to the large expansion. This expansion hypothesis effectively explains the hydration expansion of sulfate aluminate cement. However, it cannot be used to describe the long-term expansion of CBM subjected to ESA. For the latter, the formation of ettringite is in confined conditions rather than free conditions during the hydration process of sulfate aluminate cement.

Cohen[59] suggested a topochemical reaction mechanism of ettringite growth during

the hydration of $C_4A_3\overline{S}$, cf. Figure 1.5. As shown in Figure 1.5, the expansion stress originates from the anisotropic growth of ettringite crystals. Besides the swelling and topochemical reaction theories, the volume increase theory is the most frequently used one in numerical simulation work[17-18,27,42], whereas the crystallization pressure has emerged as the most widely cited hypothesis in the literature[22,30-31,50,64]. These two theories are detailed in the following text.

(b) Volume increase theory

The volumetric change in each chemical reaction in Eq. (1.1) is calculated as,

$$\frac{\Delta V_i}{V_i} = \frac{\overline{V}_{\mathrm{AFt}} - \overline{V}_{\mathrm{i}} - a_i \overline{V}_{\mathrm{CH}}}{\overline{V}_{\mathrm{i}} + a_i \overline{V}_{\mathrm{CH}}} \tag{1.16}$$

where $\overline{V}_i$ is molar volume of aluminum phase i and a_i is stoichiometric coefficient. The overall increased volume in solid matrix is calculated as,

$$\frac{\Delta V}{V} = \sum_{i=1}^{4} \frac{\Delta V_i}{V_i} \overline{V}_i \gamma_i C_{\mathrm{AFt}} \tag{1.17}$$

Once the ettringite crystal is formed in the pores, it should first fill the pore space before exerting stress on the pore walls. Due to the anisotropic growth of ettringite as shown in Figure 1.5, only a portion of the pores must be filled in order to repel the pore walls. The volume strain ϵ is shifted by such pore-filling effect,

$$\epsilon = \frac{\Delta V}{V} - f\phi_0 \tag{1.18}$$

Here the term f is the volume fraction of the initial porosity that needs to be filled with the ettringite before expansion. Assuming an isotropic expansion for CBM, the linear strain ε is defined as:

$$\varepsilon = \frac{1}{3}\epsilon_{\mathrm{v}} \tag{1.19}$$

(c) Crystallization pressure theory

In constrained pore space, the crystal size that can grow is restricted. To crystallize into a pore, an extra pressure must be imposed to increase the energy state of the crystal to overcome the crystal-liquid interfacial energy. In a cylindrical pore with a radius r as shown in Figure 1.6, for instance, the pressure at the end surface of the crystal is estimated

using the Laplace equation,

$$P_C - P_L = \frac{2\gamma_{CL}}{r} \tag{1.20}$$

where P_C and P_L denote the pressures of crystal and liquid solution. Under the equilibrium state, the crystal pressures on the end and side surfaces are equal. And the thermodynamic equilibrium relation between the ettringite crystal and solute writes,

$$\mu_C(P_C, T) = \mu_{sol}(P_L, T, \beta_{AFt}) \tag{1.21}$$

Here the term μ_i stands for the chemical potential of phase i. From Eq. (1.21), a pressure difference between crystal and liquid is derived, which is the well-known Correns' equation[66],

$$P_C - P_L = \frac{RT}{\overline{V}_C} \ln\beta_{AFt} \tag{1.22}$$

Combining Eq. (1.20) and (1.22) gives the well-known Oswald-Freundlich equation[67-68]. As shown in Figure 1.6, a thin liquid film always exists between the crystal and pore wall due to the intermolecular force and the disjoining pressure P_{dis}. The mechanical equilibrium on the side surface of the crystal gives another equation between P_C and P_L,

$$P_C = P_L + P_{dis} + \frac{\gamma_{CL}}{r} \tag{1.23}$$

The crystal pressure is the sum of liquid pressure P_L, disjoining pressure P_{dis} and surface tensile γ_{CL}. Hence, the stress imposed on the crystal side surface (on the pore wall in

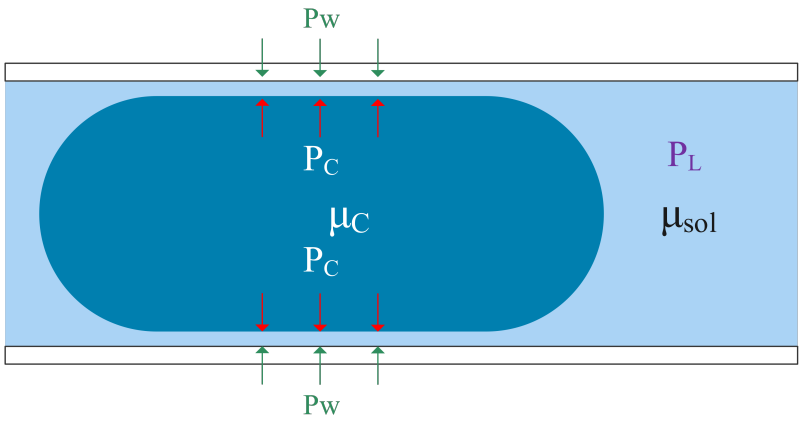

Figure 1.6 Crystallization process in a single pore. P_C and P_L stands for pressure of crystal and liquid, μ_C and μ_{sol} for the chemical potential of crystal and solute ions, and P_W for the pressure exerting on the pore wall.

turn), P_W, writes,

$$P_W = P_L + P_{dis} = P_C - \frac{\gamma_{CL}}{r} = P_L + \frac{RT}{\overline{V}_C}\ln\beta_{AFt} - \frac{\gamma_{CL}}{r} \tag{1.24}$$

(d) Summary

Table 1.3 recapitulates the aforementioned expansion mechanisms in the literature. The swelling and topochemical theories are valid for the hydration of sulfoaluminate cement. The volume growth and crystallization pressure theories are valid for the long-term expansion of CBM exposed to sulfate conditions. Both the volume increase and crystallization pressure theories provide an approach to calculating expansion stress.

Table 1.3 Expansion mechanisms in literature.

Theory	Mechanism	Valid scope
Swelling[60]	Adsorption of water by colloidal AFt crystal	Hydration of sulfoaluminate cement
Topochemical[59]	Anisotropic growth of AFt crystal	Hydration of sulfoaluminate cement
Volume increase[62]	Volume change between reactants and products	Long-term expansion of CBM exposed to ESA
Crystallization pressure[63]	Interaction between solid matrix and AFt crystal	Long-term expansion of CBM exposed to ESA

1.1.4 Role of gypsum

There are two schools of thought on the role of gypsum in the literature: supporting or contradicting the idea that the formation of gypsum leads to expansion. Gypsum is formed from the chemical reaction between portlandite and sulfate ions,

$$CH + SO_4^{2-} \longrightarrow C\overline{S}H_2 + 2OH^- \tag{1.25}$$

Hansen[69-70] and Mather[71] indicated that the volume of the newly formed gypsum in Eq. (1.25) is smaller than that of available pores where gypsum can precipitate plus the volume of the solid CH that dissolves during the gypsum formation process. Thus, the gypsum formation does not result in a volume increase of solid phases or the associated internal expansion stress.

Some experimental results on the C_3A-free system reported the contribution of gypsum to expansion and strength loss[72-74]. The use of C_3A-free cement aimed to isolate the

gypsum formation from the AFt formation. However, another problem was introduced with the use of C_3A-free cement: the alkali content is very low, and the corresponding concentrations of alkali mental ions and hydroxide ions in pore solution are also extremely low[75-77]. Thus, the major ionic composition of the pore solution in C_3A-free cement paste is different from that of ordinary Portland cement (OPC) paste, and this has a substantial effect on the precipitation condition for gypsum. The precipitation condition of gypsum will be investigated in this study. The different ionic compositions of pore solutions in C_3A-free cement paste and OPC paste can also lead to varied AFt supersaturation and crystallization pressures. Thus the findings in literature[72-74] that supports gypsum contributes to the ESA expansion are invalid for the OPC system. Therefore, it is still unclear about gypsum formation and its contribution to damage.

1.1.5 Influential factors for ESA

As stated above, the main processes involved in ESA include the diffusion of sulfates, the formation of AFt, and the expansion of CBM. The sulfate condition and material properties of CBM are the main influential factors for ESA. The former determines the extent of ESA and the latter governs the resistance of CBM to ESA. The parameters related to sulfate solution include the sulfate concentration, the pH of the sulfate solution, and the presence of other aggressive ions. The last three parameters involve different chemical mechanisms, and they will be discussed in the next section. Material properties can be described by C_3A content, w/c ratio, and size of specimens.

(a) Sulfate concentration

In engineering practice, sulfate concentration is the most important parameter for determining the severity of sulfate attack. As shown in Appendix A, codes and standards classify the sulfate-bearing environments based on the sulfate concentration. There are differences in the gradation of ESA extent in various standards. What's more, the test methods used to assess the sulfate concentration in soil are not same in different standards. The sulfate content in soils is determined by the water extraction method in Chinese standard[78] and American standard[79], but by the acid extraction method in British standard[80]. The acid extraction method overestimates the severity of the sulfate condition. Besides, for water extraction in Chinese and American standards, the test details are different for deionized water-to-soil ratio, the mass of the soil sample, the drying method on the soil sample, and the stirrer time. These differences make it difficult to compare

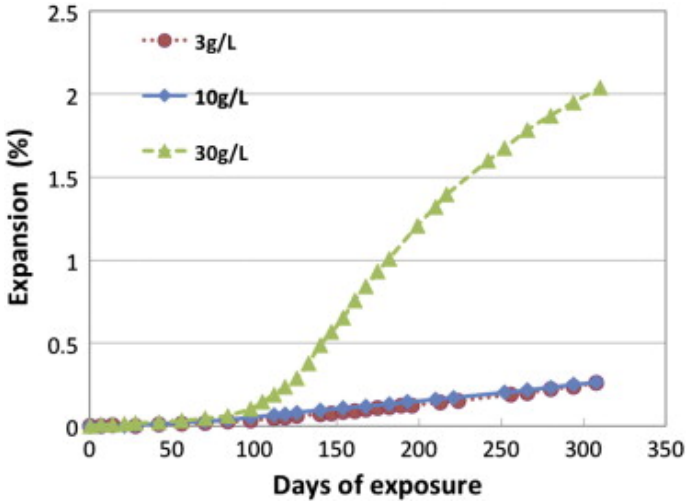

Figure 1.7 Expansion of cement mortar specimens (w/c=0.55) exposed to sodium sulfate solutions with different concentrations at different exposure ages. After Yu et al.[50]

the specifications for ESA-resistance in different standards. Moreover, the absence of a uniform test method on sulfate content in soil makes it tricky to convert the sulfate content in soils to the liquid sulfate concentration for durability design.

The impact of sulfate concentration is well investigated in laboratory studies. A highly concentrated sulfate solution (about 10~50g/L SO_4^{2-}) is usually used in laboratory research[22,38,50,81] to accelerate the attack due to a great concentration gradient and a faster penetration. The laboratory studies[48,50,82] show that the damage is more severe at high sulfate concentrations. As shown in Figure 1.7, the cement mortar exposed to three sulfate solutions shows similar expansion at the beginning 120d and then the expansion of cement mortar in a 30 g/L SO_4^{2-} solution grows much faster than the other two. Santhanam[48] and Naik[37] respectively measured the evolution of expansion of cement mortar and cement paste exposed to different sulfate concentrations, and both studies found that a higher sulfate concentration leads to a larger growth rate of expansion. For the accelerating effect of high sulfate concentration on ESA damage, there are two major explanations. Besides the fast penetration rate induced by a higher concentration gradient, the most prevalent interpretation is that a higher sulfate concentration leads to a larger AFt formation rate. This point is supported by the experimental results in [22]. However, Heller[83] suggested that there is no direct relation between AFt amount and material expansion. Recently, the crystallization pressure theory has been increasingly used to explain the impact of concentration. Yu[50] and Müllauer[22] explained that a more concentrated sulfate solution results in a higher supersaturation of AFt in Eq. (1.6) and a larger crystallization pressure in Eq. (1.23).

Interestingly, the experimental data[50,84] appear to contradict the high penetration rate under high concentrations. Lothenbach[84] measured the sulfate distribution of cement mortar specimens exposed to 4g/L and 44g/L SO_4^{2-} solution using scanning electron microscopy/energy dispersive X-ray spectroscopy (SEM/EDS), and reported that the sulfate contents inside are similar in both sulfate conditions. This phenomenon is explained by the rapid fall in sulfate diffusivity with AFt formation, which inhibits sulfate ingress.

(b) C_3A content

The use of high-sulfate-resistant (HSR) cement, Type V in ASTM C150[85], is a well-known method to improve the resistance of concrete exposed to ESA. The most significant characteristic of Type V cement is the limit on the C_3A content, no more than 5% in mass using the Bogue method[86]. In general, it is believed that a reduced C_3A content in cement can lower the AFt amount formed by the chemical equations in Eq. (1.1), resulting in a less risk for deleterious expansion and a higher resistance of CBM to ESA[5,61,87]. Adding supplementary cementitious materials (SCMs), which contain little C_3A, is an additional technique for reducing C_3A content in cementitious materials. For instance, ACI-318 requires the addition of porzzolan or slag to Type V cement when concrete is subjected to very severe sulfate conditions, above 10,000 mg/L SO_4^{2-} in ground water or 20,000 mg/kg in soil.

However, the influence of C_3A content on the formation rate of AFt is found to be

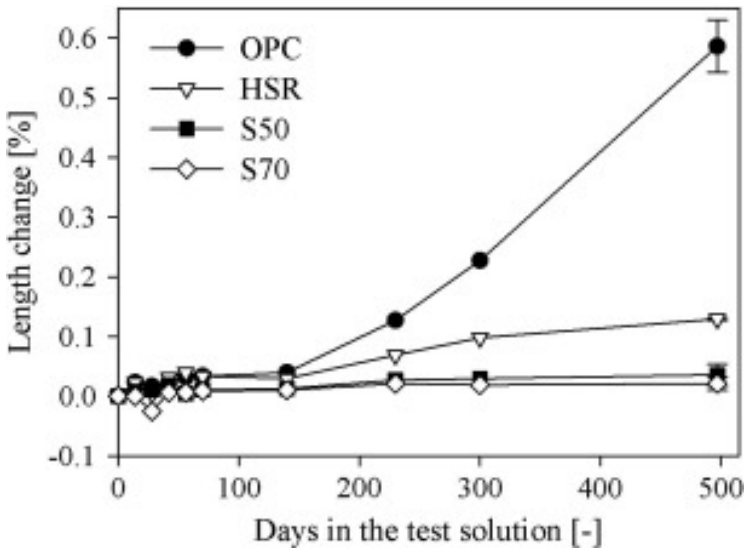

Figure 1.8 Expansion of cement mortar specimens (w/c=0.45) with different mortar mixtures exposed to sodium sulfate solution with a concentration of 50g/L at different exposure ages. OPC stands for ordinary portland cement with a mass C_3A content of 7.92%, HSR for high-sulfate resistant cement with a mass C_3A content of 2.51%, and S50 and S70 for 50% and 70% replacement of OPC by Blase-Furnace Slag. After Maes and De Belie[10].

limited in [22]. As illustrated in Figure 1.3, the kinetic process of AFt precipitation in cement mortars with different C_3A contents is almost the same. Maes[10] reported a smaller AFt amount in cement paste with less C_3A content after 6 months of immersion in a 50g/L Na_2SO_4 solution.

Nevertheless, the mitigating effect of reduced C_3A content on ESA damage was confirmed in literature[10,22,88]. As shown in Figure 1.8, similar expansions occur at the initial 140d and then the mortar specimens prepared by HSR cement show a much slower expansion rate than the mortar specimens prepared by OPC cement.

(c) w/c ratio

Controlling the concrete mix is the major approach used in standards to improve the resistance of concrete to ESA. The w/c ratio of CBM affects the permeability and strength of CBM. A higher w/c ratio results in an increased permeability of CBM and a reduced resistance of CBMs to ingress of aggressive agents. The mitigating effect of reducing w/c on ESA damage is confirmed in literature[37,49,73,89]. As shown in Figure 1.9, a lower w/c ratio of OPC mortar specimens leads to a much smaller expansion rate. Mehta[73] suggested that the permeability of CBM rather than the C_3A content is the most important factor controlling the resistance to ESA. Monteiro and Kurtis[89] found that even for concrete mixture with a 8% C_3A content the low w/c ratio as 0.45 could enhance the performance of concrete.

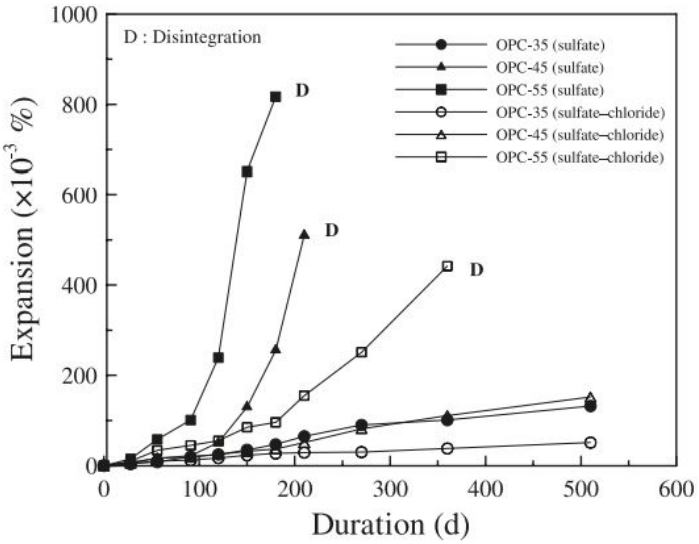

Figure 1.9 Expansion of cement mortar specimens with different w/c ratios exposed to a single sulfate solution and a mixed sulfate and chloride solution at different exposure ages. OPC stands for Ordinary Portland Cement, and 35/45/55 for w/c ratios of 0.35, 0.45, and 0.55. After Lee et al.[49].

Besides controlling the w/c ratio, a minimum cement content is required in British standard EN 206-1[90] and Chinese standard GB/T 50476[91]. In addition, American standard[92] gives the requirements on cement type when concrete is exposed to ESA.

(d) Size of pecimens

The standard size of cement mortar specimens for resistance tests in American standard ASTM C1012[93] and Chinese standard GB/T 749[94] is 25×25×285mm. Cohen and Bentur[95] suggested different failure limits for cement paste beams and cubes. Tumidajski and Turc[96] found the diffusion and expansion results are sensitive to specimen size and geometry.

The effect of specimen size on ESA is basically the impact of specimen surface area per unit volume. A greater specific surface promotes sulfate penetration. Specimens' geometry has a substantial effect on the damage rate. For example, the damage is more severe in the specimens' corners and edges than in the specimens' surfaces because of more directions for ion penetration. The specimens' size effect on ESA has been systematically investigated in literature[97-98]. As shown in Figure 1.10, Fathima Suma et al.[97] detected the evolution of expansion of prismetric cement mortar specimens with different sizes immersed into 5% Na_2SO_4 solution. Obviously, the smaller the size, the higher the expansion strain.

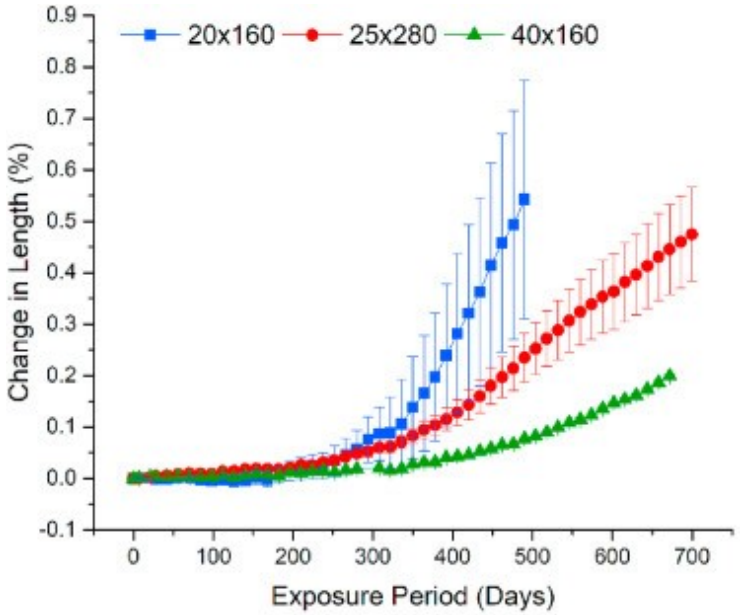

Figure 1.10 Expansion of cement mortar specimens (w/c=0.5) with different specimens size exposed to 5% Na_2SO_4 at different exposure ages. The former number is the size of the bottle's side, and the latter number is the length of the specimen. After Fathima Suma et al.[97].

1.2 Coupling actions with ESA

As aforementioned, sulfate ions coexist with other aggressive anions and cations in natural environments. Recent research has shown a growing interest in the coupling effects between pure sulfate attack and other actions, such as chlorides[10,99], leaching[100-101], magnesium[37] and bicarbonate[47]. Among these coupling actions, the leaching and chloride actions are the two most common actions coexisting with ESA in engineering practice: chlorides are normally present along with sulfates in natural environments such as seawater, saline soils, and some groundwater, and these environments have nearly neutral pH values[19,99]. These coupled actions more or less change the chemical mechanism of ESA, and the available knowledge is reviewed in this section.

1.2.1 Delayed ettringite formation (DEF)

The DEF is defined as the deterioration of CBM due to the formation of AFt after the hardening of cement paste[102]. In contrast to ESA, the source of sulfates in DEF is from the material itself. In a typical Portland cement hydration process, the gypsum supplied to control the setting time first interacts with C_3A to generate AFt. Then after the gypsum is consumed up and there is an excess of C_3A, the AFt reacts with the C3A to form the monosulphoaluminate:

$$\begin{cases} C_3A + 3C\bar{S}H_2 \longrightarrow C_6A\bar{S}_3H_{32} \\ 2C_3A + C_6A\bar{S}_3H_{32} + 3H \longrightarrow 3C_4A\bar{S}H_{12} \end{cases} \tag{1.26}$$

Such hydration process has been observed through XRD: an ettringite peak was detected within a few hours and increased in 1d, and then this peak decreased in the next few days[103]. The content of the primary AFt at the end of curing depends on the cement composition and the curing conditions. When CBM experience a heat-treatment (typically above temperature of 65°C[104]), the primary AFt is decomposed into hydrated calcium monosulphoaluminate and release sulfate ions into the pore solution. The released sulfates are partially adsorbed on the CSH surface[105-106] and this adsorption is physical[107].

The sulfate sorption is found to follow a Langmuir law[108], and the sulfate sorption capacity of CSH rises with temperature[109-110]. As shown in Figure 1.11, the reduction of gypsum peak with hydration time was evidently accelerated by the elevated temperature, showing that the adsorption of sulfates onto CSH increased with temperature. Therefore, following heating treatment, the temperature decreases during the subsequent storage un-

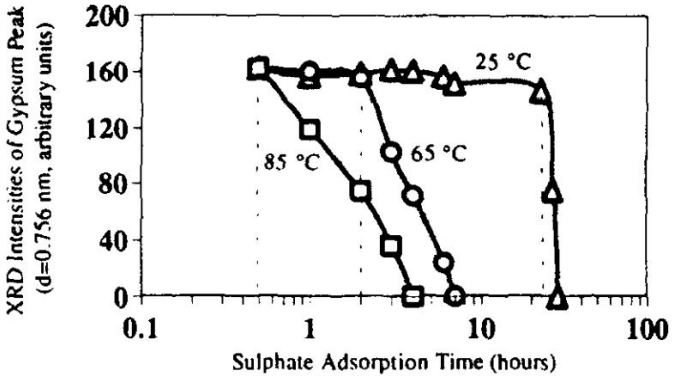

Figure 1.11 Gypsum intensity peak (in XRD) of samples mixing C_3S hydrates and gypsum in XRD with different curing temperature at different time. After Fu et al.[109].

der cooling conditions, causing the trapped sulfates on the CSH surface to be released back into pore solution, and the free sulfates to react with hydrated calcium monosulphoaluminate to create AFt once again. After such a heat-cool cycle, the AFt formation is delayed and occurs in the solid matrix, resulting in internal stress, material swelling, cracking, and a reduction in mechanical resistance.

The damage caused by DEF to CBM appears mostly as expansion, cracking, and loss of strength. Leklou et al.[111] observed a conspicuous formation of ettringite in cracks and the interfacial transition zone (ITZ). Zhang et al.[112] detected the progressive reduction in the dynamic modulus resulting from the cracking and expansion in DEF-damaged mortar. Escadeillas et al.[113] reported the loss of flexural and compressive strength in heat-cured mortars. What's more, a weight gain associated with the specimens' expansion is found in literature[112,114], which is due to the suction of external solution during the process of expansion and cracking[112]. Figure 1.12 shows a typical expansion curve of heat-treated specimens. This expansion curve shows in three stages: the latent stage, the accelerated stage, and the plateau stage. In the first latent stage, the expansion grows slowly until a critical value of 0.1-0.2%, which depends on the thermal history of the heating treatment and the mineral composition of cement. In the second stage, the expansion rate is accelerated by the appearance of cracks, and the expansion stops at the inflection point. In the last plateau stage, the expansion rate decreases to zero and the expansion stabilizes at a constant value. The plateau is due to the exhaustion of sulfates with time.

The DEF usually occurs in massive concrete, which is defined in ACI-331R[116] as "Any volume of concrete with dimensions large enough to require that measures be taken to cope with the generation of heat from hydration of the cement and attendant volume change to minimize cracking". For massive concrete, the heat originated from the cement

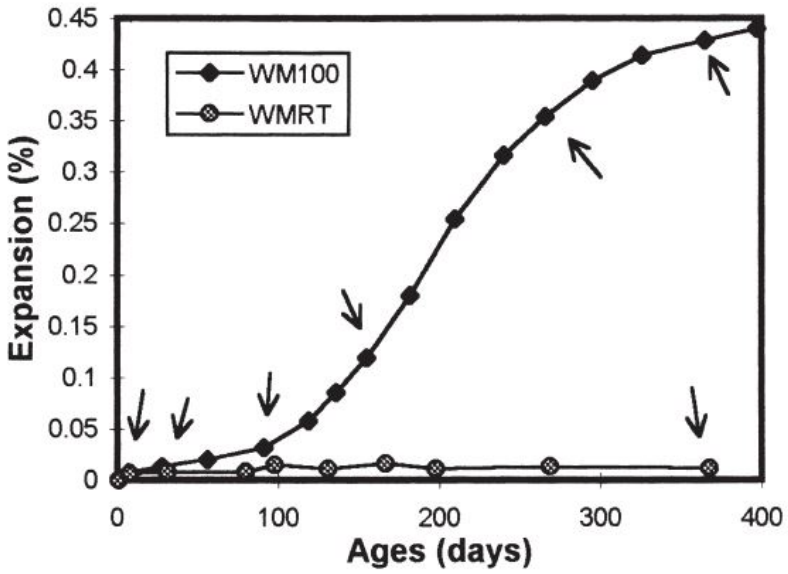

Figure 1.12 Expansion of cement mortar specimens (w/c=0.5) with different heat-treatments during curing and after being immersed in water. WM100 stands for the heat treatment at 100°C, WMRM stands for a curing at room temperature(about 20°C). The arrows represent the time to cut specimens for microstructural observation. After Yang et al.[115].

hydration dissipates slowly inside and raises the temperature of the concrete structure inside, resulting in a substantial temperature difference between the outside and inside. According to Divet and Pavoine[108], the temperature in massive concrete may exceed 70°C, which is high enough to provoke DEF in concrete. Some research[117-118] confirmed that the DEF damage occurred in massive concrete components, such as bridge piers and dams, rather than some thinner components.

A considerable number of models have been proposed to simulate the DEF damage in the literature. Flatt[119] proposed a thermodynamic model to estimate the hydrostatic tensile stress in the pore solution by estimating the supersaturation. The supersaturation of ettringite is evaluated through the thermodynamic equilibria of solid phases in cement paste. Brunetaud[120] suggested a parametric model to estimate the DEF-induced expansion based on experimental parameter analysis. Gu et al.[31] developed a poromechanical model based on an interface-controlled crystal growth mechanism to simulate the ettringite formation and expansion growth during DEF.

In some circumstances, there is a possibility of having both ESA and DEF. For example, a massive concrete component is completely buried in an environment containing sulfates, such as saline soil or some groundwater. In this situation, the sulfates to form the AFt after the hardening of cement paste originate from both the external environment and the internal sources, the released bound sulfates from CSH. Thus the AFt formation in the

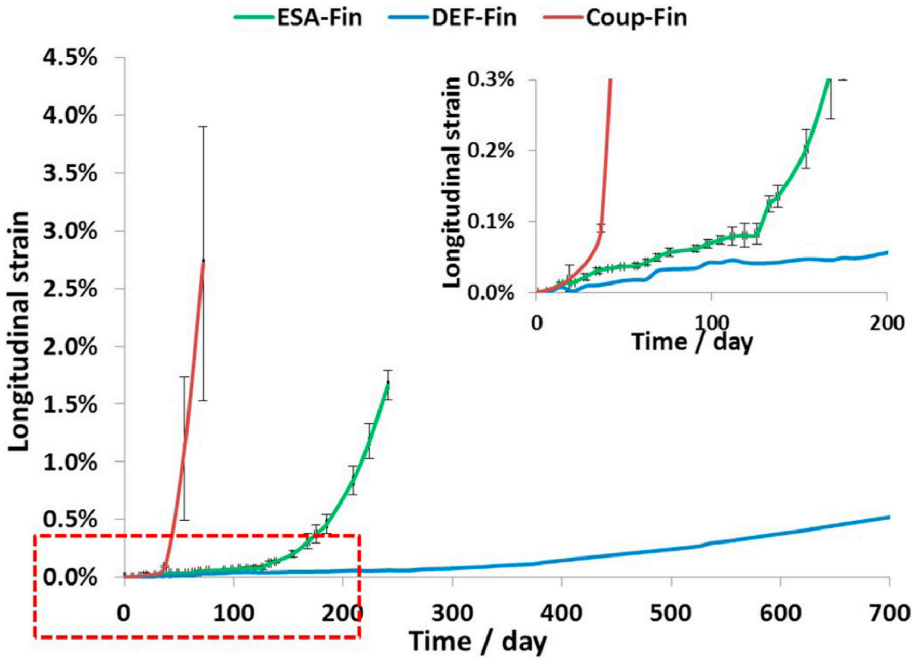

Figure 1.13 Expansion strain of cement paste prisms (w/c=0.55) exposed to ESA, DEF and the Coupling effect at different exposure ages. After Gu et al.[12].

combined ESA and DEF condition is faster than in single ESA or single DEF. In addition, the modified pore structure resulting from heat treatment allows quicker sulfate penetration compared to the sulfate ingress under ESA. Therefore, the combined condition is the most harmful type, which should be considered for the massive concrete exposed to ESA. In the literature, however, few studies have been conducted on the topic.

Gu et al.[121] systematically studied the synthetic effects of ESA and DEF. Cement paste specimens were made to expose them to three conditions (ESA, DEF and ESA + DEF), and were measured by micrometer for length change and by mercury intrusion porosimetry (MIP) for pore structure. First, the pore structure of cement paste was modified by heat treatment. According to MIP results, there was a larger porosity and more micropores (3.7-100nm) in the coupling specimens compared to the ESA specimens before immersion into sulfate solutions. And much more macropores (>100nm) were observed in the coupling specimens compared to ESA specimens at the end of attack. As shown in Figure 1.13, the coupling specimens show a much faster expansion rate in comparison with ESA specimens.

1.2.2 Chlorides

In civil engineering, chloride ingress is one of the most important concerns of durability of the reinforced concretes exposed to seawater and de-icing salts. The mechanism

by which the chloride ions attack the reinforced concretes has been well-investigated: the chlorides from external sources depassivate the steel reinforcement in concrete and initiate the corrosion with pitting patterns[122-123]. During the chloride ingress, a portion of chlorides react with hydrates of hardened cement paste (mainly with aluminum hydrates), a portion of chlorides form are absorbed by the cement matrix, and the remainder, known as free chlorides, reach the position of steel reinforcement and initiate its corrosion[124]. The product of the chemical reactions between the chlorides and the cement paste is Friedel's salt ($C_3ACaCl_2H_{10}$)[125],

$$\begin{cases} C_3A + CH + 2Cl^- \longrightarrow C_3ACaCl_2H_{10} + 2OH^- \\ 3C_4AF + 4CH + 8Cl^- \longrightarrow 4C_3ACaCl_2H_{10} + 2[(A,F)H_3] + 8OH^- \\ C_4AH_{13} + 2Cl^- \longrightarrow C_3ACaCl_2H_{10} + 2OH^- \\ C_4A\bar{S}H_{12} + 2Cl^- \longrightarrow C_3ACaCl_2H_{10} + SO_4^{2-} \end{cases} \tag{1.27}$$

A comparison between Eq. (1.1) and Eq. (1.27) reveals a competition mechanism between the sulfates and chlorides for aluminum hydrates[10]: both of them need to bind with aluminum hydrates to form AFt and Friedel's salt, respectively. Stroh et al.[126] proposed a mechanism of the phase developments under combined sulphate and chloride

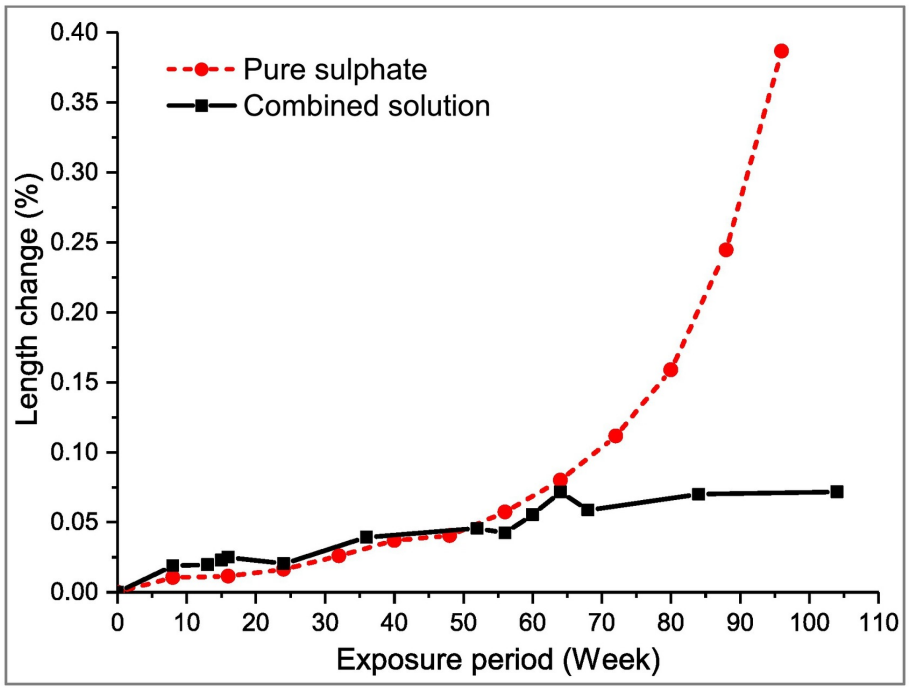

Figure 1.14 Expansion of cement mortar specimens (w/c=0.5) exposed to pure sulfate solution and combined sulfate and chloride solution at different exposure ages. After Ukpata et al.[99].

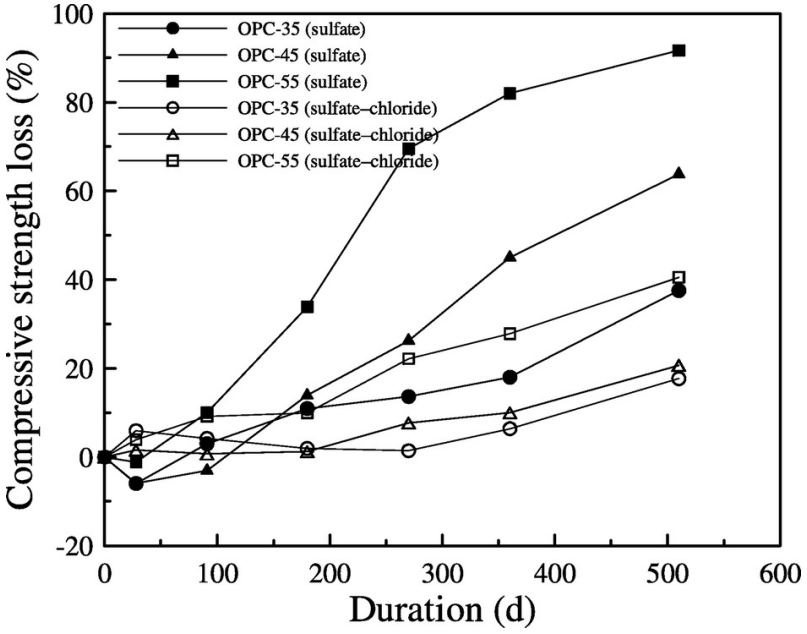

Figure 1.15 Compressive strength loss of cement mortar specimens with different w/c ratios exposed to pure sulfate solution and sulfate-chloride solution at different exposure times. OPC stands for Ordinary Portland Cement, and 35/45/55 for w/c ratios of 0.35, 0.45, and 0.55. After Lee et al.[49].

actions based on synchrotron XRD results: upon penetration, the chlorides diffuse faster in CBM than sulfates, bound by aluminum hydrates to form Friedel's salts; the sulfates, arriving after, convert the Friedel's salts into AFt. The formation of Friedel's salts under combined sulfate-chloride solutions was thought to be the cause of the reduction of AFt formation rate by chlorides. Indeed, when subjected to combined solution, aluminum hydrates are found to be more readily converted to Friedel's salts than AFt[127-128]. However, the formed Friedel's salts are found to be converted into AFt afterwards[129-130]. Therefore, it is difficult to tell whether the formation of Friedel's salt affects the formation of AFt. What's more, there is few experimental data in the literature that supports the idea that chlorides can slow down the AFt formation rate.

Another mechanism accounting for the inhibiting effect of chlorides on AFt formation in literature[49,131-132] was proposed as the reducing effect of chlorides on the solubility of AFt. Corner et al.[133] reported that the solubility of AFt in sodium chloride solution was three times greater than in water. This significant increase in solubility of sparingly soluble electrolytes, such as AFt, in a solution of another soluble electrolyte compared to water has been well reported. Actually, this is because the ionic activity coefficients of ions drop as total aqueous ionic strength increases[134]. Taking the gypsum as example, the activity of calcium and sulfate ions is reduced from 0.60 in water (calculated using

Debye-Hückel equation[135]) to 0.16 in 3.08M NaCl solution (calculated using Extended Debye-Hückel equation[136]), and thus a higher calcium and sulfate concentrations are needed to maintain dissolution equilibrium of gypsum in 3.08M NaCl solution compared to in water. However, such a significant change is only valid for dilute solutions. Indeed, the pore solution in hardened ordinary cement paste at 25 ^{o}C can hardly be considered as a dilute solution, and its ionic strength ranges between 0.25 and 0.50M[137]. The addition of 0.03M and 0.54M NaCl, typically chloride concentrations in groundwater and seawater[138], lowers the activity coefficient of divalent ions by 1.8% and 30% (calculated by [139]). Thus, the addition of chlorides into pore solution cannot substantially increase the solubility.

As for physical adsorption, there is also a competition between the sulfates and chlorides for CSH. De Weerft et al.[140] obtained the content of bound chlorides by CSH through comparing the total chloride content with the chemically bound chlorides content. The former was experimentally measured with a potentiometric titrator, and the latter was predicted by GEMs[139] with the assumption that all the possible AFm phases transformed to Friedel's salts. The results show that the sulfates can reduce the chloride binding because CSH incorporates more of the sulfates than the chlorides. This finding agrees with the simulation results by Tran et al.[141], who proposed a multi-ion adsorption model on the CSH surface.

Although experimental evidence for the role of chlorides on the AFt formation rate is lacking, the mitigating effect of chlorides on ESA damage is well accepted. The expansion of mortars in the presence of both chloride and sulfate is much less than in the pure sulfate solution[99,131,142-143], and the presence of chlorides reduces the compressive strength loss of mortars caused by ESA[49,131,142,144]. Figure 1.14[99] shows the expansion in the pure sulfate solution increases more rapidly than in the combined chloride and sulfate solution. Figure 1.15[49] shows the mitigating effect of chlorides on the strength loss for three w/c ratios. Considering the obvious inhibiting effect of chlorides on the ESA damage, improving the understanding of its mechanism is important to the correct estimate of the service life of structural concrete exposed to combined sulfate and chloride actions. Yu et al.[145] developed a coupled model based on the antagonism effect between ESA and chloride ingress. The antagonism effect consisted of the chemical competition between sulfates chlorides and aluminum hydrates through multi-phase equilibria. But this model was used to simulate the influence of sulfates on the penetration of chlorides

and the resulting steel corrosion, rather than the impact of chlorides on the ESA expansion damage.

1.2.3 Leaching

The typical pH value of pore solution is around 13 for low alkali cements and around 13.5 for high alkali cements[146]. Compared to the high pH value in the pore solution of hardened cement paste, the aqueous sulfate-containing environments (seawater and some groundwater) have a relatively low pH value (7-8). Under external conditions of low pH, the calcium phases (CH, CSH) that are stable at high pH are leached from CBM due to the transport of calcium and hydroxide ions under concentration gradients. In laboratory studies on ESA, low pH test solutions are replaced frequently to maintain constant sulfate concentrations due to the consumption of sulfates during ESA[93]. The study of Brown et al.[100] confirmed the out migration of hydroxide ion from cement mortars, and the rise of pH value as shown in Figure 1.16 appeared to decelerate the leaching process. A pH cycle from 7 (new test solution) to 12-13 (the test solution before replacement) was also observed in [100]. Therefore, leaching is the most common accompanying process for ESA both in laboratory studies and in the field, but its effect on ESA is seldom investigated separately.

The leaching, associated with the dissolution of CH and decalcification of CSH, results in an increase of ionic diffusivity[147-148] and a decrease of material strength[149-150]. The former leads to a reduction in the resistance of materials to the penetration of aggressive ions, and the latter causes a reduction in the materials' resistance to mechanical deformation. Under the combined action between ESA and leaching, the sulfate ingress is accelerated due to the increased diffusivity, and the AFt amounts needed for expansion are reduced due to the reduced strength. Both effects together result in a reduction of the time to reach a critical level of expansion. In addition, the leaching of hydroxide ions decreases the pH value of the pore solution in CBM, which impacts the stability of calcium sulphoaluminate hydrates. According to Garbrisová[151], the pH values for the stable existence of AFt and monosulfate are 10.7 and 11.6, respectively. At lower pH values, only gypsum and aluminum sulfate are present in the cement system. The dissolution of AFt in the surface zone of CBM exposed to the combined leaching and ESA actions due to the leaching-caused low pH value was confirmed in experimental studies[25,37,152-153]. Thus, leaching seems to have two opposite impacts on ESA: on the one hand, the leaching weakens material strength and promotes the penetration of sulfate ions, which aggravates

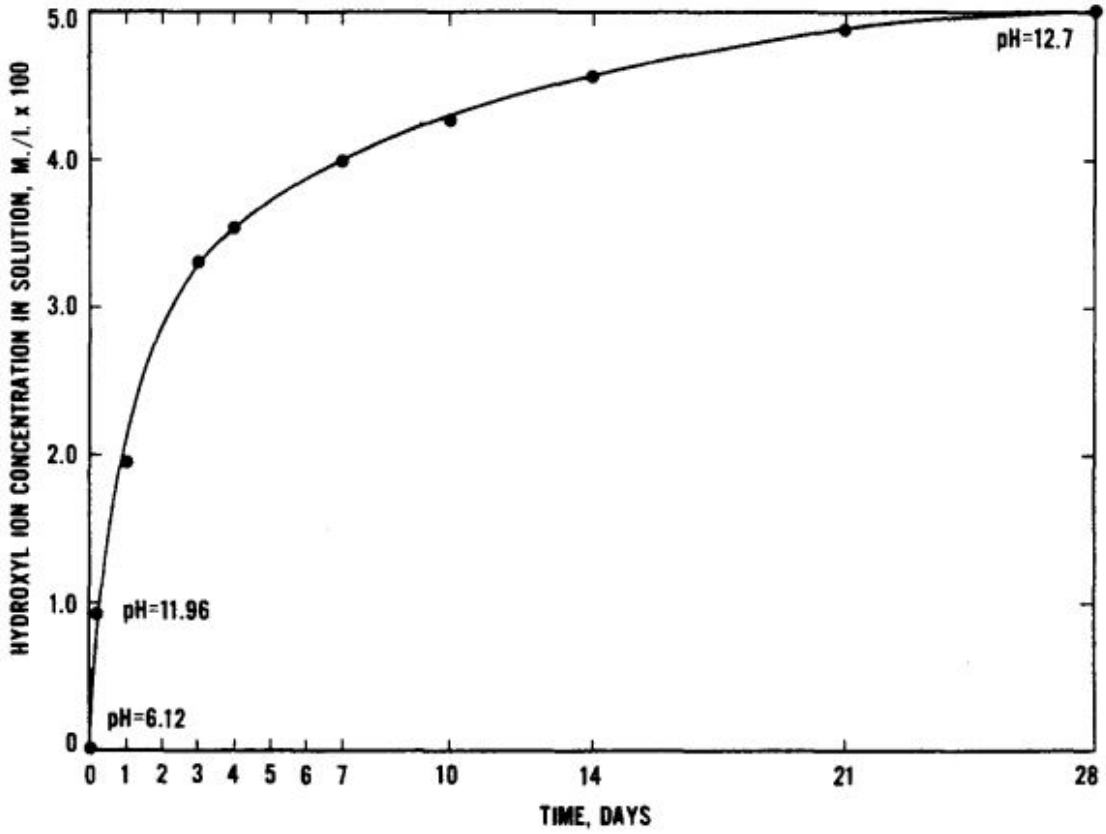

Figure 1.16 Hydroxyl ions concentration in test solution immersing cement mortar specimens (w/c=0.5) with immersion time. The volume ratio of specimens to solution is 3:1. After Brown[100].

ESA; on the other hand, the leaching destroys the stability of AFt and lowers the internal expansion stress, which retards ESA.

Due to the increasing hydroxide ion concentration in the test solution, the leaching process is prevented until the replacement of the test solution. Brown et al.[100] used an apparatus, which is composed of a pH electrode and a pH meter, to regulate the pH value of a test solution by adding sulfuric acid. As shown in Figure 1.17, the cement mortar specimens exposed to sulfate conditions for pH values below 11.5 expand much more quickly than those exposed to uncontrolled pH conditions. Ferrairs et al.[154] compared the expansion of specimens in controlled and uncontrolled pH conditions and also reported that the expansion rate at the second stage of expansion curves for the uncontrolled pH condition was twice as much as that in the controlled pH conditions.

Xiong et al.[101] confirmed the accelerating effect of leaching on ESA damage on mechanical properties. Four conditions were set in this study: saturated limewater with pH of 12.69 (as reference), 5% Na_2SO_4 with pH of 7.31 and 33.8g/L SO_4^{2-} (ESA), 5% $(NH_4)_2SO_4$ with pH of 5.74 and 36.4g/L SO_4^{2-} (ESA+leaching), and 5% NH_4Cl with pH

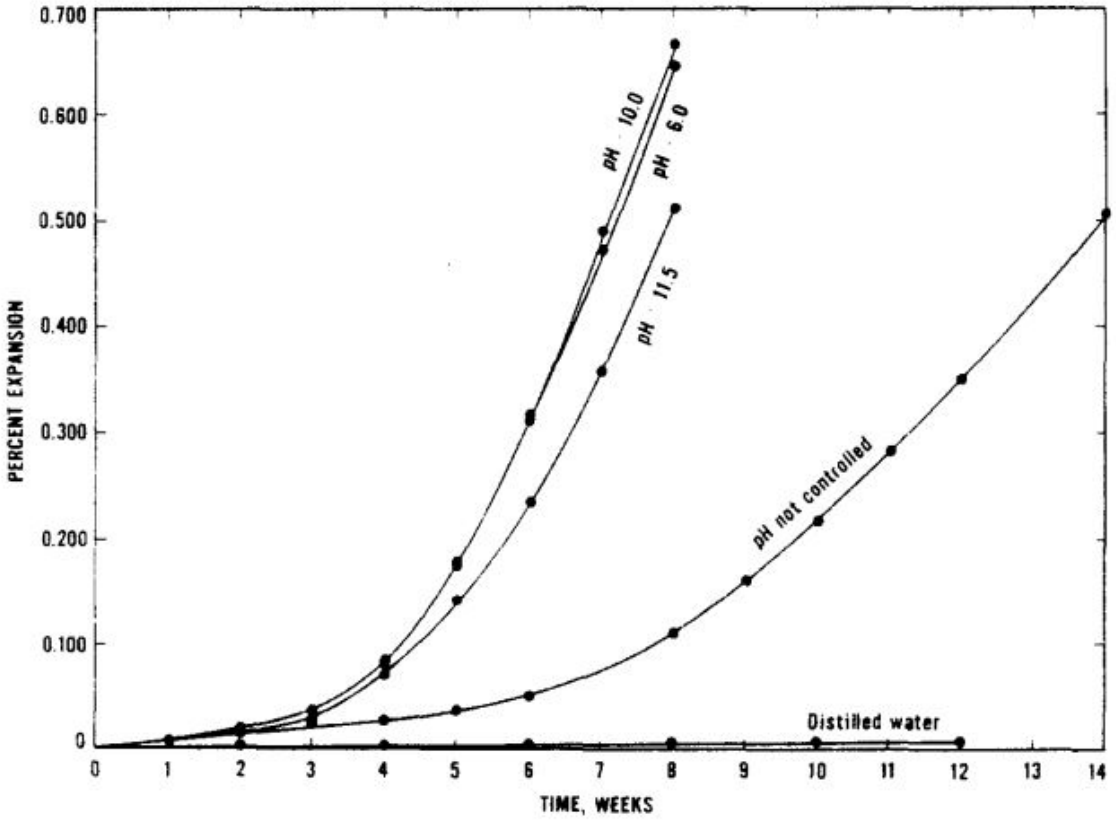

Figure 1.17 Expansion of cement mortar specimens (w/c=0.5) immersed into different conditions at different exposure ages. The experimental conditions include: distilled water, 0.35M Na_2SO_4 without pH control, 0.35M Na_2SO_4 with a controlled pH value at 6, 10 or 11.5. After Brown[100].

of 5.74 (leaching). The Vickers hardness of cement pastes exposed to such four conditions at different exposure depths and exposure times was measured by a Micro-hardness Tester. The results presented in Figure 1.18 show that the reduction of Vickers Hardness in the combined leaching and ESA condition is more severe than in the single ESA or the single leaching condition.

Besides, the leaching effect on ESA has been taken into account in several numerical models[42,155] through chemical equilibria between solid phases in the matrix and ionic species in the pore solution, and the simulation results show a dominant role of leaching on the damage process induced by ESA. Qin et al.[27] adopted a second-order kinetic law for the formation of AFt and gypsum and a classical solid-liquid equilibrium model for the leaching of CH and CSH[156-157]. The results[27] showed the significant accelerating effect of calcium leaching on ESA and suggested this effect must be taken into consideration for ESA.

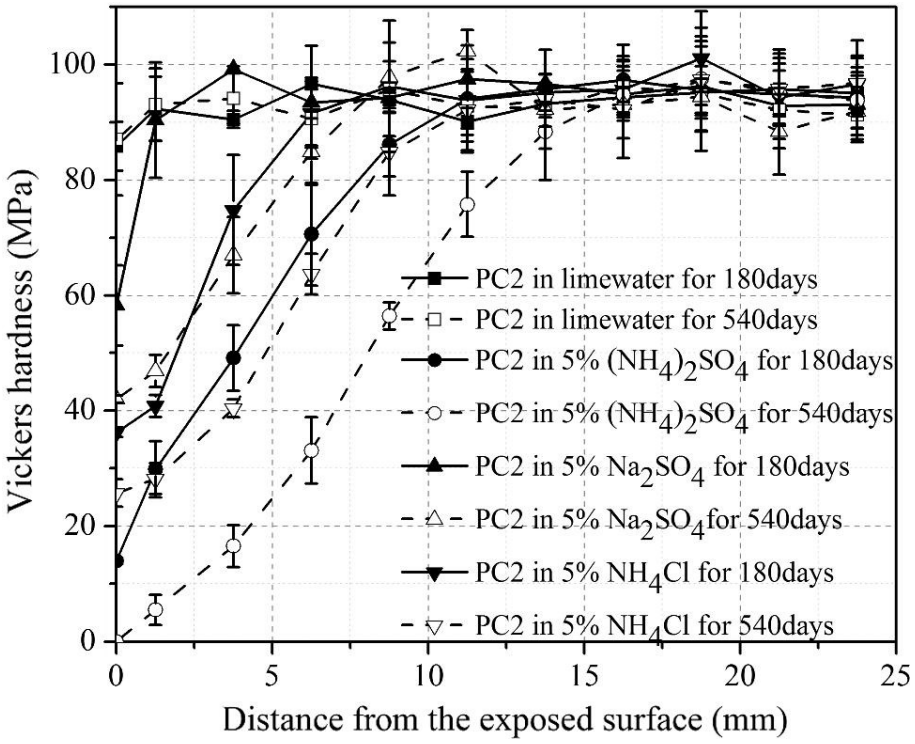

Figure 1.18 Vickers hardness on the cross section in the diffusion direction of cement paste (w/c=0.45) exposed to three different solutions with different exposure depths. The pH values of limewater, 5% Na_2SO_4 (33.8g/L SO_4^{2-}), 5% $(NH_4)_2SO_4$ (36.4g/L SO_4^{2-}) and 5% NH_4Cl are 12.69, 7.31, 5.74 and 5.18. PC2 stands for the cement paste a water/cement ratio of 0.45. After Xiong et al.[101].

1.2.4 Other actions

Except for the aforementioned actions, there are still other actions coupled with ESA but less frequently encountered, such as magnesium, bicarbonate, carbonation, freeze-thaw actions, and drying-wetting cycles. Here we only review the first two actions from the state-of-art knowledge.

(a) Magnesium

Until now it is still unclear whether the magnesium sulfate ($MgSO_4$) leads to a more severe damage than sodium sulfate (Na_2SO_4). Two opposite schools of thought were found in the literature. Magnesium hydroxide (MH) precipitates out of the pore solution due to its low solubility[158]. As portlandite is consumed, the pH of the pore solution is lowered with the decalcification of CSH. In addition, the magnesium may replace the interlayer Ca^{2+} of CSH to produce MSH or CMSH, which lose the cementitious proper-

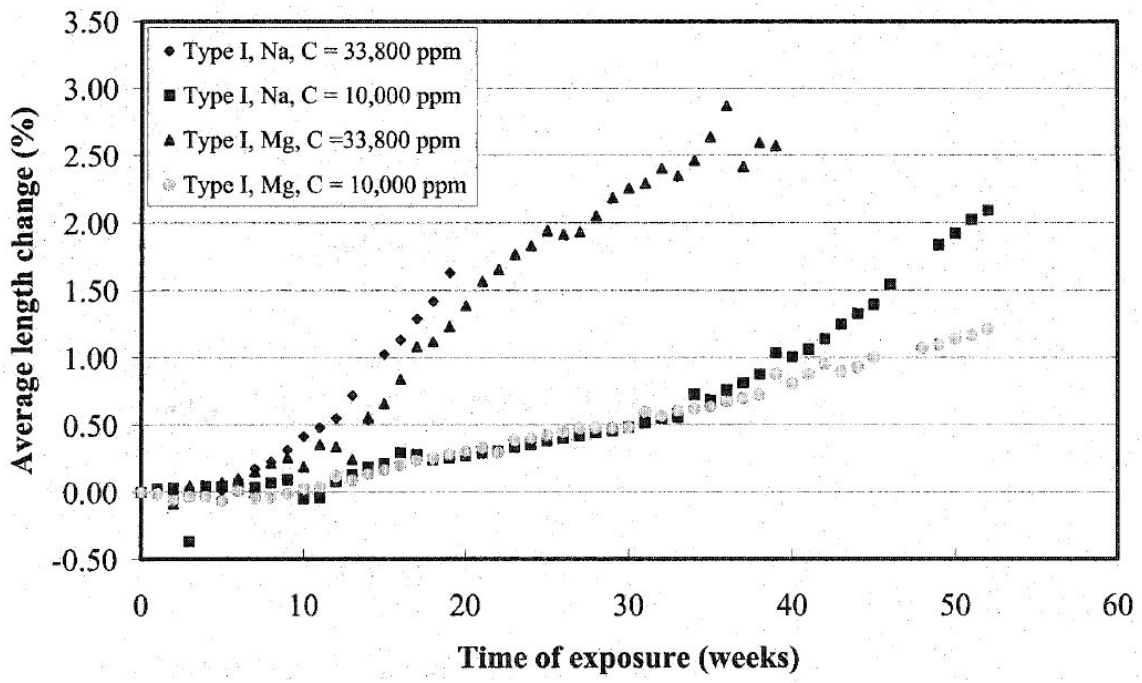

Figure 1.19 Expansion of Type I cement mortar specimens (w/c=0.485) exposed to sulfate solution with different concentrations and different cations at different exposure ages. After Naik[37].

ties[158],

$$\begin{cases} Mg^{2+} + CH \longrightarrow MH + 2Ca^{2+} \\ Mg^{2+} + CSH \longrightarrow MSH + Ca^{2+} \end{cases} \tag{1.28}$$

Thus, magnesium sulfate attack is thought to be more severe than sodium sulfate attack by compromising the adhesion and strength in the cement matrix[158-159].

However, Bonen et al.[160-161] observed a distinct band of brucite on the surface of specimens,cf Figure 1.20, and proposed that the precipitation of magnesium hydroxide causes pore blocking, suppressing the diffusion of sulfate ions. The dense band of brucite protects the interior zone of CBM against ESA. Besides, the precipitation of brucite leads to the reduction in the pH value of the pore solution, which causes the decomposition of AFt into gypsum and gibbsite[158]. Hence, magnesium sulfate may be less aggressive than sodium sulfate[160-162].

Naik[37] systematically compared the sodium sulfate attack and magnesium sulfate attack. The cation type was found to have a significant influence on the chemical products and the damage mode: in sodium sulfate, the major products are AFt and gypsum, and the dominant form of degradation in CBM is expansion, cracking and spalling; however, in magnesium sulfate, a double layer composed of outer brucite and inner gypsum at the surface zone of materials was confirmed, and the dominant form of degradation is loss

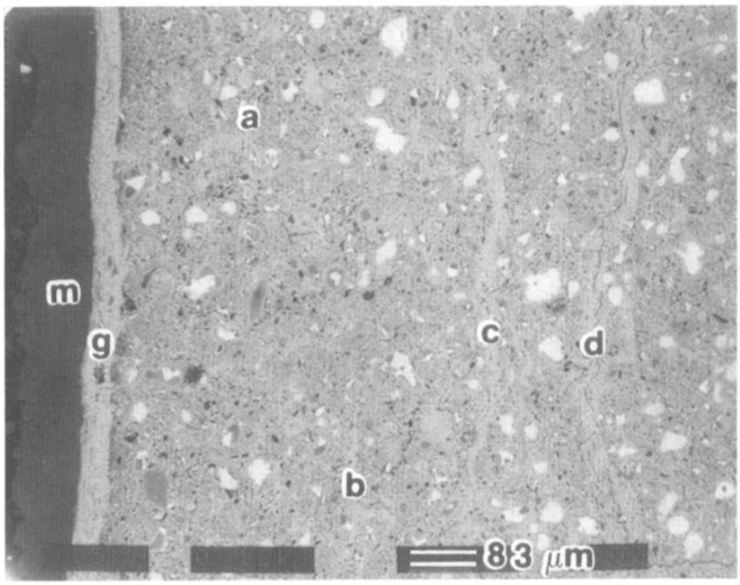

(a)

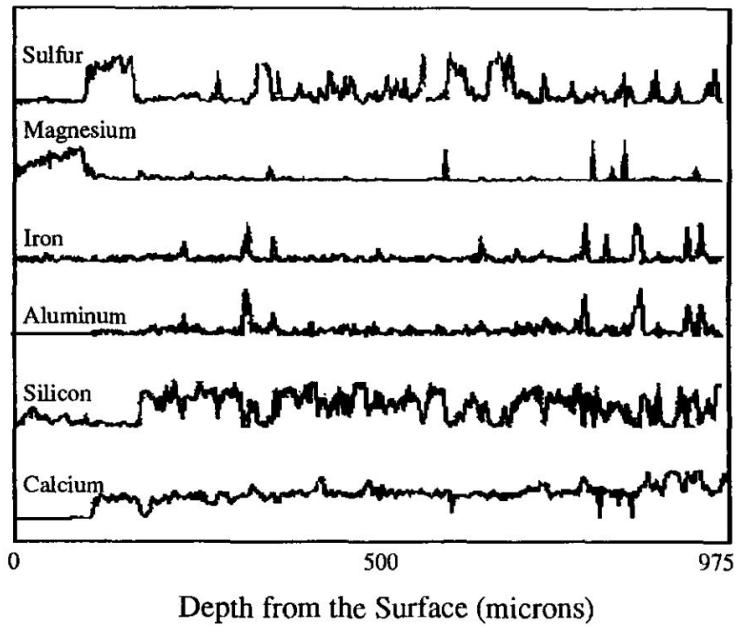

(b)

Figure 1.20 Backscatter Electron Imaging (BSI) (a) and EDS image (b) of cement paste exposed to 2.1% magnesium sulfate solution. In figure (a), there is a dark, dense band of brucite (m) and ligh grey gypsum (g). After Bonen et al.[160].

of mass and strength. As shown in Figure 1.19[37], both in 33800 ppm and 10000 ppm sulfate solutions, the expansion in magnesium sulfate is slightly smaller than in sodium sulfate attack, indicating a less severe damage in magnesium sulfate attack.

(b) Bicarbonate

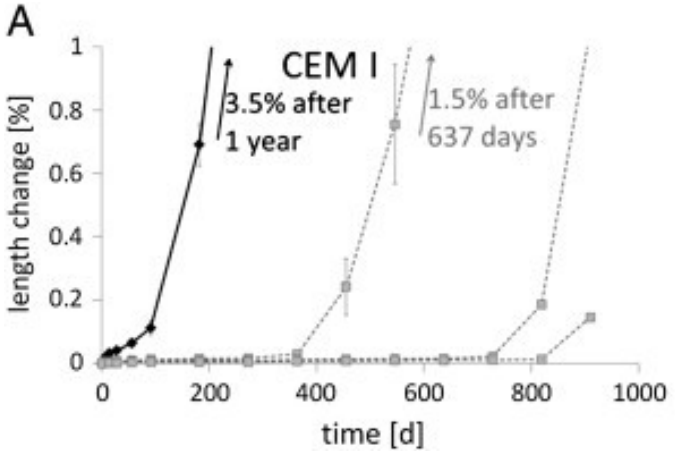

Figure 1.21 Expansion of cement mortar specimens (w/c=0.55) immersed into sulfate solution (black) and mixed sulfate and bicarbonate solution (grey) at different exposure ages. After Kunther et al.[47].

In regions containing carbonate rocks and soils, the groundwater may include up to 1000 mg/L of bicarbonates (HCO_3^-)[163]. It was believed that the carbonated concrete has a better performance in terms of ESA resistance[164-165] due to the reduction of available CH content[166-167]. Similar to the effect of carbonation, the bicarbonates were found to substantially inhibit the ESA damage[47]. As shown in Figure 1.21[47], the expansion is significantly mitigated in the combined bicarbonates and sulfates solution compared to in the single sulfate solution. Kunther et al.[47] explained that the AFt becomes unstable and no gypsum is formed in the presence of bicarbonate ions. UUsing thermodynamic modelling, the pH value in the combined solution is predicted to be around 9-10, which is lower than the value in pure sulfate solution (12.5-13.1), and the AFt will decompose under such pH conditions.

Table 1.4 Coupling actions with ESA in natural environments.

Coupling action	Effect on ESA	Mechanism
DEF	Aggravating	Supplying more sulfates from CBM itself besides from environment
Chlorides	Mitigating	Unproven: delaying the AFt formation
Leaching	Aggravating	Two-fold: promoting sulfate ingress and decreasing material strength but dissolving AFt
Magnesium	Slightly mitigating	Two-fold: inhibiting sulfate ingress but dissolving CSH
Bicarbonate	Mitigating	Dissolving AFt by reducing pH value

1.2.5 Summary

Table 1.4 summarizes the common coupling actions with ESA in natural sulfate-bearing environments. The aggravating effect of DEF and the inhibiting effect of bicarbonate are well explained in the literature, while the mechanisms accounting for the mitigating effect of chlorides and the aggravating effect of leaching on the ESA damage are still not clearly addressed.

1.3 Basis of poromechanics

In Section 1.1.3, the crystallization pressure is estimated through the thermodynamic equilibrium. Nevertheless, the estimated crystallization pressure is local and microscopic. A poromechanical approach to correlate this microscopic stress with the macroscopic mechanical characteristics of CBM with the fracture criteria has been developed by Coussy[33]. This section provides a brief introduction to the poromechanical approach.

In this study, the porous materials are assumed to be saturated by the liquid solution and solid crystals, denoted by L and C. And the properties related to these two phases are distinguished by subscripts L and C. Considering the existence of a liquid film between the crystals and pore walls as in Figure 1.6, the pressure actually exerted by the crystals on the solid matrix on the internal pore walls is the sum of the disjoining pressure and the liquid pressure in Eq. (1.24), and no shear stress is imposed on the solid matrix. Therefore, the crystal phase is regarded as a second fluid phase besides the liquid solution in the porous space.

1.3.1 Partial Lagrangian porosities and deformation

Let us introduce a representative elementary volume (REV) for porous material. For porous materials, a REV is defined as the smallest volume, over which the physical parameters are statistically meaningful[168] and the measurement yields a value representative of the whole[169]. The following discussions are based on the REV, whose volume is denoted as $d\Omega$. The porosity is the fraction of porous space to the material's volume.

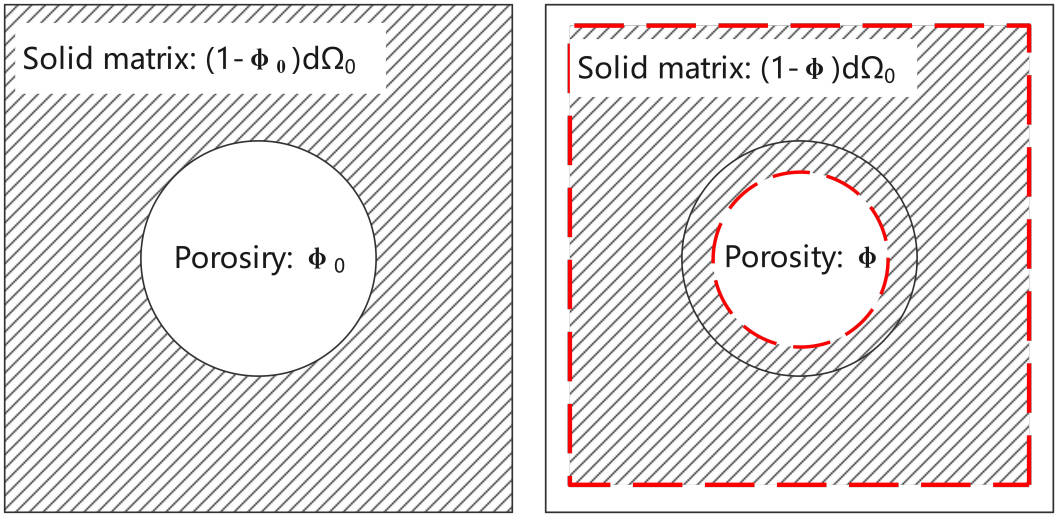

Figure 1.22 Scheme of the porous material before (a) and after deformation. $d\Omega_0$ is the volume of porous material, and ϕ is the Lagrangian porosity.

Normally, there are two ways of expressing porosity: Eulerian porosity n relates the pore volume to the current material volume; Lagrangian porosity ϕ relates the the pore volume to the initial material volume $d\Omega_0$ (see in Figure 1.22),

$$nd\Omega = \phi d\Omega_0 \tag{1.29}$$

The change in porous space is given by $(\phi - \phi_0)d\Omega_0$, where ϕ_0 is the initial Lagrangian porosity. Use the notation φ to denote the change in Lagrangian porosity,

$$\varphi = \phi - \phi_0 \tag{1.30}$$

Theoretically, the volume dilation of porous material ϵ can be split into two parts: the volumetric dilation of solid matrix ϵ_S, and the volumetric dilation of porous volume φ/ϕ. The former is defined through the change in volume of solid matrix $d\Omega^S$,

$$d\Omega^S = (1 + \epsilon_S)d\Omega_0^S \tag{1.31}$$

where

$$d\Omega^S = (1 - n)d\Omega; \quad d\Omega_0^S = (1 - \phi_0)d\Omega_0; \quad d\Omega = (1 + \epsilon)d\Omega_0 \tag{1.32}$$

Combining Eqs. (1.29)-(1.32) gives the expression of volumetric dilation,

$$\epsilon = (1 - \phi_0)\epsilon_S + \varphi \tag{1.33}$$

Eq.(1.33) shows that the dilation of porous space and solid matrix, ϕ/ϕ_0 and ϵ_S, are weighted by their volume fractions ϕ_0 and (1-ϕ_0), respectively.

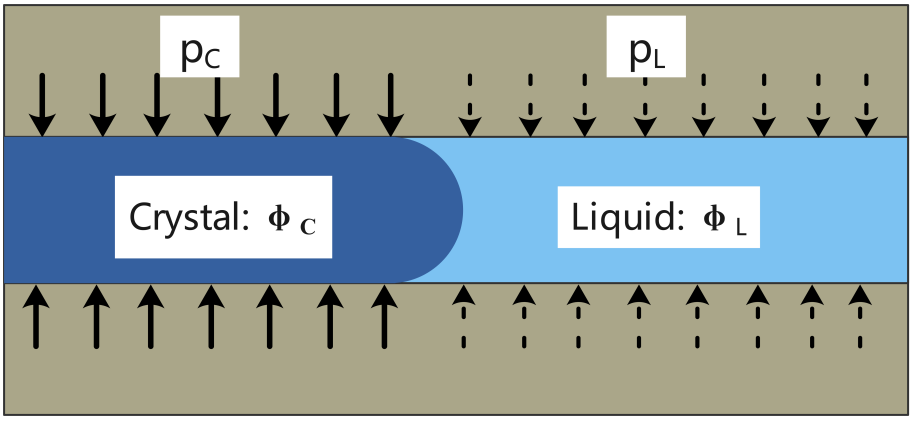

Figure 1.23 Scheme of two fluids in porous space. ϕ_C and ϕ_L denoting the porosities of the crystal phase and liquid phase, and p_C and p_L denoting the pressures exerted on the solid matrix by the crystal phase and liquid phase.

As stated before, the porous space is assumed to be filled by two fluids: pore crystal and pore solution. Hence, the Lagrangian porosity can be split into two partial Lagrangian porosities, ϕ_{C} and ϕ_{L}, as shown in Figure 1.23,

$$\phi = \phi_{\mathrm{C}} + \phi_{\mathrm{L}} \tag{1.34}$$

For each fluid phase J, the variation in its partial porous volume $\phi_{\mathrm{J}} d\Omega_0$ consists of two parts: the deformation of its partial porous volume φ_{J} caused by the action of the its pore pressure p_{J} on solid matrix, and by the change in its saturation S_{J}, defined as the fraction of partial porous volume of phase J to the overall porous space. The change in saturation is caused by the invasion or receding process of phase J.

$$\phi_{\mathrm{J}} = S_{\mathrm{J}}\phi_0 + \varphi_{\mathrm{J}}; \quad S_{\mathrm{C}} + S_{\mathrm{L}} = 1 \tag{1.35}$$

Substituting Eq. (1.35) into Eq. (1.34) shows that the overall porosity change consists of two partial porosity changes associated with the deformation of two partial porous spaces,

$$\varphi = \varphi_{\mathrm{C}} + \varphi_{\mathrm{L}} \tag{1.36}$$

Eq. (1.33) can be rewritten when combined with Eq. (1.36),

$$\epsilon = (1 - \phi_0)\epsilon_{\mathrm{S}} + \varphi_{\mathrm{C}} + \varphi_{\mathrm{L}} \tag{1.37}$$

1.3.2 Macroscopic mean stress and stress partition

With a characteristic weighting function, where function equal to zero for a point at the border of REV and equal to one for a point lying inside, the macroscopic stress in the porous material, σ_{ij}, can be split into stress in solid matrix and porous by a space average method,

$$\sigma_{ij} = (1 - n)\sigma_{ij}^{\mathrm{S}} - n_{\mathrm{C}} p_{\mathrm{C}} \delta_{ij} - n_{\mathrm{L}} p_{\mathrm{L}} \delta_{ij} \tag{1.38}$$

where σ_{ij}^{S} is the space averaged stress of microscopic stress field in solid matrix and δ_{ij} is the Kronecker index, where $\delta_{ij} = 1$ as $i = j$, and $\delta_{ij} = 0$ as $i \neq j$. In porous space, the microscopic stress field is uniform. The mean stress σ is obtained by introducing a mean stress in solid matrix σ_{S},

$$\sigma = (1 - n)\sigma_{\mathrm{S}} - n_{\mathrm{C}} p_{\mathrm{C}} - n_{\mathrm{L}} p_{\mathrm{L}} \tag{1.39}$$

By assuming a infinitesimal transformation, the Eulerian porosity can be replaced by the initial porosity ϕ_0,

$$\sigma = (1 - \phi_0)\sigma_S - \phi_0 S_C p_C - \phi_0 S_L p_L \tag{1.40}$$

1.3.3 Saturated linear poroelasticity

The variation of volumetric density of Helmholtz free energy of porous material $\mathrm{d}f$ can be split into the strain work by elastic deformation and free energy change in two fluid phases by phase transition in porous space,

$$\mathrm{d}f = \sigma \mathrm{d}\epsilon + s_{ij}\mathrm{d}e_{ij} + \sum_J \mu_J \mathrm{d}n_J - s\mathrm{d}T \tag{1.41}$$

where s_{ij} and e_{ij} strand for the deviatoric stress and strain, μ_J and n_J for the chemical potential and moles concentration of fluid phase J, and s for volumetric density of entropy of porous material. The first two terms at the right of Eq. (1.41) account for the strain work, and the last two terms account for the change of free energy in pore fluid phases.

As for the fluid phases in the porous space, the energy balance can be derived from Gibbs-Duhem Equation,

$$-\sum_J \phi_J \mathrm{d}p_J - \sum_J s_J \mathrm{d}T + \sum_J \mu_J \mathrm{d}n_J + \phi_0 \left(P_C - P_L\right) \mathrm{d}S_C = 0 \tag{1.42}$$

where s_J is the volumetric density of entropy of phase J. The last term in Eq. (1.42), $\phi_0 \left(p_C - p_L\right) \mathrm{d}S_L$, accounts for the infinitesimal work made against the interfacial force to make the interface between crystal phase and solution phase move within the porous during the invasion of porous space by the crystal phase or its receding process from pore.

Combining the relation between the volumertric density of Gibbs free energy g and Helmholtz free energy a of fluid phases in Eq. (1.43), with the definition of Gibbs free energy in fluid phases in Eq. (1.44), provides the Helmholtz free energy of solid matrix a_S in Eq. (1.45),

$$g = a + \sum_J p_J \phi_J \tag{1.43}$$

$$g = \sum_J n_J \mu_J \tag{1.44}$$

$$a_S = f - a = f - \left(\sum_J n_J \mu_J - \sum_J p_J \phi_J \right) \tag{1.45}$$

Substituting Eq. (1.45) and Eq.(1.42) into Eq. (1.41) provides the derivative of Helmholtz free energy of solid matrix,

$$\mathrm{d}a_{\mathrm{S}} = \sigma \mathrm{d}\epsilon + s_{ij}\mathrm{d}e_{ij} + \sum_{\mathrm{J}} p_{\mathrm{J}}\mathrm{d}\phi_{\mathrm{J}} - s_{\mathrm{S}}\mathrm{d}T - \phi_0\left(P_{\mathrm{C}} - P_{\mathrm{L}}\right)\mathrm{d}S_{\mathrm{C}}; \quad s_{\mathrm{S}} = s - \sum_{\mathrm{J}} s_{\mathrm{J}} \tag{1.46}$$

Under an isothermal condition, the fourth term in the right of Eq.(1.46) is omitted. For infinitesimal transformations and linear poroelasticity, the last term in Eq. (1.46) is negligible and is also omitted,

$$\mathrm{d}a_{\mathrm{S}} = \sigma \mathrm{d}\epsilon + s_{ij}\mathrm{d}e_{ij} + \sum_{\mathrm{J}} p_{\mathrm{J}}\mathrm{d}\phi_{\mathrm{J}} \tag{1.47}$$

For convenience, a Legendre transformation of Helmholtz free energy, η_{S}, with respect to φ is adopted,

$$\eta_{\mathrm{S}} = a_{\mathrm{S}} - \sum_{\mathrm{J}} p_{\mathrm{J}}\varphi_{\mathrm{J}} \tag{1.48}$$

And its derivative is obtained by the substitution of Eq. (1.48) into Eq. (1.47),

$$\mathrm{d}\eta_{\mathrm{S}} = \sigma \mathrm{d}\epsilon + s_{ij}\mathrm{d}e_{ij} - \sum_{\mathrm{J}} \varphi_{\mathrm{J}}\mathrm{d}p_{\mathrm{J}} \tag{1.49}$$

Eq. (1.49) is an exact differential of the energy function η_{S}, so η_{S} only has ϵ, e_{ij} and p_{J} as variables. Therefore, Eq. (1.49) provides the state equations of poroelastic material,

$$\sigma = \frac{\partial \eta_{\mathrm{S}}}{\partial \epsilon}; \quad \varphi_{\mathrm{C}} = \frac{\partial \eta_{\mathrm{S}}}{\partial p_{\mathrm{C}}}; \quad \varphi_{\mathrm{L}} = \frac{\partial \eta_{\mathrm{S}}}{\partial p_{\mathrm{L}}}; \quad s_{ij} = \frac{\partial \eta_{\mathrm{S}}}{\partial e_{ij}} \tag{1.50}$$

Considering the isotropic porelastic solid matrix, the energy function η_{S} must only depend on the tree principal strains in addition to pore pressure p_{J}. The three principal strains are functions of three first invariants of the strain tensor $\boldsymbol{\varepsilon}$: the first invariant ε_{ii}, the second invariant $0.5\left(\varepsilon_{ii}\varepsilon_{kk} - \varepsilon_{ik}\varepsilon_{ik}\right)$, and the third invariant $\det(\boldsymbol{\varepsilon})$. When considering linear isotropic poroelastic solid matrix, η_{S} will be a quadratic function and only two invariants needs to be considered. For convenience, we consider the first invariant volume dilation ϵ and the second invariant $e_{\mathrm{ij}}e_{\mathrm{ji}}$ of the strain deviator $\mathbf{e}$,

$$\eta_{\mathrm{S}} = \frac{1}{2}K\epsilon^2 - b_{\mathrm{C}}\epsilon p_{\mathrm{C}} - b_{\mathrm{L}}\epsilon p_{\mathrm{L}} - \frac{1}{2}\frac{p_{\mathrm{CC}}^2}{N_{\mathrm{CC}}} - \frac{1}{2}\frac{p_{\mathrm{C}}p_{\mathrm{L}}}{N_{\mathrm{CL}}} - \frac{1}{2}\frac{p_{\mathrm{LL}}^2}{N_{\mathrm{LL}}} + Ge_{ij}e_{ji} \tag{1.51}$$

Substitution of Eq. (1.51) into Eq. (1.50) gives us the state constitutive equations of linear

poroelastic materials,

$$\begin{cases} \sigma = K\epsilon - b_{\mathrm{C}} p_{\mathrm{C}} - b_{\mathrm{L}} p_{\mathrm{L}} \\ \varphi_{\mathrm{C}} = b_{\mathrm{C}}\epsilon + p_{\mathrm{C}}/N_{\mathrm{CC}} + p_{\mathrm{L}}/N_{\mathrm{CL}} \\ \varphi_{\mathrm{L}} = b_{\mathrm{L}}\epsilon + p_{\mathrm{C}}/N_{\mathrm{CL}} + p_{\mathrm{L}}/N_{\mathrm{LL}} \\ s_{ij} = 2Ge_{ij} \end{cases} \tag{1.52}$$

where K, b_{C}, b_{L}, N_{CC}, N_{LL}, N_{CL} and G are the poroelastic properties characterizing the mechanical response of the linear elastic porous solid matrix to external load σ and internal stress p_{C} and p_{L}.

In Eq. $(1.52)_{\mathrm{I}}$, K is the bulk modulus of porous materials, which relates the volumetric dilation ϵ linearly to the mean stress σ when the pore pressures, p_{C} and p_{L}, equal to zero. The Biot coefficients, b_{C} and b_{L} in Eq. $(1.52)_{\mathrm{II}}$ and $(1.52)_{\mathrm{III}}$, represent the fractions of the volumetric dilation ϵ contributed by porosity variation φ_{C} and φ_{L} providing $p_{\mathrm{C}} = p_{\mathrm{L}} = 0$. The modulus, N_{CC}, relates the pore pressure p_{C} linearly to the porosity variation φ_{C} when the volumetric deformation ϵ and the liquid pressure P_{L} are zero. Similarly, N_{LL}, relates the p_{L} linearly to the φ_{L} when ϵ and P_{C} are zero, and N_{CL}, relates the p_{C} linearly to the φ_{L} when ϵ and P_{L} are zero. The shear modulus G relates the deviatoric strain component e_{ij} linearly to the corresponding shear stress s_{ij}. The poroelastic properties depend on the mechanical properties of solid matrix and geometry of porous network and not on the properties of fluids in pores. These parameters could be experimentally measured or estimated through the homogenization method. Appendix B gives the estimation of poroelastic properties under a spherical particles assumption.

1.3.4 Simplified description for ESA expansion

Under volumetric isodeformation assumption, the Biot coefficients have relation: $b_{\mathrm{J}} = bS_{\mathrm{J}}$ as in Eq. (B.5). Thus the constitutive equation is restated as,

$$\begin{cases} \sigma = K\epsilon - b\sigma_{\mathrm{p}} \\ \varphi_{\mathrm{C}} = b\epsilon S_{\mathrm{C}} + \dfrac{\sigma_{\mathrm{p}} S_{\mathrm{C}}}{N} + \dfrac{3S_{\mathrm{C}}S_{\mathrm{L}}\phi(p_{\mathrm{C}} - p_{\mathrm{L}})}{4g_{\mathrm{S}}} \\ \varphi_{\mathrm{L}} = b\epsilon S_{\mathrm{L}} + \dfrac{\sigma_{\mathrm{p}} S_{\mathrm{L}}}{N} - \dfrac{3S_{\mathrm{C}}S_{\mathrm{L}}\phi(p_{\mathrm{C}} - p_{\mathrm{L}})}{4g_{\mathrm{S}}} \\ s_{ij} = 2Ge_{ij} \end{cases} \tag{1.53}$$

Usually, we only need to consider the volume dilation ϵ and its corresponding stress, i.e. the first equation in Eq. (1.53),

$$\sigma = K\epsilon - b\sigma_{\mathrm{p}}; \quad \epsilon = (\sigma + b\sigma_{\mathrm{p}})/K \tag{1.54}$$

Under a uniaxial strain condition, the lateral strains are equal to zero and the principal stress is expressed as,

$$\sigma_{xx} = K\epsilon_{xx} - b\sigma_{\mathrm{p}}; \quad \varepsilon_{xx} = (\sigma_{xx} + b\sigma_{\mathrm{p}})/K \tag{1.55}$$

Under a three-dimensional condition without consideration of the shear stress and strain, the principal stresses are expressed as,

$$\begin{cases} \varepsilon_{xx} = [\sigma_{xx} - \upsilon(\sigma_{yy} + \sigma_{zz}) + b(1-2\upsilon)\sigma_{\mathrm{p}}]/K \\ \varepsilon_{yy} = [\sigma_{yy} - \upsilon(\sigma_{xx} + \sigma_{zz}) + b(1-2\upsilon)\sigma_{\mathrm{p}}]/K \\ \varepsilon_{zz} = [\sigma_{zz} - \upsilon(\sigma_{xx} + \sigma_{yy}) + b(1-2\upsilon)\sigma_{\mathrm{p}}]/K \end{cases} \tag{1.56}$$

The reference state, related to a zero deformation and porosity state, is associated with a initial stress state: σ^0, p_{C}^0, p_{L}^0, s_{ij}^0. Thus, the stress in constitutive equations is restated in the form of stress variations, $\sigma^0 - \sigma$, $p_{\mathrm{C}}^0 - p_{\mathrm{C}}$, $p_{\mathrm{L}}^0 - p_{\mathrm{C}}$, $s_{ij}^0 - S_{ij}$. Typically, the atmospheric pressure p_{atm} is taken as the zero reference pressure: $p_{\mathrm{C}}^0 = p_{\mathrm{L}}^0 = p_{\mathrm{atm}}$. As a result, the pore pressure σ_{p} are obtained,

$$\sigma_{\mathrm{p}} = S_{\mathrm{C}}(p_{\mathrm{C}} - p_{\mathrm{atm}}) + S_{\mathrm{L}}(p_{\mathrm{L}} - p_{\mathrm{atm}}) \tag{1.57}$$

In most cases we studied, the liquid solution phase is connected with the external environment, so the fluid inside the pores is unrestricted to crossing the materials. So there is no pressure building-up in liquid solution and liquid pressure always equals to p_{atm}. Hence, the last term in Eq. (1.57) is omitted. For simplification, the interface stress in the solid-crystal interface is neglected. The pressure imposed on pore walls by crystal phase p_{C}, as stated in Section 1.3.2, is equal to the thermodynamic pressure P_{C} and is also homogeneous everywhere. A combination of Eq. (1.22) and (1.57) gives a simplified expression of pore pressure,

$$\sigma_{\mathrm{p}} = \frac{RT}{\overline{V}_{\mathrm{C}}} S_{\mathrm{C}} \ln \beta_{\mathrm{AFt}} \tag{1.58}$$

1.4 Research initiatives

1.4.1 Statement of problem

Despite more than 80 years of extensive laboratory studies–even "disproportionate to the practical extent of the problem"[170], the knowledge of sulphate attack is still incomplete[171] and far from being fully used in engineering practice. This is due to the complicated mechanisms of ESA in natural complex environments in engineering practice.

Based on the literature review above, the confronted problems on the ESA with combined actions can be summarized as: the kinetic law for AFt formation; the effects of AFt crystallization in pores on the transport properties and expansion behavior; and the damage caused by the pore pressure during AFt crystallization. Table 1.5 summarizes the state-of-the-art of the study on ESA and the combined actions. For ESA, extensive experiments reveal a clear mechanism, and numerous models have been proposed to simulate the ESA expansion. Nonetheless, the engineering applications are still not yet quantitative. While few studies have been conducted on the combined actions between ESA and other effects, the mechanisms are unclear, few models have been proposed, and the engineering applications are likewise empirical.

Table 1.5 State-of-the-art of the study on ESA and the combined actions.

Sulfate attack	Mechanism	Modelling	Engineering application
ESA	Determined	Numerous	Empirical
Combined actions	Undetermined	Few	Empirical

1.4.2 Research objectives

Based on the state-of-the-art of the study on ESA and the combined actions, we aim to:

(1) investigate the AFt formation kinetics in CBM subjected to ESA with and without combined actions;

(2) investigate the pore crystallization (AFt) process and the associated expansion in CBM subjected to ESA with and without combined actions;

(3) investigate the ESA damage pattern of CBM subjected to ESA with and without combined actions;

(4) propose scientific models for engineering applications.

To achieve these objectives, we conducted the experiments in three parts. In Part I, we immersed powder samples from hardened cement paste into different sulfate solutions to study the kinetics of the AFt formation in CBM subjected to ESA with and without combined actions, the objective 1; in Part II, we designed 2mm slice specimens of cement paste to be exposed to different sulfate solutions in order to examine the pore crystallization process and its effects on transport property and expansion behavior in CBM subjected to ESA with and without combined actions, the objective 2; in Part III, we used disk specimens of cement paste to expose to different sulfate solutions to observe the sulfates transport and cracking behavior in CBM subjected to ESA with and without combined actions, the objective 3. The combined actions, including DEF, chloride, and leaching on ESA in this study, were simulated by setting different sulfate solutions. Then, the kinetic data was combined with a poromechanical approach to develop a chemo-poromechanical model for simulating the ESA expansion with and without chlorides. Besides, a spalling rate model was proposed to predict the spalling damage in civil engineering based on the cracking observations in Part III.

Following this line, this thesis is organized as follows: the experimental program is given in Chapter 2, the experimental results and discussions in experimental Part I, II and III are presented in Chapter 3, 4, 5 respectively; Chapter 6 and Chapter 7 show the chemo-porochemical model and the spalling rate model, respectively; and the general conclusions are provided in Chapter 8.

CHAPTER 2 EXPERIMENTS

The experimental program includes three parts: Part I, kinetics of AFt formation; Part II, pore crystallization and expansion; and Part III, sulfate transport and cracking behavior. In Part I, the goal is to quantify the AFt amount with exposure time; in Part II, the goals are to identify the AFt crystallization process, including AFt crystal amount and crystallization sites, and to determine its effect on expansion stress and transport property; in Part III, the goals are to observe the sulfate transport and ESA damage pattern, and provide experimental validation for scientific models. The combined actions are investigated using the combined conditions throughout the three parts of the experiments. In this study, the combined actions include DEF, chlorides, and leaching.

2.1 Materials and sulfate solutions

2.1.1 Materials

The cement used in this study is CEM I Type (CEMI 52.5 N CE CP2)[172] with the chemical composition given in Table 2.1. The mineral contents of cement estimated through the Bogue method[86] are given in Table 2.2. A relatively high w/c ratio of 0.55 was adopted to allow sulfates to permeate rapidly into specimens. The mixing proportion of cement paste was calculated as,

$$v_{\text{cement paste}} = V_{\text{C}} + V_{\text{W}} = m_{\text{C}}/d_{\text{C}} + (w/c) \cdot m_{\text{C}} \tag{2.1}$$

where V_{C} and m_{C} are the volume and mass of the cement per liter of cement paste, V_{W} is the water volume, and d_{C} is the density of cement, taking the value of 3160 kg/m^3. Accordingly, the cement and water content were determined as 1.154 kg and 0.635 kg per liter of cement paste. Plastic and paper molds were employed for prismatic specimens (40×40×160mm, Part I and II) and cylindrical specimens (Φ110×220mm, Part III), cf. Figure 2.1.

2.1.2 Curing

To prevent evaporation, the top surfaces of the prismatic specimens were covered with a curing textile, while the cylindrical specimens were sealed with a plastic cover

Table 2.1 Chemical composition of CEM I cement.

Component	Symbol	Content (%)
Calcium oxide	CaO	62.81
Silicon oxide	SiO_2	20.22
Aluminum oxide	Al_2O_3	4.85
Ferric oxide	Fe_2O_3	2.92
Magnesium oxide	MgO	0.84
Sulfur oxide	SO_3	2.88
Sulfur	S	0
Chloride	Cl	0.07
Manganese oxide	MnO	0.08
Potassium oxide	K_2O	0.77
Sodium oxide	Na_2O	0.34
Ignition Loss	IL	2.59
Insoluble residue	IR	0.89
Total	-	99.58
Free calcium oxide	CaO(free)	1.58

Table 2.2 Mineral contents calculated by the Bogue method[86] of CEM I cement.

Mineral	Symbol	Content (%)
Alite	C_3S	65.2
Belite	C_2S	8.8
Aluminum	C_3A	7.9
Ferrum	C_4AF	8.9

after curing. For the plastic and cylindrical molds containing the fresh mixture dedicated to heating-treatment (combined ESA and DEF condition), the top surfaces were sealed by gluing plastic paper to prevent water entry during heating treatment. After 2h curing, all the specimens exposed to the combined ESA and DEF condition underwent a heating procedure with a temperature history[173] as in Figure 2.2. The heating treatment was performed in a tank filled with water as shown in Figure 2.3, of which the temperature was controlled by the heating device. As shown in Figure 2.2, the heating procedure, lasting for one week, consists of a rapid heating stage for 24h, stable stage at 81 ^oC for 72h and a slow cooling stage for 56h with a rate at -1^oC/h.

(a) (b)

Figure 2.1 Prismatic specimens in Part I and II (a) and cylindrical specimens in Part III (b) cast in plastic and paper molds.

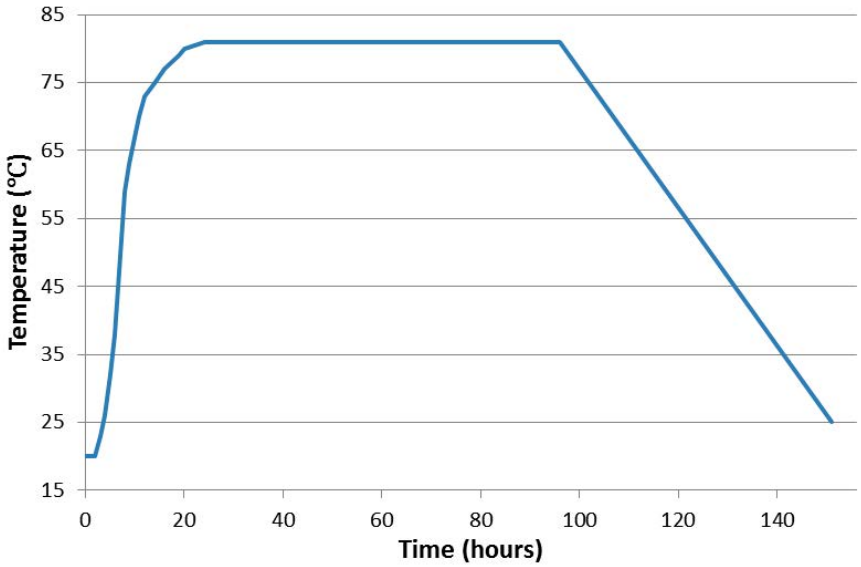

Figure 2.2 Temperature history[173] for heating treatment.

After 7d heating treatment, the specimens for coupled ESA and DEF, together with the specimens dedicated to the ESA, were put into a saturated CH solution with an ambient temperature around 20 °C, in order to avoid the leaching effect. The curing period lasted for 60d to achieve a high hydration degree for CEM I cement.

2.1.3 Preparation of specimens

We designed three experimental parts to investigate the ESA damage mechanism with and without the combined actions. In Part I–kinetics of AFt formation, powder samples were prepared to get rid of the diffusion process, and ^{27}Al NMR was used to identify AFt quantity with exposure time, and XRD was used to identify the aluminum phase types.

Figure 2.3 Bath with a heating device using in this study.

In Part II–pore crystallization and expansion, 2mm thickness slice specimens were prepared to avoid non-uniform distribution of ions and crystallization across the thickness, and ^{27}Al NMR and XRD were used to identify AFt quantity with exposure time, and simultaneously MIP, dynamic vapour sorption (DVS), and micrometer were used to detect the change in pore size distribution (PSD) and vapour diffusivity and expansion strain, respectively. The sizes we used in this part are 2mm×20mm×120mm for expansion tests and 2mm×40mm×40mm for the other characterization tests. In Part III–sulfate transport and cracking observation, disk specimens with a size of Φ100×50 were used to investigate the diffusion process. In this part, sulfate profiles, mineral phases and chemical element distribution, and cracking observations were examined by Inductively Coupled Plasma (ICP), XRD, Energy Dispersive Spectrometer (EDS), and optical microscope with Backscattered electron image (BSE), respectively. The specimens size and characteriza-

Table 2.3 Specimens size and characterization methods in three experimental parts.

Notation	Specimens size	characterization methods
Part I	Powder (<0.2mm)	^{27}Al NMR; XRD
Part II	2mm×20mm×120mm	Micrometer
	2mm×40mm×40mm	Micrometer; ^{27}Al NMR; XRD; MIP; DVS
Part III	Φ100×50	ICP; XRD; EDS; BSE; Optical microscope

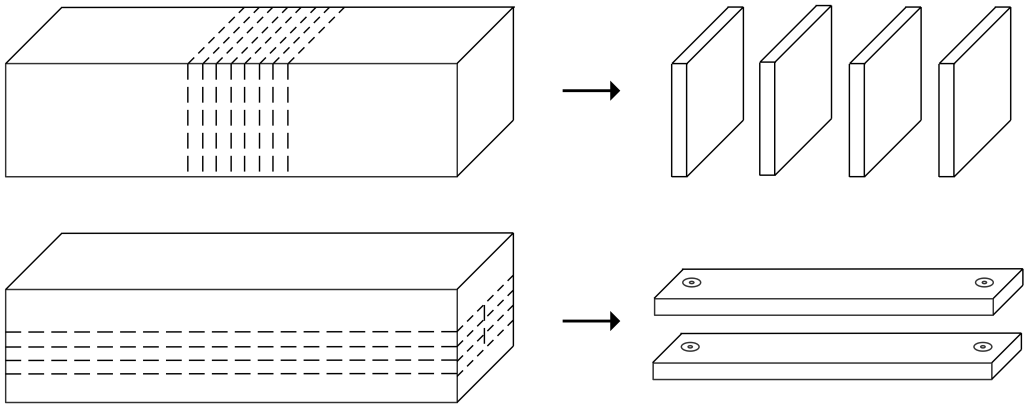

Figure 2.4 Preparation of thin cement paste slices in Part II.

tion methods employed in the three parts are given in Table 2.3.

After 60d, the prismatic and cylindrical specimens were taken out of the curing solution. As stated in Table 2.3, powder samples with a particle size around 0.2mm were ground from prismatic specimens for kinetics study in Part I. In Part II, rectangular slices of 2mm×20mm×120mm and square slices of 2mm×40mm×40mm were sawed out using a high-precision cutting machine, cf. Figure 2.4. The cutting device used is a type of Accutom-50 with a thin diamond blade of 0.4mm thickness. Each rectangular slice specimen was equipped with a pair of stainless-steel pins fixed on the two ends for expansion measurement. The pins are designed with a small hole on the surface, and the initial distance between two pins was set as 100mm along the geometric center line of the rectangular specimen, cf. Figure 2.5b. The square slice specimens were reserved for the characterization tests of NMR, MIP, and DVS, cf. Figure 2.5a.

In Part III, disk specimens of 50mm height, as shown in Figure 2.5, were sawed out

(a) (b) (c)

Figure 2.5 Prepared square slices (a), rectangular slices (b) and disk specimens (c).

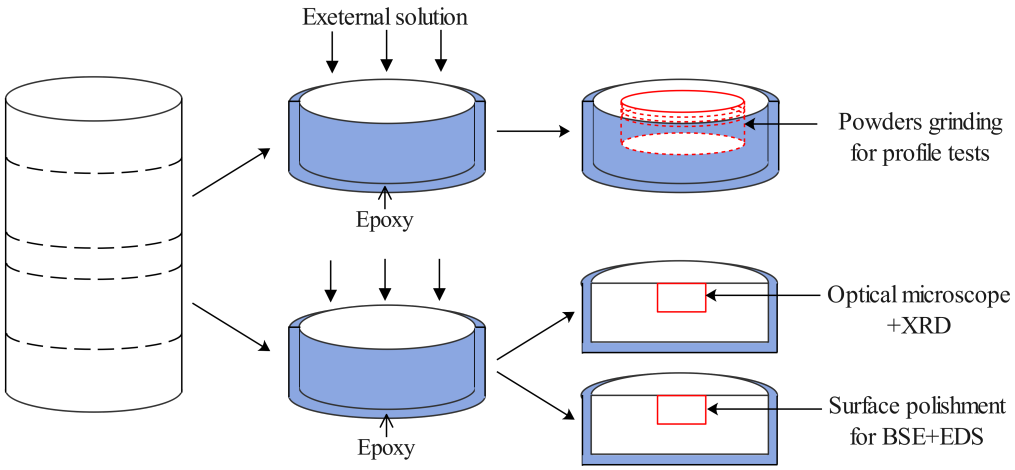

Figure 2.6 Preparation and sampling of cement paste specimens in part III.

from cylinders using a cutting machine. The sawing was performed under water to prevent the emission of dust and the destruction of specimens caused by the generated heat. The height of the specimen and the thickness of the disks are measured before and after each sawing. After sawing, an epoxy resin was applied on the lateral and bottom surfaces of disk specimens to leave the top surface exposed to test solutions, cf. Figure 2.6.

2.1.4 Exposure conditions

The sulfate concentration was fixed at 10g/L to accelerate the material damage in the laboratory, and sodium sulfate was used. Besides, to avoid the accelerating effect of leaching effect, the pH value of the test solution was maintained at 13 by adding 0.1M NaOH. The solution that consists of 10 g/L sulfate in Na_2SO_4 and 0.1M NaOH was set as a standard reference solution.

The composition of all the test solutions in the three experimental parts is given in Table 2.4. In Part I, a low sulfate concentration of 3g/L was adopted to investigate the influence of sulfate concentration on the formation rate of AFt. Besides, the effects of DEF and chlorides on the AFt formation rate were investigated through the heating treatment during the hydration of cement paste and the adding of NaCl, respectively. In Part II, different concentrations of NaCl were added into the reference solution to investigate the chloride effect on the pore crystallization process and expansion. The DEF's effect was also taken into consideration in this part. In Part III, the pH value was regulated to 7 to study the leaching effect on sulfate transport. Besides, the effects of chlorides and DEF were also studied in this part.

As shown in Table 2.4, four, five, and six exposure conditions were designed in Part

Table 2.4 Composition of test solutions in Part I, Part II and Part III.

Condition	SO_4^{2-} concentration	Cl^- concentration	pH value (-)
PI-1	3 g/L	0	13
PI-2	10 g/L	0	13
PI-3	10 g/L	10 g/L	13
PI-4	10 g/L + DEF	0	13
PII-1	10 g/L	0	13
PII-2	10 g/L	10 g/L	13
PII-3	10 g/L	19 g/L	13
PII-4	10 g/L + DEF	0	13
PII-5	10 g/L + DEF	19g/L	13
PIII-1	10 g/L	0	13
PIII-2	10 g/L	0	7
PIII-3	10 g/L	19 g/L	7
PIII-4	10 g/L + DEF	0	13
PIII-5	10 g/L + DEF	0	7
PIII-6	10 g/L + DEF	19 g/L	7

I, II, and III, respectively. In Part I: P1-1 and P1-2 were designed to determine kinetic law as aforementioned in Section 1.1.1; P1-2 and P1-3 for the impact of chloride on kinetic process; P1-2 and P1-4 for the influence of DEF on generation rate of AFt. In Part II, the first three conditions were designed to investigate the influence of chloride concentrations on the AFt crystallization process and expansion behavior; the last two conditions were for the DEF's impact. In Part III, PIII-1 and PIII-2 were designed to examine the leaching effect on sulfate transport and cracking behavior; PIII-2 and PIII-3 for chloride effect; and the last three for the influence of DEF. The ratio of the test solution volume to the sample surface area was set as $2.4 cm^3/cm^2$ [37]. These test solutions were renewed on a weekly basis (within the first month) and bi-weekly basis (afterwards) to maintain a constant sulfate concentration[36,121].

For low pH conditions in PIII-2/3/5/6, a pH controller was used to maintain the pH value at 7. The scheme of the pH-control mechanism and photos of the pH-controller device are given in Figure 2.7. The pH controller was comprised of a large tank carrying roughly 60 L of 10g/L sulfate solution and serving as a reservoir. In the large tank, a pump with a maximum flow rate of 750 L/h was submerged in order to transfer the sulfate

solution towards a series of 10 L specimen tanks in Figure 2.7b. Meanwhile, a small

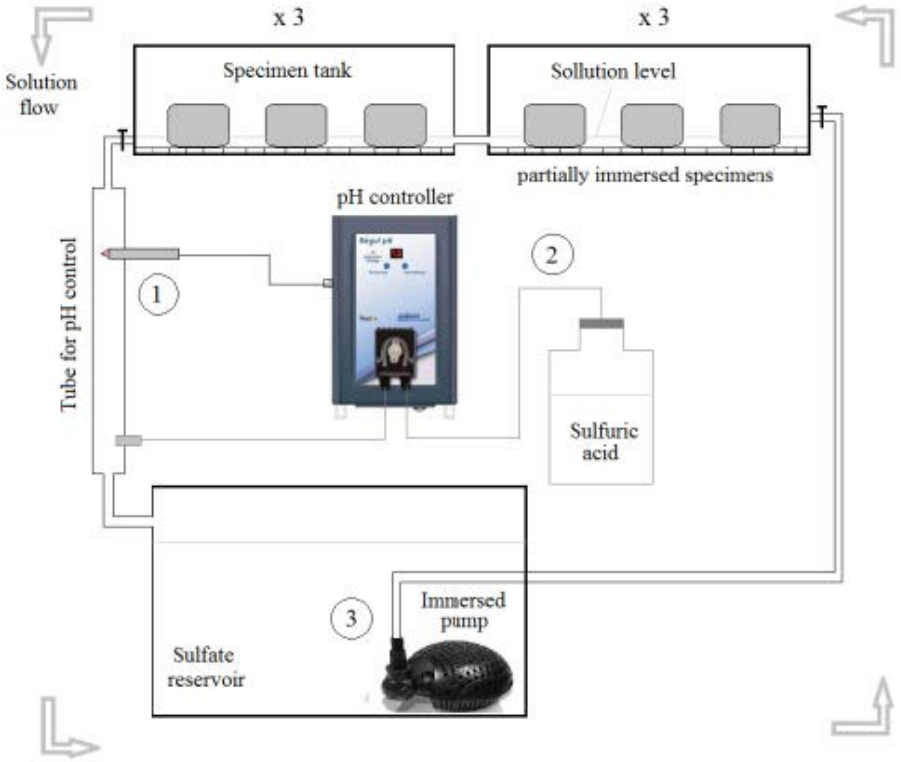

(a)

(b)

Figure 2.7 Scheme of pH-control (a) and pH controller (b).

quantity of test solution flowed via a cylindrical tube (Process 1) into the pH controller, where its pH was continuously measured and adjusted at 7.0±0.1 by a continuous titration with sulfuric acid H_2SO_4 (0.05% concentration), before returning to the reservoir tank (Process 2). As the sulfate solution moves continuously between the sulfate reservoir and the specimen tanks, the additional sulfuric acid is thoroughly well mixed in the sulfate solution (Process 3). The disk specimens are semi-immersed into sulfate solution in the 10 L specimens tanks.

2.1.5 Sampling

At given exposure ages, the powder samples in Part I and the square slices in Part II were taken out and subjected to freeze-drying treatment before the characterization tests. The freeze-drying treatment aims to stop the crystallization process by removing water from inside. The procedure consisted of storing the specimens in liquid nitrogen for 10 min, and then drying the specimens under 0.07mbar and -57 ^{o}C for 3d. The boil point of liquid nitrogen at normal temperature is -195.8 ^{o}C, which freezes the liquid water in the pores of cement paste without altering the microstructure[174]. Then ice frozen inside sublimates directly into steam under a very low pressure condition (0.07mbar) and the steam is captured in a cooling coil at a low temperature (-57 ^{o}C). In this way, all the water in cement-based materials could be removed without the drying shrinkage caused by water evaporation. The freeze-dryer used in this study is of the Christ's Alpha 1-4 LDplus type.

For the sulfate and chloride profiles measurements, one disk specimen was ground from the exposure surface to the interior layer by layer, cf. Figure 2.6, with a profile grinder. This instrument comprises a grinding wheel with a diameter of 18 mm for breaking cement paste into a fine powder. The diameter of the grinding region is 73 mm, and this diameter permits roughly 9 g powders per 1 mm, and the average particle size of powders is 300 μm. Powders in each layer were carefully collected, and the surface was vacuumed to clean the remaining powder in order to prevent cross-contamination.

2.2 Characterization methods

2.2.1 High resolution solid-state NMR

NMR is a spectroscopic technique for non-destructive chemical and structural analysis. This technique exploits the resonance of atomic nuclei under an external magnetic field. According to quantum mechanics, when a atom nucleus is exposed to a static magnetic field (field intensity of $\mathbf{B_0}$), the splitting of energy levels on its nuclear magnetic moment happens[175]. Besides, an external radio frequency field perpendicular to the constant magnetic field is applied to the nucleus. When the frequency of the radio frequency field is equal to the transition frequency of the adjacent energy levels, the nuclear magnetic moment transitions, which is so-called nuclear magnetic resonance. The resonance frequency and intensity are recorded by the instrument, constituting a spectral line. Theoretically, the resonance frequency ν is,

$$\mathrm{h}\nu = \gamma_{\mathrm{N}}\hbar\mathbf{B}_0 \tag{2.2}$$

where γ_{N} is the gyromagnetic ratio of atom nuclei and $\hbar = \mathrm{h}/2\pi$ is the Planck constant. An external radio frequency field perpendicular to the constant magnetic field is applied to the nucleus. However, the nucleus in matter is not an isolated bare nucleus but surrounded by an extranuclear electron cloud, which provides a small magnetic field shielding the external magnetic field from the nucleus. Such a shielding effect on the external magnetic field results in a small modification of resonance frequency,

$$\mathrm{h}\nu = \gamma_{\mathrm{N}}\hbar(1-\sigma_{\mathrm{E}})\mathbf{B}_0 \tag{2.3}$$

Here the term σ_{E} is the shielding constant, whose magnitude is in 10^{-6}. The chemical shielding is measured relative to the value for the nucleus in a standard (reference) sample. And the relative difference is expressed as the chemical shift:

$$\delta = \frac{\nu_{\mathrm{sample}} - \nu_{\mathrm{ref}}}{\nu_{\mathrm{ref}}} = (\sigma_{\mathrm{ref}} - \sigma_{\mathrm{sample}}) \times 10^6 (\mathrm{in\ ppm}) \tag{2.4}$$

The chemical shift is associated with the structural state of the nucleus in matter. For ^{27}Al atom, the values of chemical shift in cement paste hydrates were measured by Skibsted et al.[176] and Andersen et al.[24], given in Table 2.5. Besides, the intensity of the NMR spectrum is proportional to the number of detected nuclei in the same chemical environment, which is related to the concentration of the detected element, allowing

quantitative analysis to be performed based on the spectral line intensity.

The aluminum atoms in aluminum hydrates in cement pastes are covalently bound with oxygen atoms in octahedral and tetrahedral configurations. The octahedral configuration corresponds to AFt, AFm and TAH phases with a chemical shift around 10ppm, and the Al(V) phase with a chemical shift at ~ 35ppm, representing the substitution by aluminum of interlayer Ca^{2+} in CSH. The TAH phase is firstly detected by Andersen et al.[24] and its chemical formula is unknown. The difference in peak positions among AFt, AFm, and TAH phases is the next-nearest atom and chemical environment. For example, the Al-O octahedron is linked with six calcium atoms at two opposite ends to form a columnar structure in AFt but linked with six calcium atoms at six surrounding edges to form a layer structure in AFm. The tetrahedral configuration corresponds to the Al(IV) phase, with chemical shifts around 67 and 83ppm, denoting the replacement of SiO_4 by AlO_4 tetrahedra in CSH chains[24]. Note that the chemical shift is a relative shift of the resonance frequency of samples compared to that of the standard, as shown in Eq. (2.4). Therefore, the value of chemical shift depends on the choice of the standard, and in this study the standard is a 1.0M aqueous solution of $AlCl_3 \cdot 6H_2O$.

A typical ^{27}Al spectrum of cement paste, cf. Figure 2.8b, contains spinning sidebands as well, which represent the repetitions of major peak signals for AFm, AFt, and TAH phases at the spinning frequency. These sidebands are valid signals and need to be considered in the computation of phase content. To capture the contribution of these sideband signals, an extra spectrum with a broader range of -1000~1000 ppm was measured, cf. Figure 2.8a. During the test, each sample was examined by 27Al NMR twice, yielding two spectra with the ranges of 300 ppm and 2000 ppm, cf. Figures 2.8a and b. The high-

Table 2.5 Peak position and analytic mode for different aluminum hydrate species.

Aluminum hydrates species	Analytic Model used for peaks-decomposition	Peak position (ppm)
AFt	Lorentz	13.20[176]
AFm	Czjzek[177]	10.41[176]
TAH	Czjzek[177]	6.71[24]
Al(V)	Gaussian	35.00[176]
$Al(VI)_1$	Gaussian	83.22[176]
$Al(VI)_2$	Gaussian	66.62[176]

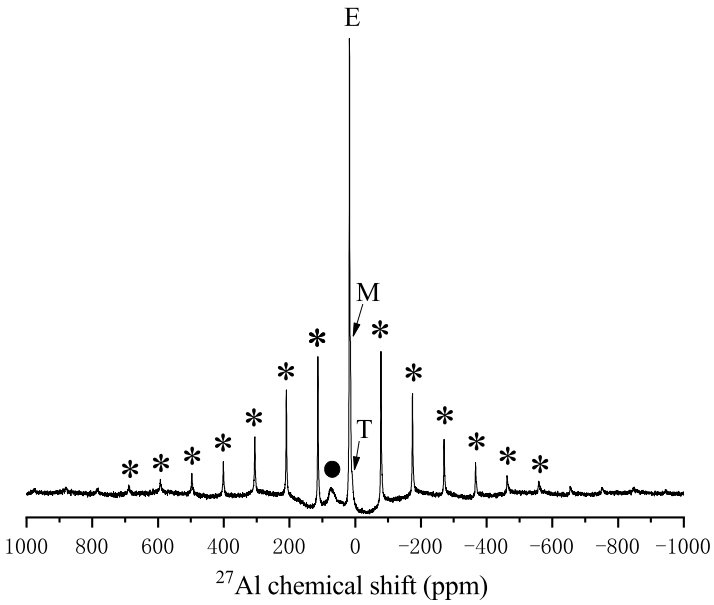

(a)

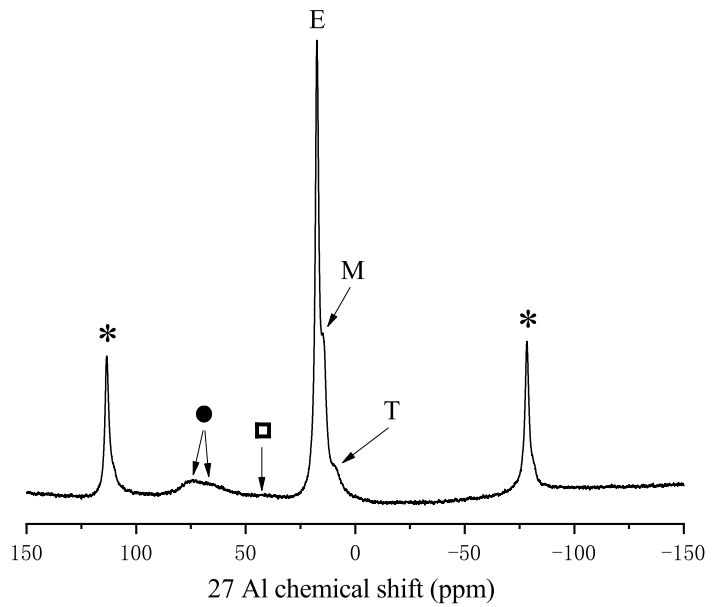

(b)

Figure 2.8 ^{27}Al MAS NMR spectra (magnetic field intensity of 14.09 T, spinning speed of 15 kHz) of cement paste (w/c=0.55) for 84-day exposure to sodium sulfate solution of 10g/L SO_4^{2-}, with ranges of 2000 ppm (a) and 300ppm (b). The symbols E, M and T denote ettringite, AFm and TAH respectively. The asterisk (∗) stands for spinning sideband from ettringite, AFm and TAH peaks, the filled circle (●) for Al(IV) phase, and the square (□) for Al(V) phase.

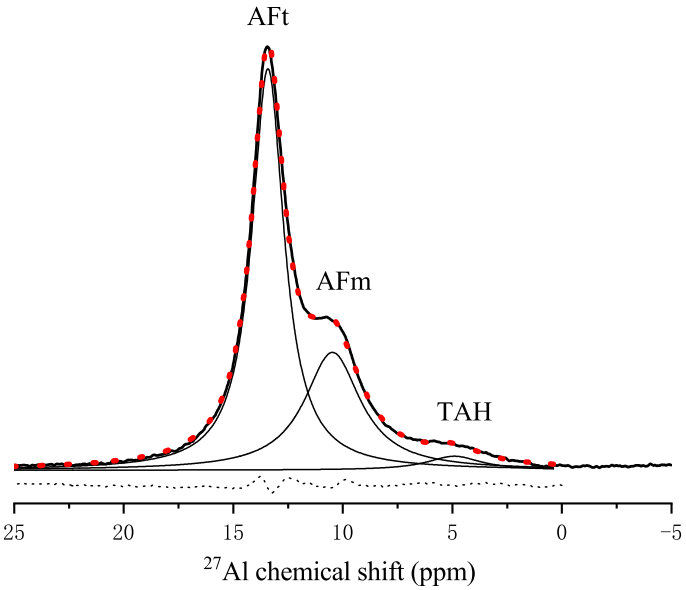

Figure 2.9 Decomposition of ^{27}Al MAS NMR spectrum of cement paste (w/c=0.55) for 84-day exposure to sodium sulfate solution of 10g/L SO_4^{2-}, using multi-peaks fitting method in[177]. The black solid line represents the experimental spectrum, and the red dotted line is the simulated total spectrum. The solid lines with single peak stand for simulated AFt, AFm and TAH spectra respectively. The lower dotted line represents the difference between simulated and experimental spectra.

precision spectrum in the 300ppm-range was used to decompose the three major peaks of AFt, AFm and TAH around 10ppm for the calculation of their relative contents while the 2000ppm-range spectrum was adopted to calculate the ratio of the major phases AFt, AFm and TAH, sum of their major peaks and spinning sidebands, to the minor phases of Al(IV) and Al(V). The decomposition of major peaks around 10 ppm is performed using the multi-peaks fitting approach following [177], cf. Figure 2.9. The analytic models and peak positions for aluminum phases are given in Table 2.5. As aforementioned, the peak areas are proportional to atom numbers, thus the relative content of aluminum phases is obtained by comparing the peak areas of two spectra. This study used a JNM-ECZ600R Solid NMR Spectrometer with a field intensity of 14.09 T. The freeze-dried square slice specimens were ground into powder samples and placed in a tube of 3.2mm in diameter with a high spinning frequency of 15kHz. The test paramters are given in Table 2.6.

Table 2.6 Test parameters used in ^{27}Al NMR method.

Field intensity	Rotor diameter	Rotation frequency	Relaxation time
600MHz	3.2mm	15kHz	5s

2.2.2 Dynamic vapour sorption + Payne diffusion cell

The DVS is a well-established method for the determination of vapour sorption isotherms through high-resolution mass measurement and stable temperature and humidity control[178]. An incubator in Figure 2.10 is adopted to contain the sample pan. The temperature and relative humidity (RH) in the incubator could be adjusted during the measurement. The RH is modified by mixing the water vapor with high purity nitrogen surrounding the sample, and each gas flow is controlled by thermal conductivity mass flow controllers. With a high precision controller, the RH can vary between 0 and 98% with a precision of 0.05%. Another major component of the DVS instrument is the microbalance, which continuously weighs the sample mass with time.

For apparent vapour diffusivity measurement, a diffusion (Payne) cell is set up within the DVS device to measure the water vapor diffusivity, cf. Figure 2.11a. The DVS device used is an Adventure DVS instrument, weighing the mass of vapor flow to the precision of 0.001 mg and controlling the RH to the precision of 0.05% (25°C). The Payne cell is composed of two parts: the cell lid with two O'rings to hold the pellet specimen allowing a maximum thickness of 2.4mm, and the cell cup containing drying agent, anhydrous

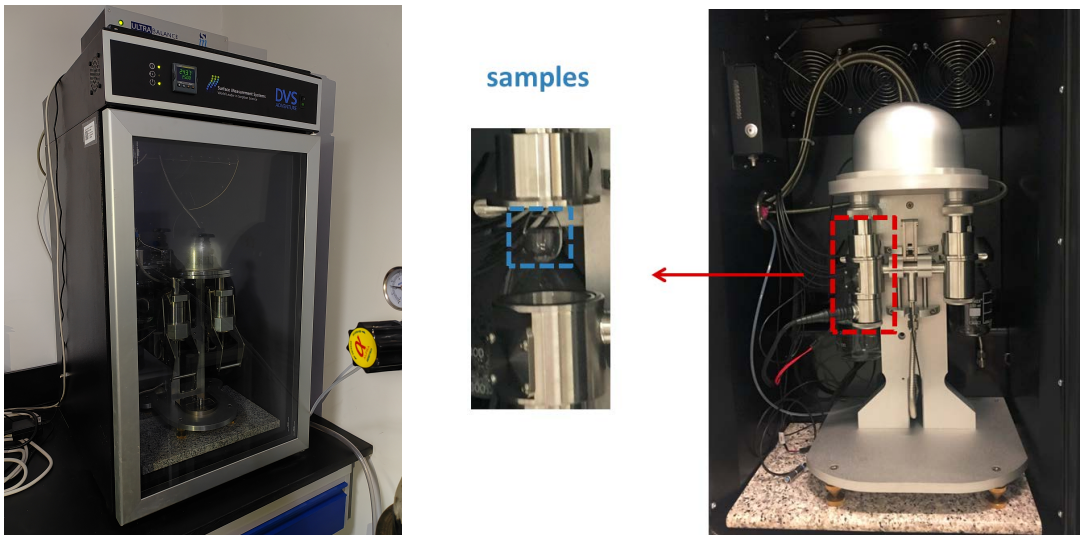

(a) (b)

Figure 2.10 DVS device(a) and its equipment (b).

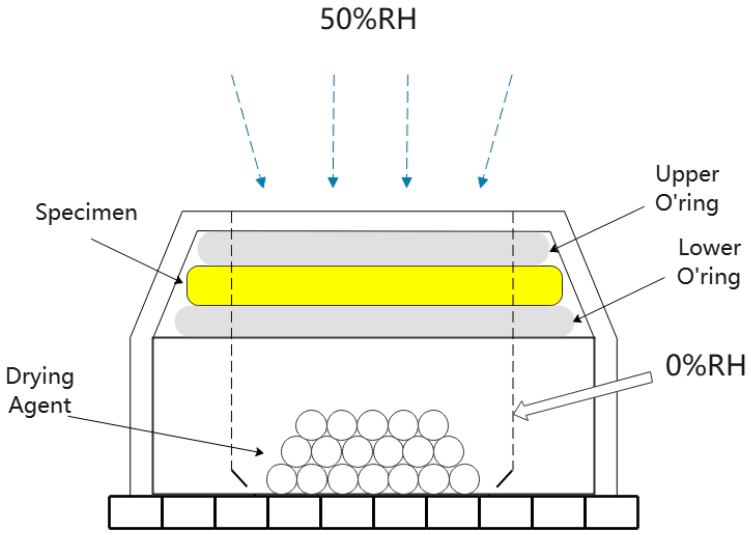

(a)

(b)

Figure 2.11 Vapor diffusivity measurement through DVS device: (a) arrangement of vapor diffusion test, and (b) cement paste specimens and diffusion (Payne) cell. The drying agent used is anhydrous calcium chloride ($CaCl_2$).

$CaCl_2$ of around 40mg, to maintain nearly 0% RH. The pellet specimens were drilled out from the square slice specimens after freeze-drying, cf. Figure2.11b. The Payne cell, loaded with drying agent and pellet specimens, was put into the chamber of DVS device with temperature controlled to 25°C and RH regulated to 50%. The total mass of the Payne cell was weighed continuously, and the mass of vapor flowing into the cell was deduced from the gain in weight of the Payne cell in the steady regime. The steady state of flow is judged from the mass evolution of a Payne cell until the relative change of flow rate during two consecutive minutes is inferior to 1%, cf. Figure 2.12. The 0-50% RH

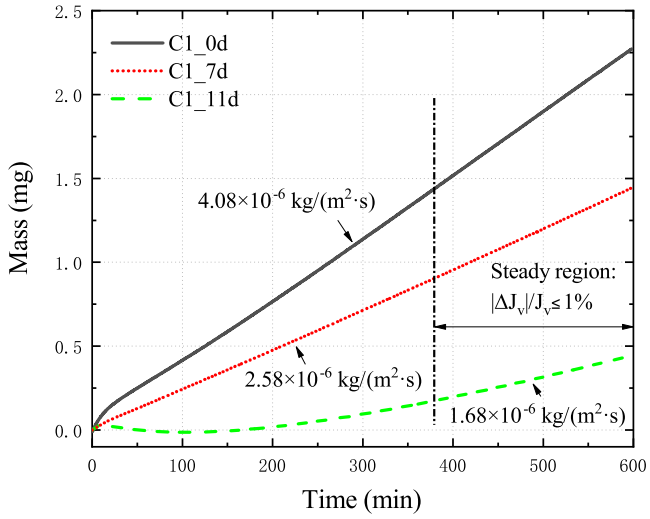

Figure 2.12 Mass evolution of Payne cell containing cement paste specimen (w/c=0.55) for 0d (black solid line), 7d(red dot line) and 11d (grain dash line) exposure to 10g/L SO_4^{2-}. The steady flow is reached as the slope becomes constant.

gradient is chosen to trade off the experiment duration and the measurement precision. By imposing this quite large RH gradient across and the thickness 2.4mm of specimens, the measurement allows to deduce the apparent vapor diffusivity D_v^a from the steady flow of water vapor via the exposed area of pellet specimens (15.54mm^2), expressed through the following equation[179],

$$D_v^a = \frac{RT}{M}\frac{e}{p_{vs}\Delta h}J_v \tag{2.5}$$

Here the term R stands for the ideal gas constant, T for the absolute temperature (25°C), M for the molar mass of water, J_v for the vapour mass flux through the diffusion surface, e for the thickness of specimen, p_{vs} for the saturated water vapour pressure at 25°C and Δh for the difference of RH (50%). According to Kelvin's equation[180], water vapour can condensate in pores of diameter smaller than 3nm at RH=50%, and the liquid water may also exist in pores as an adsorbed water film on pore walls[181]. In other words, under the imposed RH difference 0-50% most pores in cement paste, with a size of around 10–1000 nm, are open for vapor diffusion.

2.2.3 Mercury intrusion porosimetry

MIP is one of the most widely used methods for measuring the microstructure of porous materials. The test principle is based on the fact that to squeeze a non-wetting liquid (with a contact angle larger than 90°) into capillary pores a pressure must be applied.

Under a cylindrical pore assumption, the applied pressure P is related to the pore diameter (entry size) d using Washburn equation[182],

$$p = -\frac{4\gamma_{\mathrm{m}}\cos\theta_{\mathrm{m}}}{d} \tag{2.6}$$

where γ_{m} is the surface tension of mercury (0.485N/m), and θ_{m} is the contact angle , which depends on the microstructure of surface of pore walls, the curing age of specimens, and the drying method before test[183]. In this study, the contact angle is assumed to be a constant and the value is adopted as 141.3°[184]. Based on Eq. (2.6), the volume fraction of pore space occupied by pores with diameters in the interval $(d;d+\delta d)$ is deduced from the intrusion volume of mercury under the pressure range $(P;P+\delta P)$, provided that all the pore are directly accessible to mercury. The pore size distribution (PSD) curves can be obtained from the intrusion volume of mercury and the contact angle between mercury and cement paste. However, the pore structure in CBM consists of large pores connected by small throats, which is so-called "ink-bottle" pores. Therefore, the MIP method measures the size of the accessible path of the pore structure rather than its real geometry, but the measurement is still useful for comparison purpose[185-186].

A mercury porosimeter of Micromeritics' AutoPore (IV 9500 series) is used to determine the pore size distribution (PSD) of cement paste specimens. The instrument is capable of exerting an intrusion pressure in the range of 3.5 kPa-414 MPa, corresponding to intruded pore diameters of between 400μm-3.7nm in hardened cement pastes. For each MIP test, one freeze-dried square slice specimen was crushed into particles and collected into the intrusion chamber. The sample is then gradually filled with mercury at a low pressure (about 0.1 MPa). Raising the overall pressure gradually permits mercury to penetrate the sample's largest pores or voids. The quantity of mercury that has intruded is continuously measured by weighing the penetrometer. The applied pressure reached 414 MPa at the conclusion of the test.

2.2.4 Micrometer

The expansion was measured on the rectangular slice specimens, and the initial distance between the two pins on the rectangular slices was set at 100mm, denoted as L_0. The expansion measurement device is shown in Figure 2.13, composed of an electronic micrometer and a reference length bar. The reference length of the bar is exactly 100mm. For each measurement, the needles of the micrometer were inserted into the small holes

Figure 2.13 Micrometer device.

on the reference length bar, and the length on the screen of the micrometer was reset to 0 by pressing the initial setting button. Then place the needles of the micrometer in the holes of the pins on the specimens to read the length change. The first measurement was conducted after 60d curing, and the result was named as ΔL_0. Each measurement was performed three times, and a mean value was used. The expansion strain ε was calculated in Eq. (2.7),

$$\varepsilon = \frac{\Delta L - \Delta L_0}{L_0} \tag{2.7}$$

For the expansion measurement, 3 specimens were tested for each solution. The average of these three specimens was taken as the expansion strain. The expansion was recorded continuously on a weekly basis by a micrometer set with a precision of 1μm measuring the distance change between the two stuck pins. Due to the very thin thickness of the rectangular slices (2 mm), the specimens yielded more or less out of plane curving in the latter phase of ESA expansion as a large amount of AFt is formed. To minimize this error, a total of 9 specimens were initially prepared for each solution, and the three specimens with the least curving effects were retained for the above expansion analysis.

2.2.5 X-ray diffraction

The XRD is a powerful technique for detecting crystalline phases in cement hydrates, including portlandite, ettringite, and Friedel's salt. An XRD pattern is created when the crystalline substance is exposed to X-rays and X-ray diffracts. The device records

the diffraction angle and the corresponding intensity. The diffraction angle, determined through Bragg's law[187], is dependent on the size and shape of the crystal cells, while the intensities of the peaks are related to the nature of the atoms in crystal cells. Comparing the XRD spectrum of an unknown sample with standard spectra of crystallographic phases could identify the presence of crystallographic phases in the unknown sample. This technique, in this study, is qualitative rather than quantitative, as a supplementary method of NMR to identify mineral phases.

The powder samples were ground manually and passed through a sieve to obtain a homogeneous particle size of less than 80 μm. In this study, two XRD instruments in Tsinghua University and in Université Gustave Eiffel were used during the joint doctoral program. In particular, the samples in Part I and II were tested by the XRD instrument in Tsinghua University while the samples in Part III were examined by the XRD instrument in Université Gustave Eiffel. In Université Gustave Eiffel, the type of diffractometer is D8 advance diffractometer, using CoK radiation at an angular step of 0.01° per second between 3.0° and 80° [2θ] angles. In Tsinghua University, the type of diffractometer is D/max-2550, using Cu radiation at an angular step of 0.02° per second between 5.0° and 75° [2θ] angles.

2.2.6 Inductively coupled plasma

The ICP was chosen to quantify the sulfate profiles in the cement disk specimens in Part III. Before the test, the ground powders in each layer of the disk specimen were dissolved by a hydrochloric acid solution using a magnetic stirrer, following the protocol [188]. During the test, the obtained solution was brought into the atomisation system by the carrier gas (argon) for atomisation and then entered the axial channel of the plasma in the form of an aerosol. The solution was then fully evaporated, atomised, ionised and excited in a high temperature and inert atmosphere, emitting characteristic spectral lines of the contained elements. The intensity of the characteristic spectral lines was used to determine the content of the sulfur element. Finally, the sulfur element was converted into the mass ratio of SO_3 with respect to the dried cement paste through the Eq. (2.8),

$$c_{SO_3} = \frac{M_{SO_3}}{M_S} \frac{c_S}{m_{sample}} \times 100 \quad (\text{in} \quad \text{percent}) \tag{2.8}$$

where m_s is the mass of sample used, M_{SO_3} is molecular mass of SO_3, M_S is atomic mass of sulfur element and c_S is the sulfur element concentration measured by ICP (in ppm).

2.2.7 Potentiometric titrator

A potentiometric titrator is used to measure the free and total chloride profiles in disk specimens. The ground powders in the disk specimen were dissolved by nitric acid solution for total chloride content and deionized water for water-soluble chloride content, following the protocols [189] and [190]. Then a 0.01 M $AgNO_3$ solution is added to the test solutions until the electrode potential dramatically changes. The chloride contents are denoted by the mass ratio of Cl with respect to the dried cement paste according to Eq. (2.9),

$$c_{\mathrm{Cl}} = \frac{M_{\mathrm{Cl}}}{m_{\mathrm{sample}}} \frac{V_{\mathrm{ps}}}{V_{\mathrm{ts}}} c_{\mathrm{Ag}} V_{\mathrm{Ag}} \times 100 \quad (\text{in} \quad \text{percent}) \tag{2.9}$$

where m_{sample} is the mass of sample used, V_{ps} is the total volume of prepared test solution, V_{ts} is the dose of test solution for each test, M_{Cl} is atom mass of Cl, c_{Ag} is the concentration of $AgNO_3$ solution and V_{Ag} is the volume of the added $AgNO_3$ solution.

2.2.8 Optical observation

Optical microscopy and BSE-EDS are used to observe the cracking pattern inside the disk specimen in the penetration direction. A disk specimen was cut diametrically to obtain two cross-sections in diffusion direction as in Figure 2.6. One section was dried and then placed under an optical microscope to observe cracks pattern near the exposure surface. Another section was polished and carbon-coated for Backscattered electron image (BSE) and Energy Dispersive Spectrometer (EDS) observations. Based on the BSE results, the section for the optical microscope was ground into several powder samples at different exposure depths, and these powder samples were analysed by X-ray diffraction (XRD) for mineral phases.

2.3 Experimental program

The experimental programs in three parts are given in Table 2.7, 2.8 and 2.9.

Table 2.7 Experimental program in Part I.

Condition	1d	4d	7d	11d	14d	28d	29d
PI-1		NMR	NMR	NMR			NMR
PI-2		NMR;XRD	NMR;XRD	NMR;XRD			NMR;XRD
PI-3	NMR;XRD	NMR;XRD	NMR;XRD	NMR;XRD			NMR;XRD
PI-4		NMR;XRD	NMR;XRD		NMR;XRD	NMR;XRD	

Table 2.8 Experimental program in Part II.

Condition	4d	7d	11d/14d[1]	21d
PII-1		NMR;XRD;DVS	NMR;XRD;MIP;DVS	
PII-2			NMR;XRD;MIP;DVS	
PII-3			NMR;XRD;MIP	
PII-4	NMR;XRD;DVS	NMR;XRD;MIP;DVS	NMR;XRD;MIP;DVS	NMR;XRD;MIP;DVS
PII-5	NMR;XRD;DVS	NMR;XRD;MIP;DVS	NMR;XRD;MIP;DVS	NMR;XRD;MIP;DVS
Condition	28d/29d[2]	56d	70d/84d[3]	168d
PII-1	NMR;XRD;MIP;DVS	NMR;XRD;MIP;DVS	NMR;XRD;MIP;DVS	
PII-2	NMR;XRD;MIP;DVS	NMR;XRD;DVS	NMR;XRD;MIP;DVS	NMR;XRD
PII-3	NMR;XRD;MIP	NMR;XRD	NMR;XRD;MIP	
PII-4	NMR;XRD;MIP;DVS		NMR;XRD	
PII-5	NMR;XRD;MIP;DVS		NMR;XRD	

[1] 11d for PII-1/2/3 conditions and 14d for PII-4/5 conditions.
[2] 28d for PII-4/5 conditions and 29d for PII-1/2/3 conditions.
[3] 70d for PII-4/5 conditions and 84d for PII-1/2/3 conditions.

Table 2.9 Experimental program in Part III.

Condition	2m	4m	8m
PIII-1	ICP;OP[1];BSE-EDS;XRD	ICP;OP	ICP;OP
PIII-2	ICP;OP;BSE-EDS;XRD	ICP;OP	ICP;OP
PIII-3	ICP;PT[2]	ICP;PT;OP	ICP;OP;BSE-EDS;XRD
PIII-4	ICP;OP;XRD	ICP;OP	
PIII-5	ICP;OP;XRD	ICP;OP	ICP
PIII-6	ICP;PT;OP;XRD	ICP;PT;OP	ICP

[1] “OP” denoting optical microscope.
[2] “PT” denoting potentiometric titrator.

CHAPTER 3 KINETICS OF ETTRINGITE FORMATION

The kinetics of AFt formation was investigated for cement paste powders subjected to ESA with and without the combined actions in experimental Part I. Powder samples were ground from hardened cement paste, as stated in Section 2.1.3, and exposed to four sulfate-bearing conditions given in Table 3.1. The evolution of AFt formation was characterized through ^{27}Al NMR, cf. Section 2.2.1, and the XRD analysis as shown in Section 2.2.5 was also performed to identify the mineral phase species and their change pattern. The flowing chart of the test program in Part I is shown in Figure 3.1.

Table 3.1 Composition of the test solutions in Part I.

Condition	SO_4^{2-} content	Cl^- content	pH value (-)	Heating treatment
PI-1	3 g/L	0	13	-
PI-2	10 g/L	0	13	-
PI-3	10 g/L	10 g/L	13	-
PI-4	10 g/L	0	13	+

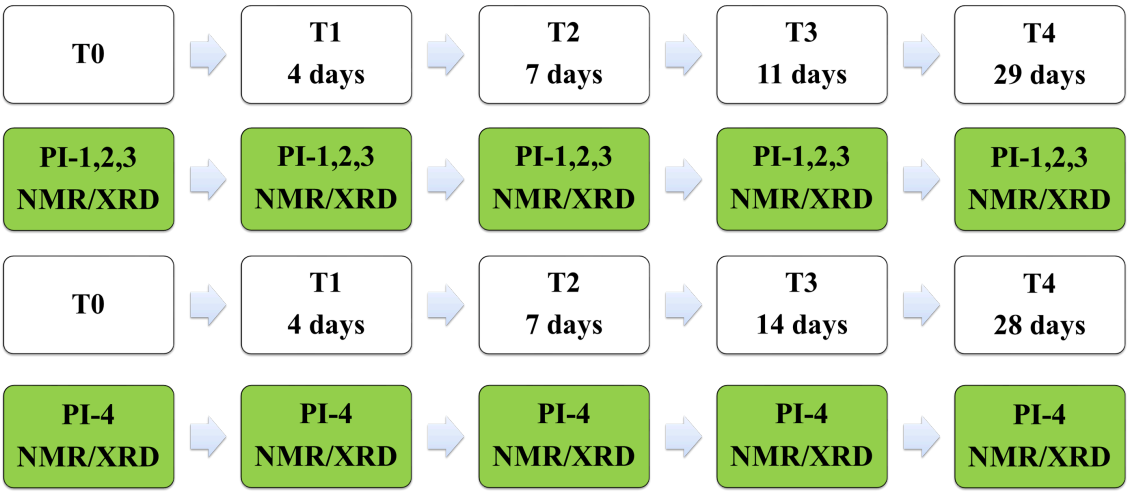

Figure 3.1 Flowing chart in Part I.

3.1 Aluminum phases contents by ^{27}Al NMR

The relative contents of aluminum phases, expressed in percentage % of aluminum

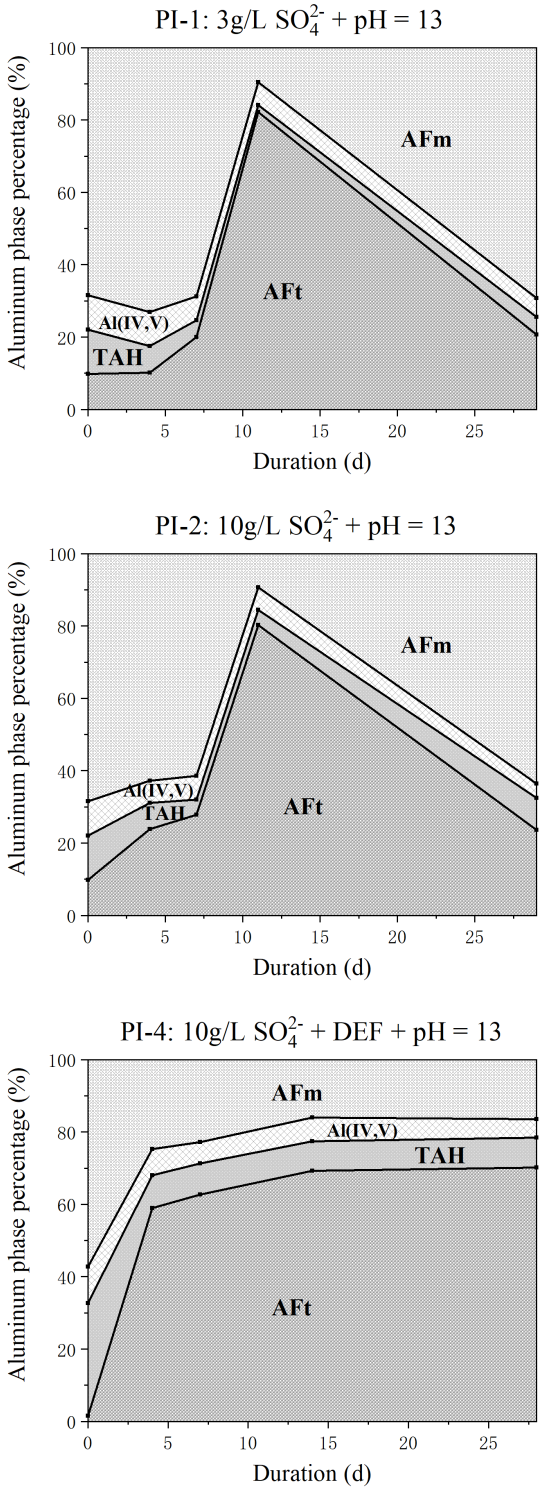

Figure 3.2 Aluminum phase contents in cement paste powder samples exposed to PI-1 (top), PI-2 (middle) and PI-4 (bottom) conditions at different exposure ages. Al(IV,V) represents the sum of IV and V aluminum phases.

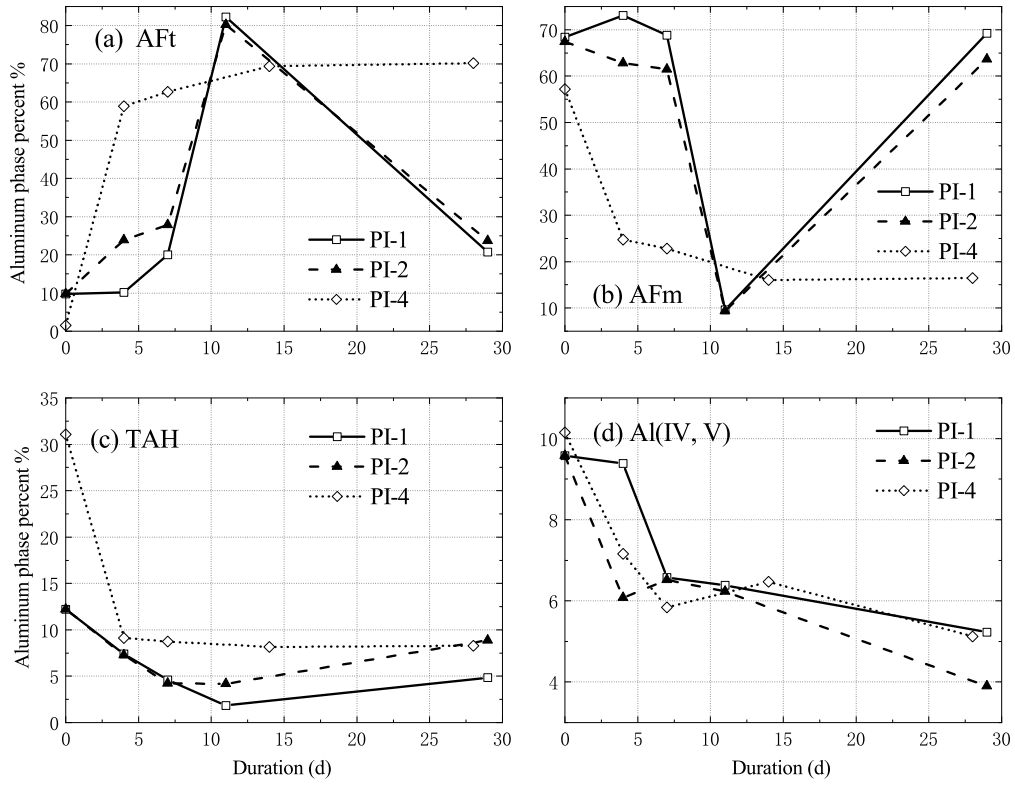

Figure 3.3 Contents of AFt (a), AFm (b), TAH (c) and Al(IV,V) (d) phases in cement paste powder samples exposed to three conditions. PI-1 stands for 3g/L SO_4^{2-}, PI-2 for 10g/L SO_4^{2-}, and PI-4 for 10g/L SO_4^{2-} + DEF.

atoms in total aluminum phases, were derived from the two-range ^{27}Al NMR spectra in Figure 2.8 through the multi-phases fitting method in Figure 2.9. As aforementioned, the Al(IV) and Al(V) phases are incorporated in CSH structure at different sites, at silicon chain for Al(IV) phase and at interlayer Ca for Al(V) phase, and their contents, about 5-10%, are relatively small compared to other aluminum phases[36]. Thus, the contents of these two phases are merged together in the results, denoted as Al(IV,V). Except for PI-3 condition (combined sulfate and chloride condition), the five aluminum phase contents in cement paste powder samples are presented in Figure 3.2 for exposure conditions PI-1/2/4 at different exposure ages. In Figure 3.2, the AFt content augments with time in the first 11/14d and then drops significantly at 29d in PI-1/2 conditions. Meanwhile, AFm phase content undergoes an opposite pattern to AFt phase, and TAH and Al(IV,V) phases decrease with time for the three conditions. The abnormal drop in AFt phase content and the rise in AFm phase content in PI-1 and PI-2 conditions at 29d will be confirmed

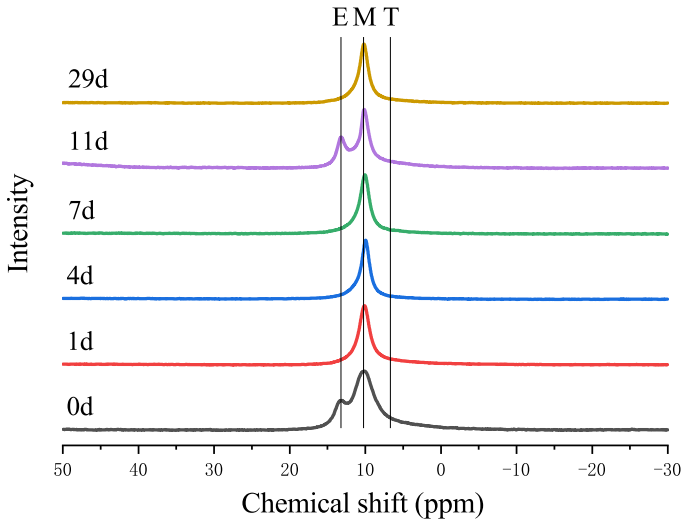

Figure 3.4 ^{27}Al MAS NMR spectra of cement paste powder samples exposed to PI-3 condition. The symbols E, M and T denote ettringite, monosulfoaluminate and third aluminum phase (TAH) respectively.

by XRD results in the following section. Globally, the results in Figure 3.2 confirm the transformation from AFm and Al(IV,V) phases to AFt phase in cement paste exposed to sulfate solutions.

Figure 3.3 illustrates the impact of sulfate concentration and heating treatment on the evolution of aluminum phases. As for the effect of sulfate concentration on AFt formation, the results show that: (1) a higher sulfate concentration leads to a higher AFt content at the same exposure age during the first 14d, cf. Figure 3.3a; (2) the difference in AFt content between PI-1 and PI-2 conditions decreases with time and even to zero at 11d. Besides, the content of AFm phases in PI-2 shows a little decrease before 7d while it increases in PI-1 condition in Figure 3.3b. TAH and Al(IV,V) phases contents decrease with time in PI-1 and PI-2 conditions and show no systematic difference between these conditions in Figures 3.3c and d. As for the influence of heating treatment in PI-4 condition, the heating treatment obviously accelerates the formation rate of AFt in Figure 3.3a and the consumption rate of AFt phases in Figure 3.3b. Besides, the significant difference in the initial AFt contents at 0d for PI-1 and PI-4 conditions in Figure 3.3a confirms the dissolution of AFt by the heating treatment within the curing period. Besides, the AFm phase content shows an obvious decrease (about 11.20%) while TAH phase shows a noticeable increase (about 18.85%). Thus, the released aluminum from AFt is stored in the TAH phase, which is an amorphous/disordered aluminium hydrate as a separate phase precipitated on the C-S-H

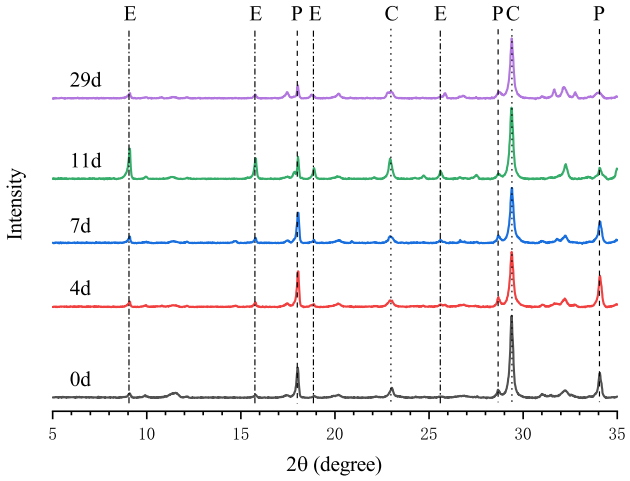

(a)

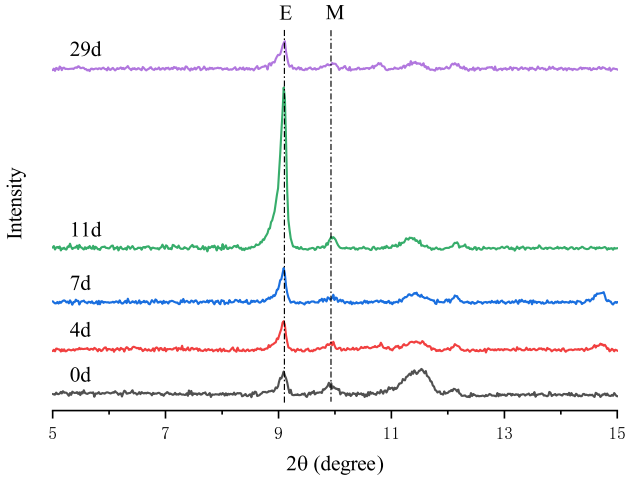

(b)

Figure 3.5 XRD analysis of cement paste powder samples exposed to PI-2 condition (a) and zoom (b). "E" and "M" stand for ettringite and monosulfoaluminate.

phase[24], rather than the AFm phases.

The ^{27}Al NMR spectra for cement paste powders exposed to PI-3 condition are given in Figure 3.4. Interestingly, the AFt peak disappears within the first 7d, indicating the transformation of AFt into AFm phases in the presence of chlorides. The re-appearance of AFt peak at 11d confirms the mitigating effect of chlorides on AFt formation.

It is worthwhile to note that the AFm phases in hardened cement pastes refer to a family of aluminium(A)-ferrite(F) hydrates with a double-layered structure, having a general formula $[Ca_2(Al,Fe)(OH)_6]\cdot X\cdot xH_2O$, where X denotes one formula unit of a single-charged anion or a half double-charged anion, and x is the interlayer water content con-

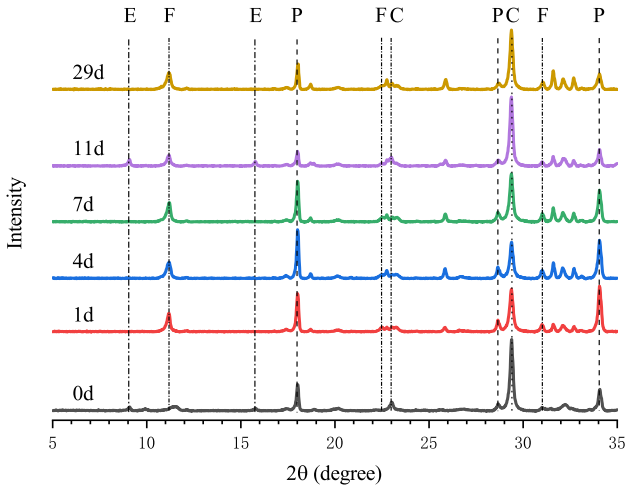

(a)

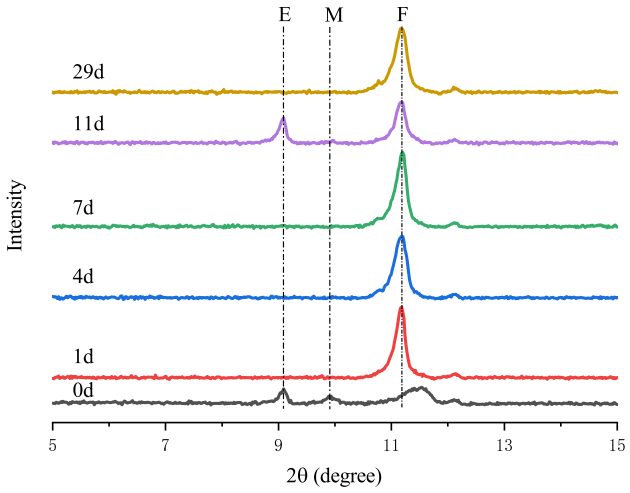

(b)

Figure 3.6 XRD analysis of cement paste powder samples exposed to PI-3 condition (a) and zoom (b). "E", "M" and "F" stand for ettringite, monosulfoaluminate and Friedel's salt, respectively.

ditioned by the temperature and RH at exposure[16]. Depending on the chemical environments, the double-layered structure could incorporate different anions to form different AFm species, such as monosulfoaluminate ($Ca_4[Al(OH)_6]_2 \cdot SO_4 \cdot xH_2O$, denoted as Ms(6+$x$)), hydroxy-AFm ($Ca_4[Al(OH)_6]_2 \cdot (OH)_2 \cdot xH_2O$, denoted as C_4AH_{7+x}) and Friedel's salts ($Ca_4[Al(OH)_6]_2 \cdot Cl_2 \cdot 4H_2O$, denoted as $C_3ACaCl_2H_{10}$)[191]. Due to the similar layered structure in these AFm species, i.e. almost the same chemical environments for Al atoms, the positions of peaks of these AFm phases in ^{27}Al NMR spectrum are very close (~ 1 ppm) compared to their peak widths (~10 ppm)[21]. Therefore, an

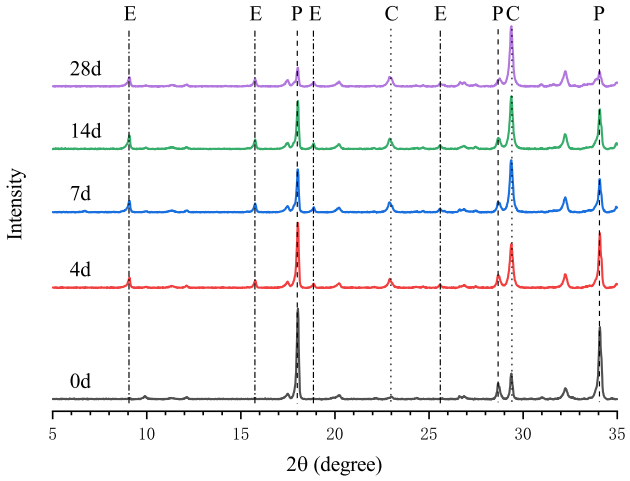

(a)

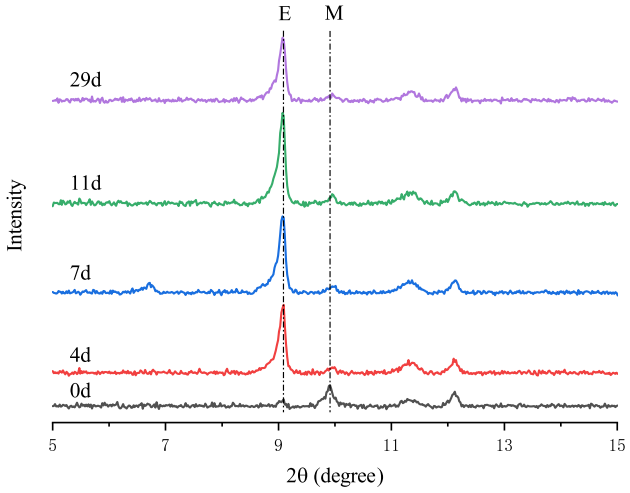

(b)

Figure 3.7 XRD analysis of cement paste powder samples exposed to PI-4 condition (a) and zoom (b). "E" , "P", "C" and "M" stand for ettringite, portlandite, calcite and monosulfoaluminate.

extremely high spinning speed would be necessary to reduce their peak widths and separate these different AFm species. These different AFm species cannot be identified from the ^{27}Al NMR spectra in this study. Actually, the OH-SO_4-AFm solid solution, solution of Ms(6+x) and C_4AH_{7+x}, is the most common aluminum hydrates in ordinary cement pastes[127,192]. When subjected to mixed solution of sulfates and chlorides, the OH-SO_4-AFm tends to concurrently convert into AFt and $C_3ACaCl_2H_{10}$. Birnin-Yauri and Glasser[193] reported that only ~14 mM chlorides are required to convert C_4AH_{7+x} to $C_3ACaCl_2H_{10}$ completely. The XRD results later confirm the existence of Friedel's salt in the mixed sulfate and chloride solution. Therefore, the AFm species are most likely to

be OH-SO_4-AFm in PI-1/2/4 conditions but $C_3ACaCl_2H_{10}$ and Ms(6+x) in PI1-3 conditions.

3.2 XRD analysis

The XRD results of cement paste powders exposed to PI-2, PI-3, and PI-4 conditions are presented in Figures 3.5, 3.6 and 3.7 respectively. The appearance of a calcite peak is due to the long-term storage. In Figure 3.5b, the intensity of the ettringite peak increases

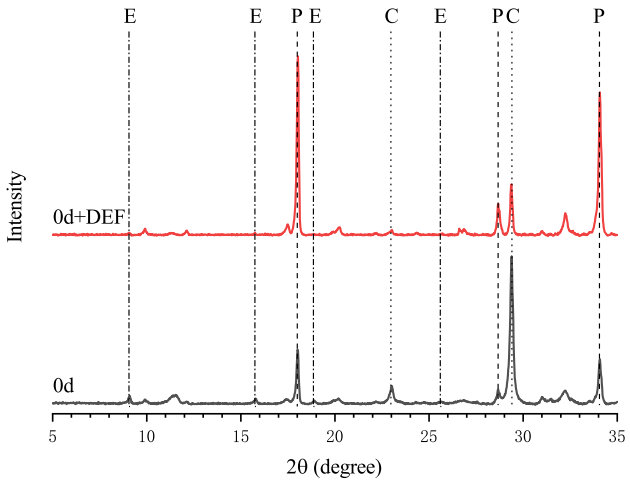

(a)

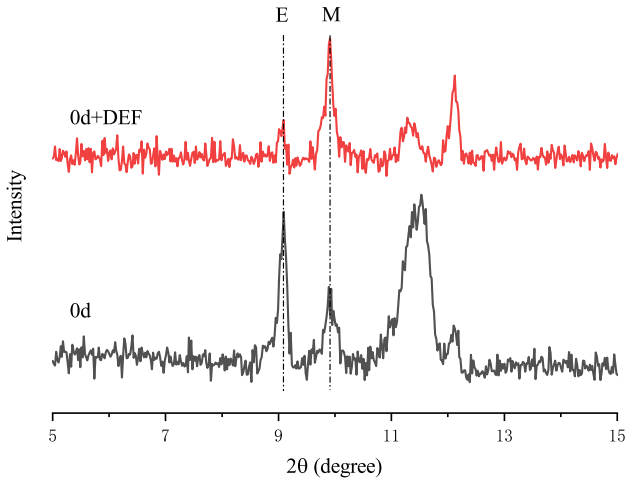

(b)

Figure 3.8 Comparison of XRD results of cement paste powder samples with and without heating treatment before immersion (a) and zoom (b). “E” , “P”, “C” and “M” stand for ettringite, portlandite, calcite and monosulfoaluminate.

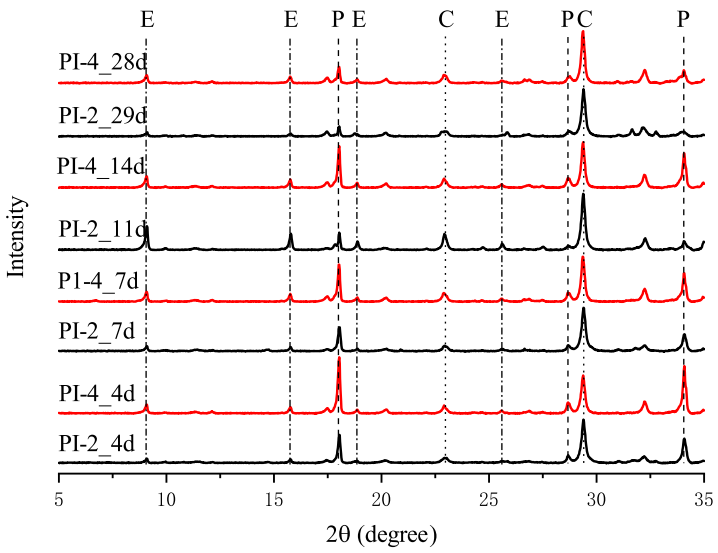

(a)

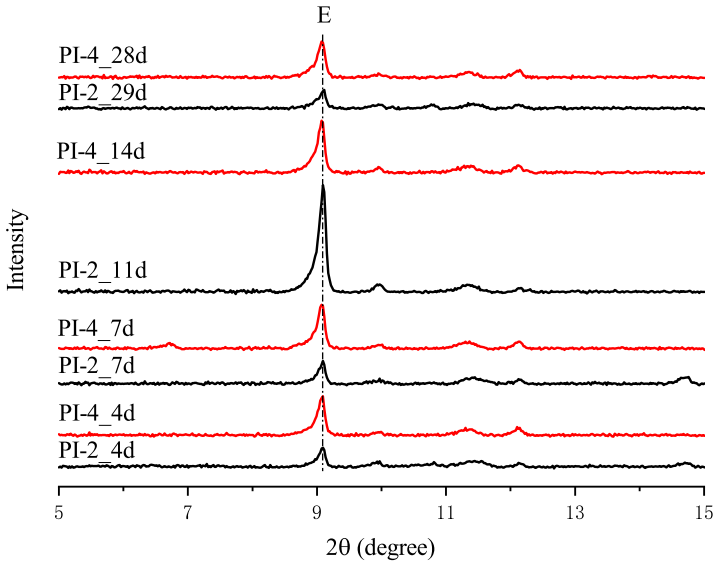

(b)

Figure 3.9 Comparison of XRD results of cement paste powder samples exposed to PI-2 and PI-4 conditions (a) and zoom (b). “E” , “P”, “C” and “M” stand for ettringite, portlandite, calcite and monosulfoaluminate. PI-2 stands for 10g/L SO_4^{2-}, and PI-4 for 10g/L SO_4^{2-} + DEF.

with time in the first 11d and subsequently decreases at 29d, which agrees with the change of AFt content in ^{27}Al NMR results in Figure 3.2a. Due to the poorly crystallized monosulfoaluminatecite[16], the peak intensity of monosulfoaluminate is slight and disproportionate to its amount. The decrease of portlandite peak is attributed to two effects: the consumption by chemical reactions in Eq. (1.1) and the carbonation during the storage

of powder samples. In Figure 3.6b, the AFt peak disappears at the beginning 7d, and re-appears at 11d and re-disappears at 29d, which shows the same evolution pattern as AFt content in Figure 3.2b. Besides, the appearance of Friedel's salt peak and disappearance of monosulfoaluminate confirm that the species of AFm phases in combined sulfate and chloride condition (Figure 3.2b) is Friedel's salt. The decrease from 7d to 11d on the intensity Friedel's salt verifies the transformation from Friedel's salt into ettringite. In Figure 3.7b, a rapid rise of ettringte peak is in line with the results of AFt content by ^{27}Al NMR in Figure 3.2c.

Figure 3.8 compares the XRD results for the cement paste powders with and without heating treatment at 0d before exposure. The decrease of ettringite peak after heating treatment confirms the dissolution of ettringite at elevated temperatures. However, the increase of monosulfoaluminate peak disagrees with the change in AFm phases in Figure 3.3b. It may be due to the re-crystallization of monosulfoaluminate during the cooling period after its dissolution by the heating treatment. After heating, the dissolved aluminate ions are uniformly distributed in the pore solution and then re-crystallized in free capillary pore with good crystal form. Figure 3.9 compares the XRD results, especially the AFt peaks in PI-2 and PI-4 conditions. The systematic higher AFt peaks in PI-4 condition compared to PI-2 condition confirm the accelerating effect of heating treatment on ettringite formation.

3.3 Conclusions

Based on the analysis of NMR and XRD results, the major findings in experimental Part I include: (1) the AFm and Al(IV,V) phases are transformed into the AFt phase in cement paste exposed to ESA conditions without chlorides, and the high sulfate concentration favors this transformation to generate more AFt phase; (2) heating treatment dissolves the initial AFt phase into the TAH phase bn the CSH surface rather than the AFm phases during curing stage, and significantly accelerates the AFt formation in the early stage of exposure; (3) chlorides mitigate the AFt formation, and the species of the AFm phases are the solid solution of monosulfoaluminate and hydroxy-AFm in cement paste under ESA but Friedel's salt and hydroxy-AFm in in cement paste under the combined ESA and chloride actions; (4) an abnormal drop of AFt content at the end of exposure appears in cement paste under ESA conditions without chlorides, and the NMR results show good agreement with XRD results.

CHAPTER 4 PORE CRYSTALLIZATION AND EXPANSION

The pore crystallization and its mechanical and physical effects were investigated for cement paste slices subjected to ESA with and without the combined actions through the experimental Part II. Slice specimens (see in Figures 2.5a and b) were sawed from prismetric cement paste, as shown in Figure 2.4, and exposed to five sulfate-bearing conditions given in Table 4.1. The evolutions of AFt formation, pore structure, transport property, and specimen expansion were characterized through ^{27}Al NMR + XRD, MIP, DVS, and micrometer, cf. Section 2.2, respectively. The flowing chart of the test program in Part II is shown in Figure 4.1.

Table 4.1 Composition of the test solutions in Part II.

Condition	SO_4^{2-} content	Cl^- content	pH value (-)	Heating treatment
PII-1	10 g/L	0	13	-
PII-2	10 g/L	10 g/L	13	-
PII-3	10 g/L	19 g/L	13	-
PII-4	10 g/L	0	13	+
PII-5	10 g/L	19 g/L	13	+

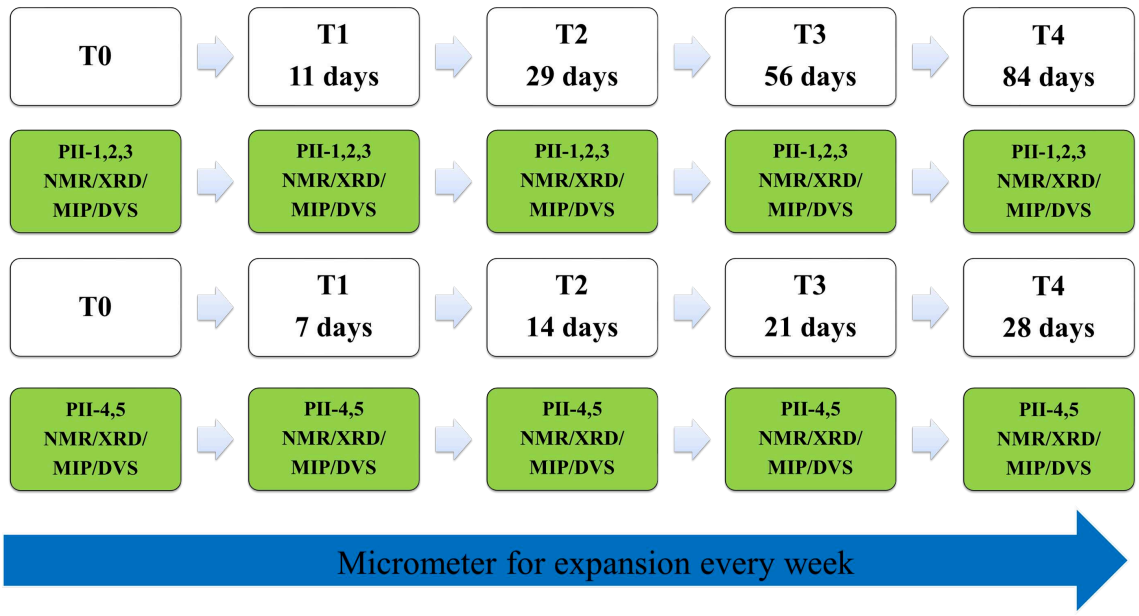

Figure 4.1 Flowing chart in Part II.

4.1 Evolution of aluminum phases

4.1.1 ^{27}Al NMR results

All the five aluminum phase contents in cement paste exposed to five conditions are presented in Figures C.1-C.5 at different exposure ages. As in experimental Part I, the contents of Al(IV) and Al(V) phases are merged together in the results, denoted as Al(IV,V). For the pure sulfate condition, i.e. PII-1 condition, in Figure C.1 the AFt content grows with time accompanied by a drop of AFm and Al(IV,V) contents, while the TAH content fluctuates between 8-18% during the first 56d immersion and decreases to 4% at 84d. For the other conditions including PII-2, PII-3, PII-4 and PII-5 as in Figures C.2-C.5, the contents of AFt, AFm and Al(IV,V) phases evolve in the same pattern as in PII-1 condition but with different change rates. The TAH phase content shows a decreasing tend with time in PII-1, PII-2, PII-4 and PII-5 conditions, while an increasing trend in PII-3

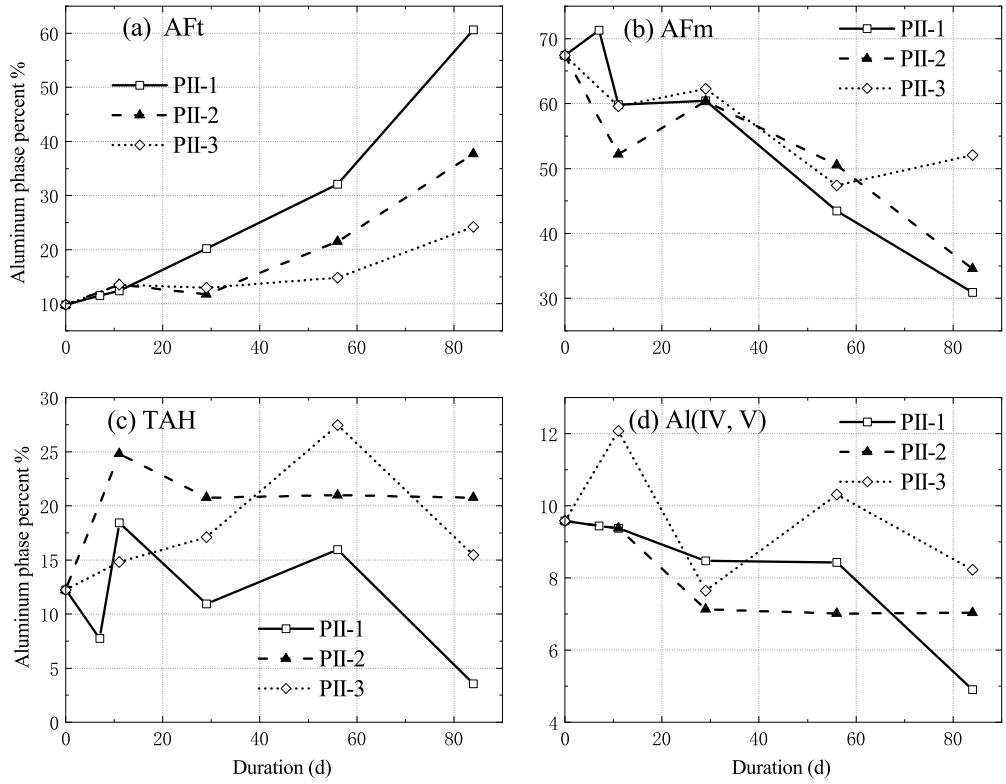

Figure 4.2 Contents of AFt (a), AFm (b), TAH (c) and Al(IV,V) (d) phases in cement paste layer specimens exposed to three conditions. PII-1 stands for 10g/L SO_4^{2-}, PII-2 for 10g/L SO_4^{2-} + 10g/L Cl^-, and PII-3 for 10g/L SO_4^{2-} + 19g/L Cl^-.

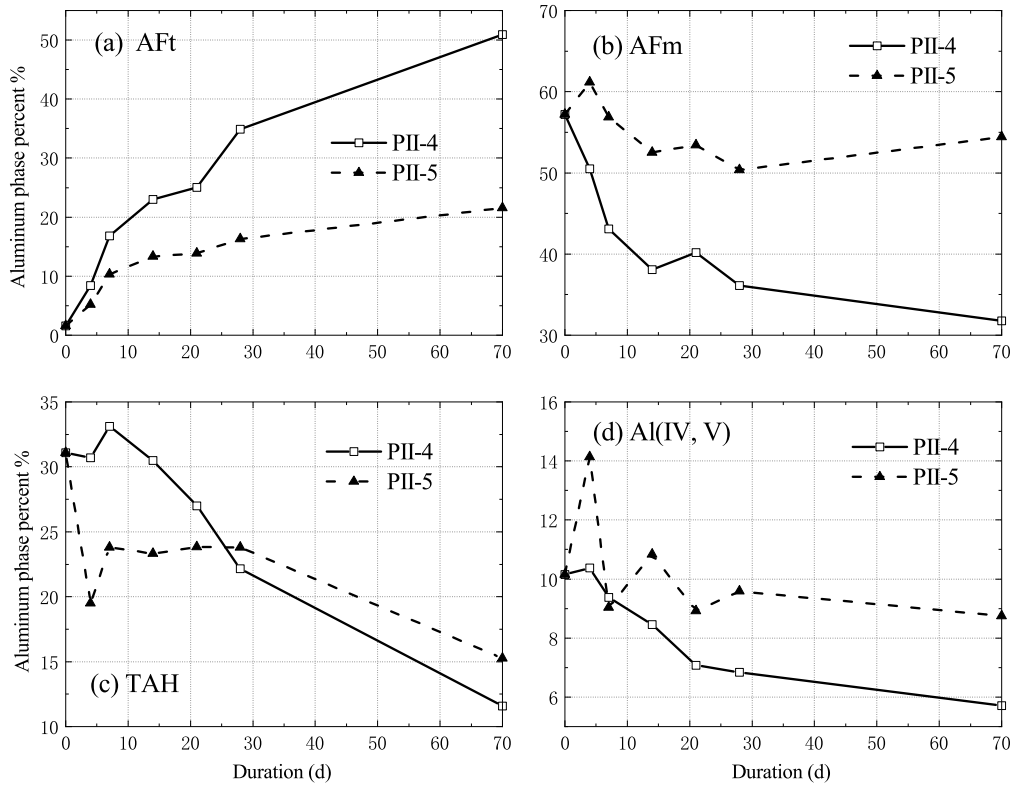

Figure 4.3 Contents of AFt (a), AFm (b), TAH (c) and Al(IV,V) (d) phases in cement paste layer specimens exposed to two conditions. PII-4 stands for 10g/L SO_4^{2-} + DEF, and PII-5 for 10g/L SO_4^{2-} + 19g/L Cl^- + DEF.

conditions within the measured period. Globally, the results in Figures C.1-C.5 confirm the transformation from AFm, Al(IV,V) and TAH phases to AFt phase in sulfate-bearing conditions, and this transformation is still in kinetic phase after 70d-168d immersion.

Figure 4.2 illustrates the impact of chlorides on the evolution of aluminum phases in ESA conditions without DEF (PII-1/2/3). Firstly, the presence of chlorides reduces notably the AFt content at the same exposure ages, cf. Figure 4.2a. Secondly, the higher chloride concentration in PII-3 condition results in a larger inhibiting effect on the AFt formation. This is direct experimental evidence for the inhibiting effect of chlorides on AFt formation. Thirdly, the content of AFm phases shows no systematic difference for the three solutions in Figure 4.2b, and the TAH content is systematically higher in mixed solutions, cf. Figure 4.2c. Finally, the content of Al(IV,V) phases seems to be less consumed in the mixed sulfate and chloride solutions, cf. Figure 4.2d. A synthesis of these results reveals that a significant amount of AFm phase transforms to TAH phase at the first

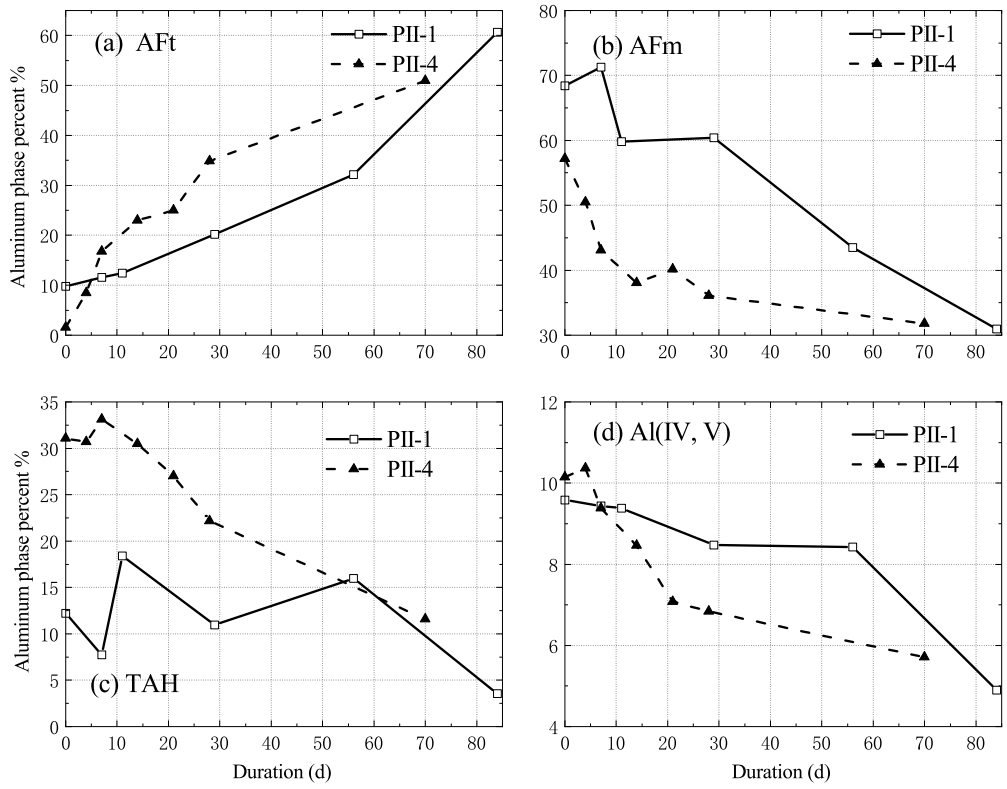

Figure 4.4 Contents of AFt (a), AFm (b), TAH (c) and Al(IV,V) (d) phases in cement paste layer specimens exposed to two conditions. PII-1 stands for 10g/L SO_4^{2-} and PII-4 for 10g/L SO_4^{2-} + DEF.

56d, besides the AFt phase, in the mixed solutions. Thus, these results seem to support the following mechanism: **a significant amount of AFm phase and a small quantity of Al(IV,V) phase are converted to AFt phase when exposed to sulfate-containing solution, and the presence of chlorides converts part of AFm phase into TAH, resulting in less AFt formation.**

Figure 4.3 illustrates the impact of chlorides on the transformation among aluminum phases in ESA conditions with DEF (PII-4/5). The conspicuously smaller AFt content in PII-4 condition compared to PII-5 condition confirms the mitigating effect of chlorides in AFt formation again. Besides, the presence of chlorides decelerates the consumption of AFm phases in combined ESA and DEF conditions. The TAH phase consumption was initially accelerated at the first 7d while the Al(IV,V) was less consumed in the presence of chlorides.

Figures 4.4 and 4.5 present the influence of heating treatment on the change of Alu-

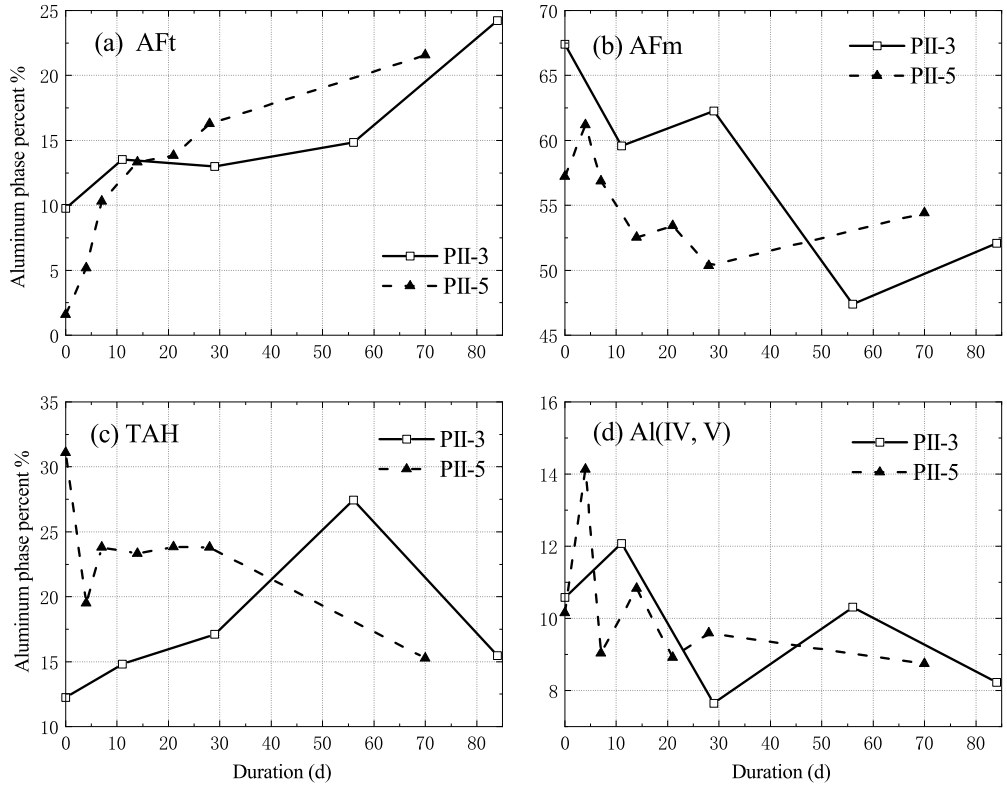

Figure 4.5 Contents of AFt (a), AFm (b), TAH (c) and Al(IV,V) (d) phases in cement paste layer specimens exposed to two conditions. PII-3 stands for 10g/L SO_4^{2-} + 19g/L Cl^- and PII-5 for 10g/L SO_4^{2-} + 19g/L Cl^- + DEF.

minum phases content. In both ESA conditions with and without DEF, as in Figures 4.4 and 4.5 respectively, the heating treatment accelerates the AFt formation and the consumption of AFm phases. Especially in combined sulfate + chloride + DEF condition, as shown in Figure 4.5, the promoting effect of heating treatment neutralizes or overweighs the inhibiting effect of chlorides on the AFt formation. Additionally, the transformation from AFt into TAH by heating treatment during curing is again observed in the layer specimens at 0d before exposure.

4.1.2 XRD results

The XRD results of slice specimens of cement paste exposed to PII-1, PII-2, PII-3, PII-4 and PI-5 conditions are presented in Figures C.6-C.10 respectively. It is clear that the intensity of the AFt peak increases with exposure time in Figure C.6b and Figure C.9b. The growing tendency of AFt peak intensity with time in the other three mixed sulfate and

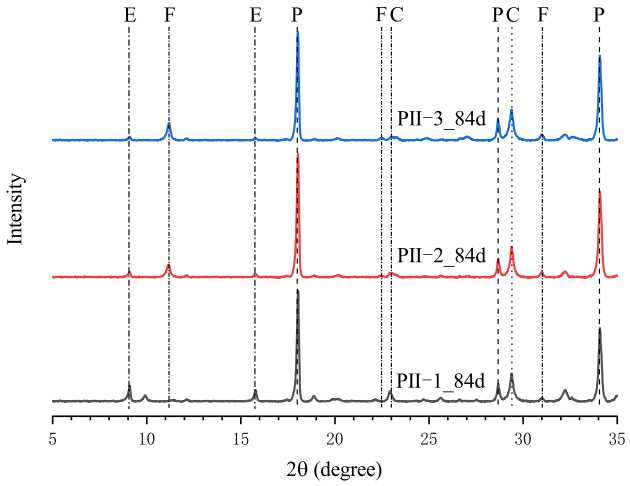

(a)

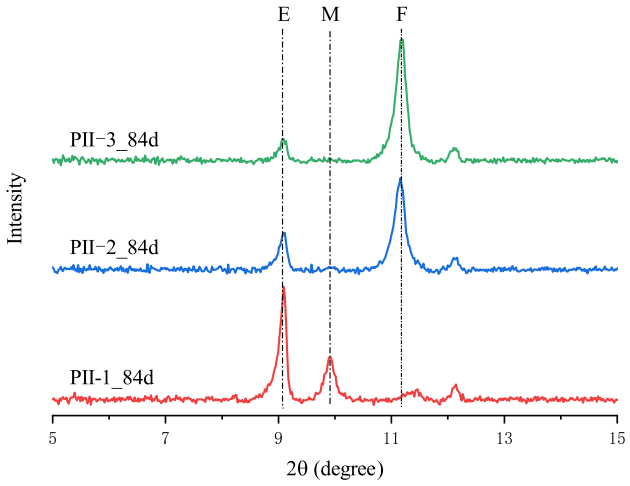

(b)

Figure 4.6 Comparison of XRD results of cement paste layer specimens exposed to PII-1, PII-2 and PII-3 conditions for 84d (a) and zoom (b). "E" , "P", "C", "M" and "F" stand for ettringite, portlandite, calcite, monosulfoaluminate and Friedel's salt. PII-1 stands for 10g/L SO_4^{2-}, PII-2 for 10g/L SO_4^{2-} + 10g/L Cl^-, and PII-3 for 10g/L SO_4^{2-} + 19g/L Cl^-.

chloride conditions (PII-2/3/5) is less notable, but it does exist. Besides, a notable peak representing Friedel's salt is detected in three mixed sulfate and chloride conditions, which agrees with the results in Part I and attributes the species of AFm phase in Figures C.2, C.3 and C.5 to Friedel's salt. It is interesting to note that no gypsum is found in all five exposure conditions, as in Figures C.6-C.10a. The absence of gypsum is inconsistent with the findings in most literature[10,22,37,49-50,99,121,143,194] and the most possible reason is the special pH value of 13 which we designed. In such a high pH environment, the leaching of

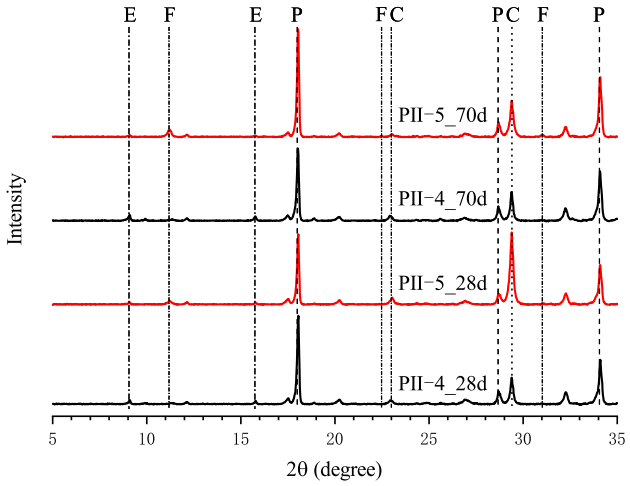

(a)

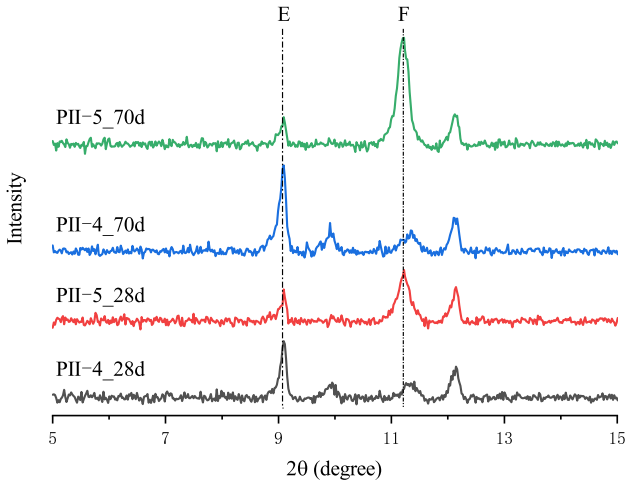

(b)

Figure 4.7 Comparison of XRD results of cement paste layer specimens exposed to PII-4 and PII-5 conditions for 28d and 70d (a) and zoom (b). "E" , "P", "C", "M" and "F" stand for ettringite, portlandite, calcite, monosulfoaluminate and Friedel's salt. PII-4 stands for 10g/L SO_4^{2-} + DEF, and PII-5 for 10g/L SO_4^{2-} + 19g/L Cl^- + DEF.

calcium and hydroxide ions is inhibited and it may affect the gypsum formation. A further investigation into the leaching effect on the ESA mechanism, especially the formation of gypsum, was conducted in the experimental Part III (Section 5.3.1).

Figure 4.6 compares the XRD results for slice specimens of cement paste exposed to PII-1, PII-2 and PII-3 conditions for 84d, and Figure 4.7 compares the XRD results for slice specimens exposed to PII-4 condition for 28d and PII-5 condition for 70d. The results in Figure 4.6 and Figure 4.7 confirm the mitigating effect of chlorides on AFt formation

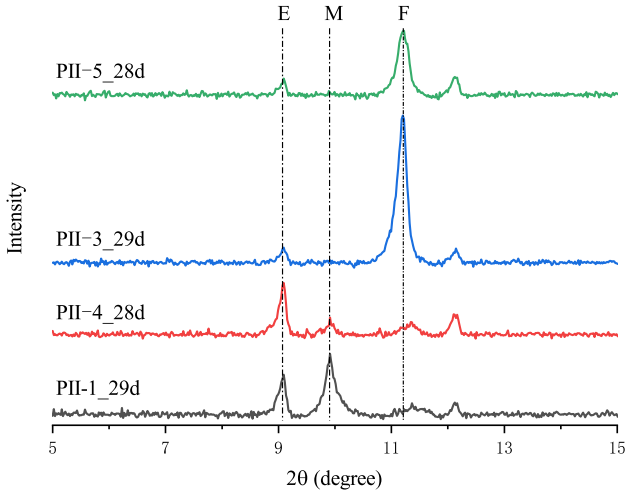

(a)

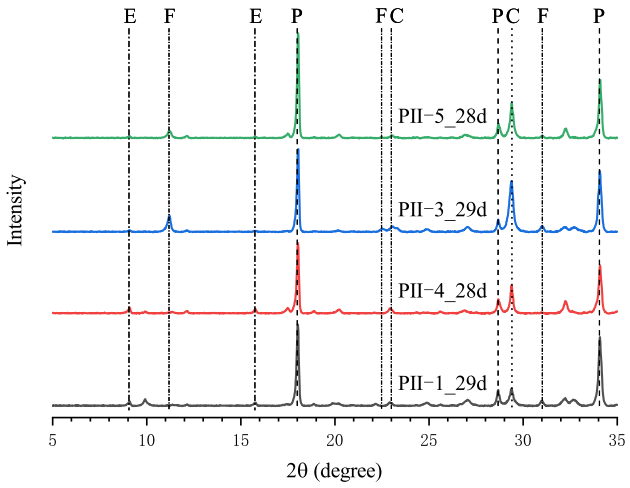

(b)

Figure 4.8 Comparison of XRD results of cement paste layer specimens exposed to PII-1, PII-3, PII-4 and PII-5 conditions about 28d (a) and zoom (b). "E" , "P", "C" and "M" and stand for ettringite, portlandite, calcite and monosulfoaluminate. PII-1 stands for 10g/L SO_4^{2-}, PII-3 for 10g/L SO_4^{2-} + 19g/L Cl^-, PII-4 for 10g/L SO_4^{2-} + DEF, and PII-5 for 10g/L SO_4^{2-} + 19g/L Cl^- + DEF.

and the transformation from AFt and monosulfoaluminate into Friedel's salt. Figure 4.8 compares the XRD results for slice specimens exposed to PII-1 and PII-3 conditions for 28d, and PII-4 and PII-5 conditions for 29d, which demonstrates the accelerating effect of heating treatment on AFt formation.

4.1.3 Mitigating effect of chlorides on AFt formation

The transformation from AFm phases to AFt under mixed solutions merits further discussion. As discussed before, the transformation from AFm phases to AFt in three solutions involves the following reactions,

$$\begin{aligned} &C_4AH_{7+x} + 3CH + 3SO_4^{2-} \longrightarrow AFt + 6OH^- \\ &Ms(6+x) + 2CH + 2SO_4^{2-} \longrightarrow AFt + 4OH^- \\ &C_3ACaCl_2H_{10} + 2CH + 3SO_4^{2-} \longrightarrow AFt + 4OH^- + 2Cl^- \end{aligned} \tag{4.1}$$

The first two reactions occur in pure sulfate solution (PII-1) while the last two equations happen in mixed solutions (PII-2,PII-3). The supersaturation of AFt, β_{AFt}, can be taken as the driving force for the crystallization process, defined through,

$$\beta_{\mathrm{AFt}} = \frac{\left(a_{Ca^{2+}}\right)^6 \left(a_{OH^-}\right)^4 \left(a_{SO_4^{2-}}\right)^3 \left(a_{Al(OH)_4^-}\right)^2}{K_{\mathrm{AFt}}} \tag{4.2}$$

with K_{AFt} standing for dissolution constant of AFt and a_i the ionic activity for species i. As a first approximation, the pore solution is regarded as a dilute solution and the ionic activity a_i is numerically equal to the ionic concentration c_i.

Now we attempt to quantify the supersaturation β_{AFt} for this study. The pore solution of specimens of 2mm thickness can be assumed to be in equilibrium with the solutions during the expansion. Thus, the concentrations of OH^- and SO_4^{2-}, c_{OH^-} and $c_{SO_4^{2-}}$, can take the values of solutions. The calcium and aluminate ions needed to form AFt are provided by the CH and AFm phases, respectively. Assuming the rapid dissolution of CH and AFm phases, these two phases are at their dissolution equilibria before they are depleted[31],

$$\begin{cases} \beta_{\mathrm{CH}} = \dfrac{\left(c_{Ca^{2+}}\right)\left(c_{OH^-}\right)^2}{K_{\mathrm{CH}}} = 1 \\ \beta_{C_4AH_{7+x}} = \dfrac{\left(c_{Ca^{2+}}\right)^4 \left(c_{OH}\right)^6 \left(c_{S,Al(OH)_4^-}\right)^2}{K_{C_4AH_{7+x}}} = 1 \\ \beta_{\mathrm{FS}} = \dfrac{\left(c_{Ca^{2+}}\right)^4 \left(c_{OH}\right)^4 \left(c_{Cl^-}\right)^2 \left(c_{Cl,Al(OH)_4^-}\right)^2}{K_{\mathrm{FS}}} = 1 \end{cases} \tag{4.3}$$

where β_{i} and K_{i} denote the supersaturation and dissolution constant of phase i, and $c_{S,Al(OH)_4^-}$ and $c_{Cl,Al(OH)_4^-}$ stand for the aluminate concentration in pure sulfate solution and mixed solution respectively.

Table 4.2 Dissolution constants at 25°C and calculated ion concentrations.

Parameter	Unit	Value
K_{CH}	$\log(K_{CH})$ (-)	-5.14[195]
$K_{C_4AH_{7+x}}$	$\log(K_{C_4AH_{7+x}})$ (-)	-25.40[195]
K_{FS}	$\log(K_{FS})$ (-)	-27.10[195]
K_{AFt}	$\log(K_{AFt})$ (-)	-44.55[195]
$c_{SO_4^{2-}}$	mol/L	0.104 (PII-1,PII-2,PII-3)
c_{OH^-}	mol/L	0.100 (PII-1,PII-2,PII-3)
$c_{Ca^{2+}}$	mol/L	0.72×10^{-3} (PII-1,PII-2,PII-3)
c_{Cl^-}	mol/L	0(PII-1), 0.282(PII-2), 0.536 (PII-3)
$c_{Al(OH)_4^-}$	mol/L	0.380×10^{-3}(PII-1), 0.019×10^{-3}(PII-2), 0.010×10^{-3}(PII-3)
$c_{Na^+(K^+)}$	mol/L	0.307(PII-1),0.589(PII-2),0.843(PII-3)
β_{AFt}	(-)	8.34×10^{11}(PII-1), 2.09×10^{9}(PII-2), 5.79×10^{8}(PII-3)

The dissolution constants involved in Eq.(4.2) and Eq.(4.3) are summarized in Table 4.2, and the concentrations of main ion species are also given. The electrical neutrality is assured through adjusting the concentration of alkali ions (Na^+, K^+) at given pH value of solution. The aluminate concentrations $c_{Al(OH)_4^-}$ are determined as 0.380 mmol/L, 0.019 mmol/L and 0.010 mmol/L for PII-1/2/3 solutions respectively. Substituting these values into Eq.(4.2) gives the β_{AFt} values as 8.34×10^{11} (PII-1), 2.09×10^{9} (PII-2) and 5.79×10^{8} (PII-3). Such a decrease of driving force for crystallization, β_{AFt} in terms of the chloride concentration c_{Cl^-}, coincides with the decrease of the AFt formation rate with chloride concentration in Figure 4.2a.

For the combined ESA and DEF conditions (PII-4/5), it is difficult to estimate the AFt supersaturation. In these combined conditions, the sulfates come from external solution and an internal source, which is the released absorbed sulfates on the CSH surface. The amount of the released sulfates from CSH is not easy to evaluate because the adsorption mechanism is still unclear. Thus, it is difficult to precisely predict the AFt supersaturation in the combined ESA and DEF conditions, but it should be larger than the estimated supersaturation in ESA conditions (PII-1/2/3).

4.2 Pore structure

4.2.1 MIP results

Figures 4.9-4.13 present the pore size distribution PSD evolution of specimens exposed to the five conditions. For the cement paste specimens exposed to ESA conditions without DEF (PII-1/2/3), three peaks are present: peak I with a typical diameter of 2-4nm,

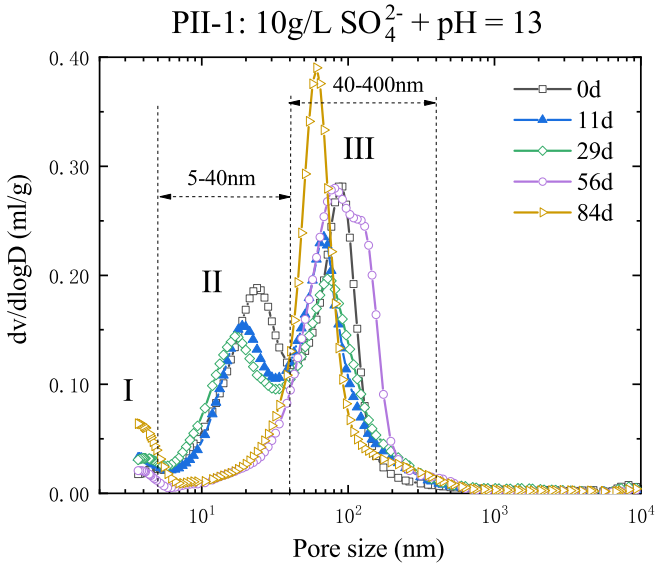

Figure 4.9 Pore size distribution of cement paste specimens exposed to 10g/L SO_4^{2-} + pH = 13 condition (PII-1) at different exposure ages.

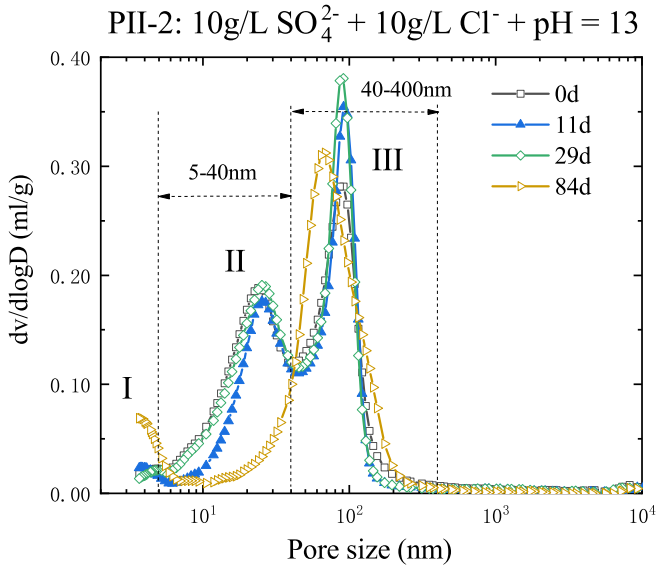

Figure 4.10 Pore size distribution of cement paste specimens exposed to 10g/L SO_4^{2-} + 10g/L Cl^- + pH = 13 condition (PII-2) at different exposure ages.

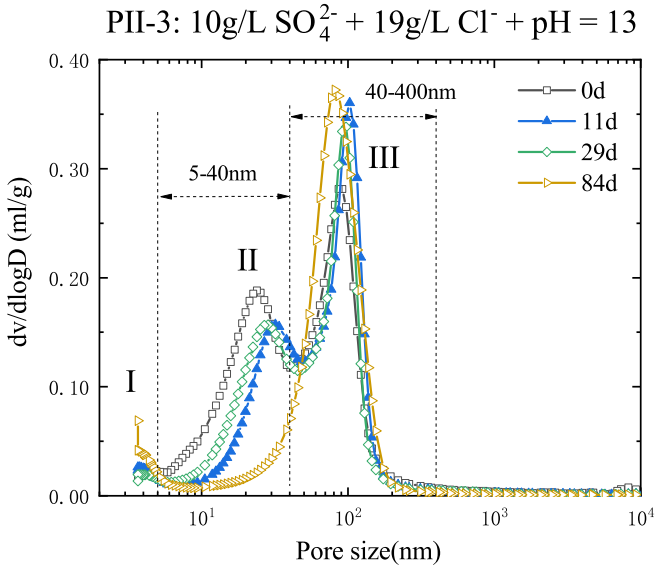

Figure 4.11 Pore size distribution of cement paste specimens exposed to 10g/L SO_4^{2-} + 19g/L Cl^- + pH = 13 condition (PII-3) at different exposure ages.

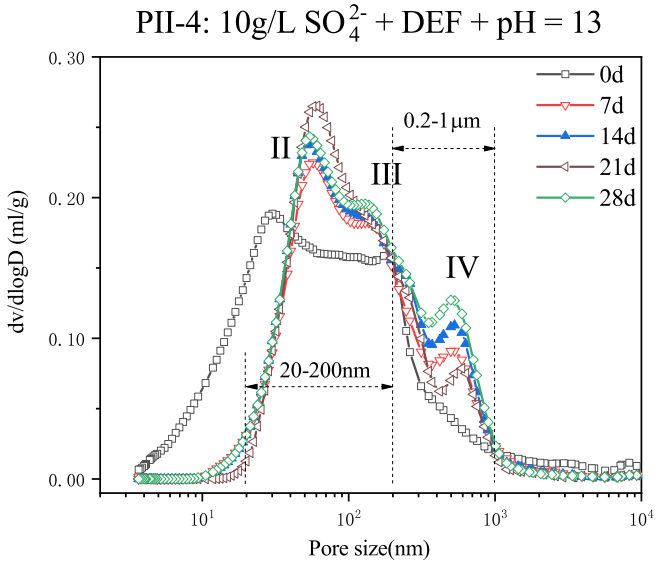

Figure 4.12 Pore size distribution of cement paste specimens exposed to 10g/L SO_4^{2-} + DEF + pH = 13 condition (PII-4) at different exposure ages.

peak II with a typical diameter around 20-30nm and peak III around 80-100nm. For Portland cement (CEM I) pastes, the peak I and the peak II can be interpreted as the pores of inner and outer CSH respectively[196-197], denoted as nanopores and micropores, and the pores around these two peaks constitute pores of CSH hydrates[198]. The peak III, much larger in size, corresponds to the capillary pores, resulting from the initial water-filled space not occupied by hydrates during hardening[16]. Usually, the capillary pore volume

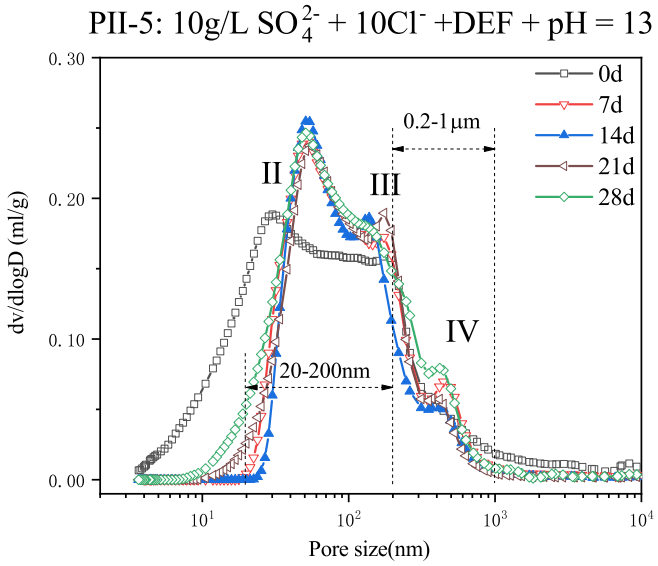

Figure 4.13 Pore size distribution of cement paste specimens exposed to 10g/L SO_4^{2-} + 19g/L Cl^- + DEF + pH = 13 condition (PII-5) at different exposure ages.

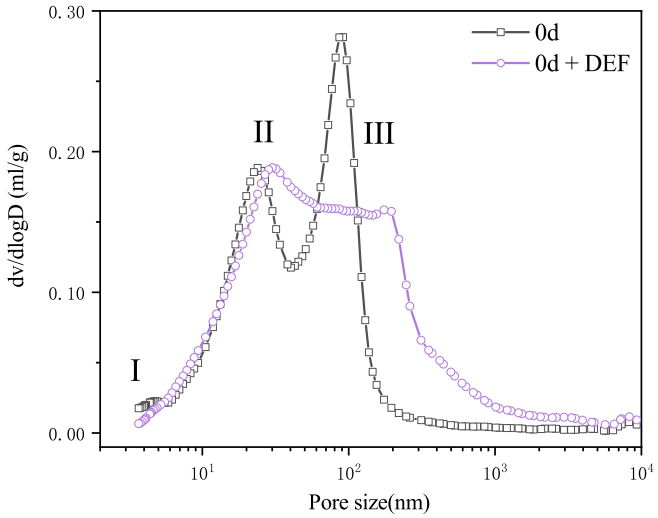

Figure 4.14 Comparison of PSD of cement paste layer specimens with and without heating treatment before immersion (a) and zoom (b).

will decrease with hydration and the peak III will disappear[186,199]. The appearance of peak III in Figure 4.9 is due to the high w/c ratio (0.55) of cement paste, resulting in a large portion of residual space among the hydrated cement grains[199]. The peak II decays with time and even disappears after 84d, indicating an important structural change of micropores. Moreover, the peak III shifts towards smaller sizes with immersion time, revealing that the crystallization of AFt also changes the geometry of pores in this range.

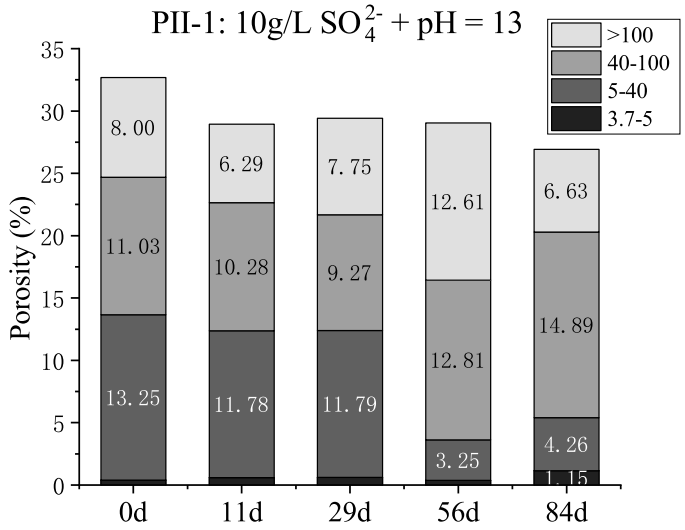

Figure 4.15 Pore volume of cement paste specimens exposed to 10g/L SO_4^{2-} + pH = 13 condition (PII-1) at different exposure ages.

The MIP curves of the cement paste specimens exposed to ESA conditions with DEF (PII-4/5) also present three peaks: peak II, peak II and a new peak IV around 400-500nm, which represents the microcracks. The peak II disappears at the very early stage (7d), and peak IV around 400-500nm appears after exposure and grows with time, confirming the severe damage in combined ESA and DEF condition[12]. Figure 4.14 compares the PSD curves in cement paste specimens with and without heating treatment before immersion (0d). After heating treatment, the peak III shifts toward a larger size, and the pore space about 0.2-10μm increases noticeably, indicating the initiation of microcracks by the heating treatment during curing[200].

Figures 4.15, C.11-C.14 show directly the change of pore volume in four size ranges for five conditions, derived from the PSD results in Figures 4.9-4.13. The pores of four size ranges are illustrated in Figure 4.16: the range 3.75-5nm refers to the pores in compact CSH (inner CSH) situated on the surface of unhydrated cement grains; the range 5-40nm refers to the pores in or enclosed by the less compacted CSH (outer CSH) situated next to inner CSH, connected to larger capillary pores and exposed to pore aqueous solution; the range 40-100nm refers to the capillary pores and probably microcracks; the range above 100nm refers to the large capillary pores, defects and microcacks[159]. Then, let us look into the change of pores in different size ranges with the help of the measured phase contents to shed new light on the pore crystallization of AFt.

For nanopores (3.7-5nm) in ESA conditions without DEF (PII-1/2/3), though small

in quantity, it increases systematically with time. This increase is related to the AFt formation[12] and the relevant change in the microstructure of CSH[25],

$$\mathrm{AFm} + \mathrm{Ca}^{2+} + \mathrm{SO}_4^{2-} \longrightarrow \mathrm{AFt} \tag{4.4}$$

In these nanopores, neither CH or AFt crystals are plausible to exist, and the AFm phases are assumed to grow preferably in outer CSH[16]. Thus, as AFt crystals form near the boundary of inner-outer CSH, cf. Figure 4.16b, the inner CSH can release Ca^{2+} ions to the reaction in Eq.4.4, leading to the decalcification of the inner CSH. According to Chen et al.[201], this decalcification can reduce the Ca/Si ratio of CSH, change the CSH structure, and induce the shrinkage of inner CSH. This mechanism may address the systematic increase of nanopores with sulfate exposure. For the micropores (5-40nm) in PII-1/2/3 conditions, the pore volume is substantially decreased for all cases with exposure ages. The pore space in this range can include both the intrinsic pores of outer CSH (Figure 4.16b) and the space enclosed by outer CSH, forming an "ink-bottle" shape (Figure 4.16a). Since all reactants for AFt formation are present in outer CSH, the AFt crystals most likely form here, resulting in the substantial decrease of pores in this range due to the filling effect of AFt crystallization[22]. However, in coupled ESA and DEF conditions (PII-4/5), the micropre space drops dramatically at 7d and then rises with time. The drop and re-rise of micropores in PII-4/5 conditions seems to be accelerated by the heating treatment compared to PII-1 condition.

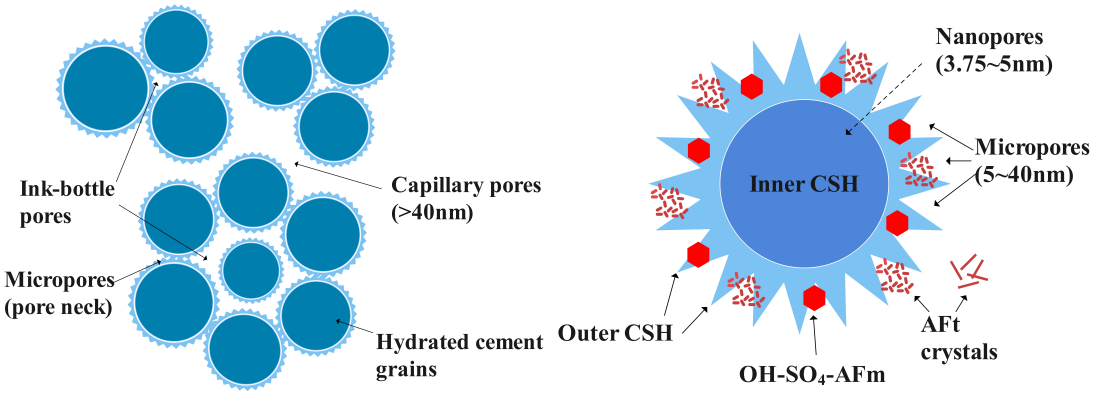

(a) (b)

Figure 4.16 Illustration of pore structure of cement paste with high w/c ratio (0.55) (a) and cement grain after hydration (b). On the left, the capillary pores represent the connected space not occupied by hydrated solid phases, and the "ink-bottle" pores refer to the space enclosed by cement hydrates with the entry size belonging to the micropore range. On the right, the CSH hydrates are divided into inner and outer parts, the AFm phases exist most likely in outer CSH[16], and the AFt crystals precipitate both in micropores in the outer CSH and capillary pores.

For capillary pores (40-100nm) in five conditions, the pore volume is globally increased with exposure age. Several factors can interplay during the AFt formation: the crystals of AFm phases and CH exist extensively[202], the AFt formation in Eq.4.4 consumes these crystals, and a trade-off between the pore filling by AFt crystallization and other crystals consumption accounts for the final pore volume change; moreover, if microcracking occurs during crystallization, e.g. from the crystallization in micropores, the formed microcracks can add to the pore volume in this range if 100nm is taken as the typical size for microcracks[203]. Quantitative analysis will be given in the following to clarify this point. The drastic increase of micropores and decrease of capillary pores in PII-4/5 conditions at 7d indicate a more rapid precipitation of AFt and dissolution of AFm/CH compared to ESA conditions without DEF. For large capillary pores (>100nm), the pore volume is relatively stable in PII-1/2/3, involving also the consumption of CH/AFm crystals, the AFt formation, the formation of microcracks, and the formation of gypsum in newly formed cracks as well[50]. Compared to PII-1 condition, the specimens in PII-2/3 conditions present smaller volume for nanopores (3.75-5nm) and micropores (5-40nm), but comparable capillary pores and possibly microcracks (40-100nm, and >100nm) at 84d of exposure. While in PII-4/5 conditions, large capillary pores show a continuous increase with time, demonstrating the rapid development of microcracks in the presence of DEF.

4.2.2 Crystallization process in pores

To investigate further the AFt crystallization in pores, a quantitative analysis is attempted for PII-1 solution using the phase content data in Figure C.1 and pore volume data in Figure 4.15. Since leaching and carbonation (the calcite detected in XRD results was formed during the storage of specimens) were screened out during immersion, and no gypsum is found in XRD results, the pore volume change is only related to the AFt crystallization and the dissolution of AFm phases and CH. As aforementioned, the AFm phases in PII-1 solution can be taken as OH-SO_4-AFm, a mixture of $C_4AH_{(7+x)}$ and Ms(6+x). To simplify the calculation, we assume the interlayer water content x to be 6[16] and the minerals in cement to be completely hydrated. The relative ratio of C_4AH_{13} and Ms12 in

OH-SO_4-AFm can be evaluated from the mole balance of Al and S elements,

$$\begin{cases} n_{SO_3} = 3n_{AFt} + n_{Ms12} \\ n_{Al_2O_3} = n_{AFt} + n_{Ms12} + n_{C_4AH_{13}} \\ n_{AFm} = n_{Ms12} + n_{C_4AH_{13}} \end{cases} \tag{4.5}$$

with n_i standing for the mole content i per unit volume of hardened cement paste. The values of n_{SO_3} and $n_{Al_2O_3}$ are determined from the chemical composition of cement in Table 2.1, and n_{AFt} and n_{AFm} can be read from Figure C.1a. The ratio of n_{Ms12} to $n_{C_4AH_{13}}$ is thus determined as 7:3. This ratio gives the equivalent molar volume of OH-SO_4-AFm as 0.30 L/mol by taking the literature values for the molar volumes of C_4AH_{13} (0.27 L/mol) and Ms12 ((0.31 L/mol))[195], and a consumption of 2.3 moles of CH per mole of OH-SO_4-AFm in AFt formation.

From PII-1 immersion at 29d in Figure C.1a, the newly formed AFt crystals amount to 0.057 mol/L, consuming 0.131 mol/L CH and dissolving 0.042 mol/L OH-SO_4-AFm. Thus, the AFt crystals fill out 4.05%, the dissolution of OH-SO_4-AFm and CH releases 1.69% and total pore volume change is -2.36% (decrease). The volume change of micropores (5-40nm), -1.46% in Figure 4.15a at 29d, indicates that AFt crystals do not precipitate only in micropores. The volume change of capillary pores (40-100nm), -1.76% in Figure 4.15a at 29d, confirms the AFt formation in these pores with dissolution of AFm/CH. Following the same line, the increase of 40-100nm volumes in PII-2/3 solutions before 29d is due to fewer AFt formation and more AFm consumption in Figure 4.2a and b. From Figure C.1a for 29d to 56d, the AFt formation leads to -4.68% volume change, and the dissolution of OH-SO_4-AFm/CH induces a change of 3.32%. The volume of micropores (5-40nm) drops as much as -8.54% in Figure 4.15a from 29d to 56d, indicating that at least 3.86% micropore volume is not induced by AFt formation. The possible cause can be attributed to the pores of ”ink-bottle” shapes in Figure 4.16a: the ”ink-bottle” structure is enclosed by hydrated solids with the pore neck size entering the range of micropores. If the AFt formation, together with AFm/CH consumption, blocks this pore neck, no mercury can be intruded into the enclosed space and this pore volume may account for the large reduction of micropores. Such an explanation can also support the significant decrease of micropore (5-40nm) volume 84d when immersed in PII-2/3 solutions.

After the above analysis, the crystallization of AFt in pores can be summarized as follows: **AFt crystals precipitate in both micropores and capillary pores, while AFm**

phases and CH dissolve more in capillary pores. With exposure age, the AFt crystals block the pore necks of ”ink-bottle” pores, resulting in a significant reduction in pore volume in micropore (5-40nm) range. **The accumulation of AFt crystals in pores, especially in the micropore range, fractures the solid matrix of hardened cement paste and reopens the ”ink-bottle” pores** in Figure 4.16a, and these microcracks and the reopened ”ink-bottle” pores most likely join the pore ranges of 40-100nm or >100nm. **The presence of chlorides delays this process by reducing both the rate and the quantity of AFt formation.** Thus, the dissolution of AFm phases and CH in PII-2/3 solutions contributes more to the pore space release in the range of 40-100nm compared to PII-1 solution.

In combined ESA and DEF conditions (PII-4/5), the faster AFt formation in Figures 4.4 and 4.5 compared to ESA conditions (PII1/3) leads to an earlier enclose of ”ink-bottle” pores at 7d compared to PII-1/2/3 conditions, which corresponds to the significant decrease of micropores at 7d in Figures C.13 and C.14. Then the re-open of ”ink-bottle” pores corresponds to the increasing micropores and large capillary pores (>100nm) volume after 7d in Figures C.13 and C.14.

4.3 Impact on transport property and expansion

4.3.1 Vapour diffusivity

The vapour diffusivity was measured through DVS with a Payne cell on slice specimens. The DVS device and Payne cell are shown in Figure 2.10 and Figure 2.11, and the slice specimens as shown in Figure 2.11b were drilled out from the square slice specimens after freeze-drying. Note that the vapour diffusivity measured through the Payne cell and evaluated from Eq.(2.5) deviates from the pure vapor diffusivity, which requires steady water flow in specimens without the interaction between the vapor and the solid matrix,

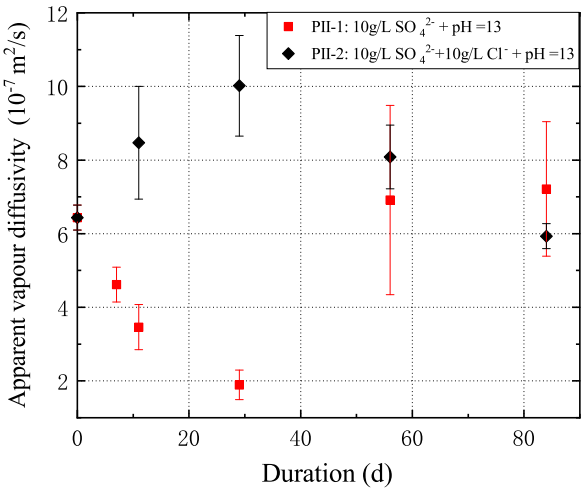

(a)

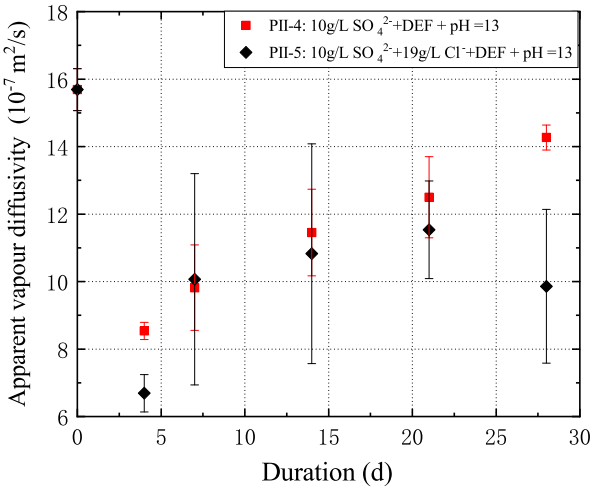

(b)

Figure 4.17 Apparent vapour diffusivity of cement paste layer specimens exposed to PII-1 and PII-2 conditions (a), and PII-4 and PII-5 conditions (b) at different ages.

and corresponds to one given value of relative humidity. If the former can be assumed to be satisfied in the steady regime in Figure 2.12, the latter cannot be met under a RH difference of 50% across the specimen thickness. The vapor diffusivity thus measured and evaluated refers to an apparent value for vapor diffusivity, depicting the resistance of the specimens to water vapor transport under a specific treatment and RH arrangement. Since all the specimens were subject to the same pre-treatment by freeze-drying and to the same RH difference of 50%, the apparent values of vapor diffusivity are comparable among these specimens and can be used to characterize their resistance to water vapor diffusion. It is from this aspect that the value of apparent diffusivity is interpreted. The apparent vapour diffusivity D_v^a is presented in Figure 4.17 for pellet cement paste specimens immersed in PII-1 and PII-2 solutions at different exposure ages. The apparent vapour diffusivity was reported as being in the range of 0.1-1$\times10^{-7}$ m^2/s under a RH gradient of 0-50% over a thickness of 30mm for concrete specimens[204]. Baroghel-Bouny[205] measured the apparent vapour diffusivity in the range of 1-10$\times10^{-7}$ m^2/s for the pore saturation range of 0.1-0.5, the same order of magnitude as D_v^a in Figure 4.17.

In PII-1 condition, the D_v^a values decrease until 28d and then rise up to 84d, corresponding to the reduction of pores in the ranges of 5-100nm before 28d and the increase of pores larger than 100nm after 56d in Figure 4.15a, respectively. The reduction of D_v^a in the early phase of ESA is caused by the refinement of pore structure, due to the synergic effect of AFt formation and AFm/CH dissolution, in pores of 5-100nm. The subsequent rise of D_v^a after 28d, along with more AFt formation, indicates the appearance of microcracks in solid matrix of cement paste, which provides a more direct and quick diffusion path for vapor transport. In PII-2 condition from 0d to 29d, the pore volume of 5-100nm in Figure 4.15b underwent a more complex change: a slight volume decrease (-0.14%) in 5-40nm pores and a relatively large volume increase (1.48%) in 40-100nm pores with important dissolution of AFm phases and CH. The larger diffusivity at 29d compared to 0d is due to this pore space release. The subsequent decrease of vapor diffusivity, from 29d to 84d exposure, is closely related to the important pore volume change in the 5-40nm range, -9.57% from Figure 4.15b. As aforementioned, this pore volume reduction reflects the blockage of pore necks for “ink-bottle” pores, cf. Figure 4.16a. Afterwards, the enclosed ”ink-bottle” pores are inaccessible either to MIP or to vapour transport. In summary, the AFt formation and the related AFm/CH consumption in pores are to reduce the transport rate of pore matter before the appearance of microcracks. Actually, this reduction has

been observed in the literature for other transport properties[35]. Once the microcracking occurs, this reduction can be totally cancelled out by the new transport channels for pore matter. Comparing PII-1 and PII-2 immersion cases, one can see that the presence of chlorides offsets this reduction effect, before microcracking, even increases the vapor diffusivity by dominating AFm/CH consumption.

The specimens with heating treatment have a higher initial apparent diffusivity compared to specimens without heating treatment, which corresponds to a higher pore volume in the microcrack range (0.2-10μm) as in Figure 4.14. In combined ESA and DEF conditions (PII-4/5), the $D_{\mathrm{v}}^{\mathrm{a}}$ values drop at 7d and rise until 28d, corresponding to the decrease of 5-40nm pores at 7d and the increase of pores larger than 5nm after 7d in Figures 4.15d and e, respectively. Besides, the presence of chlorides reduces the rise of vapour diffusivity in combined ESA and DEF conditions, which is due to a slower formation rate of AFt as in Figure 4.7a.

4.3.2 Expansion

Figure 4.18 shows the expansion behaviour of slice specimens of cement paste exposed to the five conditions PII-1/2/3/4/5. Under ESA conditions, the specimens all show progressive expansion but with different patterns for PII-1 and P2/P3 solutions. The expansion in PII-1 solution occurs in two stages: a first expansion growth stage with a moderate and linear expansion rate till 56d, named also as "induction phase"[206], and second stage with a much faster expansion rate. By contrast, the expansion of PII-2/3 specimens undergoes only the linear growth phase of expansion. During the expansion measurement, the PII-1 specimens fractured after the second stage until a rather large strain for expansion $\sim$1.1% was reached, while the specimens in PII-2/3 were broken right after the linear stage at much smaller strain $\sim$0.15%, indicating that the microcracks are far more developed in PII-1 specimens than in PII-2/3 specimens. Note that the tensile strain at the end of the first stage for all specimens, in the order of 0.15%, is one order of magnitude larger than the maximum tensile strain that the hardened cement pastes can sustain during a uniaxial tensile test[207]. This means, through the first stage of expansion scales linearly with exposure time, the specimens have largely passed the pure elastic region of stress-strain relationship of the solid matrix and contain microcracks from AFt formation. The relevance of the AFt quantity to the expansion magnitude is to be discussed later. As we compare the expansions of PII-1 specimens with PII-2/3 specimens, the inhibiting effect of chlorides on ESA expansion is obvious, which is in line with the available literature

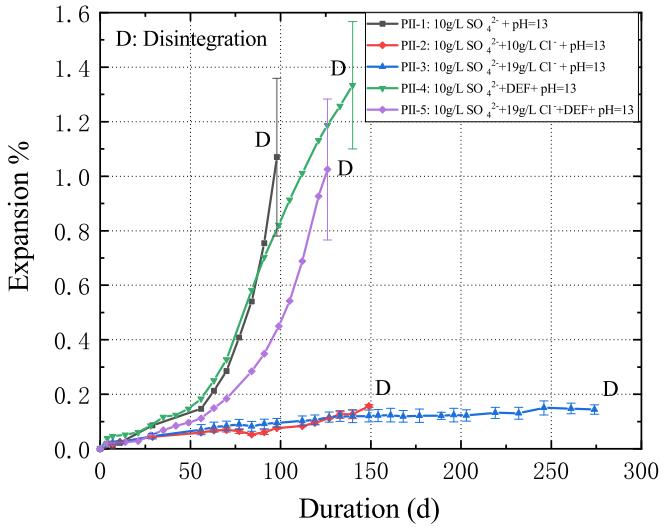

Figure 4.18 Expansion of cement paste layer specimens exposed to PII-1, PII-2, PII-3, PII-4 and PII-5 conditions at different ages.

results[49,99,142]. Moreover, this inhibiting effect becomes more important with the chloride concentration. The influence of chlorides on expansion coincides with the effect of chlorides on AFt formation rate in Figure 4.2, indicating that the crystallization of AFt is the mechanical reason for expansion.

The expansion in combined ESA and DEF conditions (PII-4/5) shows a faster growth rate in comparison to ESA conditions without DEF (PII-1/2/3). Interestingly, the aggravating impact of DEF seems to surpass the mitigating effect of chlorides in PII-5 condition, leading to a much rapider expansion rate in the combined sulfate and chloride solution in the presence of DEF.

4.4 Further discussion

4.4.1 Sulfate attack process and crystal pressure

Figure 4.19 synthesizes the evolution of AFt content, apparent vapour diffusivity and expansion of cement paste specimens exposed in PII-1 solution. One issue should be clarified before further interpretation: the thickness of specimens was set as 2mm after a careful cutting procedure in order to achieve homogeneous sulfate reactions and AFt formation throughout the specimen thickness. In this study, no systematic measurements were performed to verify the homogeneity of the AFt formation in the specimen thickness. However, a preliminary analysis of the characteristic diffusion time for sulfates to penetrate the half thickness of a specimen (1mm) is estimated as within 10h using $10^{-12}m^2/s$ as the order of magnitude of sulfate diffusivity. This diffusion time is relatively short compared to the exposure ages of specimens, and thus the homogeneous AFt formation in thickness can be taken as a reasonable assumption. From Figure 4.19, the exposure age of 56d constitutes a critical point for all results: before this age, the AFt has a clear filling effect in porosity, decreasing substantially the vapor diffusivity, and afterwards, the rate of AFt formation increase leads to much faster expansion and a jumping change of order of magnitude for vapour diffusivity, accompanied by a notable increase of pores in the range >100 nm in Figure 4.15a. On this basis, a two-stage chemo-mechanical mechanism for sulfate attack can be formulated for the specimens as follows.

In the first stage within 56d exposure, the external sulfates react with aluminum phases in cement pastes to produce expansive products (AFt crystals) in pores in the range of 5-100 nm. These crystals fill the pore volume and thus reduce the vapor transport property on the one hand and generate internal pore pressure, leading to a slow expansion rate on the other hand. With the formation of AFt crystals going on, the internal pore pressure builds up high enough, more likely in the pore necks within the micropore range (5-40nm), to fracture the solid matrix of cement paste inducing microcracks and reopen the enclosed “ink-bottle” pores. The appearance of microcracks changes cement paste from a porous continuum to a discrete one. These microcracks and the reopened “ink-bottle” pores add to the pore volume increase around sizes of 100nm and also soften the solid matrix, providing an elastic modulus lower and lower. The former results in a large vapour diffusivity and the latter corresponds to a faster expansion.

The mechanical reason for expansion is the pressure arising from the AFt crystallization in pores (confined space). A first estimate is made here for the pressure on pore wall

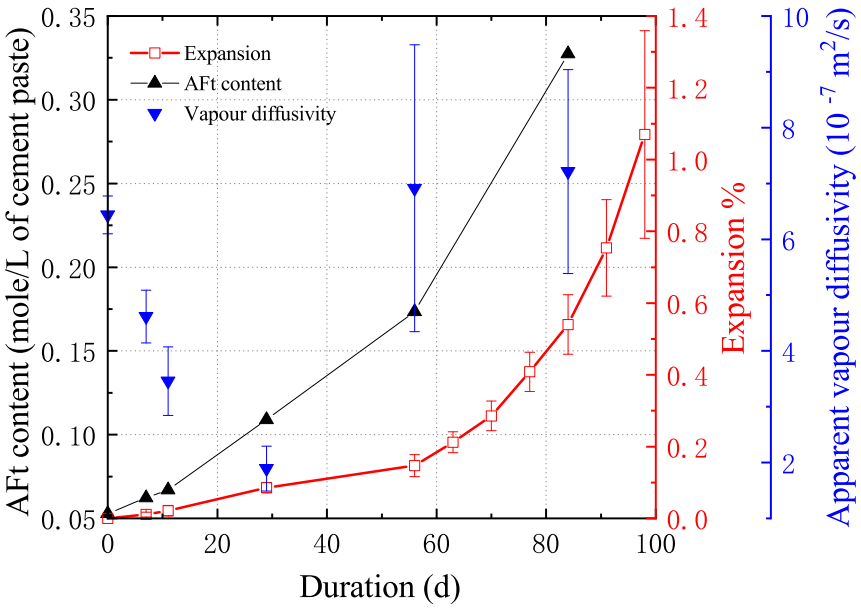

Figure 4.19 AFt content (black), expansion (red), and apparent vapour diffusivity of cement paste layer specimens exposed to PII-1 condition.

from AFt crystallization for the most ideal case: the pore geometry is cylindrical with r as radius, and the crystal is both in mechanical and thermodynamic equilibria with the pore solution. The mechanical equilibrium between the crystal tip, assumed in semi-sphere with radius r, and the liquid solution writes through the Laplace equation

$$P_C - P_L = \frac{2\gamma_{CL}}{r} \tag{4.6}$$

where $P_{C,L}$ stand for the pressures of crystals and liquid phase, and γ_{CL} for the surface energy of crystal-liquid interface, taking 0.1 J/m^2 [64]. Using the above assumptions, the pressure exerted on the cylindrical pore wall P_w is half of the capillary pressure in Eq.(4.6), γ_{CL}/r, due to surface curvature of lateral surface of crystals[64]. Using this result and releasing the liquid pressure P_L(=0), one needs to load with a pressure of P_w=6.7-10.0 MPa to grow AFt crystals in pores of 20-30nm. This pressure P_w constitutes the mechanical origin for material expansion. Considering the magnitude of this pressure and the pore geometry for crystal growth in Figure 4.16, the AFt crystallization in micropores can be assumed to be the major source of expansion. In this estimation, the thermodynamic equilibrium is imposed between the supersaturation of pore solution and the crystal pressure, expressed through Correns' equation[66]. In realistic situation, cf. micropores in Figure 4.16, the supersaturation of pore solution allowing the crystal formation in these pores

should not be lower than the corresponding pressure P_C in Eq.(4.6). Accordingly, the P_w pressure provides actually a lower limit for the possible pressure exerted on the pore wall. More realistic estimation of crystallization pressure will be performed later.

4.4.2 AFt amount and expansion during linear stage

Both the crystallization pressure theory[30-31] and the volume increase theory[17,208] relate the expansion stress to the content of newly formed AFt crystals. In the present study, if the newly formed TAH in PII-2/3 conditions in Figure 4.2c is assumed to be an amorphous phase[24], the AFt formation will be the only source to generate pore pressure. Figure 4.20 illustrates the specimen expansion strain in terms of the measured AFt content in three ESA conditions during the linear expansion stage. As aforementioned, the AFt formation is assumed to be homogeneous across the thickness of specimens. In this stage, the expansion scales almost linearly with the AFt content, but different slopes are observed for PII-1 solution and PII-2/3 conditions. This difference in slopes, i.e., the same quantity of AFt formation giving different expansion values, can be better interpreted through pore crystallization concepts. Actually, the crystallization pressure can be incorporated into the classical poromechanics[33], and the stress-free expansion by internal pore pressure

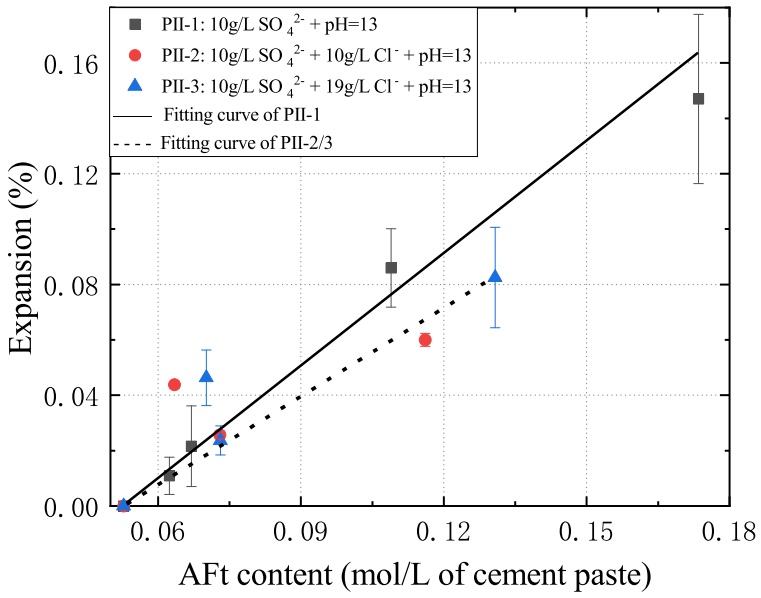

Figure 4.20 Expansion of cement paste layer specimens, exposed to PII-1, PII-2 and PII-3 conditions, in terms of AFt content.

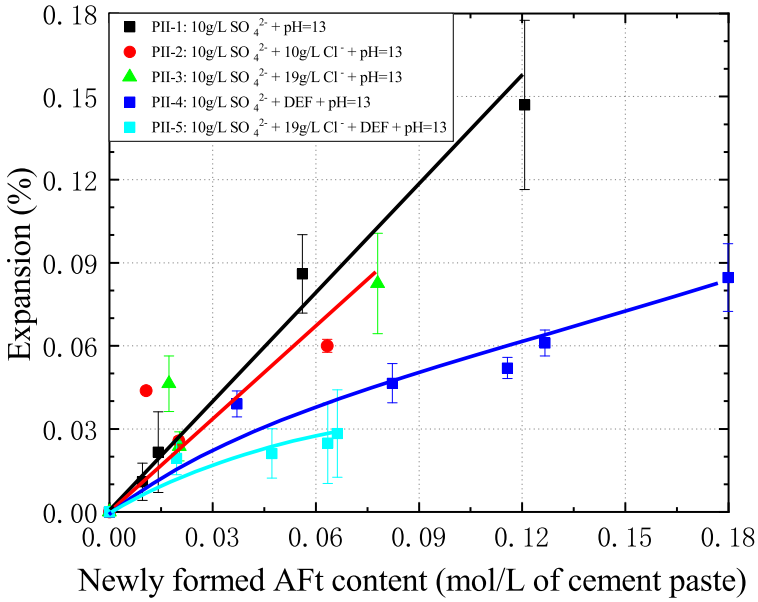

Figure 4.21 Expansion of cement paste layer specimens in terms of AFt content.

accumulation can be expressed as,

$$\sigma = 0 : 3K\epsilon_{\mathrm{ESA}} = bS_{\mathrm{C}}P_{\mathrm{C}} \quad \text{with} \quad S_{\mathrm{C}} = \frac{V_{\mathrm{C}}}{\phi_0} n_{\mathrm{AFt}} \tag{4.7}$$

with b standing for the Biot's coefficient, V_{C} for the molar volume of AFt crystals, S_{C} for the volume fraction of pore space occupied by AFt crystals, P_{C} for crystallization pressure, ϕ_0 for initial porosity of material, n_{AFt} for AFt content, K for bulk modulus and ϵ_{ESA} for free linear expansion strain under ESA. In this expression, we assume implicitly that the liquid phase pressure $P_{\mathrm{L}} = 0$, i.e. the liquid pressure serves as the reference for the solid phase. Therefore, the slopes in Figure 4.20 represent the ratio of ϵ_{ESA} to n_{AFt} and can be expressed as $[bV_{\mathrm{C}}/(3\phi_0 K)]P_{\mathrm{C}}$. The crystallization P_{C} can be evaluated following Correns' equation[66],

$$P_{\mathrm{C}} = \frac{RT}{V_{\mathrm{C}}} \ln\left(\beta_{\mathrm{AFt}}\right) \tag{4.8}$$

Substituting the estimated β_{AFt} in Section 3.2.3 into Eq. (4.8) gives P_{C} in PII-1, 2, 3 conditions as 95.83, 74.92, 70.44 MPa. By taking the typical values of mechanical properties (b, K) for hardened cement pastes in[209], the slops are determined as 9.93×10^{-6} (PII-1), 7.76×10^{-6} (PII-2) and 7.30×10^{-6} (PII-3). Compared to the measured slopes, 13.54×10^{-6} (PII-1), 10.90×10^{-6} (PII-2/3), these estimates are very close and observe the same order of magnitude, which attributes the different slopes to the different crystallization pressures.

The above analysis can help to deepen the mechanism of mitigating effect of chlorides on ESA as such: adding chlorides in pore solution alters the dissolution equilibria in the multi-species aqueous environment[210], reducing the aluminate concentration $c_{Al(OH)_4^-}$ and the supersaturation of AFt crystals β_{AFt}; these changes lead to the reduction both in AFt formation rate in Figure C.1a and in the crystallization pressure P_C; the synthetic effect of AFt amount n_{AFt} decrease and P_C decrease results in a drop in expansion according to Eq.(4.7).

Figure 4.21 presents all the specimen expansion strain in terms of the measured AFt content in five conditions. The physical significance of the slopes in Figure 4.21 is the ratio of the crystallization pressure of AFt crystals to the material's resistance against deformation. According to Eq. (4.8), the crystallisation pressure in combined ESA and DEF conditions (PII-3/4/5) should be larger than in ESA conditions (PII-1/2/3) due to an additional source of sulfates. Thus, the slopes should in PII-4/5 conditions should be larger. In Figure 4.21, however, the slope values in PII-4/5 conditions are smaller than in PII-1/2/3 and decline with time. This is because the specimens with the heating treatment (PII-4/5) undergo an initial cracking during the curing period in Figure 4.14 and these cracks continue to grow as ettringite formation as in Figures 4.12 and 4.13. Owing to the existence of cracks, the solid matrix cannot supply sufficient crystallization pressure to restrict crystallization growth, thus the real crystallization pressure is significantly lower than the value estimated by Correns' equation, i.e. the Correns' equation in Eq. (4.8) is not valid. With the ongoing production of ettringite, cracks continue to develop and the crystallisation pressure continues to diminish, so the slopes continue to decline.

4.5 Conclusions

1. Quantitative ^{27}Al NMR examination confirms the mitigating effect of chlorides on AFt formation: the presence of chlorides converts part of the AFm phases into TAH phase, reducing AFt formation, and a higher concentration of chlorides results in a slower AFt generation rate. The analysis on multi-phase dissolution equilibria in pore solution shows the reducing effect of chlorides on the supersaturation of AFt crystals, providing a possible explanation of the mitigating effect. Also, through this depressing effect on the AFt supersaturation, the same quantity of AFt crystal formation does not generate the same level of crystallization pressure, giving a lower expansion capacity of AFt crystals in mixed (PII-2/3) solutions than in pure sulfate (PII-1) solution.

2. A synthetic analysis of phase content and pore structure confirms that AFt crystallization occurs in the whole range of pore space of hardened cement paste. The comparison of pore volume filling by AFt formation, from ^{27}Al NMR data, and pore space reduction, detected by MIP in the 5–40 nm size range, reveals the role of ”ink-bottle” pores in the pore volume change. The AFt crystals, formed in the micropores of interposed outer CSH from different cement grains, fill up the neck pores and block the enclosed pore space, resulting in a substantial decrease in 5–40 nm pores. In the range of 40–100 nm, the AFt precipitation and AFm/CH dissolution interplay together to influence the pore volume. The microcracks created by AFt formation and the reopened “ink-bottle” pores eventually join the measured pore volume around the size of 100 nm.

3. The pore crystallization of AFt leads to the corresponding change in transport property and mechanical behavior. In the pure sulfate (PII-1) solution, the pore-filling by AFt crystals causes a decrease in apparent vapour diffusivity, and the subsequent AFt formation induces microcracks and augments the vapour diffusivity. The presence of chlorides offsets the pore-filling of AFt formation in early exposure and even increases the vapour diffusivity due to the synthetic effect from AFm/CH dissolution. The AFt crystallization in the pore-neck part of micropores would be the direct source for pore pressure generation and material expansion. The specimen expansion is closely related to the evolution of the measured AFt content. The linear expansion stage is well captured by the classical poromechanics and the lower expansion with chlorides is addressed by the depressed AFt supersaturation.

4. The heating treatment dissolves the formed AFt in the early curing period into the TAH phase and initiates the microcracks during the later cooling storage. Under the

combined ESA and DEF condition (PII-4/5), the sulfates come from both the external environment and the material itself, leading to a higher formation rate of ettringite. The rapid formation of ettringite accelerates the change of micropores volume in MIP curves. In addition, the microcracks formed inside the materials in DEF conditions reduce the materials' resistance to deformation. Both the faster generation rate of ettringite and the less resistance in combined ESA and DEF conditions lead to a faster expansion rate compared to ESA condition (PII-1). In combined DEF, ESA and chlorides condition (PII-5), the formation rate and expansion rate of ettringite are both high, indicating that the aggravating effect of DEF overweighs the retarding effect of chlorides.

CHAPTER 5 SULFATE TRANSPORT AND CRACKING OBSERVATION

The sulfate transport and cracking observation were investigated for cement paste disks subjected to ESA with and without the combined actions through the experimental Part III. Disk specimens (see in Figure 2.5c) were sawed from cylindrical cement paste, as shown in Figure 2.6, and exposed to six sulfate-bearing conditions given in Table 5.1. The sulfate and chloride profiles, surface cracks, and mineral phase distribution were characterized through ICP, potentiometric titrator, optical microscope, BSE-EDS, and XRD, cf. Section 2.2, respectively. The flowing chart of the test program in Part III is shown in Figure 5.1.

Table 5.1 Composition of the test solutions in Part III.

Condition	SO_4^{2-} content	Cl^- content	pH value (-)	Heating treatment
PIII-1	10 g/L	0	13	-
PIII-2	10 g/L	0	7	-
PIII-3	10 g/L	19 g/L	7	-
PIII-4	10 g/L	0	13	+
PIII-5	10 g/L	0	7	+
PIII-6	10 g/L	19 g/L	7	+

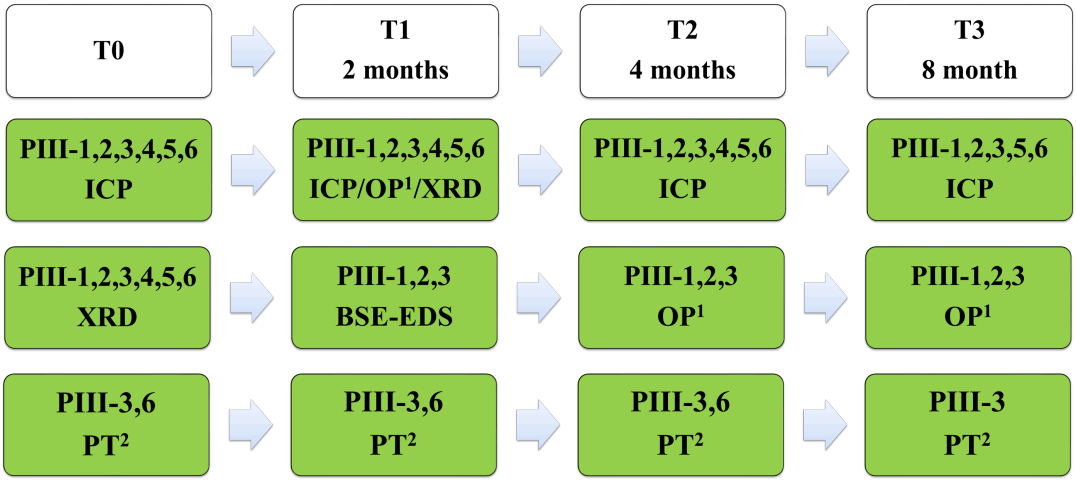

1, ''OP'' stands for optical microscopic.
1, "PT" stands for potentiometric titrator.

Figure 5.1 Flowing chart in Part III.

5.1 Mass transfer

5.1.1 Sulfate profiles

The sulfate profiles in disk specimens exposed to six conditions are presented in Figure 5.2 for ESA conditions without DEF and in Figure 5.3 for ESA conditions with DEF. For the cement paste specimens before immersion (0m), the measured sulfate content,

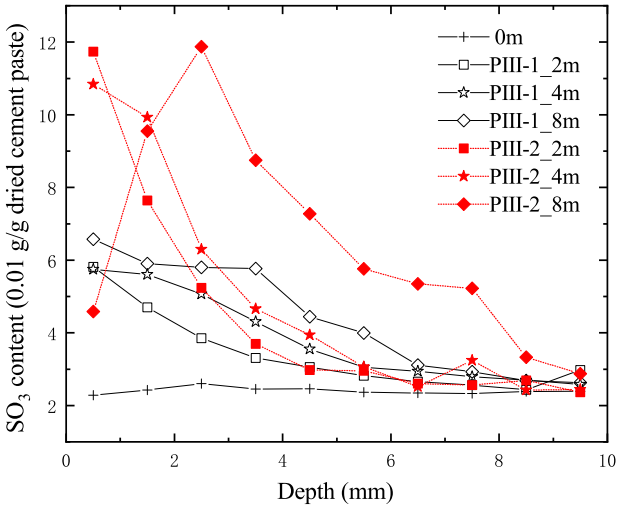

(a)

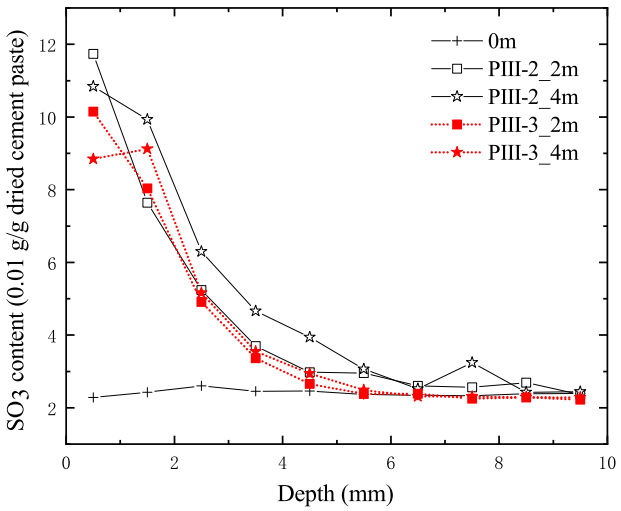

(b)

Figure 5.2 Comparisons of sulfate profiles measured by ICP-AES for cement paste disks immersed into (a) PIII-1 and PIII-2 conditions, (b) PIII-2 and PIII-3 conditions for different exposure ages. PIII-1 stands for 10g/L SO_4^{2-} + pH = 13, PIII-2 for 10g/L SO_4^{2-} + pH = 7, and PII-3 for 10g/L SO_4^{2-} + 19g/L Cl^- + + pH = 7.

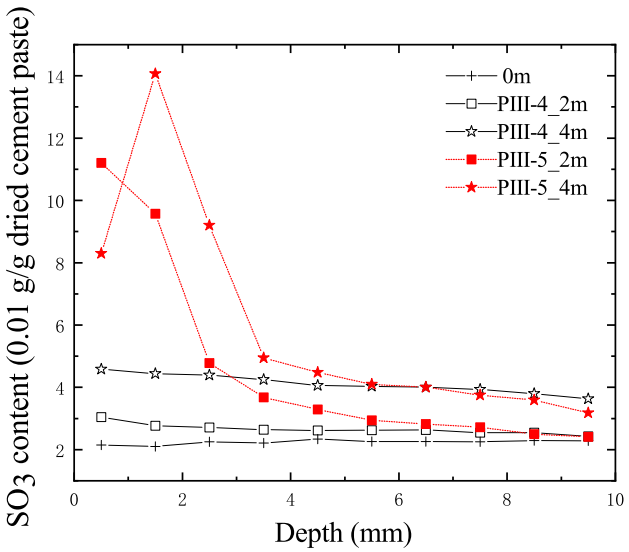

(a)

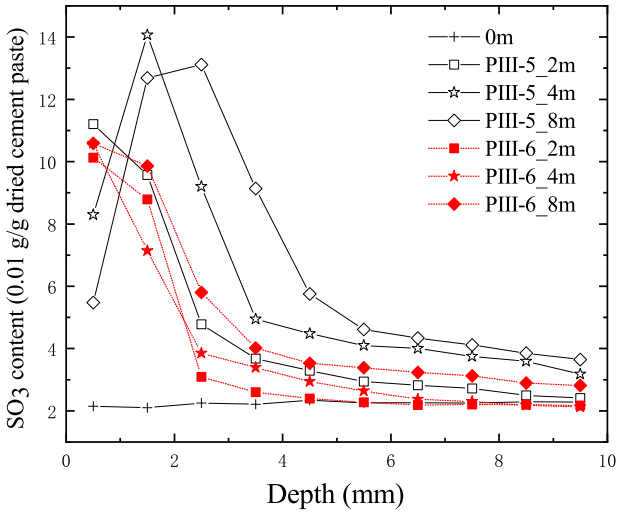

(b)

Figure 5.3 Comparisons of sulfate profiles measured by ICP-AES for cement paste disks immersed into (a) PIII-4 and PIII-5 conditions, (b) PIII-5 and PIII-6 conditions for different exposure ages. PIII-4 stands for 10g/L SO_4^{2-} + pH = 13 + DEF, PIII-5 for 10g/L SO_4^{2-} + pH = 7 + DEF, and PII-6 for 10g/L SO_4^{2-} + 19g/L Cl^- + + pH = 7 + DEF.

around 2.40% g/g dried cement paste, is comparable to the SO_3 content, 2.88% g/g cement in Table 2.1 equivalent to 2.23% g/g dried cement paste. The higher sulfate content and deeper sulfate penetration depth in specimens in ESA with leaching conditions (PIII-2 and PIII-5) than in ESA without leaching conditions (PIII-1 and PIII-4) in Figures 5.2a and 5.3, confirm the accelerating effect of leaching on sulfate ingress. Especially, the

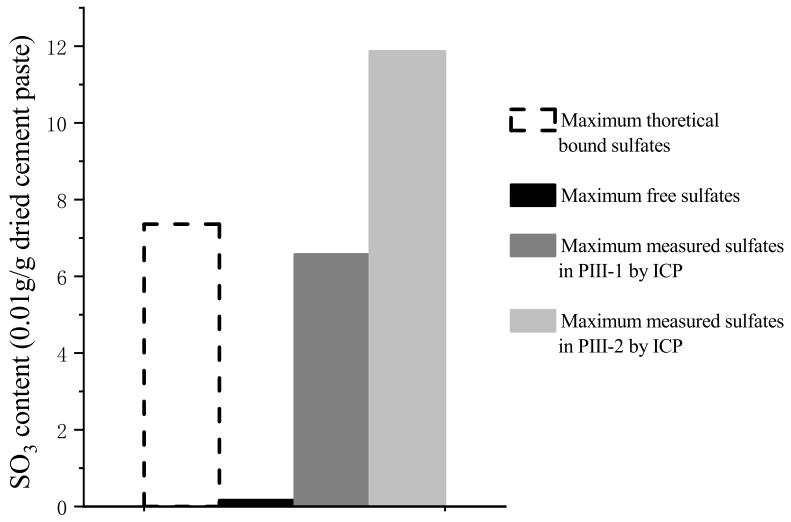

Figure 5.4 Theoretical and measured values for sulfate contents.

significant difference in the peak values of sulfate contents in specimens in PIII-1 (about 7%) and PIII-2 (about 12%) conditions, PIII-4 (about 5%) and PIII-5 (about 14%) conditions, indicates two different mechanisms for sulfate binding in leaching (PIII-2 and PIII-5) and no-leaching (PIII-1 and PIII-4) conditions. Besides, the decrease of sulfate content in 0-1mm with time in PIII-2 and PIII-5 specimens and the increase stage of sulfate contents in 0-3mm of the PIII-2-8m and PIII-5-8m specimens, suggest the dissolution of solid sulfates in the surface zone of specimens, which is caused by the low pH condition of pore solution near the surface[36]. This dissolution could promote the sulfate ingress through two mechanisms: first, the released sulfates from solid sulfates penetrate more deeply into the material interior; second, the dissolution of solid sulfates increases the porosity and thus the ionic diffusivity, facilitating the subsequent sulfate diffusion from the material surface. Figures 5.2b and 5.3b compare the sulfate profiles in specimens exposed to PIII-2 and PII-3 conditions, PIII-5 and PIII-6 conditions. The sulfate content in 0-1mm decreases with time in PIII-3-4m specimen, and confirms the dissolution of solid sulfates by leaching process in the presence of chlorides. The systematically lower sulfate contents and smaller sulfate penetration depths in ESA with chlorides conditions (PIII-3 and PIII-6) than in ESA without chlorides conditions (PIII-2 and PIII-5) confirm the mitigating effect of chlorides on sulfate ingress. Besides, the smaller difference between 2m-specimen and 4m-specimen profiles in PIII-3 and PIII-6 conditions than in PIII-2 and

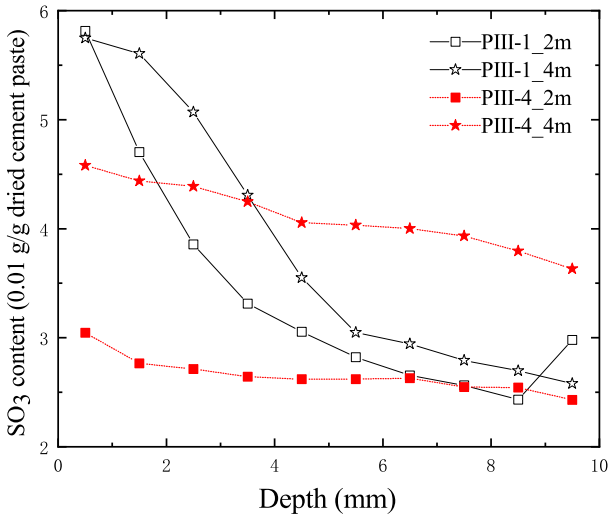

Figure 5.5 Comparisons of sulfate profiles measured by ICP-AES for cement paste disks immersed into ESA with and without DEF conditions in the absence of leaching (PIII-1 and PIII-4) for different exposure ages. PIII-1 stands for 10g/L SO_4^{2-} + pH = 13, and PIII-4 for 10g/L SO_4^{2-} + pH = 13 + DEF.

PIII-5 conditions suggests a slower binding rate of sulfates in the presence of chlorides.

Figure 5.4 compares the maximum measured sulfate contents in the PIII-1 and PIII-2 conditions: the theoretical content of free sulfates is deduced from the assumption that the pore solution is saturated by the external solution, and the theoretical content of bound sulfates is deduced from the assumption that all Al_2O_3 in Table 2.1 reacts with sulfates and forms ettringite. Note that the free sulfate content is so small in comparison to the bound sulfate content that it can be neglected when analyzing the measured sulfate contents. The maximum measured value in PIII-1 condition, being rather close to the theoretical content of bound sulfates, suggests that almost all the aluminum phases were converted into ettringite and the difference may be due to the incomplete hydration of cement grains or the existence of additional sulfate-free aluminum phases, such as the third aluminum phase (TAH), Al(VI) and Al(V) phases[24]. However in PIII-2 condition, the maximum measured sulfate content exceeds the theoretical one, and the difference between them indicates that more than 4.5% SO_3 is present in another form besides ettringite in the solid phases. The most likely product is gypsum, which has been detected in other ESA studies[10,211].

Figures 5.5, 5.6, and D.1, illustrate the effect of DEF on sulfate ingress. For ESA conditions without leaching (PIII-1 for no DEF and PIII-4 for DEF) in Figure 5.5, the sulfate ingress seems to be delayed by heating treatment at 2-month exposure, while in 4-

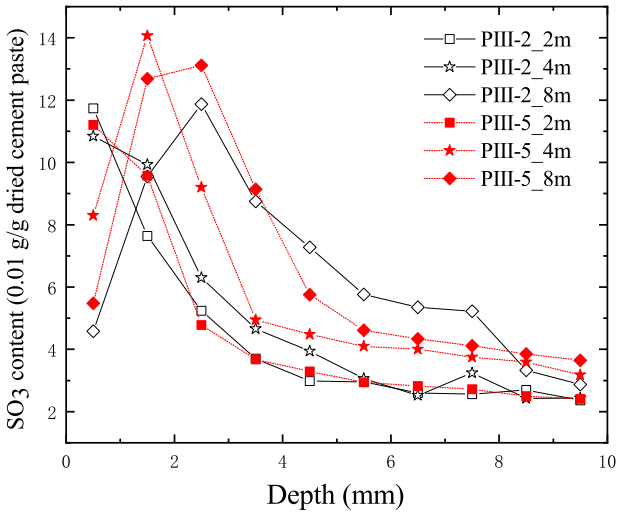

Figure 5.6 Comparisons of sulfate profiles measured by ICP-AES for cement paste disks immersed into ESA with and without DEF conditions in the presence of leaching (PIII-2 and PIII-5) for different exposure ages. PIII-2 stands for 10g/L SO_4^{2-} + pH = 7, and PIII-5 for 10g/L SO_4^{2-} + pH = 7 + DEF.

month exposure the heating treatment evidently increases sulfate ingress depth. For ESA with leaching conditions (PIII-2 for no DEF and PIII-5 for DEF) in Figure 5.6, the heating treatment obviously promotes sulfate ingress kinetics, leading to higher sulfate content and sulfate penetration depth, while for ESA conditions with leaching and chlorides (PIII-3 for no DEF and PIII-6 for DEF) in Figure D.1 the heating treatment has little impact on sulfate ingress.

5.1.2 Chloride profiles

Figures 5.7 and 5.8 present the chloride profiles of disk specimens in PIII-3 and PIII-6 conditions, respectively. Firstly, the high free chloride concentration at 9-10mm in Figures 5.7a and 5.8a indicates an over-10mm penetration depth of chlorides, confirming a larger penetration rate of chlorides than sulfates in Figures 5.2b and 5.3b. Note that an increase range of chlorides content, within 0-5mm, exists in both the total and bound chloride profiles in Figures 5.7 and 5.8 and that range coincides with the penetration depth of sulfates in PIII-3 and PIII-6 conditions in Figures 5.2b and 5.3b, indicating the influence of sulfates on the transport of chlorides. The observed reciprocal interaction between sulfate and chloride transports can be explained through a competition mechanism[10]: Upon penetration, the sulfates and chlorides will bind with aluminum phases to form ettringite and Friedel's salts respectively; the chlorides diffuse faster in cement pastes than sulfates,

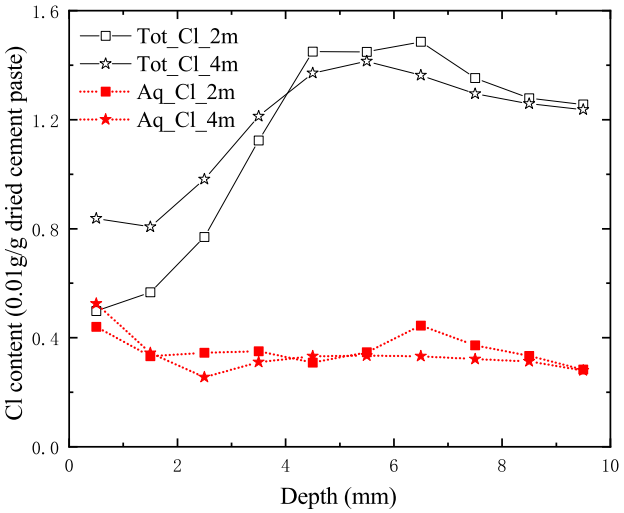

(a)

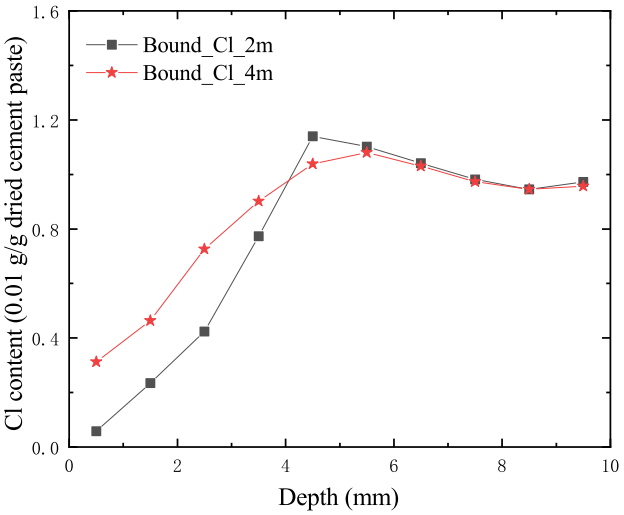

(b)

Figure 5.7 Total and water-soluble chloride profiles (a) and bound chloride profile of cement paste disks immersed into PIII-3 conditions of 10g/L SO_4^{2-} + 10g/L Cl^- (pH=7) for different exposure ages, measured using potentiometric titrator.

bound by aluminum phases in the form of Friedel's salts; the sulfates, arriving tardily, convert the Friedel's salts into ettringite[126], leading to a decrease in bound chlorides in Figures 5.7b and 5.8b. Therefore, there are two zones in cement pastes subjected to combined sulfate and chloride actions: a sulfate-rich zone near the material surface followed by a chloride-rich zone in material interior, which is consistent with the long-term observation of exposed specimens in the literature[212-213].

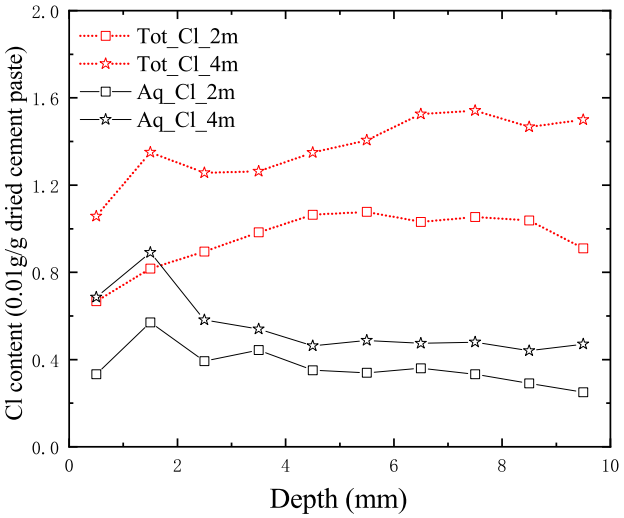

(a)

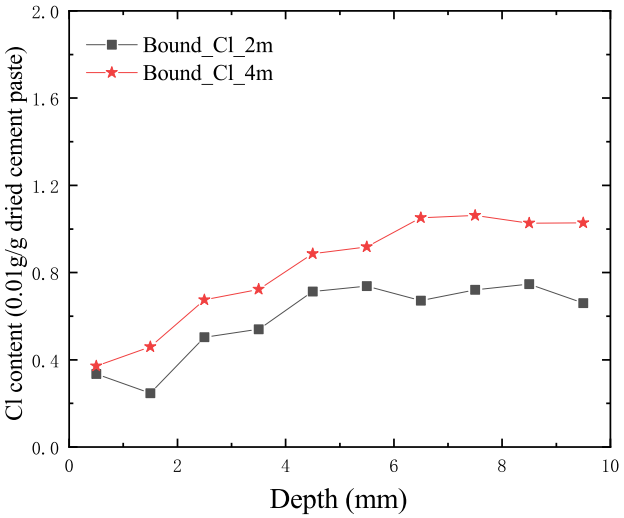

(b)

Figure 5.8 Total and water-soluble chloride profiles (a) and bound chloride profile of cement paste disks immersed into PIII-6 conditions of 10g/L SO_4^{2-} + 10g/L Cl^- (pH=7) +DEF for different exposure ages, measured using potentiometric titrator.

Figures D.2, D.3 and D.4 compare the total, free and bound chloride profiles in disk specimens exposed to PIII-3 and PIII-6 conditions, respectively. There is little difference in the bound chlorides contents of specimens in PIII-3 and PIII-6 conditions in D.4, while the free chloride contents in PIII-6 condition are significantly larger than in PIII-3 condition. Thus, heating treatment has no effect on the chloride binding but accelerates the chloride penetration due to the DEF-caused microcracks.

5.2 Surface damage observation

5.2.1 Cracking observation

Figure 5.9 presents the cracks on the cross-sections of disk specimens in ESA conditions without DEF (PIII-1, PIII-2 and PIII-3) at different exposure ages. In PIII-1 condition, no obvious crack was observed before 4-month exposure, and just a tiny crack perpendicular to the surface appeared at 8-month exposure. While in PIII-2 condition, the cracks were almost parallel to the exposure surface, which agrees with the cracking pattern in literature[214]. What's more, the cracking depth in the PIII-2 condition increased with time. The faster cracking rate and larger crack widths in PIII-2 condition than in PIII-1 condition correspond to the faster ingress of sulfates in PIII-2 condition in Figure 5.2a, confirming the accelerating effect of leaching on ESA-caused damage. For PIII-3 condition, several cracks parallel to the exposure surface appeared at 8 months, and a more porous zone was found around the cracks. The delay of cracking in PIII-3 specimens shows the mitigating effect of chlorides on ESA damage.

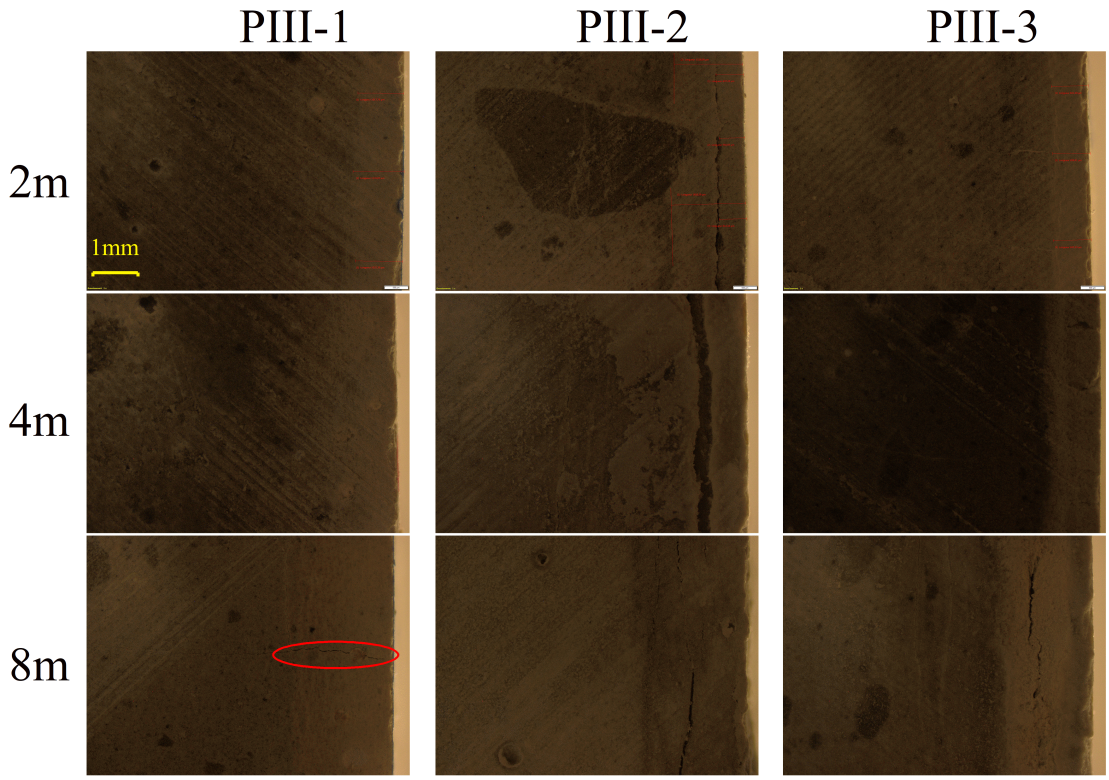

Figure 5.9 Cracking observation on cross sections of cement paste disks with w/c of 0.55 exposed to PIII-1, PIII-2 and PIII-3 conditions at different exposure ages by optical microscope. PIII-1 stands for 10g/L SO_4^{2-} + pH = 13, PIII-2 for 10g/L SO_4^{2-} + pH = 7, and PIII-3 for 10g/L SO_4^{2-} + + 19 g/L Cl^- + pH = 7.

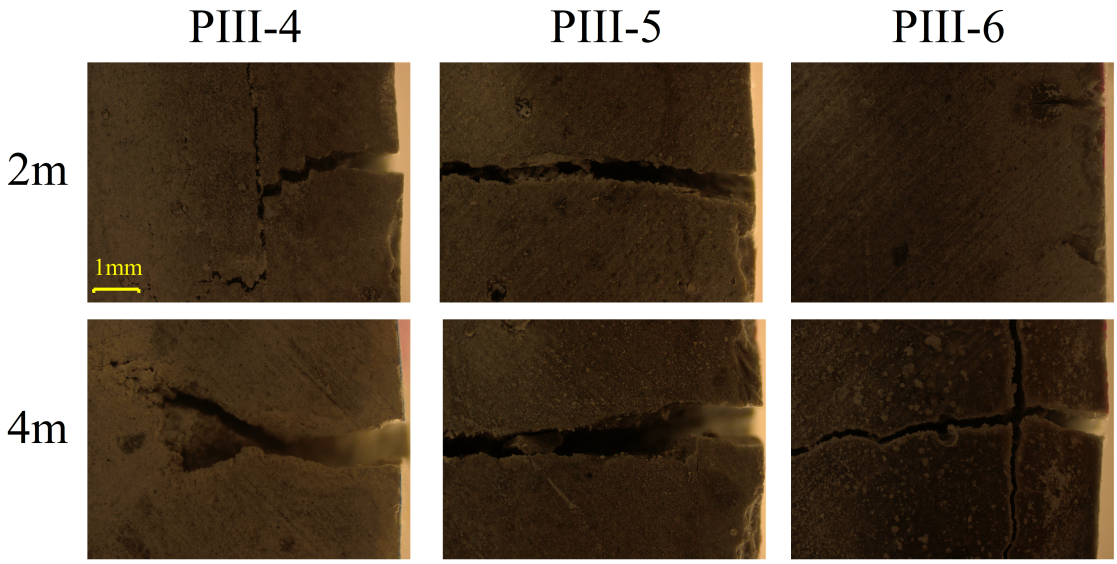

Figure 5.10 Cracking observation on cross sections of cement paste disks with w/c of 0.55 exposed to PIII-4, PIII-5 and PIII-6 conditions at different exposure ages by optical microscope. PIII-4 stands for 10g/L SO_4^{2-} + pH = 13 + DEF, PIII-5 for 10g/L SO_4^{2-} + pH = 7 + DEF, and PIII-6 for 10g/L SO_4^{2-} + + 19 g/L Cl^- + pH = 7 + DEF.

The different crack patterns in PIII-1 and PIII-2 conditions indicate different damage mechanisms. In PIII-1 solution, the ettringite is formed by the reaction between the penetrated sulfates and the aluminum phases in hardened cement paste, filling the pores and generating crystallization pressure in the region near the surface. The maximum sulfate concentration and ettringite amount at the surface lead to the maximum crystallization pressure and effective stress in the solid matrix at the surface, localizing the material fracture at the surface. In PIII-2 condition, the leaching, dissolving the calcium-containing phases such as CH, CSH, and formed ettringite at the surface, releases the pore space and degrades the solid matrix of materials, also setting free the pore crystallization pressure by ettringite formation in the surface zone; in the interior zone adjacent to the surface zone affected by leaching, a high pore pressure exists due to the crystallization of ettringite. The difference in stress state and fracture resistance between the surface zone and the adjacent interior zone causes cracking between these two zones, in the form of spalling damage.

Figure 5.10 presents the cracks on the cross-sections of disk specimens in ESA conditions with DEF (PIII-4, PIII-5 and PIII-6) at different exposure ages. The visible cracks perpendicular to the exposure surface penetrated deeper into the interior with time in three conditions. The severity of cracking damage decreases from PIII-5 to PIII-4 to PIII-6 conditions, revealing an order of aggravating effects on ESA damage: DEF > leaching >

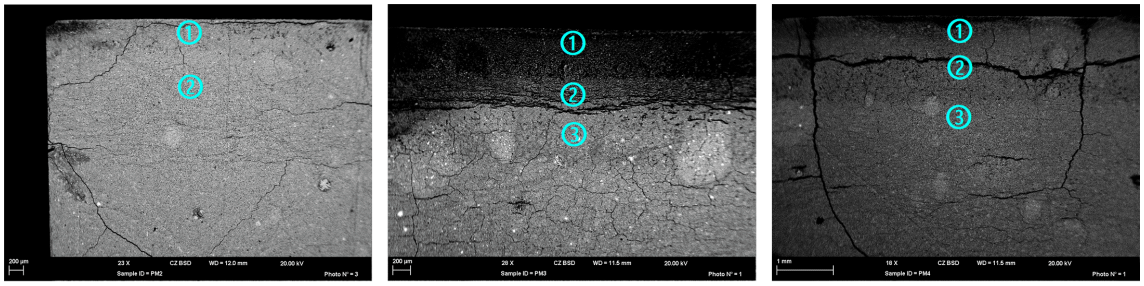

(a) (b) (c)

Figure 5.11 BSE images on the cross section of cement paste disks immersed into (a) PIII-1 condition for 2months, (b) PIII-2 condition for 2months and (c) PIII-3 condition solution for 8months. PIII-1 stands for 10g/L SO_4^{2-} + pH = 13, PIII-2 for 10g/L SO_4^{2-} + pH = 7, and PIII-3 for 10g/L SO_4^{2-} + + 19 g/L Cl^- + pH = 7.

chloride. The cracks with considerable opening widths are due to the initial microcracks during the curing period, cf. Figures 4.12 and 4.13.

Figure 5.11 presents the BSE images of 0-1mm surface depth of specimens exposed to PIII-1 and PIII-2 conditions for 2 months, and to PIII-3 condition for 8 months. Compared to the smooth surface in the PIII-1-2m specimen, the PIII-2-2m specimen in Figure 5.11b shows multiple tiny cracks constituting the single big large crack in Figure 5.9 while the PIII-3-8m specimen in Figure 5.11c presents a 2D network of cracks.

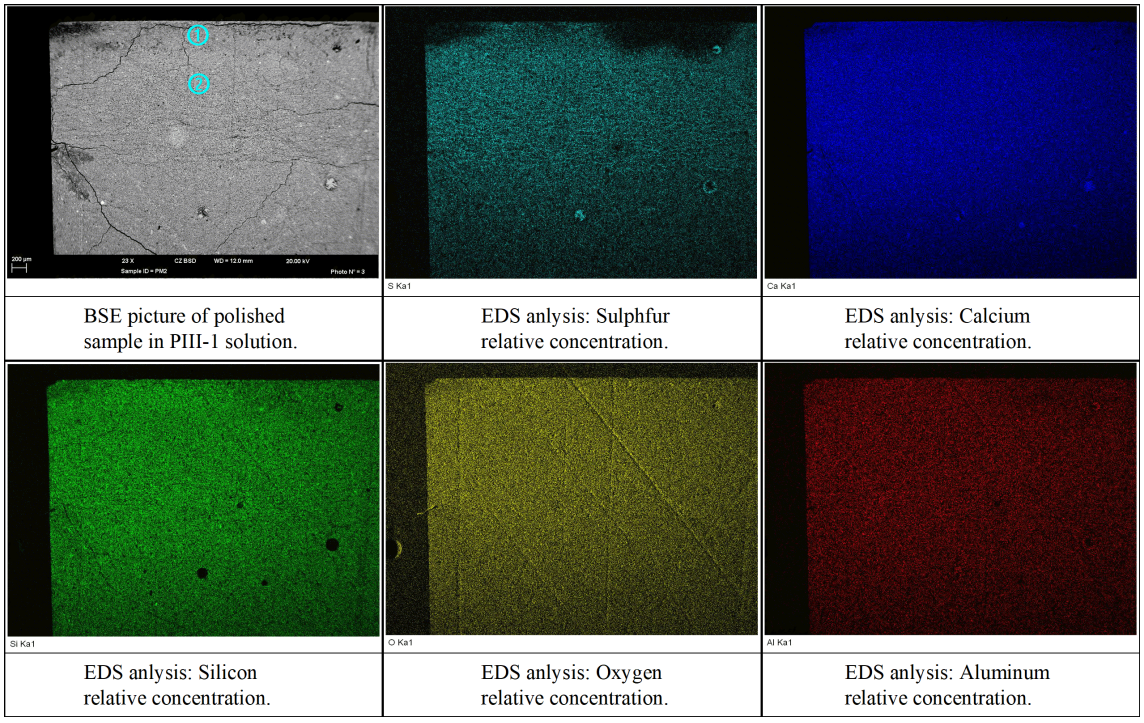

BSE picture of polished sample in PIII-1 solution.	EDS anlysis: Sulphfur relative concentration.	EDS anlysis: Calcium relative concentration.
EDS anlysis: Silicon relative concentration.	EDS anlysis: Oxygen relative concentration.	EDS anlysis: Aluminum relative concentration.

Figure 5.12 BSE and EDS element maps on the cross section of cement paste disk immersed into PIII-1 condition (10g/L SO_4^{2-} + pH = 13) for 2 months. Top edge of each image is the exposure surface.

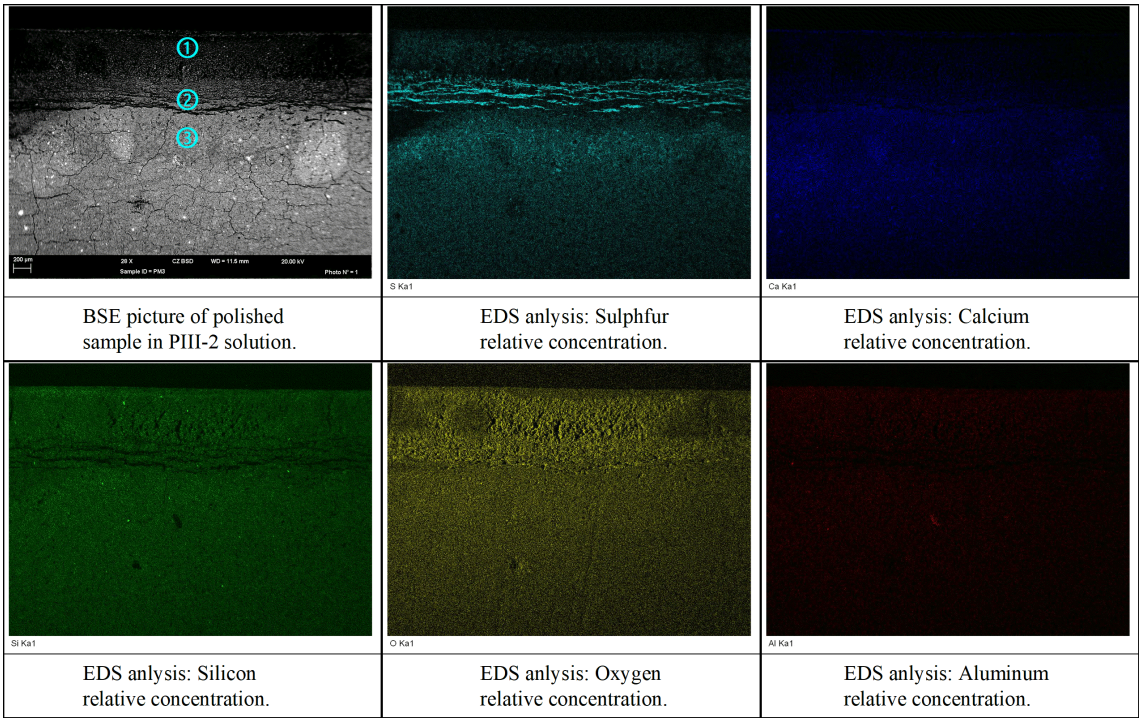

BSE picture of polished sample in PIII-2 solution.	EDS anlysis: Sulphfur relative concentration.	EDS anlysis: Calcium relative concentration.
EDS anlysis: Silicon relative concentration.	EDS anlysis: Oxygen relative concentration.	EDS anlysis: Aluminum relative concentration.

Figure 5.13 BSE and EDS element maps on the cross section of cement paste disk immersed into PIII-2 condition (10g/L SO_4^{2-} + pH = 7) for 2 months. Top edge of each image is the exposure surface.

5.2.2 Chemical elements and mineral phase distribution

Figures 5.12 and 5.13 show the distribution of chemical elements in 0-1mm of PIII-1-2m and PIII-2-2m specimens, respectively. Compared to the homogeneous distribution of sulfur element in PIII-1-2m in Figure 5.12, the sulfur distribution in PIII-2-2m in Figure 5.13 presents three zones: the outermost Zone 1 with low sulfur content, the cracking Zone 2 rich in sulfur, and the inner Zone 3 with a sulfur content decreasing with depth. Such distribution agrees with the sulfate profiles of PIII-2-4m and PIII-2-8m specimens in Figure 5.2a. The drop of sulfate and calcium elements near the surface corresponds to the dissolution of solid sulfates and calcium phases by leaching, respectively.

Several powder samples were taken from the marked positions in Figure 5.11 and the intact zone of disk specimens exposed to the ESA conditions without DEF (PIII-1, PIII-2 and PIII-3), and subjected to XRD analysis. The analysis results are given in Figure 5.14. Firstly, the intact zones of disk specimens have the same composition of mineral phases: small quantity of ettringite and a large amount of portlandite. For PIII-1 condition exposure in Figure 5.14a, there is a reduction of ettringite from surface to interior (Zone 1/2 to the intact zone), corresponding to the sulfate profile in Figure 5.2a. For PIII-2 condition exposure in Figure 5.14b, the ettringite and CH appear in Zone 3 and the intact

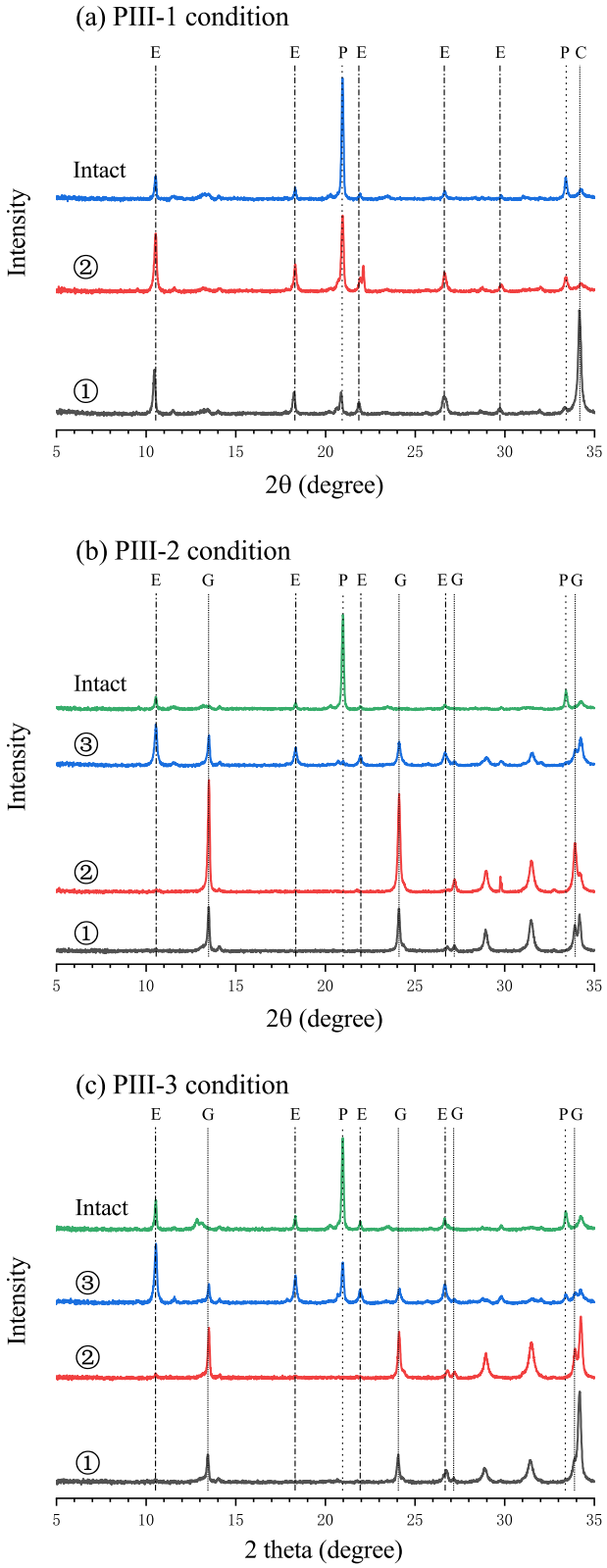

Figure 5.14 XRD analysis of cement paste disks immersed in (a) PIII-1 condition for 2 months, (b) PIII-2 condition for 2 months and (c) PIII-3 condition for 8 months. The sample marks correspond to the marked positions in Figure5.11. The "intact" samples correspond to the intact zone of cement paste disks. "E", "P", "G" and "C" stand for ettringite, portlandite, gypsum and calcite. PIII-1 stands for 10g/L SO_4^{2-} + pH = 13, PIII-2 for 10g/L SO_4^{2-} + pH = 7, and PIII-3 for 10g/L SO_4^{2-} + + 19 g/L Cl^- + pH = 7.

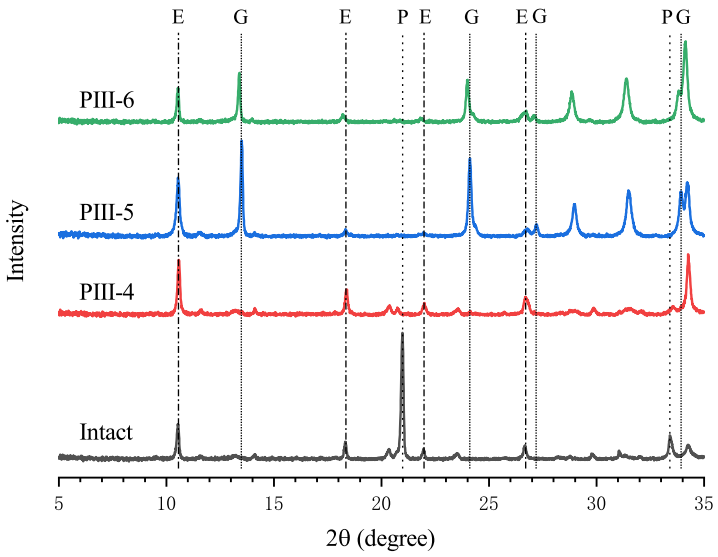

Figure 5.15 XRD analysis of samples in surface area of cement paste disks immersed in PIII-4 condition (b) PIII-5 condition and (c) PIII-6 condition for 2 months. The "intact" samples correspond to the intact zone of cement paste disks. "E", "P", "G" and "C" stand for ettringite, portlandite, gypsum and calcite.

zone, and the gypsum shows a maximum intensity peak in Zone 2. For PIII-3 condition exposure in Figure 5.14c, the mineral phase distribution shows the same pattern as for PIII-2 solution. Comparing the results of samples in PIII-1 and PIII-2 conditions shows that the leaching process results in not only the dissolution of ettringite but also the precipitation of gypsum, which accounts for the big difference in the maximum sulfate contents in specimens exposed to PIII-1 and PIII-2 conditions in Figure 5.2a. In other words, the gypsum is a special product in ESA conditions with leaching.

Figure 5.15 presents the XRD analysis on the mineral phases of surface of disk specimens exposed to ESA conditions with DEF (PIII-4, PIII-5 and PIII-6). The results in Figure 5.15 confirm the formation of gypsum in leaching condition again. Like the XRD results in experimental Part I and Part II (in Section 3.2 and Section 4.1.2), the high pH value seems to prevent the formation of gypsum in cement paste exposed to sulfate-bearing condition. The condition for gypsum precipitation will be explored further in the following.

5.3 Further discussion

5.3.1 Formation of gypsum

As discussed above, gypsum is a product only formed when the Portland cement pastes are subjected to combined ESA and leaching actions, and the crucial questions raised are: when and where the gypsum forms. Theoretically, to precipitate gypsum, the activity product of reactants (calcium and sulfate activities) in the pore solution must be larger than the solubility constant of gypsum,

$$\beta_{\mathrm{gp}} = \frac{a_{\mathrm{Ca^{2+}}} a_{\mathrm{SO_4^{2-}}}}{K_{\mathrm{gp}}} = \frac{\gamma_{\pm 2}^2 c_{\mathrm{Ca^{2+}}} c_{\mathrm{SO_4^{2-}}}}{K_{\mathrm{gp}}} > 1 \tag{5.1}$$

The terms β_{gp} and K_{gp} stand for the supersaturation and the solubility constant of gypsum, a_i and c_i for the activity and the concentration of ion i, and $\gamma_{\pm 2}$ for the activity coefficient of divalent ions. The ionic activity coefficients in the pore solution can be determined through an extended Debye-Hückel equation[139],

$$\lg \gamma_i = \frac{-A_\gamma z_i^2 \sqrt{I}}{1 + aB_\gamma \sqrt{I} + b_\gamma I} \tag{5.2}$$

Here A_γ and B_γ stand for two parameters depending on the temperature and the pressure, a for an average distance of approach of two ions of opposite charges, b_γ for a semi-empirical coefficient, z_i for the formula charge of ion i, and I for the ionic strength. The ionic strength is a measurement of the concentration of all ions present in the solution, defined as,

$$I = 0.5 \sum c_i z_i^2 \tag{5.3}$$

Actually, the predominant ionic species (about 98.5% in molar amount) in pore solution of Portland cement paste are K^+, Na^+ and OH^-n ions[215]. Therefore, the ionic strength can be estimated as the sum of the concentrations of these ions,

$$I \approx 0.5 \left(c_{\mathrm{Na^+}} + c_{\mathrm{K^+}} + c_{\mathrm{OH^-}} \right) \approx c_{\mathrm{Na^+}} + c_{\mathrm{K^+}} \tag{5.4}$$

The concentrations of sodium and potassium, $c_{\mathrm{Na^+}}$ and $c_{\mathrm{K^+}}$, can be evaluated from the mass conservation of Na and K in cement paste[216],

$$c_{\mathrm{Na^+}} = \frac{n_{\mathrm{Na}}^{\mathrm{tot}}}{V_{\mathrm{w}} + R_{\mathrm{Na}} m_{\mathrm{CSH}}}, \quad c_{\mathrm{K^+}} = \frac{n_{\mathrm{K}}^{\mathrm{tot}}}{V_{\mathrm{w}} + R_{\mathrm{K}} m_{\mathrm{CSH}}} \tag{5.5}$$

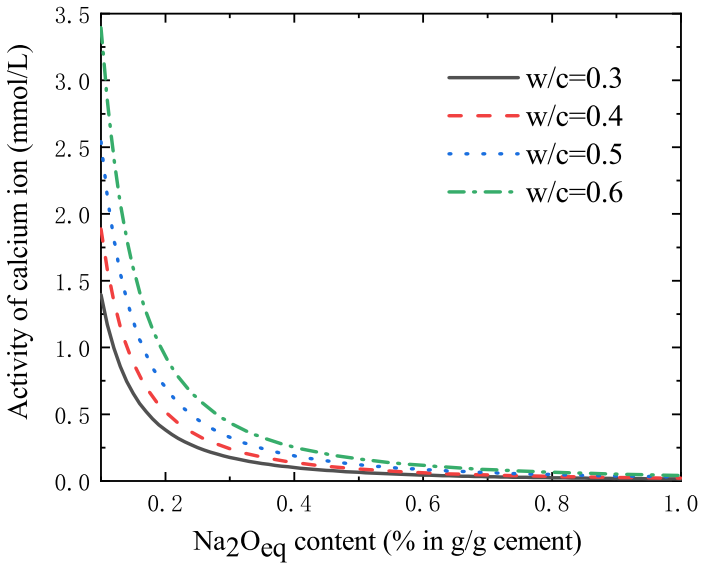

(a)

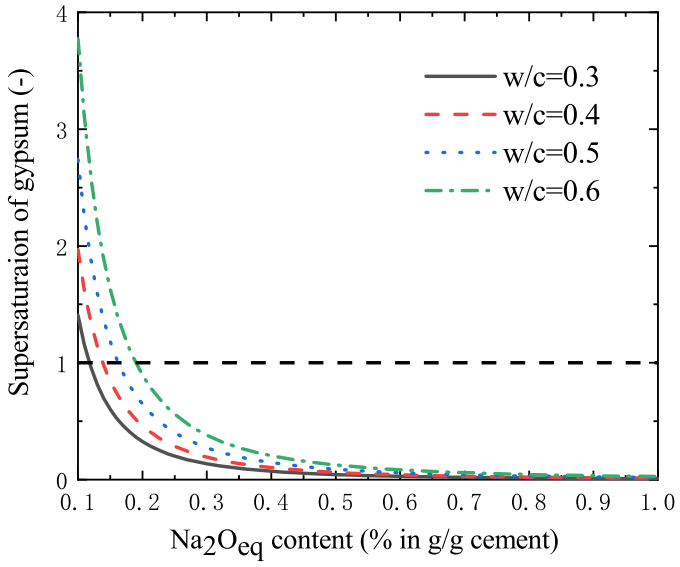

(b)

Figure 5.16 Activity of calcium ion in pore solution (a) and supersaturation of gypsum of pore solution after adding 0.1M Na_2SO_4 (b) in terms of Na_2O_{eq} for different w/c ratio.

where n_i^{tot} stands for the total amount of element i in unit volume of cement paste, obtained from the cement composition in Table 2.1, R_i for the adsorption ratio of ion i in CSH, V_w and m_{CSH} for the volume of pore solution and the mass of CSH in unit volume of cement paste. In this study, the adsorption ratios take the values in[216], and the ionic strength I of the intact pore solution is determined as 0.27M. The activity of Ca^{2+} is determined

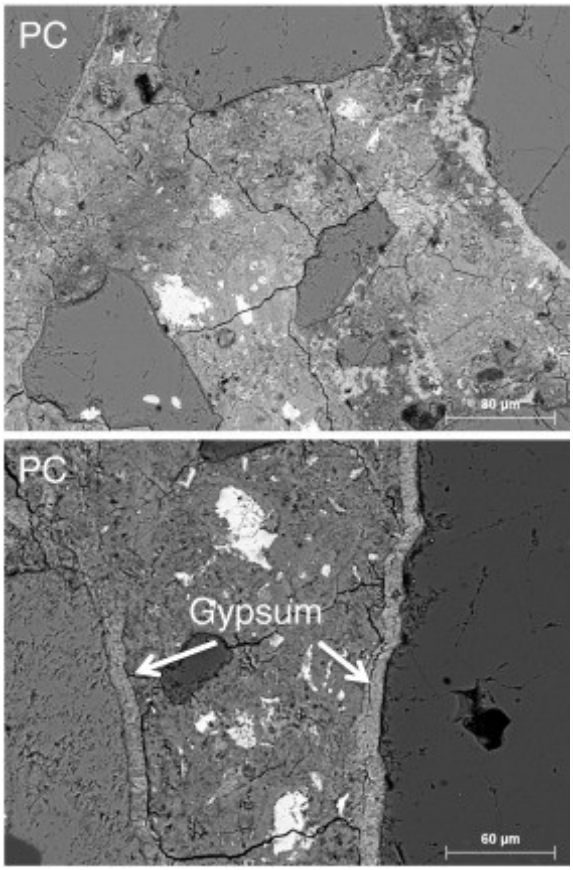

Figure 5.17 BSE images of surface of Portland cement concrete specimens exposed to 10g/L Na_2SO_4 for 120d. After Yu et al.[211].

from the dissolution equilibrium of CH,

$$a_{Ca^{2+}} = \frac{K_{CH}}{\gamma_{\pm 1}^2 \cdot c_{OH^-}^2} \tag{5.6}$$

where K_{CH} stands for the dissolution constant of CH. The calcium activity and the supersaturation of gypsum, $a_{Ca^{2+}}$ and β_{gp}, in the pore solution of cement paste exposed to PIII-1 condition are determined as 0.18mmol/L and 0.18, by blending the intact pore solution with PIII-1 condition. Thereby, no gypsum is formed in cement paste exposed to PIII-1 condition. Keeping the sodium/potassium ratio as in Table 2.1, Figure 5.16 presents the estimated $a_{Ca^{2+}}$ and β_{gp} in terms of equivalent alkali ($n_{Na_2O_{eq}} = n_{Na_2O} + 0.658 n_{K_2O}$) content in cement, for different w/c ratios. As shown in Figure 5.16, $a_{Ca^{2+}}$ drops with Na_2O_{eq} content. Figure 5.16b shows that the gypsum is precipitated only when the alkali content is below 0.2%.

For Portland cement pastes exposed to sulfate solution with leaching condition (PIII-2: pH = 7), the calcium activity is lower than the estimated values for PIII-1 condition

(no leaching: pH = 13) exposure due to the calcium leaching. Thus, it is less likely to form gypsum, especially in the leaching zone. However, the formation of gypsum has been reported in literature[211,217] for Portland cement pastes exposed to solutions similar to PIII-2. A likely mechanism for the gypsum formation in Portland cement pastes subjected to ESA with leaching condition can be proposed as follows: the ettringite initially formed in pores, along with the penetration of sulfates, fractures the solid matrix by high crystallization pressure, allowing the low-pH sulfate solution to penetrate into the cracks; the penetrated low-pH sulfate solution reacts directly with CH to form gypsum in cracks,

$$Ca(OH)_2 + SO_4^{2-} \longrightarrow CaSO_4 \cdot 2H_2O + 2OH^- \tag{5.7}$$

That is to say, the gypsum is the consequence of solid matrix cracking rather than its cause, and the gypsum formation does not contribute to the crack initiation. The gypsum found in cracks of specimens in literature studies[211,217] as shown in Figure 5.17 could support this mechanism.

5.3.2 Growth of gypsum crystal in cracks

As illustrated in Figure 5.16b, the low-alkali cement pastes allow the formation of gypsum in pore solution when exposed to sulfate solutions without leaching. Literature studies confirmed this observation[72,74,218]: low-alkali cement (C_3S cement and alite cement) mortars were immersed into sulfate solution and the formation of gypsum was detected. In these studies, the gypsum is the only source for material expansion since very little ettringite forms in such low-C_3A cement mortars. The expansion is induced by the crystallization of gypsum in pores, and the crystallization pressure can be evaluated by Correns' equation[66],

$$P_C = \frac{RT}{\overline{V}_{gp}} \ln(\beta_{gp}) \tag{5.8}$$

Here the term R stands for the ideal gas constant, T for the Kelvin temperature, and $\overline{V}_{gp}$ for the molar volume of gypsum crystal, taking 75 cm^3/mol according to[195]. The crystallization pressure of gypsum in pores, P_C, is evaluated as 43MPa in[72], constituting the mechanical origin for material expansion.

For Portland cement pastes exposed to sulfate solution with leaching, the gypsum is the consequence of cracking and forms in cracks. Now the following questions seem tempting: how fast the gypsum forms in cracks and does it provide enough crystallization

pressure to propagate the cracks ? To address these questions, we idealize the shape of a single crack as a cylinder with d as diameter and the shape of gypsum crystal as a growing sphere with D_{gp} as the diameter, cf. Figure 5.16. Some further assumptions are made: (1) the cracks are totally saturated by the external sulfate solution and the concentrations of OH^- and SO_4^{2-} in cracks are taken as the concentrations in the external solution; (2) the number of crystallization nuclei for gypsum formed in a crack has the same order of magnitude as the number of CH crystals exposed on the crack wall available to gypsum formation. Based on the chemical reaction in Eq. (5.7), the mass conservation of calcium writes,

$$\mathrm{d}(c_{Ca^{2+}} V_a) + \mathrm{d}n_{gp} + \mathrm{d}n_{CH} = 0 \tag{5.9}$$

where V_a denotes the volume of the crack space (filled by low pH solution due to the appearance of cracks), and n_i stands for molar content of phase i in the crack space. The dissolution of CH crystals, taking spherical shapes, is assumed to be governed by an interface-controlled mechanism[219],

$$\frac{\mathrm{d}n_{CH}}{\mathrm{d}t} = k_{CH} s_{CH} A_{CH} \ln(\beta_{CH}) \quad \text{with} \quad \beta_{CH} = \frac{a_{Ca^{2+}} a_{OH^-}^2}{K_{CH}}, \; A_{CH} = 4\pi r_{CH}^2 \tag{5.10}$$

where k_{CH} and K_{CH} stands for the kinetic constant and the dissolution constant of CH, β_{CH} for the CH undersaturation, A_{CH} and r_{CH} for the surface area and the radius of a single CH crystal, and s_{CH} for the number of CH crystals. The initial content of portlandite in cement paste in leaching zone, n_{CH}^0, is equal to $\alpha V_a C_{CH}$, with α standing for the residual CH ratio in the leaching zone, and C_{CH} for the CH content in intact cement paste, determined from the mineral composition of cement in Table 2.1 and the w/c ratio using the method

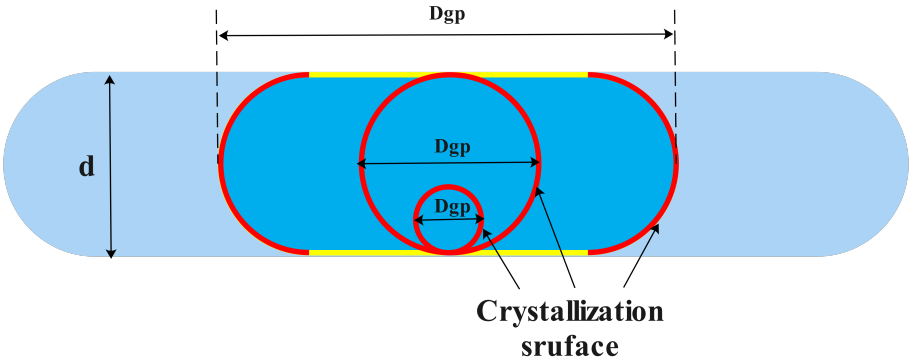

Figure 5.18 Illustration of gypsum crystal growth in a crack. Red lines represent the crystallization surface, and yellow lines mark the lateral surfaces of gypsum crystal where the crystal growth is confined.

Table 5.2 Parameters used in the simulations for gypsum crystal growth in crack space.

Parameter (unit)	Symbol	Value
Volume of crack space (-)	V_a	0.01
Initial radius of portlandite (μm)	r_{CH}^0	20
Initial portlandite content (mol/L cement paste)	C_{CH}^0	4.27
Discount ratio on portlandite concent (-)	α	0.01
Number of portlandite crystals (-)	s_{CH}	4.21×10^5
Molar volume of gypsum ($\mathrm{cm^3/mol}$)	$\overline{V}_{\mathrm{gp}}$	75[195]
Molar volume of portlandite ($\mathrm{cm^3/mol}$)	$\overline{V}_{\mathrm{CH}}$	33[195]
Dissolution constant of gypsum (-)	$\lg(K_{\mathrm{gp}})$	-4.6[195]
Dissolution constant of portlnadite (-)	$\lg(K_{\mathrm{CH}})$	-5.2[195]
Kinetic constant of gypsum ($\mathrm{mol\cdot s^{-1}\cdot m^{-2}}$)	k_{gp}	4.88×10^{-4} [220]
Kinetic constant of portlandite[a] ($\mathrm{mol\cdot s^{-1}\cdot m^{-2}}$)	k_{CH}	8.98×10^{-4} [221]

[a] Calculated from[221].

in[121]. The kinetics of gypsum crystallization is assumed to follow a polynucleation crystal growth mechanism[220],

$$\frac{\mathrm{d}n_{\mathrm{gp}}}{\mathrm{d}t} = k_{\mathrm{gp}} s_{\mathrm{gp}} A_{\mathrm{gp}} \left(\sqrt{\beta_{\mathrm{gp}}} - 1\right)^{3.4} \tag{5.11}$$

where k_{gp} and A_{gp} stand for the kinetic constant of crystallization and the surface of gypsum crystals, and s_{gp} for the number of crystallization nuclei of gypsum. The physico-chemical parameters of gypsum and CH, together with other parameters in this model, are given in Table 5.2. Considering the cylindrical geometry of the crack in Figure 5.18, once the gypsum crystal reaches the crack wall, the lateral crystal growth is stopped and the crystal surface achieves its maximum value,

$$A_{\mathrm{gp}} = \begin{cases} \pi D_{\mathrm{gp}}^2, & D_{\mathrm{gp}} < d \\ \pi d^2, & D_{\mathrm{gp}} \geqslant d \end{cases} \tag{5.12}$$

The size of gypsum crystals D_{gp} is determined through the gypsum crystal volume V_{gp}, cf. Figure 5.18,

$$D_{\mathrm{gp}} = \begin{cases} \left(\dfrac{6V_{\mathrm{gp}}}{4\pi}\right)^{1/3}, & V_{\mathrm{gp}} < \dfrac{1}{6}\pi d^3 \\ d + 4(V_{\mathrm{gp}} - \dfrac{1}{6}\pi d^3)/(\pi d^2), & V_{\mathrm{gp}} \geqslant \dfrac{1}{6}\pi d^3 \end{cases} \tag{5.13}$$

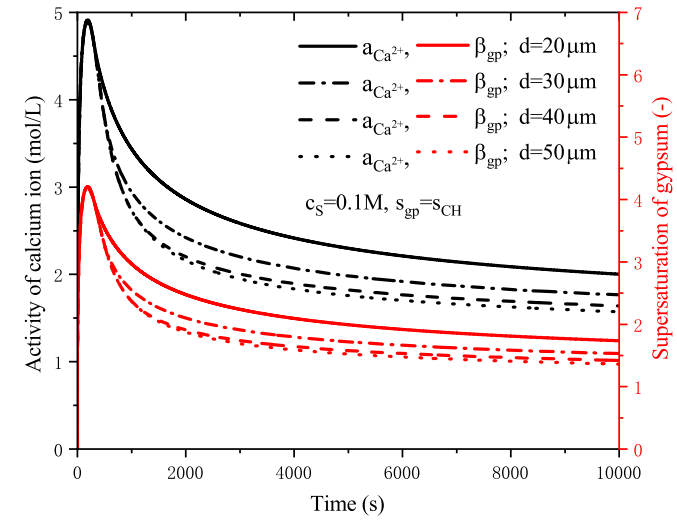

(a)

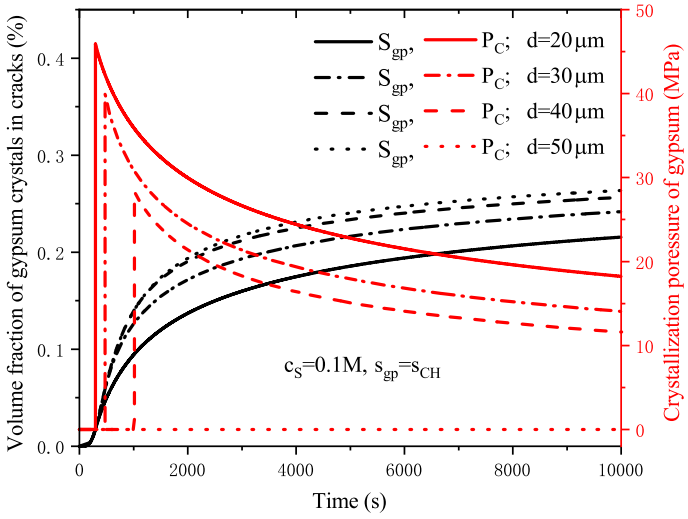

(b)

Figure 5.19 Calcium activity $a_{Ca^{2+}}$ and supersaturation of gypsum β_{gp} (a), volume fraction of gypsum crystals in cracks S_{gp} and crystallization pressure P_C (b) in terms of time for different cracking widths. The terms d, c_s, s_{gp}, and s_{CH} stand for the crack width, sulfate concentration, number of crystallization nuclei of gypsum and portlandite crystals, respectively.

with

$$V_{gp} = \frac{n_{gp}\overline{V}_{gp}}{s_{gp}} \tag{5.14}$$

According to the crystallization pressure theory[64], the occurrence of crystallization pressure needs two conditions: (1) the crystal grows in confined space, i.e. $D_{gp}>d$; (2) the

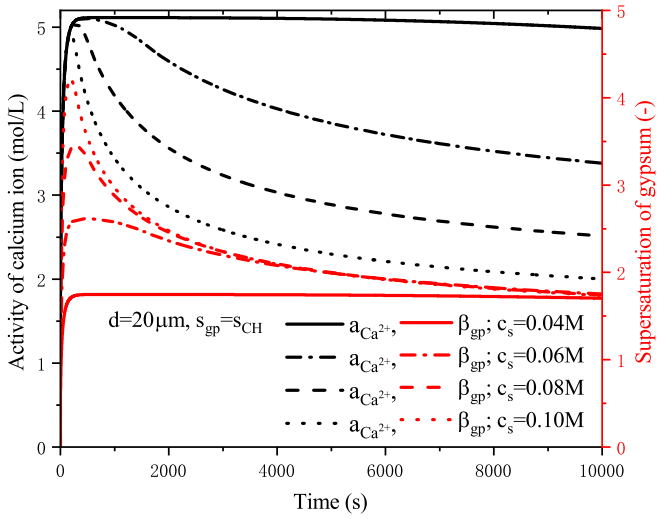

(a)

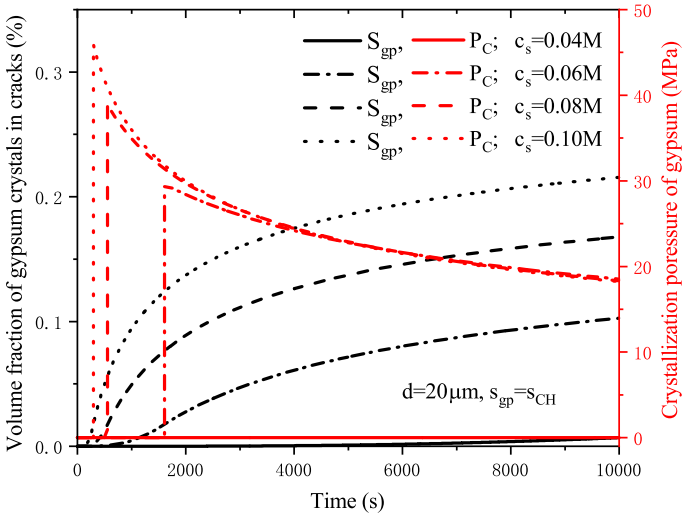

(b)

Figure 5.20 Calcium activity $a_{Ca^{2+}}$ and supersaturation of gypsum β_{gp} (a), volume fraction of gypsum crystals in cracks S_{gp} and crystallization pressure P_C (b) in terms of time for different sulfate concentrations. The terms d, c_s, s_{gp}, and s_{CH} stand for the crack width, sulfate concentration, number of crystallization nuclei of gypsum and portlandite crystals, respectively.

supersaturation of crystal is superior to 1, i.e. β_{gp} >1. Therefore, Eq. (5.8), when applied to the case of Figure 5.18, should be rewritten as,

$$P_C = \begin{cases} \dfrac{RT}{\overline{V}_{gp}} \ln(\beta_{gp}), & D_{gp} > d \\ 0, & D_{gp} \leqslant d \end{cases} \tag{5.15}$$

So far, the crystal growth of gypsum is described by Eq.(5.9) to Eq.(5.15) with the crack size d, external sulfate concentration c_s as variables. Figures 5.19 and 5.20 presents the calcium activity $a_{Ca^{2+}}$, the supersaturation of gypsum β_{gp}, the volume fraction of gypsum crystal formed in cracks S_{gp} and the pressure P_C evaluated in Eq. (5.15 for the cement paste specimens exposed to PIII-1 condition for a duration of 10^4s, around 2.7h.

Figures 5.19a and 5.20a provide the evolution of $a_{Ca^{2+}}$ and β_{gp} in solution in crack space in terms of different crack size d and different sulfate concentration for given $s_{gp,CH}$ respectively, showing larger cracks sizes and higher sulfate concentrations give lower calcium activity. Both the calcium activity and the supersaturation show rapidly a peak then follow a decrease with time, resulting from the calcium consumption rate by gypsum crystallization in Eq. (5.11) exceeding the generation rate from the CH dissolution in Eq. (5.10). The volume of formed gypsum crystals and the corresponding pressure calculated by Eq.(5.15) are given in Figures 5.19b and 5.20b. Generally, the gypsum formation in crack space is slow within the simulation duration of 2.7h, and still follows an increasing path at the end of simulation. The larger crack sizes allow higher crystallization surface areas, resulting in higher formation rates in Figure 5.19b; the higher sulfate concentrations cause higher supersaturation values and formation rates in Figure 5.20b. The corresponding pressure, following the same pattern as the supersaturation, presents an instantaneous peak, 30-50 MPa, and then relaxes with time, down to 10-20MPa at the end of the simulation. For the case of large crack size d=50μm in Figure 5.19b, the pressure is completely cancelled out due to the fact that crystal size D_{gp} has not yet attained 50μm. When the sulfate concentration is lowered to 0.04M, the formation rate is too small for the crystal to touch the crack wall, thus no pressure is generated either. Noted that the pressure thus calculated is not the real pressure exerted on the pore wall in Figure 5.18 and Figure 5.20 but the crystal pressure in equilibrium with the supersaturation of gypsum in the external solution, and the real pressure during the crystal growth should be lower than this value. Thus, this pressure can be taken as the upper bound value of the attainable pressure during the crystal growth. Considering further the volume fraction of formed gypsum in the crack space, around 0.3%, the effective pressure from the gypsum crystallization in crack space will be within, or inferior to, the upper bound value of $P_C S_{gp}$, i.e. 0.09-0.15MPa, a rather small value for fracture of cement-based materials. This would imply that the formed gypsum cannot contribute to the crack propagation.

5.3.3 Effect of leaching and chlorides

Compared to the sulfate diffusion and sulfate binding by ettringite formation under non-leaching condition (PIII-1), the mass transfer and reactions involved in leaching condition (PIII-2) are more complex. Initially, the sulfates diffuse into the materials due to the high sulfate concentration in PIII-2 condition and the calcium dissolves and diffuses outward by leaching as indicated in Figure 5.13. The former produces ettringite and crystallization pressure in pores while the latter causes the dissolution of ettringite and the degradation of solid matrix, cf. Figure 5.13. As a result of the combined effect of solid matrix degradation in surface zone and the buildup of crystallization stress in the interior adjacent zone, cracks occur parallel to the exposure surface in Figure 5.11b, showing a spalling damage pattern. Once the cracking occurs, the external PIII-2 condition, low-pH and sulfate-containing, penetrates into the cracks, resulting in the crystallization of gypsum in the cracks as in Figure 5.13 and Figure 5.14b. From the analysis in the precedent section, the crystallization of gypsum in cracks is not likely to contribute to the subsequent crack propagation, but the gypsum formation consumes the calcium phases in the solid matrix and can accelerate the leaching and solid matrix degradation. Thus, the processes occurring in the cement paste specimens under PIII-2 condition involve the sulfate ingress, the calcium leaching, cracking of solid matrix in spalling pattern, the gypsum formation in cracks, and these chemo-physical processes promote one another, resulting in a self-accelerating damage process for the specimens. Acting as a ”start button,” the initial cracking due to the ettringite formation and the solid matrix leaching causes the material to damage more and more quickly afterwards.

Chlorides reduce the formation of ettringite, resulting in a delay of first cracking as shown in Figures 5.9b,c. As a result, the above self-accelerating process is postponed, and the sulfate ingress in the PIII-3 condition is much slower compared to the PIII-2 condition as indicated in Figure 5.4b. Moreover, adding chlorides will lower the activity coefficient of ion species in pore solution, resulting in a reduction in the calcium activity and thus the supersaturation of gypsum crystals. Hence, the formation rate of gypsum, expressed in Eq. (5.11), in the mixed solution (PIII-3) is smaller than in the pure sulfate solution (PIII-2). Consequently, chlorides mitigate the ESA damage also through the inhibiting effect on the gypsum and its promoting effect on the leaching damage for solid matrix of cement paste specimens.

5.4 Conclusions

1. Compared to the non-leaching specimens, the leaching specimens show more rapid sulfate ingress and contain more bound sulfates, and the difference in solid sulfates between the two groups of specimens is identified as the newly formed gypsum through the raw material composition and XRD analyses. Besides, the leaching specimens crack faster and show larger cracks, and the cracks parallel to the exposure surface display a spalling pattern of damage. For the mineral phase distribution, the ettringite content decreases and the portlandite content increases with exposure depth in the non-leaching specimens, whilst in leaching specimens the contents of gypsum and ettringite first rise and then drop with exposure depth.

2. The leaching specimens in mixed chloride-sulfate solution show the same patterns of mineral phase distribution and cracking damage as in the single sulfate solution. The presence of chlorides mitigates the sulfate ingress, the sulfate binding rate, and the occurrence of cracking, indicating the inhibiting effect of chlorides on ESA damage. Adding chlorides reduces the activity coefficients of calcium ions and the supersaturation of gypsum, leading to a smaller generation rate of gypsum, and a less promotion effect on leaching damage of solid matrix of materials as well. The sulfates, in turn, reduce the bound chlorides significantly through the transformation of Friedel's salts. These aspects constitute the interaction mechanism between sulfates and chlorides during ESA.

3. The absence of gypsum in the non-leaching specimens is due to the very low calcium activity in the highly alkaline pore solution whilst the formation of gypsum in the leaching specimens is due to the direct reaction between the portlandite and the low-pH sulfate-bearing solution (PIII-2) which penetrates into the cracks in the solid matrix. The formation of gypsum is the consequence of solid matrix fracture rather than its cause in the leaching specimens. Through a gypsum formation model in a cylindrical crack, the gypsum formation in cracks depends closely on, among other factors, the crack size and the external sulfate concentration, and the possible pressure during gypsum crystal growth in cracks is too low to be likely to contribute to the crack propagation.

4. Heating treatment (DEF) accelerates sulfate ingress in specimens exposed to sulfate-bearing conditions. Though DEF has little impact on chloride binding, it promotes the penetration of free chlorides into specimens due to the initiation of microcracks by heating treatment. Due to the microcracking in DEF specimens during curing, the cracking damage in DEF specimens during sulfate exposure is much severer than no DEF

specimens. And the aggravating effect of DEF exceeds the mitigating effect of chlorides on sulfate penetration and cracking damage. The aggravating effects of the studied coupling actions on ESA damage are ordered as: DEF > leaching > chlorides.

CHAPTER 6 POROMECHANICS OF ESA EXPANSION

In this chapter, we try to construct a poromechanical model to simulate the expansion damage caused by ESA. In this model, a kinetic law of AFt crystallization is proposed to simulate the AFt formation, and the pore stress from crystallization and the consequent damage especially cracking are addressed in a poromechanical approach. This model is now only available for water-saturated CBM and the diffusion process is neglected. Through this model, we attempted to explain the influence of chlorides and sulfate concentrations on ESA expansion and incorporate the available ESA knowledge.

6.1 Basis for pore crystallization

Let us recall the chemical potential equilibrium between crystal and aqueous solutes,

$$\mu_C\left(P_C, T\right) = \mu_{\text{sol}}\left(P_L, T, Q\right) \quad \text{with} \quad Q = \prod a_i^{\gamma_i} \tag{6.1}$$

where Q is activity product of solute, a_i and γ_i are activity and stoichiometric coefficient of the component ions of solute. Eq. (6.1) shows that the crystal pressure P_C is a function of liquid pressure P_L and activity product Q relative to solute at a given temperature. In general unconfined condition, the crystal pressure equals the liquid pressure, and the equilibrium equation can be rewritten in the form of dissolution-precipitation equilibrium,

$$P_C = P_L : \quad Q = K, \beta_{\text{sol}} = 1 \tag{6.2}$$

where K and β_{sol} are solubility constant and supersaturation of solute. For a supersaturated solution, the solute tends to precipitate in the form of solid to reduce the activity product. The crystal can keep growing without restraint until the activity product reduces to solubility constants.

6.1.1 Equilibrium crystal pressure under confined spaces

Under confined condition, such as porous materials, the growth of crystals is limited by the confined spaces. Depending on the geometry of porous space, the crystal could only grow in an unlimited direction. Taking a cylindrical pore as an example, cf. Figure 1.6, once the AFt crystals reach the pore walls, the radial growth of AFt crystal towards

pore walls is restrained and the interaction between AFt crystals and the pore wall is yielded. The interaction inhibits the AFt growth on the one hand. On the other hand, the extra pressure (interaction) applied on the AFt crystal elevates the chemical potential of the crystal phase in Eq.(6.1). Thus, the equilibrium activity product Q should be larger than the solubility constant K, i.e. supersaturation greater than 1,

$$P_C > P_L : \quad Q > K, \beta_{AFt} > 1 \tag{6.3}$$

Eq. (6.3) shows that the AFt crystal is allowed to be in equilibrium with a supersaturated solution under confined condition due to the extra pressure supplied by pore walls. From the thermodynamic equilibrium between AFt crystal and liquid solution the extra pressure could be derived, in the form of wel-known Correns' equation,

$$\mu_C\left(P_C, T\right) = \mu_{sol}\left(P_L, T, \beta_{AFt}\right) : \quad P_C - P_L = \frac{RT}{\overline{V}_C}\ln\left(\beta_{AFt}\right) \tag{6.4}$$

The derivation of Correns' equation from thermodynamic equilibrium is given in Appendix E. According to Eq. (6.3), the interaction between crystal and pore walls is a function of AFt supersaturation under thermodynamic equilibrium condition. Under such condition, the mechanical balance between the AFt crystal and the surrounding liquid solution is reached, and the crystal pressure is the same everywhere. As shown in Figure

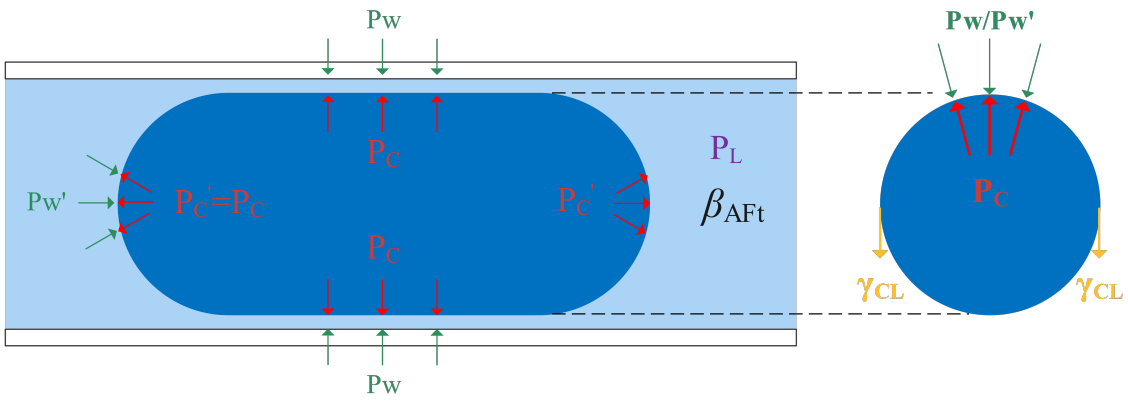

Figure 6.1 Mechanical equilibrium between AFt crystal and the liquid solution under thermodynamic equilibrium condition. P_C and P_L are the pressures of AFt crystal crystal and liquid solution, P_W and $P_W^{'}$ are the confining pressures on AFt crystal at the lateral and end sides, γ_{CL} is the surface tension of crystal-liquid interface, and β_{AFt} is the supersaturation of solute in pore solution.

6.1, the mechanical balance writes,

$$P_C = P_w + \gamma_{CL}\kappa_{CL} \tag{6.5}$$

The term κ_{CL} stands for the curvature of the crystal-liquid interface. At the crystal end sides, the confining pressure $P_W^{'}$ equals to the liquid pressure P_L and the curvature is $2/r$, thus the mechanical balance writes,

$$P_C = P_L + \frac{2\gamma_{CL}}{r} \tag{6.6}$$

Substituting the Correns' equation into Eq. (6.6) gives the well-known Oswald-Freundlich equation,

$$\frac{RT}{\overline{V}_C}\ln\left(\beta_{AFt}\right) = \frac{2\gamma_{CL}}{r} \tag{6.7}$$

Eq. (6.7) show the dependence of r on the AFt supersaturation β_{AFt}, and r is the minimum accessible radius for AFt crystal surrounded by a supersaturated solution with β_{AFt}.

At the lateral sides of the AFt crystal, there is a solution film of a nanometric size, which provides a path for ion transport to supply ion source for crystallization reaction, separating the crystal and pore wall[63,222]. The curvature at this side is $1/r$ and the confining pressure P_W is the sum of liquid pressure P_L and the disjoining pressure P_{dis} which separates the crystals from the pore walls to avoid direct contact between the crystal and the pore walls, thus the mechanical balance writes,

$$P_C = P_L + P_{dis} + \frac{\gamma_{CL}}{r} \tag{6.8}$$

The replacement of Eq. (6.6) and the Correns' equation (6.7) into Eq. (6.8) provides the estimation of disjoining pressure,

$$P_{dis} = \frac{\gamma_{CL}}{r} = \frac{1}{2}\frac{RT}{\overline{V}_C}\ln\left(\beta_{AFt}\right) \tag{6.9}$$

The interaction between crystal and pore walls is the sum of liquid pressure and disjoining pressure. Eq. (6.9) provides two approaches to evaluating the interaction under a thermodynamic equilibrium state: the first one is derived from mechanical balance, and the force is the product of surface tensor and the difference of curvature; the second one is in the form of thermodynamics. The interaction does work on the pore wall, resulting in deformation of the porous material and transforming the free energy of the crystal-solution

system in pores into the strain energy of the pore wall. Without considering dissipation, the whole strain energy of the pore wall comes from the internal energy of crystal-solution system. For linear poroelastic materials, the constitutive equations are derived from the energy balance of the pore material, cf. Eqs. (1.53)-(1.58).

6.1.2 Crystallization pressure during crystal growth in pores

The driving force for AFt crystallization is the supersaturation of the corresponding solute in pore solution, which is the deviation of chemical potential of solute relative to thermodynamic equilibrium state. Thus, there should be a difference between the chemical potentials of AFt crystal and liquid solution for AFt crystallization,

$$\mu_{\mathrm{sol}}\left(P_{\mathrm{L}}, T, \beta_{\mathrm{AFt}}\right) > \mu_{C}\left(P_{\mathrm{C}}, T\right) \ : \text{ AFt formation} \tag{6.10}$$

The thermodynamic equilibrium in Eq. (6.4) gives a theoretical supersaturation index of solute β_i which equilibrates with AFt crystal carrying a crystal pressure P_{C},

$$\beta_i = \exp\left[\frac{\overline{V}_{\mathrm{C}}}{RT}\left(P_{\mathrm{C}} - P_{\mathrm{L}}\right)\right] \approx \exp\left(\frac{\overline{V}_{\mathrm{C}}}{RT}P_{\mathrm{C}}\right) \tag{6.11}$$

Hence, the chemical potential difference in Eq. 6.10 could be restated as the oversaturation condition,

$$\beta > \beta_i \tag{6.12}$$

Here the term β represents the real supersaturation of solute in pore solution β_{AFt}. In the following the β_{AFt} is simplified as β providing no further indication is given.

For crystallization in a cylindrical pore, the different confined conditions in the radial and axial directions provide two different crystal pressures P_{C} and $P_r^{'}$ and their associated imaginary supersaturation indexes β_p and β_r at these two directions, cf. Figure 6.2. For simplification, the interface between the pore wall and the solution film is called the crystal-solid interface, while the interface between the crystal and the solution in the axial direction is called the crystal-liquid interface. On the one hand, the crystal growth at the crystal-solid interface is limited by the pore wall while the growth at the crystal-liquid interface is free; on the other hand, the supersaturation indexes in equilibrium with crystal pressure are different due to the different limits on the two interfaces.

For the growth at the crystal-liquid interface, the related theoretical supersaturation index β_r should be less than the supersaturation of solute β. The mechanical balance and

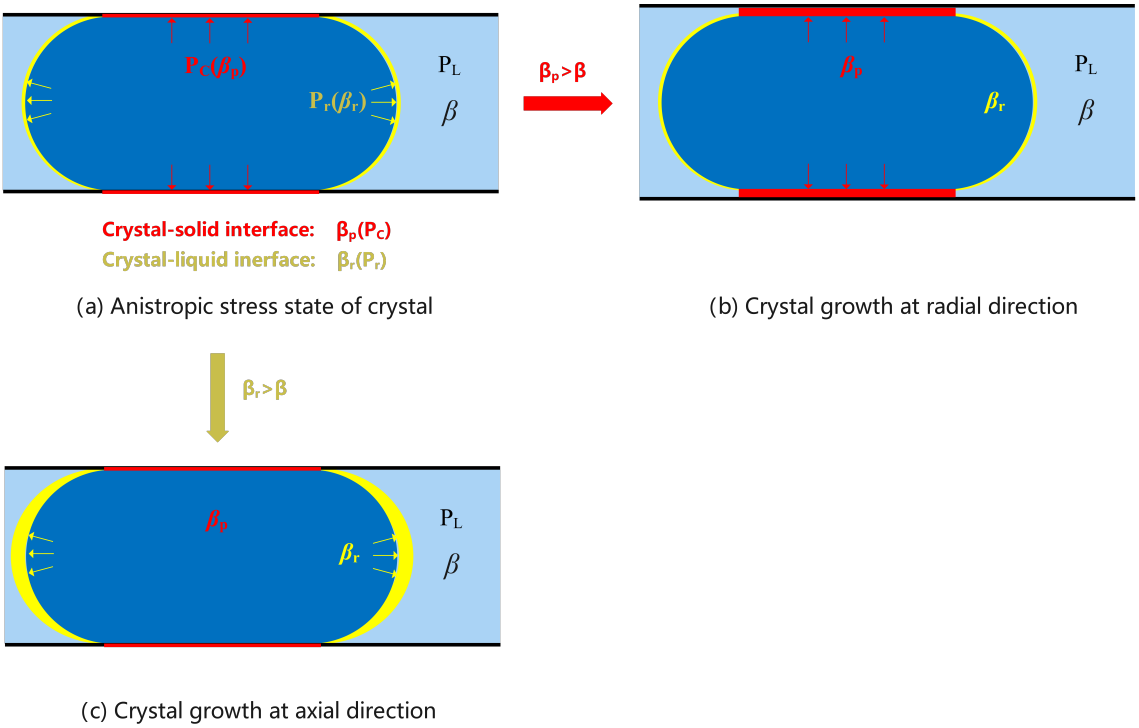

Figure 6.2 Anisotropic stress state of AFt crystal (a) and crystal growth at the radial direction (b) and crystal growth at the axial direction. P_C and P_r are the pressures of AFt crystal crystal at the crystal-solid interface and crystal-liquid interface, P_L is the pressure of liquid solution, β_p and β_r are the associated supersaturation indexes of AFt crystal related to crystal pressures at the crystal-solid interface and crystal-liquid interface, and β is supersaturation index of solute in the pore solution.

thermodynamic equilibrium at the crystal-liquid interface write,

$$P_r = P_L + \frac{2\gamma_{CL}}{r} \tag{6.13a}$$

$$P_r = P_L + \frac{RT}{\overline{V}_C}\ln(\beta_r) \tag{6.13b}$$

Eliminating P_r and P_L between Eq. (6.13a) and (6.13b) can derive,

$$\frac{RT}{\overline{V}_C}\ln(\beta_r) = \frac{2\gamma_{CL}}{r} \tag{6.14}$$

Eq. (6.14) show that, the associated supersaturation index β_r, which is the required supersaturation to equilibrate with AFt crystal pressure P_r at the crystal-liquid interface, depends on the radius of AFt crystal is precipitating.

For the AFt growth at crystal-solid interface, β_p is no more than β. The thermody-

namic equilibrium writes,

$$P_{\mathrm{C}} = P_{\mathrm{L}} + \frac{RT}{\overline{V}_{\mathrm{C}}} \ln\left(\beta_p\right) \approx \frac{RT}{\overline{V}_{\mathrm{C}}} \ln\left(\beta_p\right) \tag{6.15}$$

6.1.3 Deformation of porous material

The crystal growth at two interfaces leads to the change on the volume fraction occupied by AFt crystal, ϕ_{C}, expressed as[223],

$$\phi_{\mathrm{C}} = \phi_0 S_{\mathrm{C}} + \varphi_{\mathrm{C}} \tag{6.16}$$

where the first term $\phi_0 S_{\mathrm{C}}$ on the right side is the volume fraction filled by crystal phase before any deformation, accounting for the volume change by the invasion of the porous volume occupied by crystal (the crystal growth at the crystal-liquid interface) phase under the action of the surface tension γ_{CL} between the crystal and solution, while the last term φ_{C} accounts for the deformation of pore space, which is induced by the pressure of crystal phase applied on the pore walls and related to the the crystal growth at the crystal-solid interface.

The formation of AFt crystals n_{C} in pores could also be splitted into two parts: the newly formed AFt content in the pore invasion process by accretion of new crystals at the crystal-solid interface n_p, and in the pore deformation at the crystal-liquid interface n_r,

$$n_{\mathrm{C}} = n_p + n_r \tag{6.17}$$

These two parts of formed AFt crystal are presented as the red lines in Figure 6.2b and the yellow binds in Figure 6.2c and related to S_{C} and φ_{C}, respectively,

$$\phi_0 S_{\mathrm{C}} = \overline{V}_{\mathrm{C}} n_r \tag{6.18a}$$

$$\varphi_{\mathrm{C}} = \overline{V}_{\mathrm{C}} n_p \tag{6.18b}$$

(a) Pore invasion process

According to Eq. (6.14), a higher pore size leads to a smaller supersaturation index β_r, which allows a lower concentrated solution for AFt crystallization. Thus, it is reasonable to assume that AFt starts the crystallization from the biggest pores to the smallest ones during the pore invasion process. Under such assumption, the crystal saturation S_{C} is

Table 6.1 Typical values of a and m in Van Genuchten model[224] for cement paste, mortar and concrete[121].

Parameter	Cement paste	Mortar	Concrete
a (nm)	16	156	128
m (-)	0.44	0.25	0.38

related to the space of pores lager than a given size r,

$$S_C = 1 - S(r) \tag{6.19}$$

where the function $S(r)$ representing the volume fraction occupied by pore having a pore entry radius lower than r. Usually, $S(r)$ is characterized by MIP methods. Here, the thickness of the solution film is neglected, i.e., the entry radius of the pore equals the curvature radius of the crystal at the crystal-solid interface. $S(r)$ is calibrated from Van Genuchten model[224] as,

$$S(r) = \left(1 + \left(\frac{a}{r}\right)^{\frac{1}{1-m}}\right)^{-m} \tag{6.20}$$

where a and m are parameters dependent on the type of materials (cement paste, mortar, or concrete) and mixture ratio, and their typical values are given in Table 6.1.

An example of the volume fraction curve, $S(r)$, which results from the pore size

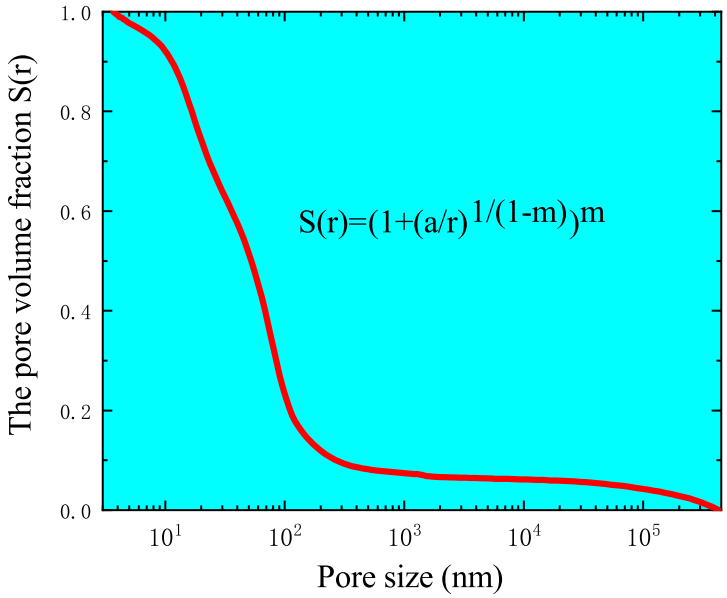

Figure 6.3 Evolution of the pore volume fraction $S(r)$ with the pore radius.

distribution of cement paste specimen without heating before immersion in experimental Part II measured by MIP (see Section 4.2.1 and the black line in Figure 4.14), in terms of pore size r, is presented in Figure 6.3.

(b) Pore deformation process

The partial porosity change φ_C is a fraction of overall porosity change φ. Under a isotropic deformation process, the proportional ratio between φ_C and φ could be assumed as the saturation degree of crystal phase S_C,

$$\varphi_C = S_C \varphi \tag{6.21}$$

According to Eq. (1.37), the overall porosity change φ leads to the volume dilation of porous material. An assumption that the solid matrix is considered as incompressible grains so that $\epsilon_S = 0$, simplifies Eq. (1.37) as,

$$\epsilon = \varphi \tag{6.22}$$

Combining Eq. (6.18b), (6.21)-(6.22) provides a relation between AFt formation at

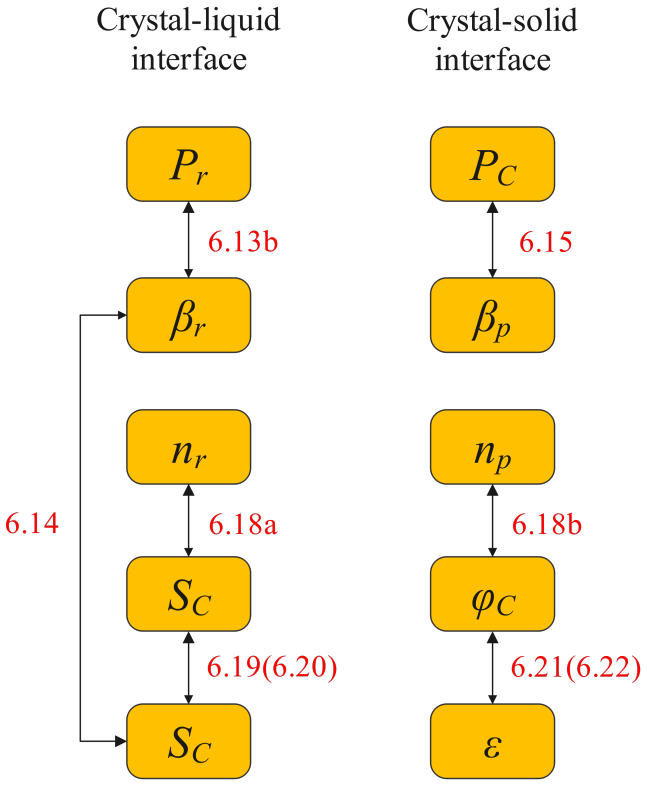

Figure 6.4 Relationship of variables in Section 6.1. The numbers represent the Equation, and the number in the brackets is the supplementary equation.

the crystal-solid interface n_p and the overall volumetric strain ϵ,

$$n_p = \frac{S_{\mathrm{C}}}{\overline{\overline{V}}_{\mathrm{C}}}\epsilon \tag{6.23}$$

6.1.4 Summary

For clarity, Figure 6.4 depicts the variables in this section and their relationship through equations. Each line linking two variables in Figure 6.4 represents an equation bridging these two variables. From Figure 6.4, there are 10 variables (five at the crystal-liquid interface: P_r, β_r, n_r, S_c, r; and five at the crystal-liquid interface: P_{C}, β_p, n_p, φ_{C}, ϵ) and 7 equations in Section 6.1. Hence, we need three more equations to solve the problems.

6.2 Kinetics of AFt crystallization in pores

6.2.1 Kinetic law for AFt formation

The crystallization process can be divided into three stages in this study: (1) achieving the supersaturated state through the penetration of sulfate ions; (2) forming the crystal's initial clusters or nuclei, called nucleation; and (3) growing nuclei to larger crystals. It is believed that the surface of hydrates could provide enough nuclei for ettringite growth due to the existence of hydration products, such as AFt and CH crystal. So the nucleation stage is achieved during a negligible duration of time.

As aforementioned, the supersaturation, β, is the driving force for crystal growth and it influences the formation rate of AFt crystals. Besides, the rate is also related to the reactive surface area of the AFt crystal A_{AFt}. A general form of the growth rate of ettringite can be written as[225],

$$R_{\mathrm{AFt}} = \frac{\mathrm{d}n_{\mathrm{C}}}{\mathrm{d}t} = k_0 A_{\mathrm{AFt}} f(\beta) \tag{6.24}$$

where k_0 is the rate constant dependent on temperature, and $f(\beta)$ describes the functional dependence of generation rate R_{AFt} on β. The function $f(\beta)$ accounts for the important change in the rate with the deviation from thermodynamic equilibrium (β=1). Thus one restriction in thermodynamics must be satisfied,

$$f(\beta = 1) = 0 \tag{6.25}$$

The $f(\beta)$ function depends on the reaction mechanism of dissolution/precipitation of AFt crystals. Normally, this function is determined from experimental kinetic rate data.

Table 6.2 Effective reaction order n for different reaction mechanisms of crystal growth[226].

n	Probable mechanisms
1	Volume diffusion; Adsorption; Volume diffusion + Adsorption
1-2	Combined mechanisms such as: Adsorption + Surface diffusion; Adsorption; Integration; Volume diffusion + Surface diffusion; Volume diffusion + Integration; Volume diffusion + Polynucleation
2	Surface diffusion; Integration; Surface diffusion + Integration
>2	Polynucleation growth; Polynucleation + Spiral growth; Polynucleation dissolution; Spiral dissolution controlled by surface diffusion and/or detachment; Polynucleation + Spiral dissolution

An empirical form of the function $f(\beta)$ is presented[220],

$$f(\beta) = \sigma_{\mathrm{AFt}}^{n} \tag{6.26}$$

Here the term n is the effective reaction order, and σ_{AFt} is the relative supersaturation, which is defined as,

$$\sigma_{\mathrm{AFt}} = (\beta)^{1/\upsilon} - 1 \tag{6.27}$$

where the stoichiometric coefficient υ is the total number of ions per formula unit of the electrolyte, equal to 15 for AFt crystal. Accordingly, the effective reaction order, n, can be deduced from the logarithmic form of Eq. (6.26),

$$n = \frac{\partial \ln f(\sigma)}{\partial \ln \sigma_{\mathrm{AFt}}} \tag{6.28}$$

The value of n depends on the reaction mechanism of dissolution/precipitation of crystals. The relation between n and possible reaction mechanism(s) are given in Table 6.2[226]. The incorporation of ions into the crystal structure occurs through at least two mechanisms: diffusion-controlled transport of ions to the growing crystal surface and surface-mediated processes. According to Burton[227] and Nielsen[228], the latter may be broken down into a series of rate-determined phases: convective transport of a growth unit to

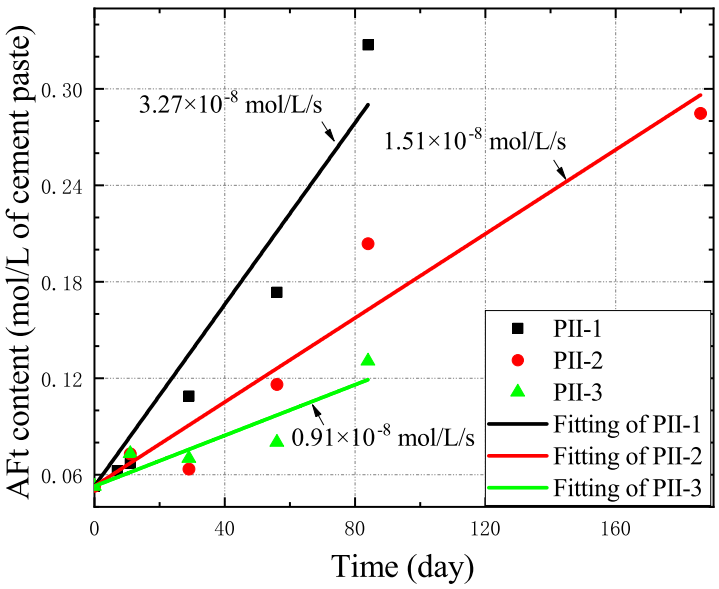

Figure 6.5 AFt content in cement layer specimens exposed to three conditions in terms of exposure time and the fitting rates.

the surface, diffusion from the solution to the crystal surface, adsorption at the hydrated adsorption layer, two-dimensional diffusion within the hydrated adsorption layer, adsorption at the step, one-dimensional diffusion along the step, integration at the kink site on the step, and finally, partial or complete dehydration of the lattice ion. The first four phases are examples of transport processes, whereas the final four are examples of surface reactions[229].

In Part II experiments, we measured the kinetic process of ettringite crystallization in cement pastes exposed to five conditions. Considering the difficulty in the estimation of supersaturation of AFt under combined ESA and DEF conditions (PII-4/5), here we only use the kinetic data on three ESA conditions (PII-1/2/3). Due to a lack of understanding and for the sake of simplification, it is assumed here that the effective surface area A_{AFt} is constant, so that the AFt formation rates are constant. Note that the diffusion process is ignored for 2 mm thick specimens so that the ionic concentrations in pore solutions are equal to the stable concentrations in the test solutions. Thus, Eq. (6.24) can be rewritten by combining Eq. (6.27),

$$\mathrm{R}_{\mathrm{AFt}} = k_1 \sigma_{\mathrm{AFt}}^{n} \quad \text{with} \quad k_1 = k_0 A_{\mathrm{AFt}} \tag{6.29}$$

The kinetic data and the fitting rates are presented in Figure 6.5. The estimated supersaturation in Section 3.2.3 and fitting kinetic rates in three conditions are given in Table 6.3. Figure 6.6 plots the logarithmic of estimated growth rate as a function of $\ln\sigma_{\mathrm{AFt}}$, giving a slope of 1.90 suggesting a combined crystal growth mechanism. Based on the fitting results in Figure 6.6, a kinetic law for ettringite crystallization is stated as,

$$\mathrm{R}_{\mathrm{AFt}} = k_{\mathrm{AFt}} \left(\sqrt[15]{\beta} - 1 \right)^{1.90} \tag{6.30}$$

The kinetic parameter k_{AFt}, the combination of kinetic constant k_0 with effective surface area A_{AFt}, is fitted as 1.40×10^{-9} mol/L/s. Thus, k_{AFt} is influenced by temperature (k_0), and initial ettringite content and size (A_{AFt}).

Table 6.3 Estimated supersaturation indexes of AFt and fitting rates in three conditions.

Condition	Supersaturation index	Growth rate (mol/L/s)
PII-1	8.34×10^{11}	3.27×10^{-8}
PII-2	2.09×10^{9}	1.51×10^{-8}
PII-3	5.79×10^{8}	0.91×10^{-8}

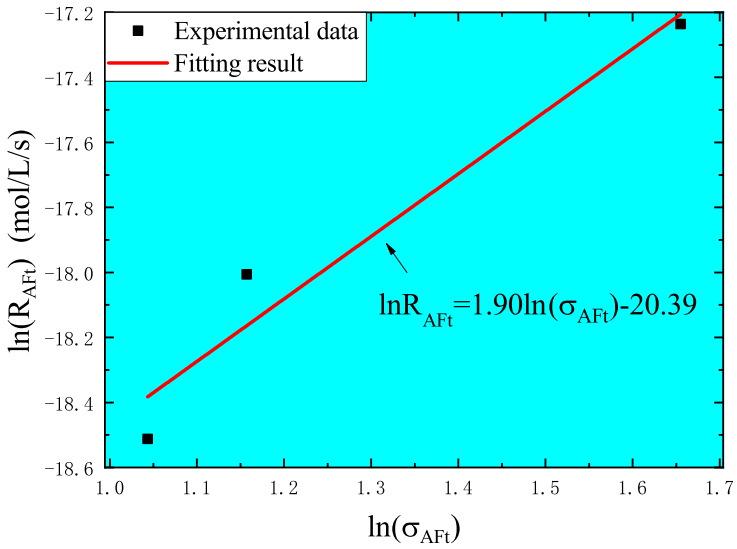

Figure 6.6 Logarithm of the growth rate of AFt R_{AFt} in terms of the logarithm of the relative supersaturation σ_{AFt}.

6.2.2 Kinetic law of AFt growth in pores

AAs stated before, the supersaturation is a measure of the departure of free energy from an equilibrium state. At the crystal-liquid interface and crystal-solid interface, the pressure of AFt crystal P_r and P_C are elevated by the crystal-liquid interface tension and interaction between AFt crystal and solid matrix, thus these two pressure are larger than the pressure of liquid solution P_L. Therefore, the equilibrium states of crystal at two interfaces are changed and should be in equilibrium with a supersaturated solution with a supersaturation index of β_r and β_p, respectively. Hence, the relative supersaturation indexes at these two interfaces, σ_r and σ_p, are written as,

$$\sigma_r = \left(\frac{\beta}{\beta_r}\right)^{1/15} - 1 \tag{6.31a}$$

$$\sigma_p = \left(\frac{\beta}{\beta_p}\right)^{1/15} - 1 \tag{6.31b}$$

Substituting Eq. (6.31) into Eq.(6.30), the kinetic laws at two interfaces can be formulated under the form:

$$\frac{\mathrm{d}n_r}{\mathrm{d}t} = k_r\left(\sqrt[15]{\frac{\beta}{\beta_r}} - 1\right)^{1.90} \tag{6.32a}$$

$$\frac{\mathrm{d}n_p}{\mathrm{d}t} = k_p \left(\sqrt[15]{\frac{\beta}{\beta_p}} - 1 \right)^{1.90} \tag{6.32b}$$

where k_r and k_p are the kinetic parameters related to the active surface areas at two interfaces. Here for the sake of simplification, we assume that (1) the active surface area of AFt crystal at the crystal-liquid interface is constant so that the kinetic parameter k_r is a constant; (2) the surface area of AFt crystal at the crystal-solid interface is proportional to the crystal saturation so that $k_p = S_{\mathrm{C}} k_p^{'}$, where $k_p^{'}$ is a constant dependent on temperature. Combining Eq. (6.18a) and (6.32a) gives the kinetic law of the saturation degree of crystal, S_{C}, during the pore invasion process,

$$\frac{\mathrm{d}S_{\mathrm{C}}}{\mathrm{d}t} = \frac{\overline{V}_{\mathrm{C}}}{\phi_0} k_r \left(\sqrt[15]{\frac{\beta}{\beta_r}} - 1 \right)^{1.90} = K_r \left(\sqrt[15]{\frac{\beta}{\beta_r}} - 1 \right)^{1.90} \tag{6.33}$$

Combining Eq. (6.18b) and (6.32b) provides the kinetic law of the partial porosity change, φ_{C}, during the pore deformation process,

$$\frac{\mathrm{d}\varphi_{\mathrm{C}}}{\mathrm{d}t} = \overline{V}_{\mathrm{C}} S_{\mathrm{C}} k_p^{'} \left(\sqrt[15]{\frac{\beta}{\beta_p}} - 1 \right)^{1.90} = K_p S_{\mathrm{C}} \left(\sqrt[15]{\frac{\beta}{\beta_p}} - 1 \right)^{1.90} \tag{6.34}$$

The terms K_r and K_p are two kinetic constants in the pore invasion and pore deformation processes, respectively. Substituting Eq. (6.21) and (6.22) into Eq.(6.34) provides us a kinetic law of dilation of porous material ϵ,

$$\frac{\mathrm{d}\epsilon}{\mathrm{d}t} = K_p \left(\sqrt[15]{\frac{\beta}{\beta_p}} - 1 \right)^{1.90} \tag{6.35}$$

In addition, the dilation could also be expressed through a poromechanical approach as in Eq .(1.53). Under a stress-free condition without external loading, Eq .(1.53) is simplified as,

$$K\epsilon = bP_{\mathrm{C}} S_{\mathrm{C}} \tag{6.36}$$

Substituting Eq. (6.15) and (6.33) into (6.36) produces another kinetic law of ϵ,

$$\frac{\mathrm{d}\epsilon}{\mathrm{d}t} = \frac{bRT}{\overline{V}_{\mathrm{C}}} \frac{K_r}{K} \ln\left(\beta_p\right) \left(\sqrt[15]{\frac{\beta}{\beta_r}} - 1 \right)^{1.90} \tag{6.37}$$

Eliminating dϵ/dt between Eq. (6.35) and (6.37) provides a estimation of β_p (P_C),

$$\frac{1}{\ln(\beta_p)}\left(\sqrt[15]{\frac{\beta}{\beta_p}}-1\right)^{1.90}=\frac{bRT}{V_C}\frac{1}{K}\frac{K_r}{K_p}\left(\sqrt[15]{\frac{\beta}{\beta_r}}-1\right)^{1.90} \tag{6.38}$$

Eq. (6.38) is a transcendental equation, showing that $\beta_p(P_C)$ depends on the bulk modulus K, the ratio between two kinetic constants K_r/K_p, the supersaturation of solute β and the radius $r(\beta_r)$ of pores where AFt crystal is forming.

6.2.3 Summary

In this section, we added two equations (6.33) and (6.34) and three variables (β, K_r, K_p). And the updated relationships among variables are presented in Figure 6.7. According to Figure 6.7, we have 13 variables and 10 equations. Indeed, the two kinetic constants, K_r and K_p, are input variables (parameters), and thus we only require one more equation giving the value of β. In the following next, the value of β is estimated through multi-phase dissolution/precipitation equilibria in the pore solution.

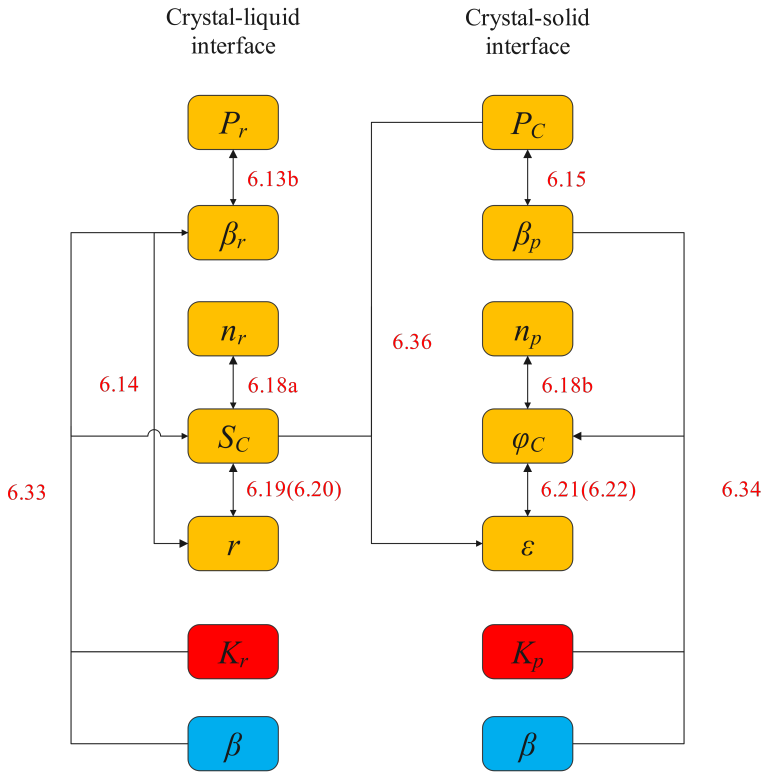

Figure 6.7 Updated relationship of variables in Section 6.1 and 6.2. The numbers represent the Equation, and the number in the brackets is the supplementary equation.

6.3 Supersaturation of AFt in pore solution

6.3.1 Composition of cement hydrates

Before the determination of the supersaturation of AFt, we firstly estimate the initial contents of main hydrates in hardened cement paste. As aforementioned in Section 1.1, ettringite forms from the chemical reactions between sulfates and aluminium hydrates. Several assumptions are made to simplify the calculation without loss of generality: (1) the cement hydrates consist of CH, CSH, C_4AH_{13} (hydrogarnet, the most common hydrates in ordinary cement paste[16]) and AFt, i.e. no $C_4\bar{S}H_{12}$ is formed; (2) the free Si, Ca and Al dissolved in the pore solution are neglected; (3) the Ca/Si ratio of CSH is 1.7. The initial contents of cement hydrates are evaluated from the mole balance equations for oxides,

$$n_{CaO} = CH + 1.7n_{CSH} + 4n_{C_4AH_{13}} + 6n_{AFt} \tag{6.39a}$$

$$n_{Al_2O_3} = n_{C_4AH_{13}} + n_{AFt} \tag{6.39b}$$

$$n_{SO_3} = 3n_{AFt} \tag{6.39c}$$

$$n_{SiO_2} = n_{CSH} \tag{6.39d}$$

where n_i stands for the mole content of i per liter of CBM. The oxides contents (n_{CaO}, $n_{Al_2O_3}$, n_{SO_3} and n_{SiO_2}) are estimated from the oxide components of cement. Solving the above equations gives us the contents of cement hydrates at the initial state (t=0),

$$n_{CSH} = n_{SiO_2} \tag{6.40a}$$

$$n_{AFt} = \frac{1}{3}n_{SO_3} \tag{6.40b}$$

$$n_{C_4AH_{13}} = n_{Al_2O_3} - \frac{1}{3}n_{SO_3} \tag{6.40c}$$

$$n_{CH} = n_{CaO} - 1.7n_{SiO_2} - 3n_{Al_2O_3} - n_{SO_3} - n_{C_4AH_{13}} \tag{6.40d}$$

When the CBM is exposed to a chloride-bearing solution, the primary C_4AH_{13} is transformed into Friedel's salt($C_3ACaCl_2H_{10}$). Here we assume that this transformation happens to all the C_4AH_{13} at a much faster rate than the transformation from C_4AH_{13} into AFt. This assumption is confirmed by the experimental results in Figure 3.4, Figure 3.6, and Figures C.7-C.8. Thus, the chemical reaction for ettringite formation and initial

cement hydrates are rewritten for the chloride case,

$$C_3ACaCl_2H_{10} + 2Ca^{2+} + 3SO_4^{2-} \longrightarrow C_6A\overline{S}_3H_{32} + 2Cl^- \tag{6.41}$$

and

$$n_{CSH} = n_{SiO_2} \tag{6.42a}$$

$$n_{AFt} = \frac{1}{3}n_{SO_3} \tag{6.42b}$$

$$n_{FS} = n_{Al_2O_3} - \frac{1}{3}n_{SO_3} \tag{6.42c}$$

$$n_{CH} = n_{CaO} - 1.7n_{SiO_2} - 3n_{Al_2O_3} - n_{SO_3} - n_{FS} \tag{6.42d}$$

6.3.2 Supersaturation of AFt

The estimation of supersaturation of ettringite is based on the multi-phase equilibria with pore solution. As shown in Figure 6.8, portlandite, hydrogarnet or Freidel's slat (for mixed sulfate and chloride solution), and ettringite keep dissolution-precipitation equilibria with pore solution, releasing ions from crystals as supersaturation smaller than 1, and incorporating ions into crystals as supersaturation larger than 1. The dissolution-precipitation equilibria of these phases write,

$$C_3A \cdot 3C\overline{S} \cdot H_{32}(AFt) \rightleftharpoons 6Ca^{2+} + 2Al(OH)_4^- + 3SO_4^{2-} + 4OH^- \tag{6.43a}$$

$$C_4AH_{10}(\text{hydrogarnet}) \rightleftharpoons 4Ca^{2+} + 2Al(OH)_4^- + 6OH^- \tag{6.43b}$$

$$C_3ACaCl_2H_{10}(\text{Friedel's salt}) \rightleftharpoons 4Ca^{2+} + 2Al(OH)_4^- + 4OH^- + 2Cl^- \tag{6.43c}$$

$$CH(\text{portlandite}) \rightleftharpoons Ca^{2+} + 2OH^- \tag{6.43d}$$

Accordingly, the saturation indexes of these phases (β_i) in the pore solution are defined as,

$$\beta = \left(a_{Ca^{2+}}\right)^6 \left(a_{Al(OH)_4^-}\right)^2 \left(a_{SO_4^{2-}}\right)^3 \left(a_{OH^-}\right)^4 \Big/ K_{AFt} \tag{6.44a}$$

$$\beta_{C_4AH_{13}} = \left(a_{Ca^{2+}}\right)^4 \left(a_{Al(OH)_4^-}\right)^2 \left(a_{OH^-}\right)^6 \Big/ K_{C_4AH_{13}} \tag{6.44b}$$

$$\beta_{CH} = a_{Ca^{2+}} \left(a_{OH^-}\right)^2 \Big/ K_{CH} \tag{6.44c}$$

where a_i stands for the activity of i ion in the pore solution and K_j stands for the sol-

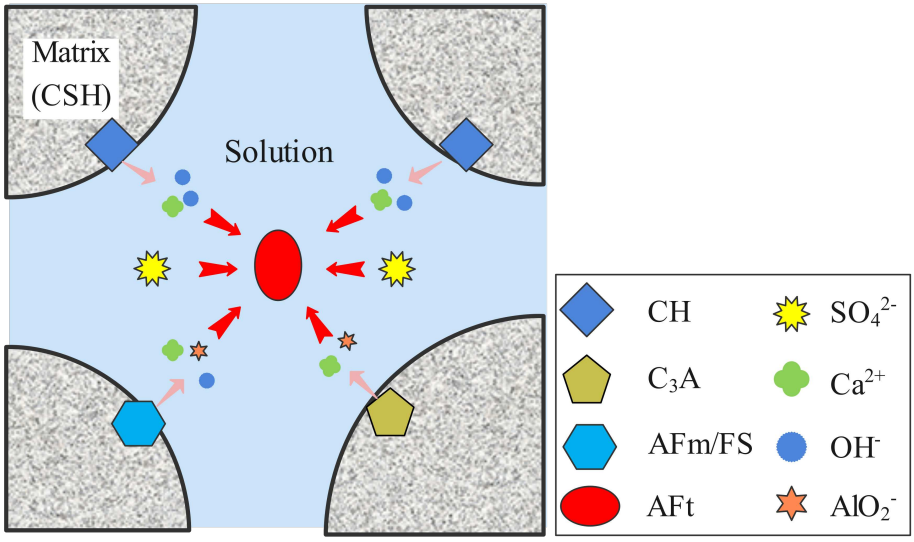

Figure 6.8 Scheme of multi-phase dissolution/precipitation equilibria with pore solution. The pink arrows represent the dissolution of solid phases, and the red arrows stands for the precipitation of solid phases.

ubility constant of phase j. Here the ionic activity is approximated to its concentration c_i in mol/L. Besides, the ion concentrations must satisfy the electroneutrality of the pore solution,

$$2c_{Ca^{2+}} + c_{Na^{+}} = 2c_{SO_4^{2-}} + c_{Al(OH)_4^{-}} + c_{OH^{-}} \tag{6.45}$$

where the concentration of sodium and sulfate ions, $c_{Na^{+}}$ and $c_{SO_4^{2-}}$, in the pore solution are considered to be equal to the corresponding concentrations in the exterior solution when neglecting the ionic diffusion between cement-based materials and exterior solution,

$$c_{Na^{+}} = c_{Na^{+}}^{ext}; \quad c_{SO_4^{2-}} = c_{SO_4^{2-}}^{ext} \tag{6.46}$$

Here we have 6 equations (Eqs. (6.44)-(6.46)) and 8 unknowns: 5 ionic concentrations ($c_{Ca^{2+}}$, $c_{Na^{+}}$, $c_{SO_4^{2-}}$, $c_{Al(OH)_4^{-}}$ and $c_{OH^{-}}$) and 3 saturation indexes (β_{AFt}, $\beta_{C_4AH_{13}}$ and β_{CH}). Two more equations are required to determine the saturation index of ettringite. Now let us make a further discussion on the dissolution/precipitation of CH. As mentioned in Section 1.1.1 and Section 3.3.3, the kinetic constants of ettringite and portlandite are given as 7.08×10^{-13} mol/(m^2·s)[34] and 8.98×10^{-4} mol/(m^2·s)[221], respectively. Considering the enormous magnitude difference, it is reasonable to assume that the portlandite is at its solubility limit before it is depleted. Once the portlandite is depleted, its saturation index is smaller than 1,

$$n_{CH} \geqslant 0; \quad \beta_{CH} \leqslant 1; \quad n_{CH}\left(\beta_{CH} - 1\right) = 0 \tag{6.47}$$

Under the same assumption, the aluminum hydrate C_4AH_{13} is at its solubility limit once it is not depleted and otherwise $\beta_{C_4AH_{13}} < 1$,

$$n_{C_4AH_{13}} \geqslant 0; \quad \beta_{C_4AH_{13}} \leqslant 1; \quad n_{C_4AH_{13}} \left(\beta_{C_4AH_{13}} - 1\right) = 0 \tag{6.48}$$

For the combined sulfate and chloride solution, hydrogarnet (C_4AH_{10}) is replaced by Friedel's salt ($C_3ACaCl_2H_{10}$) and the chloride concentration c_{Cl^-} is an extra unknown. Therefore, Eqs. (6.44), (6.46) are re-arranged as,

$$\beta = \left(a_{Ca^{2+}}\right)^6 \left(a_{Al(OH)_4^-}\right)^2 \left(a_{SO_4^{2-}}\right)^3 \left(a_{OH^-}\right)^4 \Big/ K_{AFt} \tag{6.49a}$$

$$\beta_{FS} = \left(a_{Ca^{2+}}\right)^4 \left(a_{Al(OH)_4^-}\right)^2 \left(a_{Cl^-}\right)^2 \left(a_{OH^-}\right)^4 \Big/ K_{FS} \tag{6.49b}$$

$$\beta_{CH} = a_{Ca^{2+}} \left(a_{OH^-}\right)^2 \Big/ K_{CH} \tag{6.49c}$$

and

$$2c_{Ca^{2+}} + c_{Na^+} = 2c_{SO_4^{2-}} + c_{Al(OH)_4^-} + c_{OH^-} + c_{Cl^-} \tag{6.50}$$

In the same way, Friedel's salt is assumed to be at the solubility limit when it is not depleted,

$$n_{FS} \geqslant 0; \quad \beta_{FS} \leqslant 1; \quad n_{FS} \left(\beta_{FS} - 1\right) = 0 \tag{6.51}$$

And the chloride concentration is assumed to be equal to the chloride concentration in external solution,

$$c_{Cl^-} = c_{Cl^-}^{ext} \tag{6.52}$$

6.3.3 Summary

In this section, the composition of cement hydrates is simplified as four main phases: CSH, CH, AFt, and hydrogarnet (for ESA condition)/Friedel's salt (for combined ESA and chloride condition), and their initial contents are calculated from the mass conservation of oxides. The supersaturation of AFt is obtained from multi-phase dissolution-precipitation equilibria with pore solution (the supersaturation indexes of CH and hydrogarnet//Friedel's salt was assumed to be fixed at 1), electroneutrality of pore solution and equal concentrations of Na^+/K^+, Cl^- and SO_4^{2-} between pore solution and exterior solution. In this section, the input variables are three ion concentration (c_{Na^+}, $c_{SO_4^{2+}}$, c_{Cl^-}) and output variable is the supersaturation of AFt.

6.4 Damage model for solid matrix

A damage model is retained here to simulate the two-stage expansion behavior of CBM submitted to the pore pressure $\sigma_{\mathrm{p}} = S_{\mathrm{C}}P_{\mathrm{C}} + S_{\mathrm{L}}P_{\mathrm{L}}$. In this study, the CBM is assumed to be saturated by the liquid and solid crystal and no gas phase exists in the porous space, i.e., unsaturated situations are not taken into consideration. The mechanical behavior of the CBM is described by the effective stress tensor $\sigma_{ij}^{'}$ and the corresponding strain tensor ε_{ij}. The damage theory is adopted to describe the stress-strain relationship, which is given by [230-231],

$$E_{\mathrm{d}}\varepsilon_{ij} = (1+\nu)\sigma_{ij}^{'} - \nu\sigma_{kk}^{'}\delta_{ij} \tag{6.53}$$

where ν is the Poisson's ratio, $\sigma_{kk}^{'}$ is the trace of strain tensor, δ_{ij} is Kronecker index, and E_{d} is the current Young's modulus, defined as,

$$E_{\mathrm{d}} = (1-d)E \tag{6.54}$$

Here the term E is the Young's modulus of material before damage, and d is the damage parameter. A tensile damage model[51] is illustrated in Figure 6.9, composed of two stages: elastic (0-1) and damage (1-2) ranges. Define a loading function of damage as,

$$f(\varepsilon_{ij}, \kappa) = \tilde{\varepsilon}_{ij} - \kappa \tag{6.55}$$

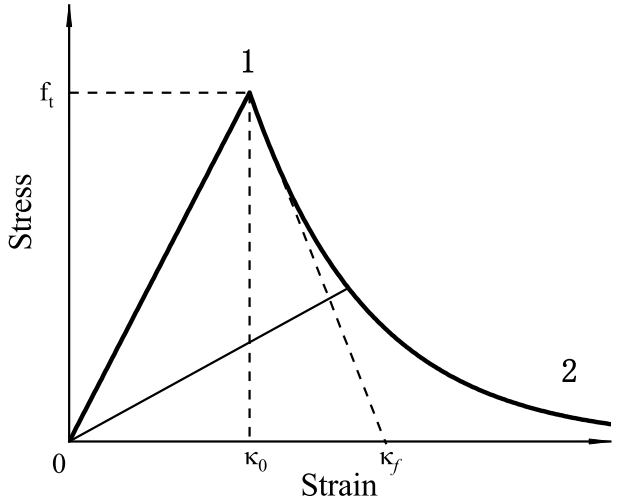

Figure 6.9 Typical stress-strain curve of cement-based materials under uniaxial tensile load[51].

where $\tilde{\varepsilon}_{ij}$ is equivalent strain, which is usually defined as the positive square root of the sum of square of principal strains. The term κ is the largest equivalent strain reached in the previous loading history up to the current state, expressed with respect to the current equivalent strain,

$$\kappa = \kappa_0, \quad f(\varepsilon_{ij}, \kappa) = \tilde{\varepsilon}_{ij} - \kappa_0 \qquad \text{if } \tilde{\varepsilon}_{ij} < \kappa_0 \tag{6.56a}$$

$$\kappa = \varepsilon_{ij}, \quad f(\varepsilon_{ij}, \kappa) = 0 \qquad \text{if } \tilde{\varepsilon}_{ij} \geqslant \kappa_0 \tag{6.56b}$$

where κ_0 is the strain related to the tensile strength f_t of the cement-based material under uniaxial tension load in Figure 6.9, $\kappa_0 = f_\mathrm{t}/E$. Only when the current state reaches the boundary of the elastic range, i.e. $\kappa \geqslant \kappa_0$, damage can increase. A exponential softening law in Figure 6.9 is used to state the function of d in terms of κ,

$$d = 0 \qquad \text{if } \kappa \leqslant \kappa_0 \tag{6.57a}$$

$$d = 1 - \frac{\kappa_0}{\kappa}\exp\left(-\frac{\kappa - \kappa_0}{\kappa_f - \kappa_0)}\right) \qquad \text{if } \kappa > \kappa_0 \tag{6.57b}$$

where κ_f is a parameter associated with the ductility of the response and can be related to the local dissipation density g_t via: $g_\mathrm{t} = f_\mathrm{t}\left(\kappa_f - \kappa_0/2\right)$. The term g_t is the energy dissipation per unit volume of the damaged material under uniaxial tension, and it is estimated through the fracture energy G_f and the crack width w[235],

$$g_\mathrm{t} = \frac{G_f}{w} \tag{6.58}$$

The effective stress tensor is related to the pore pressure through a poromechanical

Table 6.4 Typical values of mechanical parameters for cement paste, mortar and concrete.

Parameter (unit)	Symbol	Cement paste	Mortar/concrete
Young's modulus (GPa)	E	21.7[209]	30.0[209]
Poisson's ratio (-)	ν	0.24[209]	0.26[209]
Porosity (-)	ϕ	0.34[209]	0.23[209]
Biot's coefficient (-)	b	0.69[209]	0.54[209]
Tensile strength (MPa)	f_t	2.0[232]	3.1[233]
Fracture energy (N/m)	G_f	15[233]	75[233]
Crack width (μm)	w	2[234]	3[233]
Local dissipation density (kPa)	g_t	7.5	25.0

approach,

$$\sigma_{ij}^{'} = \sigma_{ij} + b_d(P_{\mathrm{C}}S_{\mathrm{C}} + P_{\mathrm{L}}S_{\mathrm{L}})\delta_{ij} \tag{6.59}$$

Here σ_{ij} is the stress tensor induced by the external load, and b_d is the Biot's coefficient of the damaged material, which is related to Biot's coefficient of undamaged material b and the damage parameter d,

$$b_d = b + d(1 - b) \tag{6.60}$$

The typical values of mechanical properties for CBM are given in Table 6.4.

6.5 Chemo-poromechanical model for ESA expansion

In this model, several assumptions were made to reduce the complexity of the numerical solution: (1) the CBM are considered as water-saturated media, i.e. no air existing in the pore space; (2) AFt crystals crystallize from the biggest pore to the smallest ones; (3) the deformation of the pore space is assumed to be isotropic; (4) the solid matrix is assumed to be incompressible; (5) an exponential relation between AFt supersaturation and AFt formation rate is adopted; (6) the portlandite and hydrogarnet (or Friedel's salt) were at their solubility limits; (7) a uniaxial tensile damage model is applied.

So far, the kinetic laws of pore crystallization, the pore pressure, the pore chemistry, and the damage model constitute the comprehensive chemo-poromechanical modelling for ESA expansion on CBM. This model contains 23 (ESA) or 24 (ESA + chlorides) variables in total: two crystal pressures (P_C and P_r), two theoretical supersaturation indexes (β_p and β_r), two AFt amount (n_p and n_r), saturation degree of AFt crystal (S_C), partial porosity change (φ_C), volume dilation ϵ, pore radius r, four hydrates contents (n_{CSH}, n_{CH},

Table 6.5 Equations for poromechanical model.

Equations/relations	Numbers	Equation number	Involved variables
Thermodynamic equilibrium	2	Eq. (6.13a), (6.15)	P_C, P_r, β_p, β_r
Mechanical balance	1	Eq. (6.13b)	P_r, r
Crystal volume equations	2	Eq. (6.18a), (6.18b)	n_p, n_r, S_C, φ_C
Pore invasion assumption	1	Eq. (6.19)	S_C, r
Deformation assumptions)	1	Eq. (6.21)	φ_C, ϵ
kinetic laws	2	Eq. (6.33), (6.34)	S_C, φ_C, K_p, K_r, β_p, β_r, β
Poroelasticity relation	1	Eq. (6.36)	S_C, P_C, ϵ
Mass conservation of oxides	4	Eq. (6.40) or (6.42)	n_{CSH}, n_{CH}, n_{AFt}, n_{FS} or $n_{C_4AH_{10}}$
Supersaturation indexes	3	Eq. (6.44) or (6.49)	β_{CH}, β, $\beta_{C_4AH_{10}}$ or β_{FS}, $c_{SO_4^{2+}}$, $c_{AlO_2^-}$, c_{Cl^-}
Solubility limits	2	Eq. (6.47), (6.48) or (6.51)	β_{CH}, $\beta_{C_4AH_{10}}$ or β_{FS}
Electroneutrality equation	1	Eq. (6.45) or (6.50)	c_{Na^+}, $c_{Ca^{2+}}$, c_{OH^-}, $c_{SO_4^{2+}}$, $c_{AlO_2^-}$ and c_{Cl^-}
Ion concentrations	2 or 3	Eq. (6.46) ((6.52))	c_{Na^+},$c_{SO_4^{2+}}$ (c_{Cl^-})
Damage model	1	Eq. (6.57)	d
Total	23 or 24	-	23 or 24

n_{AFt}, $n_{C_4AH_{10}}$ or n_{FS}), six ion concentrations (c_{Na^+}, $c_{Ca^{2+}}$, c_{OH^-}, $c_{SO_4^{2+}}$, $c_{AlO_2^-}$ and c_{Cl^-}), three supersaturation indexes (β_{CH}, β, $\beta_{C_4AH_{10}}$ or β_{FS}), and damage parameter (d). Equal number of equations are established in Table 6.5, ensuring that the problem is mathematically closed. In the simulation procedure, two kinetic constants, K_r and K_p, are inputs and the variables are outputs (volumetric strain ϵ is the major output). Besides, the physico-chemical parameters used in this model are listed in Table 6.6.

Table 6.6 Physico-chemical parameters at 25 °C.

Parameter (unit)	Symbol	Value
Molar volume of ettringite (cm^3/mol)	$\overline{V}_C$	710[236]
Surface energy of ettringite(J/m^2)	γ_{CL}	0.1[64]
Solubility of AFt (-)	$\lg K_{AFt}$	-44.55[195]
Solubility of C_4AH_{10} (-)	$\lg K_{C_4AH_{10}}$	-25.40[195]
Solubility of Friedel's salt (-)	$\lg K_{FS}$	-27.10[195]
Solubility of CH (-)	$\lg K_{C_H}$	-5.14[195]
Kinetic coefficient 1 (1/s)	K_r	-
Kinetic coefficient 2 (1/s)	K_p	-

6.6 Simulation of experiments

6.6.1 Cement paste specimens in PII-1/2/3

In the simulation of expansion results in experimental Part II (PII-1, PII-2, and PII-3 conditions), the initial content of hydrates is calculated as: n_{CH} = 4.32 mol/L, n_{CSH} = 3.92 mol/L, n_{AFt} = 0.17 mol/L, $n_{C_4AH_{13}}$ (for pure sulfate case PII-1)= $n_{C_3ACaCl_2H_{10}}$ (for combined sulfate and chlorides cases PII-2/3) = 0.32 mol/L. The sodium sulfate solution and mixed solutions with a high pH value of 13 were renewed to keep a constant ionic concentrations as: c_{OH^-} = 0.1 mol/L, $c_{SO_4^{2-}}$ = 0.104 mol/L, c_{Cl^-} = 0 (PII-1), 0.282 (PII-2), 0.535 (PII-3) mol/L. Two kinetic constants K_r and K_p are calibrated from the expansion curve of the specimen in PII-1 condition as shown in Figure 6.10. The fitting results are: $K_r = 1.8\times10^{-9}$ s^{-1}, $K_p = 1.25\times10^{-10}$ s^{-1}. Then these two parameters are used to predict the expansion curves of specimens in PII-2/3 conditions in Figure 6.10. The simulated expansion curve fits well with the experimental data in the PII-2 condition, while in the PII-3 condition the simulated curve more or less shows a more rapid expansion rate than the measured one.

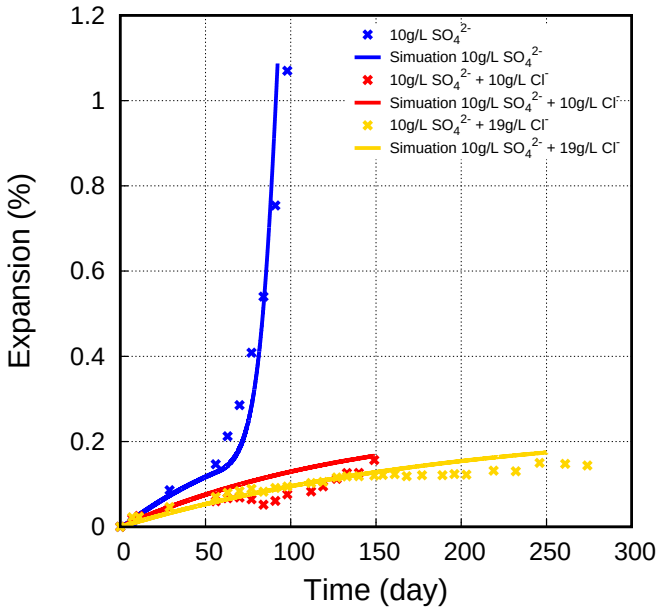

Figure 6.10 Simulation of expansion data of cement layer specimens in PII-1/2/3 condition.

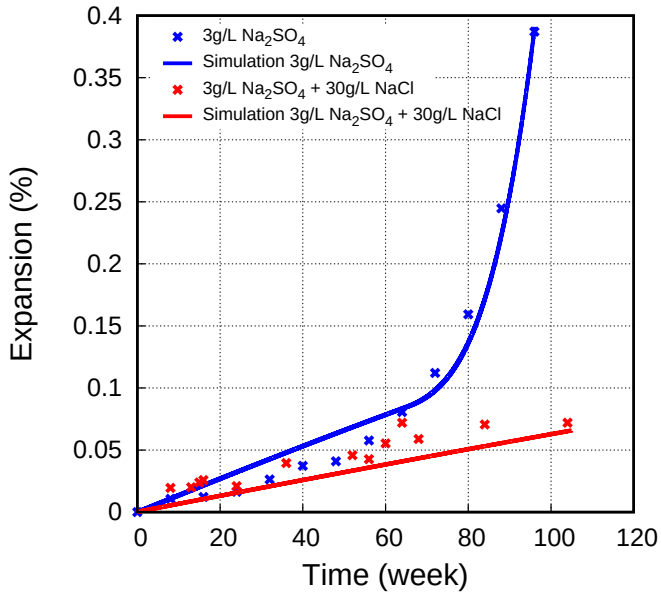

Figure 6.11 Simulation of expansion data of prismetric mortar specimens in two conditions. Pure sulfate data taken from Whittaker[237] and data for combined condition taken from Ukpata et al.[99].

6.6.2 Expansion under combined ESA and chlorides from Ukpata et al.

Ukpata et al.[99] immersed prismatic mortar specimens (25×25×200mm) into a combined sulfate and chloride solution and measured their expansion curve. The specimens were cast in CEM I 42.5R Portland cement with a w/c ratio of 0.5 and sand-to-cement (s/c) ratio of 3 (in weight). The prisms were cured at 20°C for 28d and the test solution was composed of 30g/L NaCl and 3g/L Na_2SO_4. The measured expansion curve was then compared with the expansion data of the same specimens in pure sulfate condition, cf. Figure 6.11. The two parameters, $K_r = 2.0 \times 10^{-10}$ s^{-1} and $K_p = 2.0 \times 10^{-11}$ s^{-1}, are calibrated from the pure sulfate condition and then are applied to predict the swelling of the specimens in combined sulfate and chloride solution. The delay of expansion behavior of mortar specimens by chlorides is well predicted as shown in Figure 6.11.

Figure 6.12 presents the simulated ion concentrations in two conditions. As shown in Figure 6.12a, the addition of chloride lowers the aluminate concentration without alteration of other ions (calcium and sulfate concentrations in Figure 6.12b). This is due to the change of aluminum-phase equilibrium from Eq. (6.48) to Eq. (6.51) with the transformation from hydrogarnet to Friedel's salt, which has a lower solubility constant than hydrogarnet. The lower aluminate concentration leads a smaller AFt supersaturation and

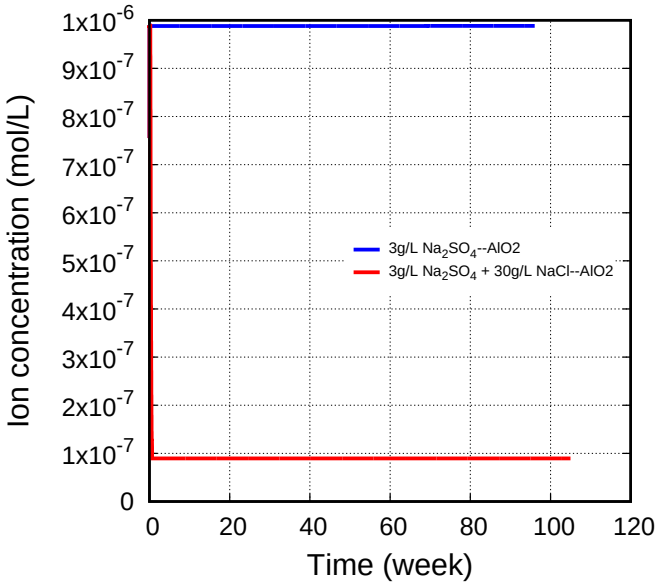

(a)

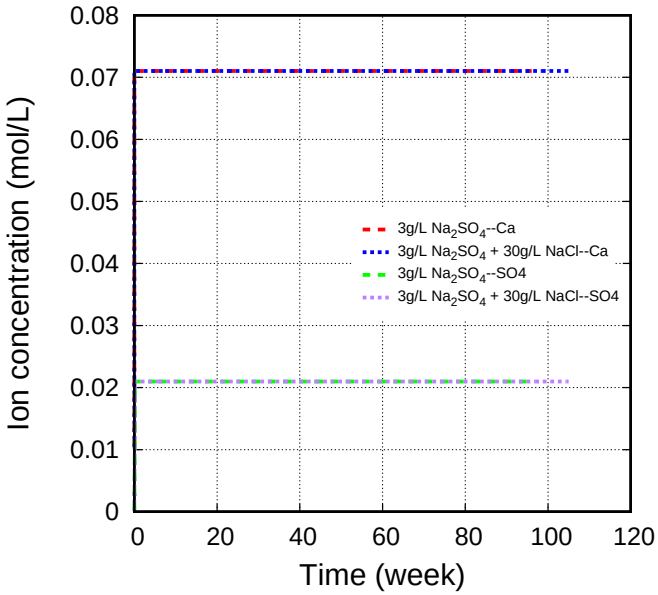

(b)

Figure 6.12 Predicted concentrations of aluminate ion (a) and calcium and sulfate ions (b) for specimens immersed into sulfate solutions with and without chlorides in Ukpata et al.[99].

formation rate.

Figure 6.13a presents the simulated AFt formation with time for mortar specimens in two conditions. The mitigating effect of chlorides on ettingite formation is well predicted. The supersaturation index β and β_p in two conditions are given in Figure 6.13b. According to Eq. (6.33) and (6.35), the larger ettringite supersaturation β for pure sulfate condition in Figure 6.13b causes a faster ettringite formation rate in Figure 6.13a and a

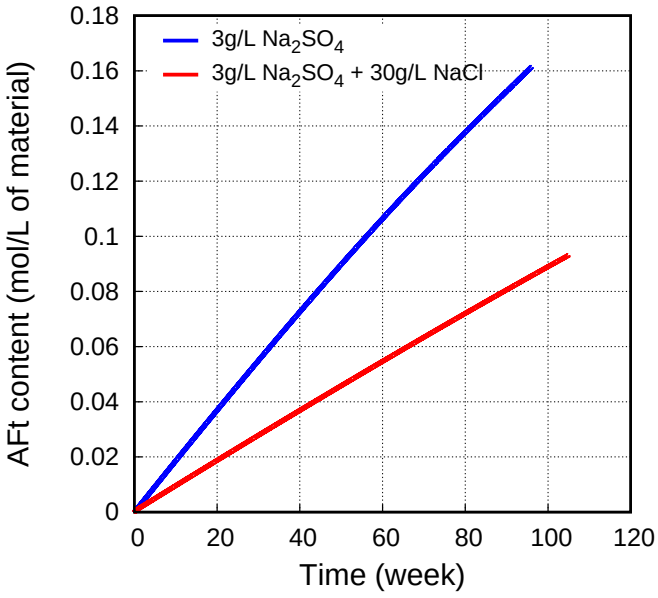

(a)

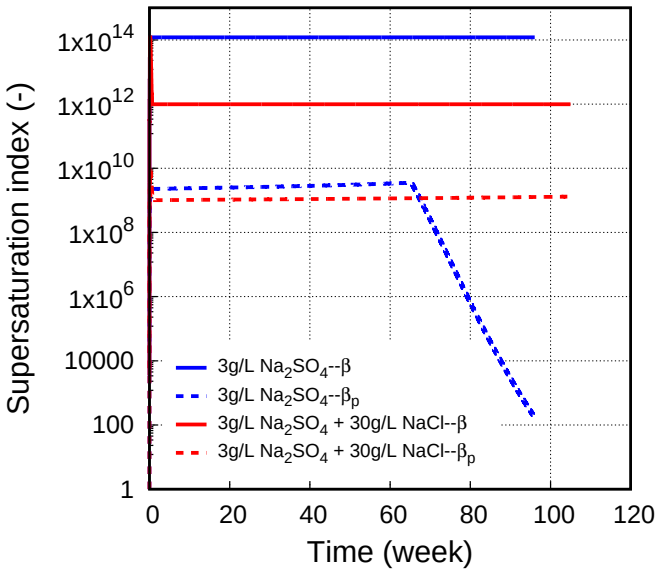

(b)

Figure 6.13 Predicted AFt formation (a) and evolution of supersaturation index (b) for specimens immersed into sulfate solutions with and without chlorides in Ukpata et al.[99].

rapid expansion rate in Figure 6.11. Besides, the difference in β_p is small, and it suggests that the interactions between ettringite crystal and pore wall are fairly similar under both conditions.

Table 6.7 Calibration of parameters in two different sulfate concentrations in Naik[37].

Condition	κ_0	K_r (s^{-1})	K_p (s^{-1})
10 g/L SO_4^{2-}	4.0×10^{-4}	6.5×10^{-10}	0.75×10^{-11}
33.8 g/L SO_4^{2-}	4.0×10^{-4}	6.5×10^{-10}	1.5×10^{-11}

6.6.3 Expansion under different sulfate concentrations from Naik

Naik[37] prepared prismatic mortar specimens with a size of 25×25×285mm and the cement used is ASTM type I Portland cement. The w/c and s/c ratios are 0.485 and 0.2, respectively. After 28d curing, the specimens were exposed to test solutions. The sulfate concentrations in two solutions were 10 g/L and 33.8 g/L and the test solutions were renewed on a weekly basis. The measured expansion curve was then compared with the expansion data of same specimens in pure sulfate condition, cf. Figure 6.11. The two parameters calibrated from two expansion curves, K_r and K_p, are given in Table 6.7 and the simulation results are given in Figure 6.14. The lower the sulfate concentrations, the slower the expansion rates both in the linear stage and the damage stage. In the linear stage, the first kinetic coefficient K_r is identical, so the difference of expansion rates in this stage can only originate from the difference in sulfate concentration. The second kinetic coefficient K_p in two conditions is predicted to have two different values, which needs more investigation.

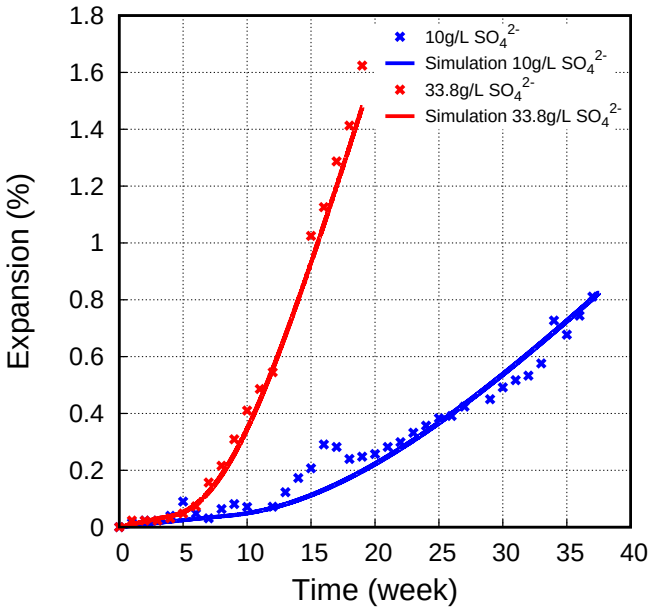

Figure 6.14 Simulation of expansion data of prismetric mortar specimens for two different sulfate concentrations. Experimental data taken from Naik[37].

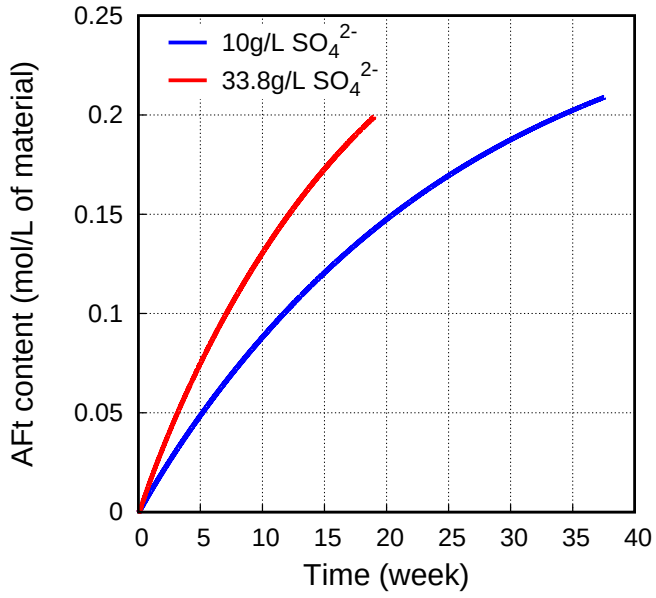

(a)

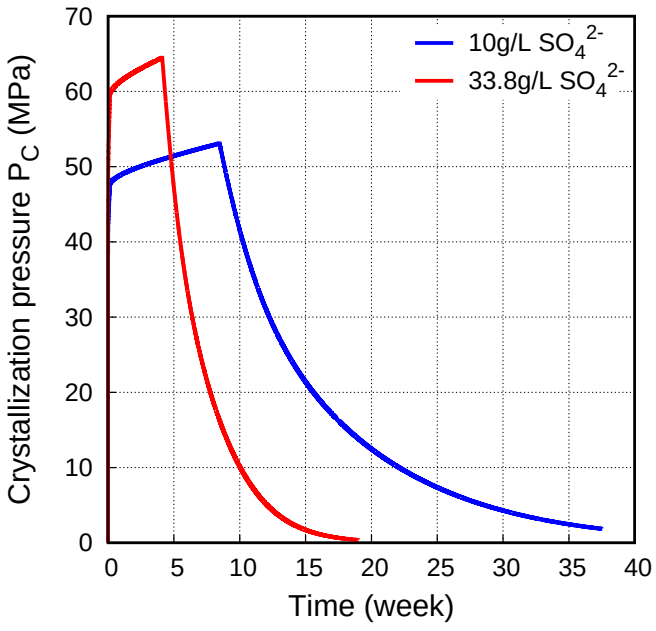

(b)

Figure 6.15 Predicted AFt formation (a) and evolution of crystallization pressure (b) for specimens immersed into sulfate solutions with different concentrations in Naik[37].

Figure 6.15 presents the simulated AFt content and crystallization pressure in terms of exposure time. The larger AFt supersaturation resulted from higher sulfate concentration, which led to a faster AFt formation rate in Figure 6.15a and associated expansion rate. In Figure 6.15b, the interactions between AFt crystal and pore solution (crystallization pressure) in both conditions decrease rapidly in the damage stage, and a higher sulfate concentration in 33.8g/L SO_4^{2-} leads to a higher crystallization pressure. The decrease of

crystallization pressure corresponds to the decrease in modulus in the damage stage. In the damage stage, cracks appear and the pore walls cannot provide enough restraint on crystals, thus the crystallization pressure (interaction, β_p) declines with the development of cracks. According to Eq. (6.32), the crystal at the crystal-solid interface grows faster with time in the damage stage.

6.7 Conclusions

1. A chemo-poromechanical model based on the crystallization pressure and crystal growth kinetics is proposed to predict the expansion damage of CBM subjected to the combined actions of ESA and chlorides. The kinetic law is fitted from the measured AFt content with time in the results of experimental Part II in Figure 4.2a. An exponential relation between the AFt formation rate and the AFt supersaturation is adopted, and the exponential order is fitted as 1.90. This kinetic law is applied to the pore crystallization processes in two directions of crystal, the pore invasion process in the axial direction and the pore deformation process in the radial direction. And two corresponding rate constants, K_r and K_p, are proposed in this model. The crystallization pressure during the crystallization process is derived from the deformation assumption and stress-strain relation of linear elastic porous materials. As shown in Eq. (6.38), the crystallization pressure is a function of the material's bulk modulus, the pore radius where AFt is penetrating, the AFt supersaturation, and the ratio of two kinetic coefficients. The AFt supersaturation is evaluated by a pore chemistry model. The effective stress is the combination of crystallization pressure and crystal content (saturation) through a poromechanical approach. Based on the estimated effective stress, a typical damage model is introduced to interpret the two-stage stage of the expansion curve.

2. The established model is validated by three sets of experiments of cement paste/mortar exposed to sulfate-bearing solutions. In the validation of expansion results in this study (PII-1/2/3), the constant parameters K_r and K_p are calibrated from the pure sulfate case (PII-1). Then these two calibrated parameters are used to predict the expansion behavior of two combined sulfate and chloride solutions (PII-2/3). The simulation results fit well with the experimental results. Following the same procedure, the mitigating effect of chlorides on ESA-induced expansion in mortar specimens is well reproduced, and the simulation results show that the AFt formation rate is reduced in the presence of chlorides due to the lower AFt supersaturation in the combined sulfate and chloride

solution compared to the pure sulfate solution. The reduced AFt supersaturation results from the lower aluminate concentration, and the lower aluminate concentration is due to the change in the multi-phase equilibria with the pore solution: the chlorides convert the hydrogarnet into Friedel's salt. In addition, the impact of sulfate concentration on the AFt formation and expansion is verified by simulating the expansion results of cement mortar exposed to different sulfate concentrations. The higher concentration leads to a higher AFt formation rate and crystallization pressure, which both result in a higher expansion rate. The decline of crystallization pressure, which results from the appearance of cracks in the damage stage, is well predicted in this model.

CHAPTER 7 SPALLING RATE OF ESA

In the last chapter, we established a chemo-porochanical model to simulate the expansion behavior of CBM exposed to ESA with and without chlorides. This model agrees well with experimental findings but is complicated to use in engineering practice. What's more, this model damage is not related to the usual damage pattern–surface spalling of CBM–in engineering practice as reviewed in Section 1.1.3. So we also need an engineering model to address the spalling damage rate in ESA in a direct way. In addition, the ESA is usually accompanied by leaching (see Section 1.2.3) in engineering practice, and the experimental results in Part III (see Section 5.2.1 and Figure 5.9) confirm that the damage of CBM in the combined ESA and leaching conditions shows a spalling pattern.

In this chapter, we aim to develop a simplified model for engineering use to predict the spalling depth of CBM subject to ESA and leaching. To simplify, the contribution of gypsum to sulfate reactions is neglected. In this model, the pore species transport is described by the sulfate and hydroxide ions through a dual moving boundary problem (MBP). The pore stress is estimated through poromechanics for ettringite crystallization in pores. Together with the adopted fracture criterion, the spalling depth is solved.

7.1 Spalling rate model

7.1.1 Statement of problem

The combined action of ESA and leaching is illustrated in Figure 7.1 as a unidimensional problem in semi-infinite domain with given sulfate concentration and neutral pH value on the CBM surface. The CBM are regarded to be totally saturated by aqueous phases. The ionic transport is described by the inward diffusion of sulfate ions (ESA) and outward diffusion of hydroxide ions, cf. Figures 7.1a,b. The existence and stability of AFt crystals, ettringite, is determined through its supersaturation degree, β_{AFt}, in the aqueous pore solution. The newly formed ettringite after CBM hardening is assumed to be produced from the chemical reaction between the external sulfates and the hydrogarnets C_3AH_6, the most stable form of aluminum hydrates[238],

$$C_3AH_6 + 3Ca^{2+} + 3SO_4^{2-} + 26H_2O \rightarrow C_3A(C\overline{S})_3H_{32} \tag{7.1}$$

and the supersaturation degree of AFt writes,

$$\beta_{\mathrm{AFt}} = \frac{a_{\mathrm{Ca^{2+}}}^{6} a_{\mathrm{Al(OH)_4^-}}^{2} a_{\mathrm{OH}}^{4} a_{\mathrm{S}}^{3}}{K_{\mathrm{AFt}}} \tag{7.2}$$

with K_{AFt} standing for dissolution constant of AFt and a_i the ionic activity for species i (mol/m^3). The dilute solution is assumed for CBM pore solution, taking the ionic activity a_i numerically equal to the ionic concentration c_i.

Under these circumstances, the CBM can be divided into several zones following the sulfate ingress direction: the dissolved zone (Z_1) where the formed ettringite dissolves due to the outward diffusion of OH^- ions with $\beta_{\mathrm{AFt}} < 1$[82], the crystallized zone (Z_2) where enough sulfate ions exist with $\beta_{\mathrm{AFt}} \geqslant 1$. In the deeper part of crystallized zone (Z_2), the pore solution is not yet perturbed by the leaching, i.e. the OH^- ions remain at the intact level for pore solution, corresponding to the intact zone with respect to leaching but not necessarily to sulfate ingress. This part is denoted as the intact zone (Z_3). Some lengths are defined accordingly: X_C refers to the crystallization front, delimiting the zones $Z_{1,2}$; X_L refers to the position of leaching front[181,239], positioning the Z_3 zone. For easier notation, the zone Z_2 refers to only the part between X_C and X_L hereafter. Using the definition of supersaturation β_{AFt} in Eq.(7.2), one can make the following judgements: it will increase from the CBM surface to deeper part of Z_1 due to the increasing of OH^- concentration with depth, it will decrease after $x > X_L$ due to the decreasing of sulfate concentration and stable concentrations of other ions, and a maximum supersaturation must exist in Z_2 if the crystallization of ettringite has ever occurred, cf. Figure 7.1c. In other words, these lengths observe

$$\beta_{\mathrm{AFt}} = 1 \ : \ x = X_C \quad \text{and} \quad X_C \leqslant X_L \tag{7.3}$$

To build a solvable problem, we make further assumptions for the leaching and related physical properties for these three zones. For leaching, only the dissolution equilibrium of CH is taken into account and the buffering effect of CSH for Ca^{2+} and OH^- ions in pore solution is neglected. The analytical solutions of leaching front X_L are available following such assumptions[181,239]. For solid phases, Z_1 contains neither AFt nor CH, Z_2 contains AFt but no CH, and Z_3 contains CH and AFt if the supersaturation in Eq.(7.2) reaches 1. For porosity in different zones, the porosity ϕ_1 in Z_1 corresponds to the CBM totally leached, the porosity ϕ_2 in Z_2 corresponds to leached CBM with pores refilled by

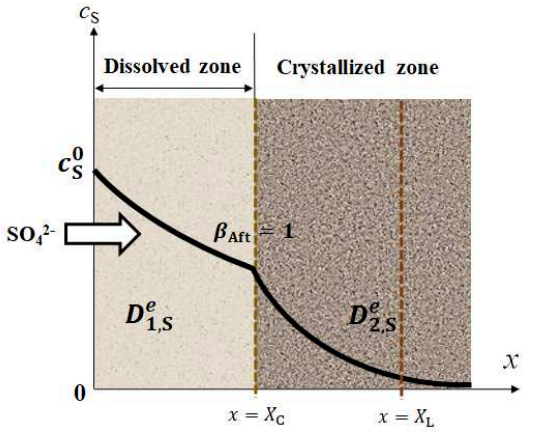

(a)

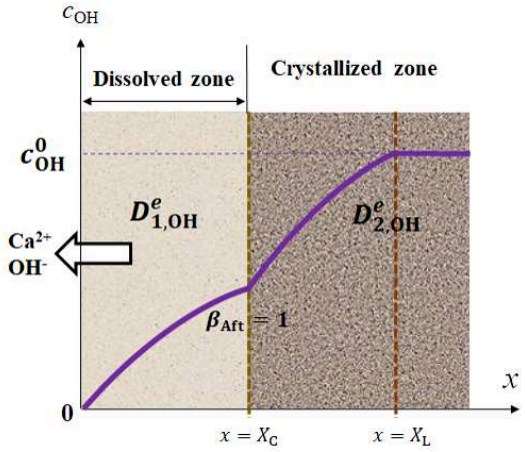

(b)

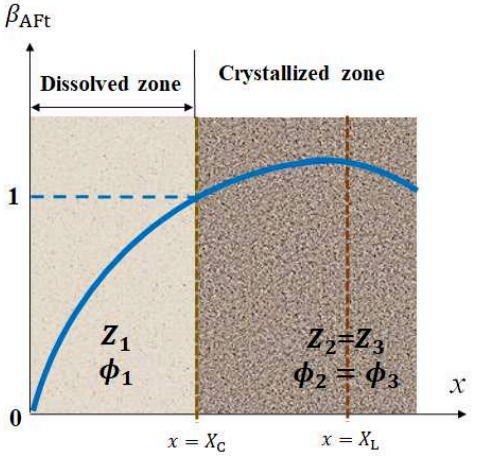

(c)

Figure 7.1 Transport and ionic distribution during ESA and leaching: (a) sulfate ions transport inwards across (AFt-)dissolved zone and (AFt-)crystallized zone; (b) hydroxide ions transport outwards across the crystallized and dissolved zones; (c) supersaturation degree distribution of AFt. The terms $D^e_{1,2;S,OH}$ stand for the effective diffusivities of SO_4^{2-} and OH^- for dissolved and crystallized zones, $\phi_{1,2}$ refer to the porosities of the two zones, $X_{C,L}$ represent the crystallization and leaching fronts, $C^0_{S,OH}$ are boundary SO_4^{2-} concentration and OH^- concentration of intact pore solution respectively. The term β_{AFt} denotes the supersaturation of AFt in aqueous solution.

ettringite crystals, and the porosity ϕ_3 in Z_3 to the intact CBM with possible AFt formation. Following this argument, the porosity and transport properties are assumed to observe

$$\phi_1 = \text{const}, \phi_2 = \phi_3 = \text{const} \quad \text{and} \quad D^e_{1,2;i} = \text{const}. \tag{7.4}$$

with $D^e_{1,2;i}$ representing effective diffusivities of i ion in Z_1 and Z_2 respectively.

7.1.2 Diffusion of sulfate and hydroxide ions

The mass conservation of sulfate ions writes,

$$\frac{\partial C_S}{\partial t} = D^e_S \frac{\partial^2 c_S}{\partial x^2} \quad \text{with} \quad C_S = \phi c_S + n_S \tag{7.5}$$

where C_S and n_S represent the total sulfates in CBM (mol/m^3 CBM) and the bound sulfates in AFt (mol/m^3 CBM), D^e_S denotes the effective sulfate diffusivity (m^2/s), and ϕ the CBM porosity. Using the second part of equation, the mass conservation can be rewritten using aqueous sulfate concentration c_S as basic variable,

$$\frac{\partial c_S}{\partial t} = D_S \frac{\partial^2 c_s}{\partial x^2} \quad \text{with} \quad D_S = \frac{D^e_S}{\phi + n'_S} \tag{7.6}$$

Here n'_S denotes the derivative of n_S with respect to time, and D_S stands for the apparent sulfate diffusivity, combining the pore diffusion and the chemical AFt formation. Retaining Eq.(7.6)

$$\begin{cases} \dfrac{\partial c_S}{\partial t} = D_{1,S} \dfrac{\partial^2 c_S}{\partial x^2}, \quad x < X_C \quad \text{with} \quad D_{1,S} = \dfrac{D^e_{1,S}}{\phi_1 + n'_S}, \; n'_S = 0 \\ \dfrac{\partial c_S}{\partial t} = D_{2,S} \dfrac{\partial^2 c_S}{\partial x^2}, \quad x \geqslant X_C \quad \text{with} \quad D_{2,S} = \dfrac{D^e_{2,S}}{\phi_2 + n'_S} \end{cases} \tag{7.7}$$

with $D_{1,2;S}$ denoting the apparent sulfate diffusivities in dissolved and crystallized zones respectively. Further, a linear relation is assumed between the bound sulfates n_S and aqueous sulfate concentration c_S, leading to constant apparent sulfate diffusivity in Z_2, i.e.

$$n_S = \phi_2 r_S c_S n_{C_3AH_6} : \quad D_{2;S} = \text{const} \tag{7.8}$$

where $n_{C_3AH_6}$ is the available content of aluminum hydrates (mol/m^3 CBM), and r_S a chemical factor related to AFt formation. This expression also suggests that the chemical binding of sulfates by AFt formation is a reversible and instantaneous reaction. The initial

and boundary conditions write,

$$\begin{cases} c_{\mathrm{S}}(x>0,t=0)=0,\ c_{\mathrm{S}}(x=0,t>0)=c_{\mathrm{S}}^{0} \\ c_{\mathrm{S}}|_{x=X_{\mathrm{C}}^{-}}=c_{\mathrm{S}}|_{x=X_{\mathrm{C}}^{+}},\ D_{1,\mathrm{S}}\dfrac{\partial c_{\mathrm{S}}}{\partial x}\Big|_{x=X_{\mathrm{C}}^{-}}=D_{2,\mathrm{S}}\dfrac{\partial c_{\mathrm{S}}}{\partial x}\Big|_{x=X_{\mathrm{C}}^{+}} \end{cases} \tag{7.9}$$

with c_{S}^{0} representing boundary sulfate concentration in external environment. The second expression depicts the concentration continuity and mass conservation of aqueous sulfates across the crystallization front X_{C}.

Also derived from the mass conservation, the hydroxide diffusion in the dissolved, crystallized and intact zones writes,

$$\begin{cases} \dfrac{\partial c_{\mathrm{OH}}}{\partial t} &= D_{1,\mathrm{OH}}\dfrac{\partial^{2}c_{\mathrm{OH}}}{\partial x^{2}}, & x<X_{\mathrm{C}} \\ \dfrac{\partial c_{\mathrm{OH}}}{\partial t} &= D_{2,\mathrm{OH}}\dfrac{\partial^{2}c_{\mathrm{OH}}}{\partial x^{2}}, & X_{\mathrm{C}}\leqslant x<X_{\mathrm{L}} \\ \dfrac{\partial c_{\mathrm{OH}}}{\partial t} &= 0, & x\geqslant X_{\mathrm{L}} \end{cases} \tag{7.10}$$

with $D_{1,2;\mathrm{OH}}$ representing the apparent hydroxide diffusivities in $\mathrm{Z}_{1,2}$ respectively. The initial and boundary conditions write,

$$\begin{cases} c_{\mathrm{OH}}(x=0,t>0)=0, \quad c_{\mathrm{OH}}(x\geqslant X_{\mathrm{L}})=c_{\mathrm{OH}}^{0} \\ c_{\mathrm{OH}}|_{x=X_{\mathrm{C}}^{-}}=c_{\mathrm{OH}}|_{x=X_{\mathrm{C}}^{+}}, \quad D_{1,\mathrm{OH}}\dfrac{\partial c_{\mathrm{OH}}}{\partial x}\Big|_{x=X_{\mathrm{C}}^{-}}=D_{2,\mathrm{OH}}\dfrac{\partial c_{\mathrm{OH}}}{\partial x}\Big|_{x=X_{\mathrm{C}}^{+}} \\ n_{\mathrm{CH}}\dfrac{\mathrm{d}X_{\mathrm{L}}}{\mathrm{d}t}=-\phi_{2}D_{2,\mathrm{OH}}\dfrac{\partial c_{\mathrm{OH}}}{\partial x}\Big|_{x=X_{\mathrm{L}}} \end{cases} \tag{7.11}$$

with c_{OH}^{0} standing for OH^{-} concentration in intact pore solution, n_{CH} denoting CH content ($\mathrm{mol/m^3}$ CBM). The second expression describes the concentration continuity and mass conservation of aqueous hydroxide ions across $\mathrm{X_C}$, and the third expression depicts the mass conservation of hydroxide ions across the leaching front $\mathrm{X_L}$.

7.1.3 Solution of crystallization front

The Eqs.(7.7)-(7.11) constitute a dual moving boundary problem (MBP) for combined ESA and leaching. In 1D semi-infinite domain, a single MBP, with fixed concentration at external boundary and mass continuity across the moving boundary, provides the moving rate of boundary proportional to square root of time[240-241]. On this basis, we express the crystallization front X_{C} and leaching front X_{L} in terms of square root of

time with their respective rate coefficients,

$$X_{\mathrm{C}} = k\sqrt{t}, \quad X_{\mathrm{L}} = \kappa\sqrt{t} \quad \text{with} \quad k \leqslant \kappa \tag{7.12}$$

with k and κ denoting the moving rates for the crystallization and leaching fronts (m/s$^{0.5}$). As long as the two rate coefficients can be determined uniquely using the conditions in this dual MBP, the above expression can be proved to be the correct solution for $X_{\mathrm{C,L}}$, which will be demonstrated later in this section. On the basis of above linear relations, the general solution takes the following form with the mathematical details given in Appendix F,

$$\begin{cases} \dfrac{c_{\mathrm{S}}}{c_{\mathrm{S}}^0} = A_1 \mathrm{erfc}\left(\dfrac{x}{2\sqrt{D_{1,\mathrm{S}}t}}\right) + A_2, \dfrac{c_{\mathrm{OH}}}{c_{\mathrm{OH}}^0} = a_1 \mathrm{erf}\left(\dfrac{x}{2\sqrt{D_{1,\mathrm{OH}}t}}\right), & x < k\sqrt{t} \\ \dfrac{c_{\mathrm{S}}}{c_{\mathrm{S}}^0} = A_3 \mathrm{erfc}\left(\dfrac{x}{2\sqrt{D_{2,\mathrm{S}}t}}\right), \quad \dfrac{c_{\mathrm{OH}}}{c_{\mathrm{OH}}^0} = a_2 \mathrm{erf}\left(\dfrac{x}{2\sqrt{D_{2,\mathrm{OH}}t}}\right) + a_3, & k\sqrt{t} \leqslant x < \kappa\sqrt{t} \\ \dfrac{c_{\mathrm{S}}}{c_{\mathrm{S}}^0} = A_3 \mathrm{erfc}\left(\dfrac{x}{2\sqrt{D_{2,\mathrm{S}}t}}\right), \quad \dfrac{c_{\mathrm{OH}}}{c_{\mathrm{OH}}^0} = 1, & x \geqslant \kappa\sqrt{t} \end{cases} \tag{7.13}$$

with the constants dependent on materials parameters,

$$A_{1,2,3} = A_{1,2,3}(k, D_{1,\mathrm{S}}, D_{2,\mathrm{S}}), \quad \text{and} \quad a_{1,2,3} = a_{1,2,3}(k, \kappa, D_{1,\mathrm{OH}}, D_{2,\mathrm{OH}}) \tag{7.14}$$

Now we turn to determine the two moving rates using the mass conservation of CH across the leaching front in Eq.(7.11)$_3$ and the dissolution equilibrium of AFt in Eqs.(7.2),(7.3)$_1$. Putting the leaching front in Eq.(7.12) and the profile of OH^- in Eq.(7.13) into Eq.(7.11)$_3$, the mass conservation of CH across the leaching front is expressed in terms of the two rate coefficients k and κ,

$$\kappa \exp\left(\frac{\kappa^2}{4D_{2,\mathrm{OH}}}\right) = \frac{2}{\sqrt{\pi}} \frac{\phi_2 c_{\mathrm{OH}}^0 \sqrt{D_{2,\mathrm{OH}}}}{n_{\mathrm{CH}}} a_2(k, \kappa) \tag{7.15}$$

The calculation of supersaturation degree of AFt needs to specify the ionic concentrations not explicitly included in Eq.(7.13), such as $c_{\mathrm{Ca}^{2+}}$ and $c_{\mathrm{Al(OH)}_4^-}$. Actually the two concentrations should satisfy all the dissolution equilibria in multi-species ionic aqueous environment of pore solution[210]. Here for simplification, CH is regarded as the only dissolution source for Ca^{2+} and the two ions, Ca^{2+} and OH^-, transport strictly together.

These assumptions lead to,

$$\frac{c_{Ca^{2+}}}{c_{OH}} = \frac{c^0_{Ca^{2+}}}{c^0_{OH}} = \frac{K_{CH}}{\left(c^0_{OH}\right)^3} \tag{7.16}$$

with $c^0_{Ca^{2+}}$ and $c^0_{OH^-}$ as the initial calcium and hydroxide ions concentrations in Z_3. Due to its very small value, the aluminate concentration is considered as a constant by neglecting its pore transport and by assuming C_3AH_6 always available in solid phases. These assumption lead to the aluminate concentration equal to its initial value in Z_3. Together with the only Ca^{2+} source from CH, the aluminate concentration can be expressed as,

$$c_{Al(OH)_4^-} = c^0_{Al(OH)_4^-} = \sqrt{\frac{K_{C_3AH_6}}{K^3_{CH}}\left(c^0_{OH}\right)^5} \tag{7.17}$$

with $c^0_{Al(OH)_4^-}$ as the initial concentration in Z_3. Putting Eqs.(7.16),(7.17) into Eq.(7.2) gives the AFt supersaturation,

$$\beta_{AFt} = K' c^{10}_{OH} c^3_S \quad \text{with} \quad K' = \frac{K_{C_3AH_6} K^3_{CH}}{K_{AFt}} \frac{1}{\left(c^0_{OH}\right)^{13}} \tag{7.18}$$

Then, substituting the profiles in Eq.(7.13) into Eq.(7.18) gives the second relation for the two moving rate coefficients k and κ,

$$\left[a_1(k,\lambda)\mathrm{erf}\left(\frac{k}{2\sqrt{D_{1,OH}}}\right)\right]^{10}\left[A_3(k)\mathrm{erf}\left(\frac{k}{2\sqrt{D_{2,S}}}\right)\right]^3 = \frac{1}{K'} \tag{7.19}$$

So far, the two moving rate coefficients can be solved through the CH mass conservation and the AFt dissolution equilibrium expressed respectively in Eq.(7.15) and Eq.(7.19), which are mathematically solvable. This observation also confirms the correctness of the proportionality between $X_{C,L}$ and $\sqrt{t}$, taken in Eq.(7.12). With solved moving rate coefficients, we can determine the profiles in Eq.(7.13), the parameters in Eq.(7.14) and the AFt supersaturation profile through Eq.(7.18), which lays ground for the pore pressure analysis. More generally, any law, which defines the relation between c_S and c_{OH} at X_C, can serve as the second constraint, in the place of Eq.(7.19), to solve the two rate coefficients.

7.1.4 Spalling depth

In this model, we assume that the pore pressure arises from the crystallization of ettringite and constitutes the physical source for CBM expansion and damage. The crystallization pressure, P_C, is related to AFt supersaturation through the Correns' equation[66],

$$P_C - P_L = \frac{RT}{V_C}\ln(\beta_{AFt}) \tag{7.20}$$

where P_L represents liquid pressure (Pa), R stands for the ideal gas constant (J/(mol·K)), T denotes the absolute temperature (K), and V_C the molar volume of ettringite crystal (m^3/mol). The poromechanics expresses the effective stress on solid matrix for 1D problem, σ'_{xx}, as[33],

$$\sigma'_{xx} = \sigma_{xx} + b(S_C P_C + S_L P_L) \quad \text{and} \quad S_C + S_L = 1 \tag{7.21}$$

where σ is the material total stress (Pa), b is the Biot's coefficient, $S_{C,L}$ are the volume fractions of pore space occupied by the crystals and the liquid respectively. Due to the dissolution of AFt and CH in Z_1, it is assumed that there is no pressure building-up for liquid phase and the liquid pressure is equal to atmosphere pressure. The crystal saturation S_C can be evaluated from the bound sulfates content n_S,

$$S_C = \frac{n_S V_C}{\phi_1} = r_S n_{C_3AH_6} V_C \frac{\phi_2}{\phi_1} c_S \tag{7.22}$$

Under a stress-free condition without external loading, the effective stress writes,

$$\sigma = 0 : \sigma' = \gamma c_S \ln(\beta_{AFt}) \quad \text{with} \quad \gamma = r_S n_{C_3AH_6} \frac{\phi_2}{\phi_1} bRT \tag{7.23}$$

(a) Spalling rate without cracking effect on diffusivity

Consider first a uniaxial strain problem. The lateral strains are fixed to zero, $\epsilon_{yy,zz} = 0$, and the stress is free in x axis, $\sigma_{xx} = 0$, leaving ϵ_{xx} as the only possible strain, cf. Figure 7.2a. Under these conditions, the effective stress in solid matrix along x axis writes,

$$\sigma_{xx} = 0 : \sigma'_{xx} = \gamma c_S \ln(\beta_{AFt}) \tag{7.24}$$

In this case, the tensile stress σ'_{xx} induced by pore crystallization is the only cause of fracture of solid matrix and the cracks induced by the pore crystallization are assumed to

be arranged perpendicular to x axis, corresponding to the layered spalling damage pattern. This pattern most probably occurs for elements such as walls with very large (infinite) surface, perpendicular to x axis, of which the in-place strains $\epsilon_{yy,zz}$ can be assumed to be cancelled out. Under this cracking pattern, the ionic diffusivity remains unaffected in the sulfate penetration direction. Holding this assumption and using the expression in Eq.(7.24), we can express the effective stress σ'_{xx} through the Boltzmann variable η in Eq.(F.1),

$$\sigma'_{xx} = \begin{cases} 0, & 0 \leqslant \eta < k \\ \gamma c_S^0 A_3 \mathrm{erfc}\left(\eta_2\right) \ln\left\{K'\left[a_2 \mathrm{erf}\left(\eta_1\right) + a_3\right]^{10}\left[A_3 \mathrm{erfc}\left(\eta_2\right)\right]^3\right\}, & k \leqslant \eta < \kappa \\ \gamma c_S^0 A_3 \mathrm{erfc}\left(\eta_2\right) \ln\left\{K'\left[A_3 \mathrm{erfc}\left(\eta_2\right)\right]^3\right\}, & \eta \geqslant \kappa \end{cases} \tag{7.25}$$

with

$$\eta_1 = \frac{\eta}{2\sqrt{D_{1,\mathrm{OH}}}}, \quad \eta_2 = \frac{\eta}{2\sqrt{D_{2,\mathrm{S}}}} \tag{7.26}$$

The fracture criterion is simply taken as the effective stress σ'_{xx} attaining the tensile strength of CBM σ_{ft}. Considering Eq.(7.25), the spalling rate coefficient η' can be solved,

$$\sigma'_{xx}(\eta = \eta') = \sigma_{\mathrm{ft}} : \quad \eta' = \frac{X_{\mathrm{spalling}}}{\sqrt{t}} \tag{7.27}$$

where X_{spalling} stands for the spalling depth by ESA and leaching action. This solution

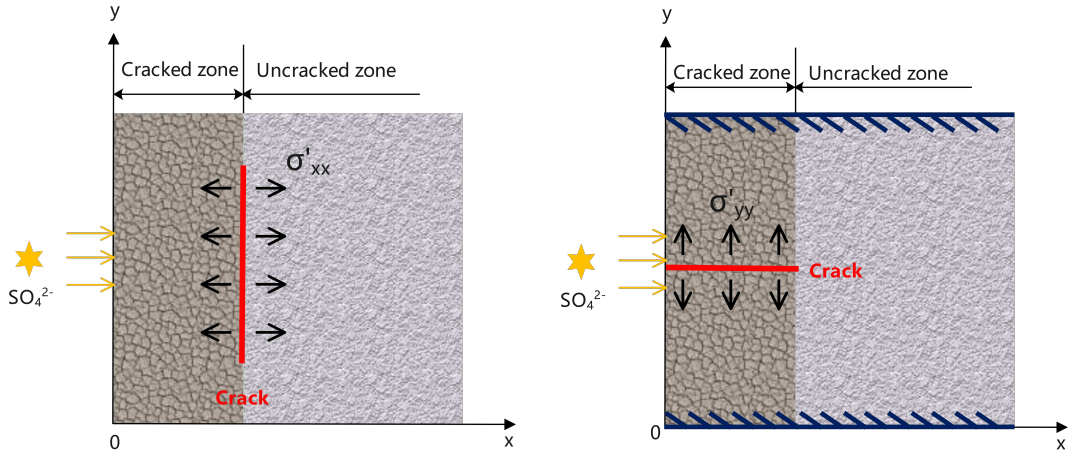

Figure 7.2 Scheme of uniaxial stress condition (a) and free stress condition (b). Along the Y axis, the material is infinite in the left figure while limited in the right figure. Along the X axis, the material is semi-infinite in both figures.

reveals that, like crystallization front and leaching front, the spalling depth is also proportional to the square root of time.

(b) Spalling rate with cracking effect on diffusivity

Here we release the conditions of zero lateral strains in the precedent uniaxial strain problem and replace by free stress conditions $\sigma_{yy,zz} = 0$, making $\epsilon_{yy,zz}$ as possible strains (see in Figure 7.2b). Under these conditions, the effective stress in lateral directions writes,

$$\sigma_{yy,zz} = 0 : \sigma'_{yy,zz} = \gamma c_{\mathrm{S}} \ln(\beta_{\mathrm{AFt}}) \tag{7.28}$$

In this case, the tensile stress $\sigma'_{yy,zz}$ induced by the pore crystallization can cause the fracture of solid matrix when reaching σ_{ft}. This fracture process will generate cracking parallel to the x axis, possibly together with the spalling pattern of cracking. This pattern may occur for elements such as beams and columns with finite size of surface, perpendicular to the x axis, and bearing the free lateral surface, where the lateral stress $\sigma_{yy,zz}$ can be assumed to be zero. Another particular case for this pattern refers to the 1D diffusion-crystallization process in axisymmetric coordinates where the hooping (circumferential) tensile stress in solid matrix dominates over other stress components and induces cracking parallel to the radical axis.

Since the presence of parallel cracks affect substantially the ionic diffusivity in the x axis direction, we need to adapt the dual MBP illustrated in Figure 7.1 to spalling-cracking case illustrated in Figure 7.3 to evaluate the spalling depth and rate: the zones $\mathrm{Z}_{1,2,3}$ represent now the spalling-cracking zone, the un-cracked zone and the intact zone by leaching. The delimiting lengths are spalling depth X_{spalling} and leaching depth X_{L}. Like the solution to the original dual MBP, we assume,

$$X_{\mathrm{spalling}} = \eta' \sqrt{t}, \quad X_{\mathrm{L}} = \kappa \sqrt{t} \tag{7.29}$$

We can substitute η' for k in the original MBP and solve the new problem following the same procedure as Section 2.3 and the sulfate and hydroxide profiles take the same form as in Eq.(7.13). The only difference is the determination of the two new moving rate coefficients η' and κ. Instead of using the CH mass conservation and AFt dissolution equilibrium, the CH mass conservation and fracture criterion are used for their determination. And in this case, unlike in Eq.(7.12), the spalling-cracking front X_{spalling} can surpass the leaching front X_{L}, cancelling out the zone Z_2.

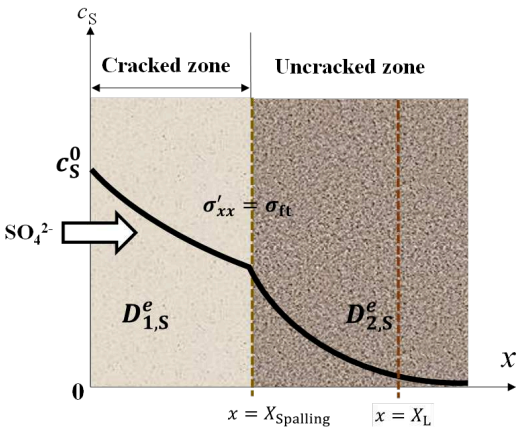

(a)

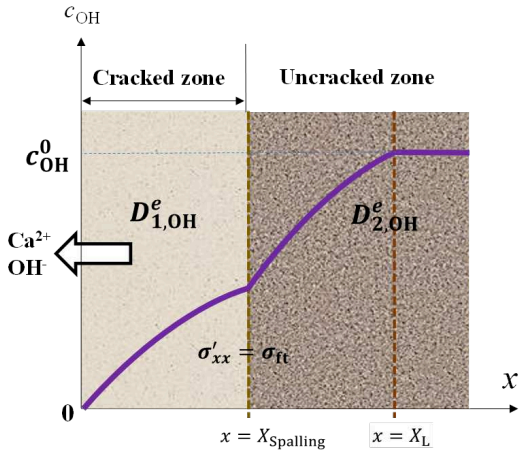

(b)

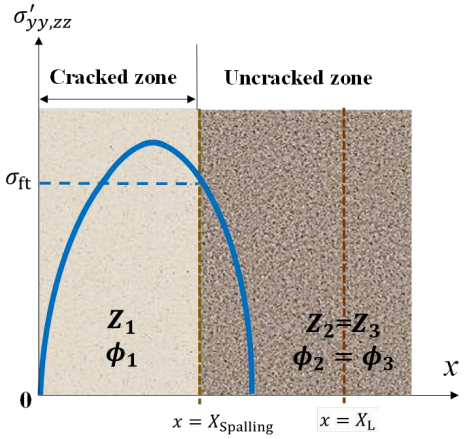

(c)

Figure 7.3 Transport and ionic distribution during ESA and leaching considering cracks: (a) sulfate ions transport inwards across spalling-cracking zone and uncracked zone; (b) hydroxide ions transport outwards across the uncracked zone and spalling-cracking zone; (c) effective stress distribution. The terms $D^e_{1,2;S,OH}$ stand for the effective diffusivities of SO_4^{2-} and OH^- for spalling-cracking zone and uncracked zone, $\phi_{1,2}$ refer to the porosities of the two zones, $X_{spalling,L}$ represent the spalling and leaching fronts, $C^0_{S,OH}$ are boundary SO_4^{2-} concentration and OH^- concentration of intact pore solution, and σ'_{xx} and σ_{ft} denote effective stress and tensile strength of CBM respectively.

As $X_{\text{spalling}} < X_{\text{L}}$, the relations for solving the two moving rate coefficients are constituted by Eq.(7.15) and Eq.(7.28) using the fracture criterion $\sigma'_{yy,zz} = \sigma_{\text{ft}}$,

$$\begin{cases} \kappa \exp\left(\dfrac{\kappa^2}{4D_{2,\text{OH}}}\right) = \dfrac{2}{\sqrt{\pi}} \dfrac{\phi_2 c_{\text{OH}}^0 \sqrt{D_{2,\text{OH}}}}{n_{\text{CH}}} a_2(\eta', \kappa) \\ \sigma_{\text{ft}} = \gamma c_{\text{S}}^0 A_3(\eta') \text{erfc}\left(\dfrac{\eta'}{2\sqrt{D_{2,\text{S}}}}\right) \ln\left\{ K' \left[a_1(\eta', \kappa) \text{erf}\left(\dfrac{\eta'}{2\sqrt{D_{1,\text{OH}}}}\right)\right]^{10} \right. \\ \qquad \left. \left[A_3(\eta') \text{erfc}\left(\dfrac{\eta'}{2\sqrt{D_{2,\text{S}}}}\right)\right]^3 \right\} \end{cases} \tag{7.30}$$

As $X_{\text{spalling}} \geqslant X_{\text{L}}$, the two relations still come from the same expressions but totally decoupled,

$$\begin{cases} \kappa \exp\left(\dfrac{\kappa^2}{4D_{1,\text{OH}}}\right) = \dfrac{2}{\sqrt{\pi}} \dfrac{\phi_2 c_{\text{OH}}^0 \sqrt{D_{1,\text{OH}}}}{n_{\text{CH}}} a_2(\kappa) \\ \sigma_{\text{ft}} = \gamma c_{\text{S}}^0 A_3(\eta') \text{erfc}\left(\dfrac{\eta'}{2\sqrt{D_{2,\text{S}}}}\right) \ln\left\{ K' \left[A_3(\eta') \text{erfc}\left(\dfrac{\eta'}{2\sqrt{D_{2,\text{S}}}}\right)\right]^3 \right\} \end{cases} \tag{7.31}$$

Again, the unique determination of the two moving rate coefficients confirms the correctness of the relations taken in Eq.(7.29) for the new dual MBP problem. The spalling depth is also proportional to the square root of time.

7.2 Validation

7.2.1 Cracking depths in PIII-2

In experimental Part III, disk specimens were prepared to investigate the sulfate transport and cracking behavior during ESA. Disk specimens were cut from cylinders of cement paste, and then were sealed by epoxy on the lateral and bottom surfaces, cf. Figure 2.5c. The disks were then immersed into PIII-2 condition, 10g/L sulfate with pH = 7. After being exposed to PIII-2 condition for 8, 16, and 32 weeks, the disk specimens were cut diametrically to obtain the diffusion direction cross-section, cf. Figure 2.6. These cross-sections were observed by optical microscope, as shown in Figure 7.4. The cracks are almost parallel to exposure surface, and the measured cracking depths are given in Figure 7.5 in terms of the exposure time.

Due to the damage pattern of layered spalling in Figures 7.4a-c, we adopt the spalling rate model without cracking effect on diffusivity in Section 2.4.1 for model validation, wi

Table 7.1 Parameters adopted in the spalling rate models

Parameter(unit)	Disk	Small cylinder[37]	Parameter analysis
Material type	Paste		Concrete
w/c ratio (-)	0.55	0.485	0.40
Initial capillary porosity ϕ_0 (-)	0.33	0.25	0.11
Porosity in Z_1 zone ϕ_1 (-)	0.402	0.335	0.155
Porosity in Z_2 zone ϕ_2 (-)	0.347	0.248	0.121
Chemical reaction coefficient r_S (m^3/mol)	0.035		
Aluminum hydrates content $n_{C_3AH_6}$ (mol/m^3)	320	520	198
CH content n_{CH} (mol/m^3)	2158	2557	1345
Magnification factor θ (-)	-	4, 5, 6, 7	-
Apparent OH^- diffusivity in Z_1 zone $D_{1,OH}$ (10^{-11} m^2/s)	4.20	1.25, 1.56, 1.87, 2.18	1.23
Apparent OH^- diffusivity in Z_2 zone $D_{2,OH}$ (10^{-12} m^2/s)	6.76	3.12	5.83
Apparent SO_4^{2-} diffusivity in Z_1 zone $D_{1,S}$ (10^{-12} m^2/s)	8.52	1.36, 1.70, 2.04, 2.38	2.50
Apparent SO_4^{2-} diffusivity in Z_2 zone $D_{2,S}$ (10^{-13} m^2/s)	1.12	0.34	1.50
Dissolution equilibrium constant of AFt at 25^{o}C log(AFt) (-)	-44.55[236]		
Dissolution equilibrium constant of C_3AH_6 at 25^{o}C log(C_3AH_6)(-)	-20.49[236]		
Dissolution equilibrium constant of CH at 25^{o}C log(CH) (-)	-5.14[236]		
Molar volume of ettringite V_C (10^{-3} m^3/mol) (-)	0.710[236]		
Biot's coefficient b (-)	0.69[209]		0.54[209]
Tensile strength σ_{ft} (MPa)	2.0[209]		3.1[209]
Measured spalling rate (10^{-4}mm/$s^{0.5}$)	3.19	5.73	-

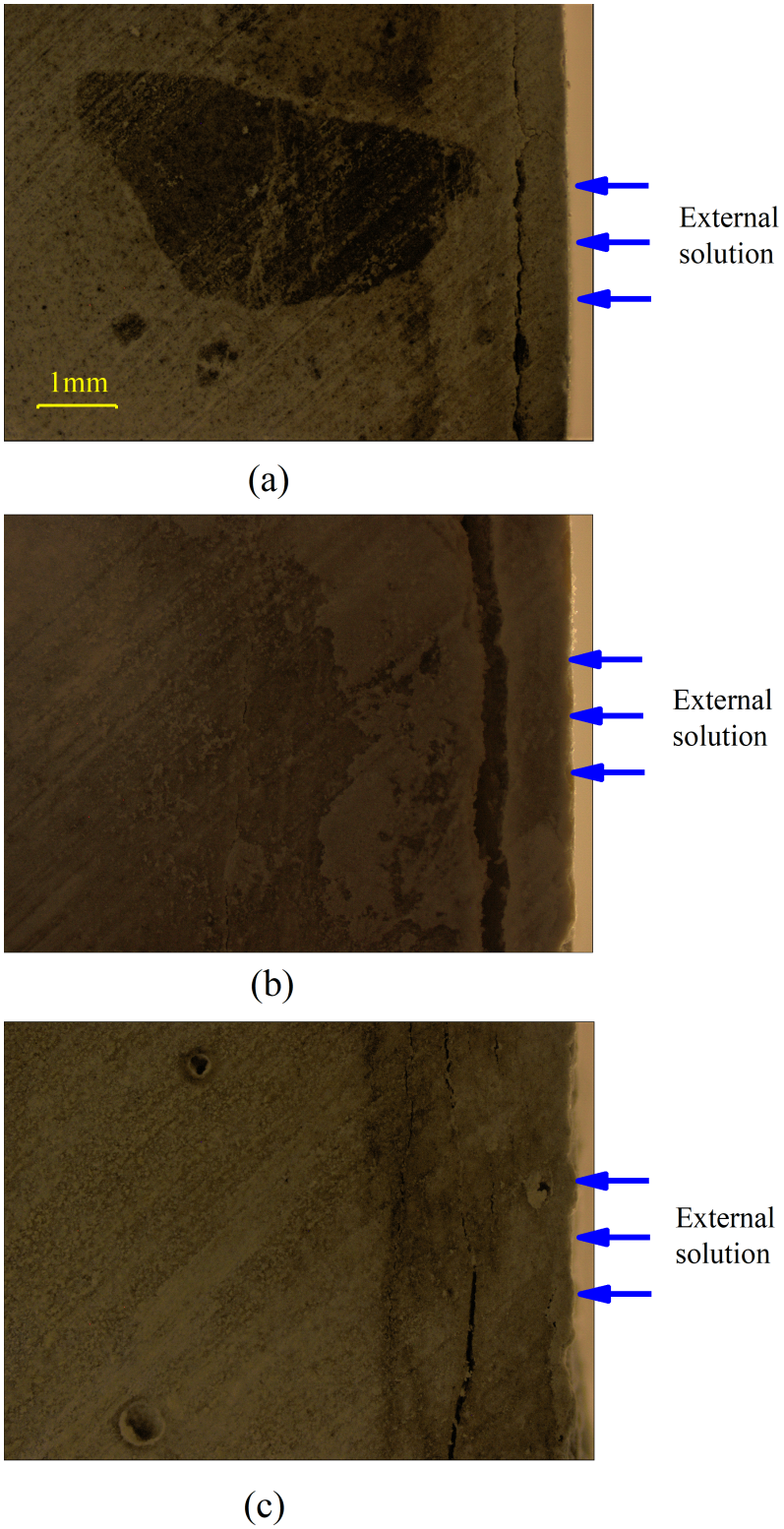

Figure 7.4 Cracking observation on cross sections of cement paste disks (w/c=0.55) by optical microscope for (a) 8-week, (b)16-week and (c) 32-week immersion in sodium sulfate solution of 10g/L SO_4^{2-} with pH value controlled to 7.0±0.1. Right edge of each image is the exposure surface.

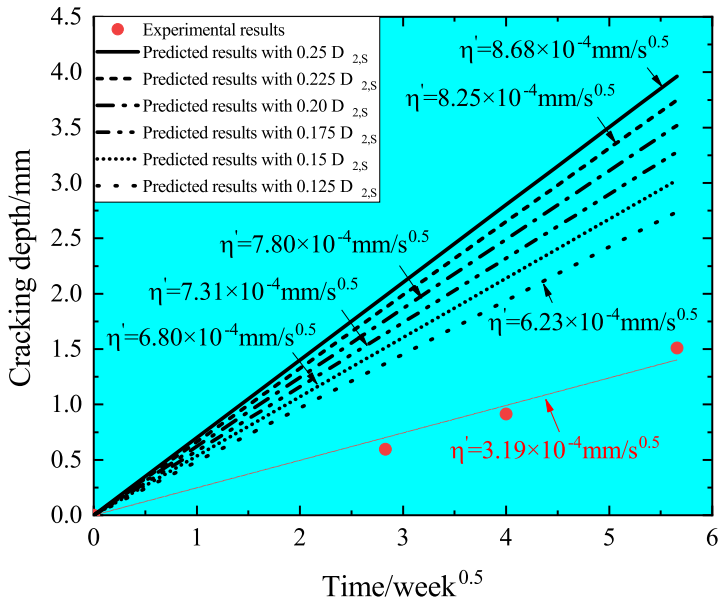

Figure 7.5 Cracking depth measured in experiments and spalling rate predicted by models for disk cement paste specimens (w/c=0.55) immersed in sodium sulfate solution of 10g/L SO_4^{2-}.

-th the material parameters provided in Table 7.1. The chemical reaction coefficient r_S is calibrated from the works in[25], where the AFt amount was quantified through ^{27}Al Nuclear Magnetic Resonance (NMR). The contents of cement hydrate phases, n_{CH} and $n_{C_3AH_6}$, were determined from the mineral composition of cement and w/c ratio, following the method in[31]. The initial porosity ϕ_0 was measured by the mercury intrusion porosimetry (MIP), and porosity values in dissolved zone ϕ_1 and crystallized zone ϕ_2 were calculated from the pore release volume by CH dissolution and pore-filling volume by AFt formation. Using these values of porosity, the apparent diffusivities for sulfate and hydroxide ions in the two zones were evaluated through porosity-based models in Appendix G[242]. Literature has reported the rapid reduction of diffusivity, i.e. ageing effect of diffusivity, in the early phase of ESA[25]. To account for this important change, a discount ratio of 1/8-1/4 is applied to the computed apparent diffusivities in the crystallized zone on the basis of experimental observations in [35,37].

The model prediction and the measured spalling (cracking) depths are given in Figure 7.5. From the experimental results, a linear relation does exist between the spalling (cracking) depth and the square root of exposure time. Accordingly, the proportionality between X_C and $\sqrt{t}$ is validated, confirming that the spalling damage is dominated by diffusion process. For the predicted and measured values of spalling depth, the two groups of

values are at the same order of magnitude, and the predicted values are systematic larger than the measured values. Apart from the various sub-models borrowed from literature, the main reason behind is the neglected buffering effect of CSH on leaching. Actually the CSH can provide both Ca^{2+} and OH^- ions into pore solution as CH is consumed out, and this effect can notably slow down the leaching front[181]. Nevertheless, this overestimation can be acceptable for engineering use which prefers conservative results.

7.2.2 Small cylinder specimens

Naik et al.[37] prepared cylinder cement paste specimens with diameter of 12.5mm and length of 45mm. The specimens were cast in ASTM type I Portland cement with a w/c ratio of 0.485. Naik et al.[37] prepared cylinder cement paste specimens with diameter of 12.5mm and length of 45mm. The specimens were cast in ASTM type I Portland cement with a w/c ratio of 0.485. The small cylinders were sealed with parafilm and cured in a saturated lime bath for 1d, then demoulded and cured in a saturated lime bath for 2d. The cured samples were then immersed into sodium sulfate solution containing 10g/L sulfate,

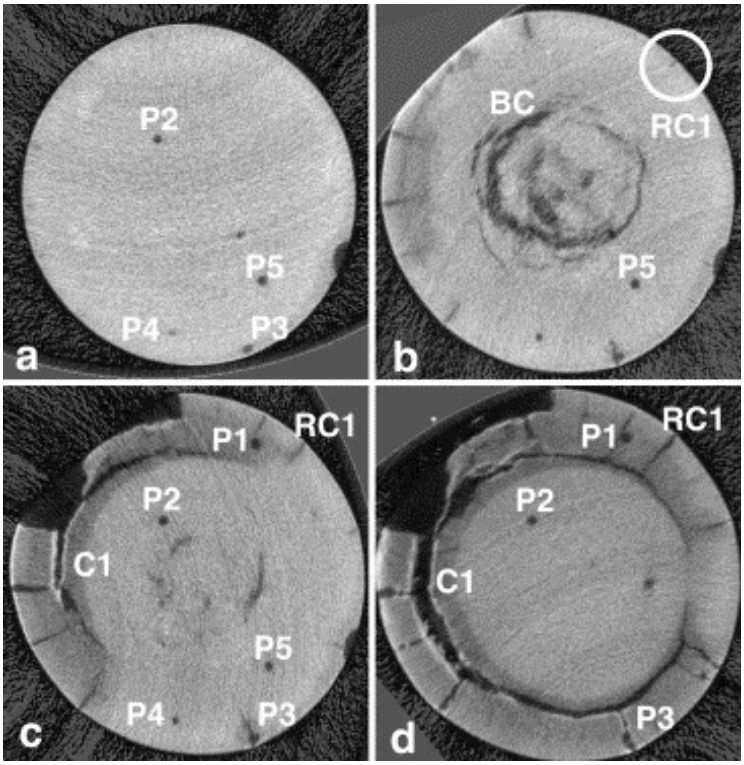

Figure 7.6 Cracking observation by microCT for Type I cement paste specimens (w/c=0.485) exposed to sodium sulfate solution of 10g/L SO_4^{2-} for (a) 21 weeks, (b) 36 weeks, (c) 42 weeks and (d) 52 weeks. The symbol C1 and RC1 stand for ring crack and radical crack, P1-P5 represent voids, and the field of view is 15.3mm(a), 15.1mm(b), 16.1mm(c) and 15.2mm(d). After Naik et al.[82].

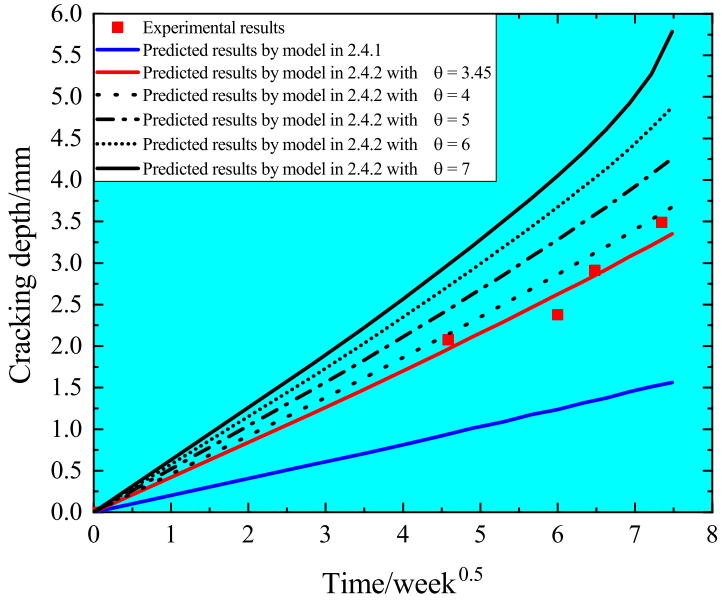

Figure 7.7 Cracking depth measured in experiments and spalling rate predicted by models for small cylinder cement paste specimens (w/c=0.485) exposed to 10g/L SO_4^{2-} in sodium sulfate solution[37]. θ is the magnification coefficient of apparent diffusivities in the cracked zone in Figure 7.3.

and the test solution was replaced on a weekly basis. After being exposed to sulfate solution for 21, 36, 42 and 52 weeks, the cylinder specimens were taken out for crack observation through X-ray microtomography (microCT) method, as shown in Figure 7.6. The measured values for cracking (spalling) depth are given in Figure 7.5b.

From the microCT images in Figure 7.6, the damage pattern includes obvious radical cracks. These cracks will provide more direct transport channel for external ions than the capillary pores, and this cracking impact should be considered in model validation. To this aim, the spalling rate model with cracking effect on diffusivities, in Section 2.4.2, is adopted to simulate the damage behaviors of the small cylinder specimens. Another issue to perform the analysis involves the coordinate system: the spalling rate model expressed in 1D semi-infinite domain should be converted to 1D axis-symmetric coordinate. The mathematical expression is given in Appendix H. Since there is no explicit analytical solution for the spalling depth X_C in 1D axis-symmetric coordinate, the spalling rate model is solved numerically through the platform Bil[243]. Table 7.1 lists all the parameters needed in the spalling rate model except the impact of cracking on the diffusivity value in Z_1 zone. A magnification factor, θ, is adopted here to quantify the cracking effect on

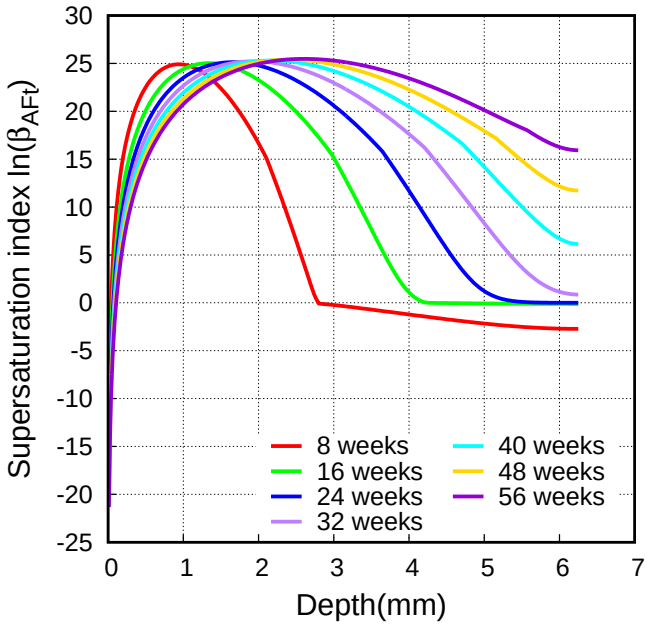

(a)

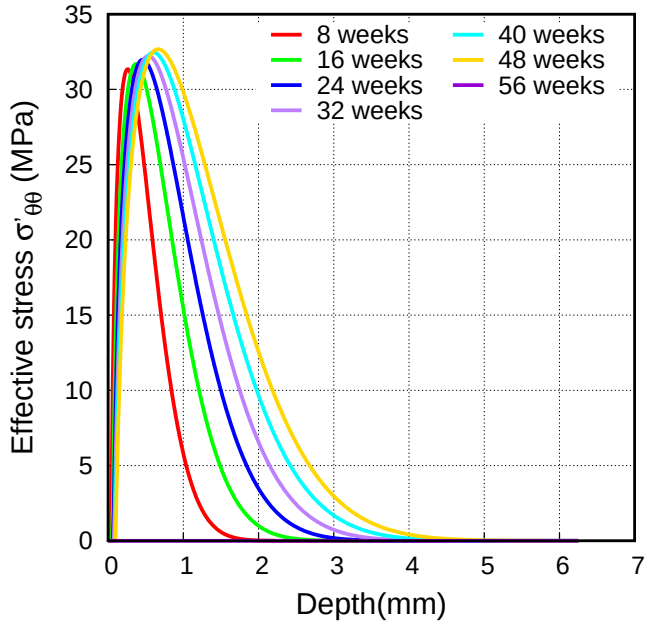

(b)

Figure 7.8 Profiles of AFt supersaturation (a) and effective stress in tension (b) predicted by spalling rate model for small cylinder specimens (w/c=0.485) exposed to sodium sulfate solution containing 10g/L SO_4^{2-}.

diffusivity in Z_1,

$$\theta = \frac{D_{1,S}}{D_{2,S}} = \frac{D_{1,OH}}{D_{2,OH}} > 1 \tag{7.32}$$

Gérard and Marchand[244] measured the parameter θ in the range of 4-7 on cracked disk specimens, and this value range is adopted to simulate the spalling depths. The results are

given in Figure 7.7 and this figure also includes the simulation results from the spalling rate model without cracking effect on diffusivity in Section 2.4.1. From these results, some observations can be made: first, the cracking effect should be taken into account otherwise the spalling depth will be largely underestimated; second, the spalling rate model considering the cracking effect, with reasonable values for the magnification factor, successfully reproduces the spalling depths. Again, the conservative results with correct magnitude order are obtained from the model predictions. The supersaturation degree β_{AFt} and the effective stress σ'_{xx} are calculated and shown in Figure 7.8 for θ=4. The results show that both the supersaturation and the effective stress have an extremum (local maximum), and within 8-week immersion the supersaturation and effective stress accumulate to high values within 1-2mm from the surface. Note that the large values in Figure 7.8b do not refer to the actual levels of tensile stress in the solid matrix which will be released by fracture. With 1D axis-symmetry transformation and reasonable assumption for cracking impact on diffusivities, the results in Figure 7.5b confirm the concept of spalling depth and validate the related modeling.

7.3 Further discussion

7.3.1 Parameter analysis

Multiple parameters intervene in the spalling rate models in Eq.(7.27) and Eq.(7.30). This section is dedicated to the analysis of key parameters to obtain some generalized observations using these models. Conceptually, the spalling rate scales to four groups of parameters: the ionic diffusivity in different zones, the surface boundary ionic concentrations, the chemical contents in CBM, and the mechanical properties related to crystallization and fracture, i.e.

$$\eta' = f\left(D_{1,\mathrm{S}}, D_{2,\mathrm{S}}; D_{1,\mathrm{OH}}, D_{2,\mathrm{OH}}; c_{\mathrm{S}}^{0}, c_{\mathrm{OH}}^{0}; n_{\mathrm{CH}}, n_{\mathrm{C_3AH_6}}; \sigma_{\mathrm{ft}}, \frac{RT}{V_{\mathrm{C}}}\right) \tag{7.33}$$

The dimension basis in Eq. (7.33) consists of four dimensions: length(L), mass(M), time (T) and amount of substance (N). Note that the absolute temperature T is combined into the variable group RT/V_{C} and the dimension is cancelled out. In this dimension basis, all the physical quantity Q can be expressed as its dimension function $[Q]=\mathrm{L}^{\alpha}\mathrm{M}^{\beta}\mathrm{T}^{\gamma}\mathrm{N}^{\theta}$. For example, the unit of spalling rate η' is $\mathrm{mm}\cdot s^{-0.5}$, thus its dimension function is $[\eta']=\mathrm{LT}^{-1/2}$. The dimension functions of 11 variables in Eq. (7.33) are summarized in Table 7.2, where the exponents,α, β, γ and θ, forms the columns,

Table 7.2 Dimension analysis of variables in Eq. (7.33).

Dimensions	η'	$D_{1,\mathrm{S}}$, $D_{2,\mathrm{S}}$, $D_{1,\mathrm{OH}}$, $D_{2,\mathrm{OH}}$	c_{S}^{0}, c_{OH}^{0}, n_{CH}, $n_{\mathrm{C_3AH_6}}$	σ_{ft}, RT/V_{C}
L	1	2	-3	-1
M	0	0	0	1
T	-1/2	-1	0	-2
N	0	0	1	0

The rank of dimension matrix in Table 7.2 is 3. According to the Buckingham theorem[245], eight independent dimensionless quantities exist and Eq.(7.33) can be converted into a function of these eight dimensionless quantities. We retain the hydroxide diffusivity in dissolved zone $D_{1,\mathrm{OH}}$, boundary hydroxide concentration c_{OH}^{0} and tensile strength σ_{ft}

as basic variables, and express Eq.(7.33) through the following dimensionless quantities,

$$\eta^- = f'\left(D_S^-, k_1, \frac{D_S^-}{K_1}; c_S^-, \frac{n_{CH}}{c_{OH}^0}, \frac{n_{C_3AH_6}}{c_{OH}^0}; \frac{\sigma_{ft} V_C}{RT}\right)$$
$$\text{with } \eta^- = \frac{\eta'}{2\sqrt{D_{1,OH}}}, D_S^- = \sqrt{\frac{D_{2,S}}{D_{1,OH}}}, k_1 = \sqrt{\frac{D_{2,OH}}{D_{1,OH}}}, K_1 = \sqrt{\frac{D_{1,S}}{D_{2,S}}}, c_S^- = \frac{c_S^0}{c_{OH}^0} \tag{7.34}$$

Not attempting to make parametric analysis for all these quantities, we retain two dimensionless variables related to sulfates, the normalized boundary sulfate concentration c_S^- and the relative apparent sulfate diffusivity D_S^- in crystallized zone, to study their impact on the normalized spalling rate η^-. The simulation results are shown in Figure7.9, indicating that η^- falls rapidly with the reduction of normalized boundary concentration c_S^- and relative diffusivity D_S^-. Obviously, the lower sulfate concentration on surface boundary and smaller sulfate diffusivity lead to a slower and lower sulfate profile, which in turns gives lower supersaturation degree and effective stress level. Besides, the spalling rate η^- becomes zero as c_S^- and D_S^- become low/small enough. As shown in Figure 7.8, both the supersaturation degree and effective stress have a local maximum, the zero spalling

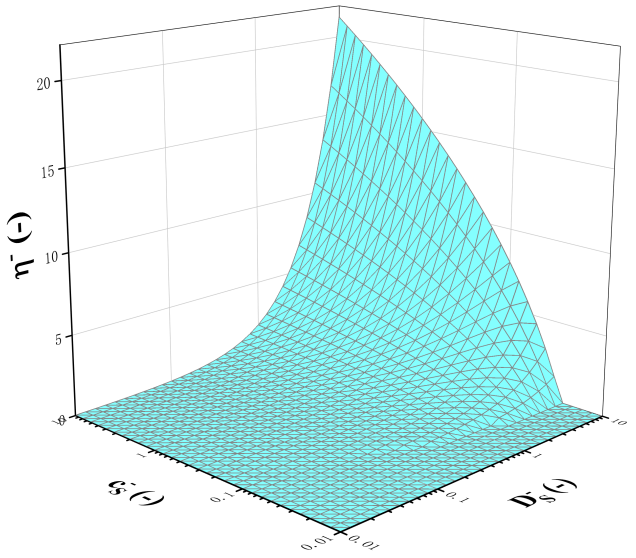

Figure 7.9 Normalized spalling rate in terms of normalized boundary sulfate concentration and relative sulfate diffusivity. Normalized spalling rate η^- is the ratio of spalling rate η' to the square root of apparent hydroxide diffusivity in dissolved zone $D_{1,OH}$: $\eta^- = \eta'/2\sqrt{D_{1,OH}}$. Normalized concentration c_S^- is the ratio of boundary sulfate concentration c_S^0 to the boundary hydroxide concentration c_{OH}^0: $c_S^- = c_S^0/c_{OH}^0$. Relative sulfate diffusivity D_S^- is ratio of apparent sulfate diffusivity in crystallized zone $D_{2,S}$ to the apparent hydroxide diffusivity in dissolved zone $D_{1,OH}$: $D_S^- = \sqrt{D_{2,S}/D_{1,OH}}$.

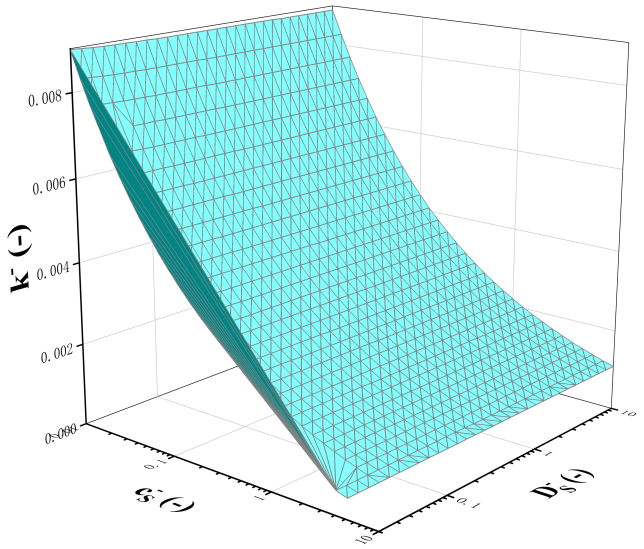

(a)

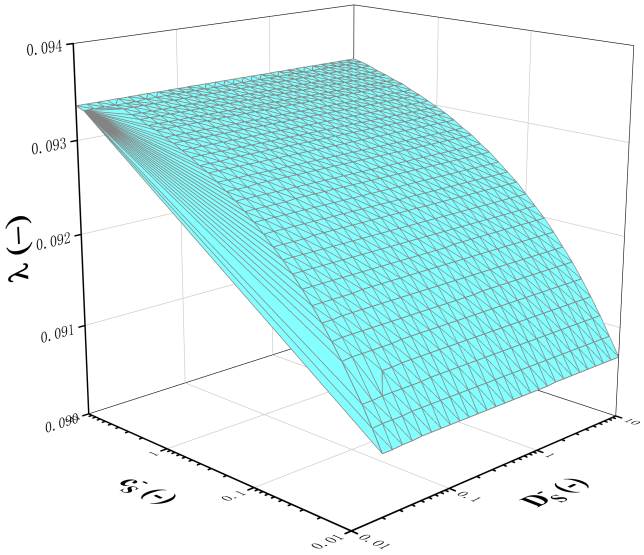

(b)

Figure 7.10 Normalized moving rate of crystallization front (a) and leaching coefficient in terms of normalized boundary sulfate concentration and relative sulfate diffusivity. Normalized moving rate of crystallization front k^- is the ratio of leaching front k to the square root of apparent hydroxide diffusivity in dissolved zone $D_{1,\mathrm{OH}}$: $k^- = k/2\sqrt{D_{1,\mathrm{OH}}}$.

rate is either due to the maximum $\beta_{\mathrm{AFt}} < 1.0$ with no AFt formed or due to the maximum $\sigma' < \sigma_{\mathrm{ft}}$. Figure 7.10 presents the normalized moving rate of crystallization front, $k^- = k/2\sqrt{D_{1,\mathrm{OH}}}$, and leaching coefficient λ in terms of c_{S}^- and D_{S}^-. The k^- drops rapidly as the decrease of c_{S}^- while few change with D_{S}^-. Figure 7.10b presents that c_{S}^- and D_{S}^- have few influence on leaching coefficient λ. Thus it seems that we can decouple the

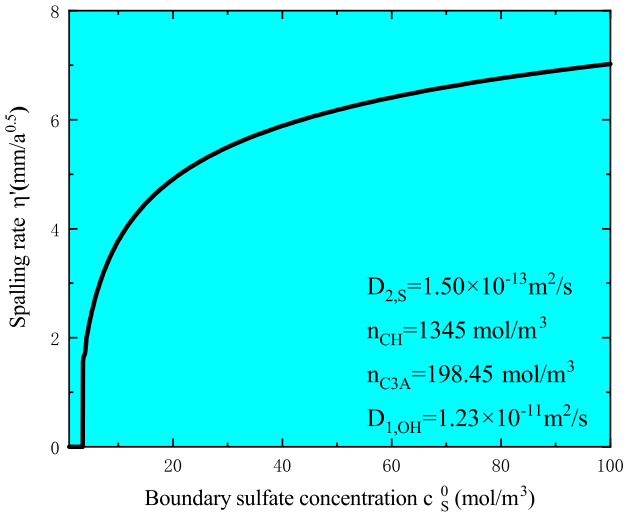

(a)

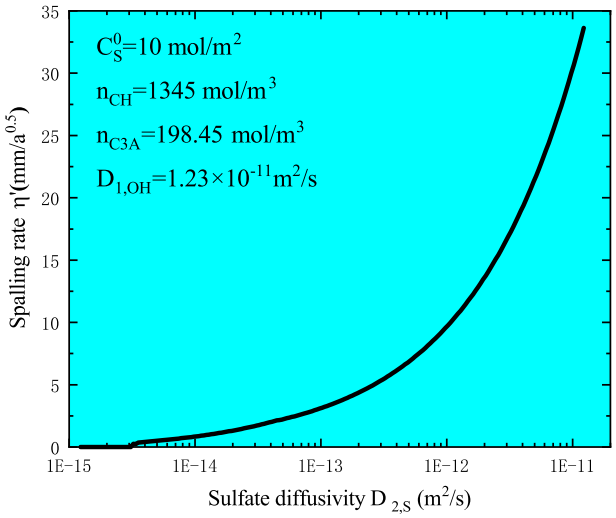

(b)

Figure 7.11 Influence on spalling rate by a)boundary sulfate concentration, b)sulfate diffusivity on a concrete material with a w/c of 0.4.

leaching front out in this problem.

Four single parameters are selected for parametric analysis to deliver clearer messages for engineering use: the boundary sulfate concentration c_S^0 representing the intensity of environmental sulfates, the apparent sulfate diffusivity in crystallized zone $D_{2,S}$ depicting the concrete compactness, the aluminium phase content n_{C_3A} and the portlandite content n_{CH} describing the main chemical characteristics of concrete. The other parameters for a typical concrete material are given in Table 7.1 and Table G.2. The simulation results are

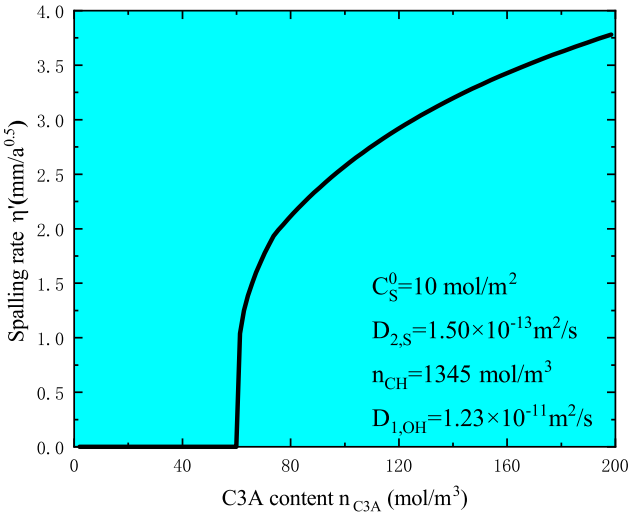

(a)

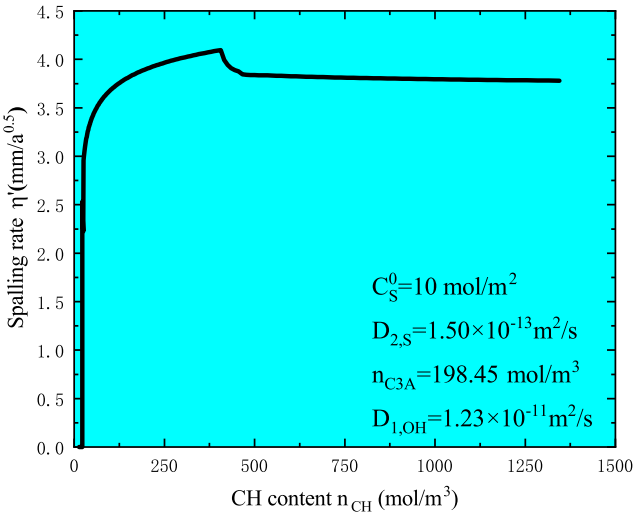

(b)

Figure 7.12 Influence on spalling rate by a)aluminum phase content, b)portlandite phase content on a concrete material with a w/c of 0.4.

shown in Figure 7.11. The spalling rate η' increases rapidly with c_S^0 till 30 mol/m^3, then increase with slower rates in Figure 7.11a. The message for engineering use would be the gradation of environmental action intensity in terms of external sulfate concentration should better be made in logarithm scale. Figure 7.11b shows η' increases with $D_{2,S}$: if $D_{2,S}$ is limited to 10^{-12} m^2/s, the usual value of concrete cover thickness, 50mm, can resist the sulfate spalling for 100 years for the given conditions. Figure 7.12a presents three stages for spalling rates in terms of C_3A content: $\eta' = 0$ when n_{C_3A} is in the range of 0-60

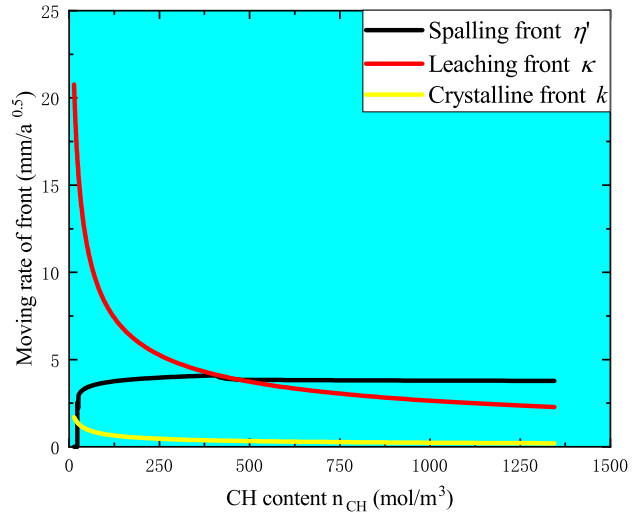

(a)

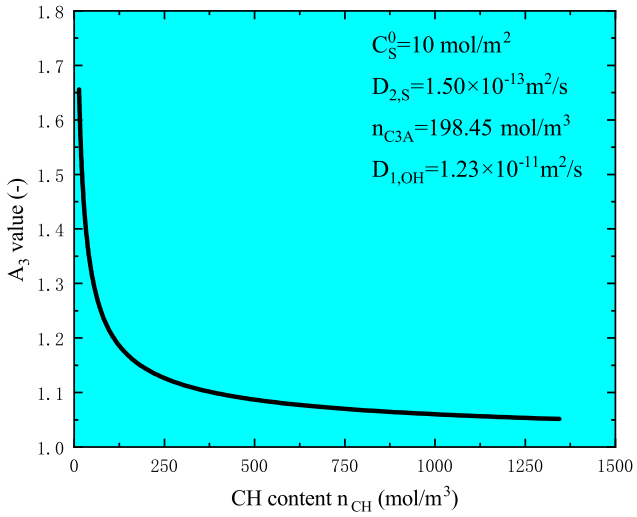

(b)

Figure 7.13 Further analysis of impact of CH content of typical concrete with w/c=0.4: (a) moving rates of the fronts, (b) A_3 value in spalling rate models.

mol/m^3; η' quickly rises to around 2.5 mm/a$^{0.5}$ for n_{C_3A} in the range of 60-100 mol/m^3; slower increase of η' with n_{C_3A} over 100 mol/m^3. The significant influence of n_{C_3A} is due to the assumption for sulfate reactions in Eq.(7.8): bound sulfates n_S are proportional to n_{C_3A}. It is interesting to compare this simulation results with some engineering rules of thumb: for concretes exposed to severe sulfate environments, the C_3A content is normally limited to 5% of the cement contents[85]. For typical concretes with 300-400 kg Portland cement in binders, the limit of C_3A is 15-20 kg, rather near to the simulation result of 60

mol/m^3, i.e. 16.2 kg/m^3 concrete. On the contrary, the results in Figure 7.12b shows the CH content n_{CH} has little influence on spalling rate until decreasing to about 120 mol/m^3 or 8.88 kg/m^{3}concrete.

To explore further η' in Figure 7.12b, we plot the moving rates of three fronts and the A_3 parameter in spalling rate model in terms of n_{CH} in Figure 7.13. The results in Figure 7.13a show that higher n_{CH} leads to slower moving rates for crystallization front k and leaching front κ, resulting in smaller A_3 values in Eq.(F.5) in Figure 7.13b. Figure 7.13a shows moreover the drop in η' occurs after intersecting with κ curve, indicating the spalling front reaching into intact zone Z_3 in Figure 7.1. Under this condition, the effective stress takes Eq.$(7.25)_3$, where the A_3 value is relevant to the effective stress level. Because of the decreasing A_3 value with the CH content n_{CH} in Figure 7.13b, the effective stress is decreased, leading to the the smaller spalling rate. But again, this occurs only after the spalling font reaching the intact zone Z_3 and this decrease of spalling is less important in magnitude compared to the range $n_{CH} < 400$ mol/m^3 in Figure 7.12b.

7.3.2 Critical analysis

In order to obtain simplified and analytical solution for the spalling rates, we inevitably introduced some strong assumptions, including the activity assumption, the constant diffusivity in different zones, the leaching of only solid phase of CH, the constant concentration of aluminates in pore solution, and the instantaneous formation of AFt. This section is dedicated to the discussion of the advantages and limits of these assumptions so that the valid application scope of spalling rate models can be clarified.

The activity assumption comes first. Normally the ionic concentration and ionic activity are only equal in dilute solutions. The usual ionic strength of concrete (cement paste) pore solution is in the range of 0.25-0.5M[215], and this ionic environment does have impact on the value of ion activity: the activity coefficients of monovalent and divalent ions are estimated as 0.73∼0.74 and 0.19∼0.25 respectively, using the extended Debye-Hückel equation in Eq. (5.2). Then substituting these two ranges into Eq. (7.18) shows the supersaturation of ettringite, β_{AFt}, is decreased by $3\sim7\times10^{-4}$ when considering ionic strength and activity coefficients. Though the reduction of β_{AFt} is significant, the impact of activity coefficients on spalling rates, through Eq. (7.25) and Eq. (7.30), is found to be rather limited: the spalling rates in disk specimens and spalling depths in cylinder specimens are increased by up to 5% and 7% respectively when considering activity coefficients, see in Figure 7.14. Thus, considering activity coefficient or not will

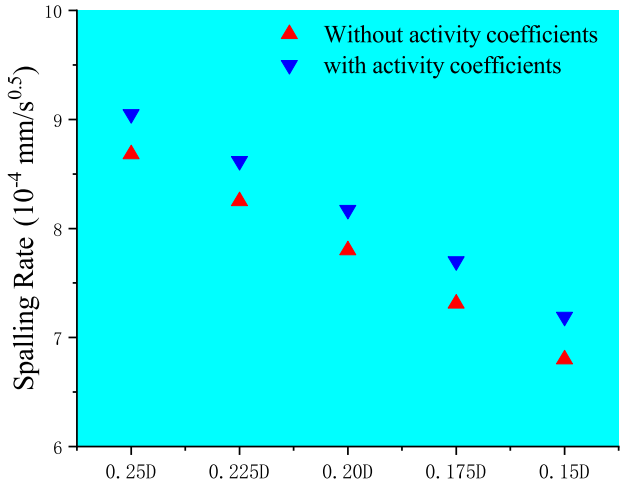

(a)

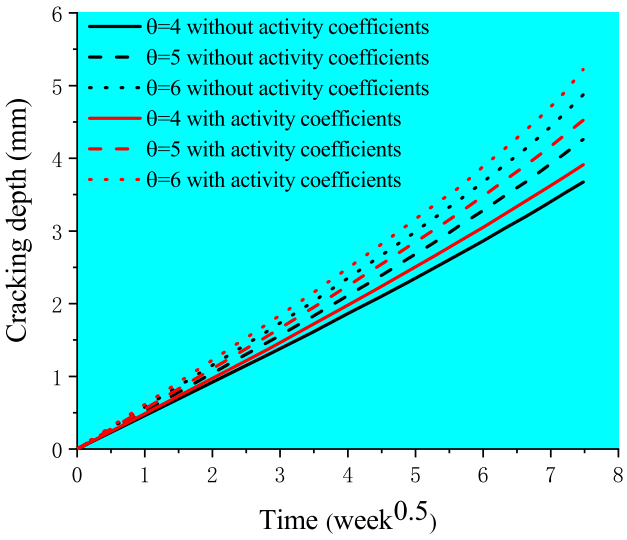

(b)

Figure 7.14 Spalling rates in terms of apparent sulfate diffusvities (same range as Figure 6(a) in the text) considering or not the activity coefficients for disk cement paste specimens (w/c=0.55) exposed to sodium sulfate solution of 10 g/L SO_4^{2-} (a) and spalling depths in terms of exposure time for different magnification coefficient (θ) of apparent sulfate diffusvities considering or not the activity coefficients for cylinder cement paste specimens (w/c=0.485) exposed to sodium sulfate solution of 10 g/L $_4^{2-}$.

has very limited impact on the spalling rates calculated from the models.

Then come the constant diffusivity. On space scale, constant values of apparent diffusivity are attributed to the three zones: the dissolved zone Z_1, the crystallized zone Z_2 and the intact zone Z_3 in Figure 7.1, or the cracked zone Z_1, the uncracked zone Z_2

and the intact zone Z_3 in Figure 7.3. For Z_1 in Figure 7.1, the AFt and CH are assumed totally dissolved, the pore structure is altered accordingly, and it is rational to assume a constant diffusivity. For Z_1 in Figure 7.3, the crack openings provide more efficient transport channels for pore species to transport. Considering the relevant experimental results(θ=4-7[244]), it is rational to attribute a different diffusivity from the bulk concrete. But here, the attributed diffusivity remains constant during the spalling process, meaning that the crack openings should be stable otherwise the model in Section 2.4.2 should be reviewed. For Z_2, either the crystallized zone (Figure 7.1) or uncracked zone (Figure 7.3), the formation of AFt and the leaching of CH are assumed to cancelled their respective effect, pore filling or enlarging, on pore structure, and the diffusivity of intact concrete is taken. For Z_3 zones, the intact concrete properties are retained due to the very limited AFt formation and no leaching state. Thus, the zone Z_2 and Z_3 merge into one region in terms of the transport properties. On time scale, the diffusivity is also assumed constant. This is challenged by some experimental works[25,35,37], which showed the apparent diffusivity decreasing rapidly with exposure time during ESA. It is an alert for the model application: for real engineering cases, one should use long-term diffusivity values instead of the short-term diffusivity values measured in laboratory.

Then come the leaching, the aluminate concentration and AFt formation. As aforementioned, if leaching involves only portlandite, the buffering capacity of CSH, the main cement hydrates, is neglected, leading to the overestimation of leaching rate κ and leaching front X_L. This assumption will be reasonable for CBM using the Portland cement as the main component of binder of which the CH content is important compared to CSH. For binders containing large quantity of SCMs, this assumption possible gives spalling rates too overestimated to be useful due to the (very) low CH content. Further, the assumption of constant aluminate concentration as its value in intact pore solution, cf. Eq.(7.17), also overestimates its real value, which should be scaled to the actual concentrations of Ca^{2+} and OH^-. Accordingly, the supersaturation in Eq.(7.2) is also overestimated, in turn leading to the overestimation of spalling rate. Thus, both assumptions lead to overestimation of spalling rates, i.e. results on conservative side in engineering terms. An improvement may be to include the aluminate ions into the pore transport and establish a new dissolution front for the solid aluminate phases. In our models, the AFt amount is set to be proportional to the sulfate concentration in pore solution, cf. Eq.(7.8). This has double implications: first, the sulfate reaction is complete and will consume out all the solid alu-

minate phase; second, the AFt formation is instantaneous without kinetics. So far, there is no unanimity on the kinetics of ettringite crystallization: authors adopted the first-order or second-order reaction assumption in the literature[17,30,208]. But, some experimental results seem to support, at least partially, our assumption: the relative ettringite content measured by the energy dispersive X-ray diffraction (EDXRD) approches the sulfate concentration profile[37]. So, our assumption tends to overestimate the quantity and rate of AFt formation, leading to the overestimation of the supersaturation, effective stress and spalling rate.

To summarize, the assumptions taken in the models, such as leaching of only CH phase, constant aluminate concentration and complete/instantaneous AFt formation, all lead to the overestimation of the effective stress and the spalling rate. In engineering terms, the models provide predictions on conservative side. The constant diffusivity assumption makes trade-off of detailed pore chemistry with simplified and analytical solutions for spalling rates. The model validations in Section 3 confirm the correct magnitude order and the conservative nature of spalling rates predicted by our models, and such models can already help the engineers to choose the appropriate design options. Actually, such models are just expected to provide correct prediction on the order of magnitude of spalling rate, and prudence should be taken as the models are confronted with experimental results. The models should be more reasonably applied to CBM using mainly Portland cement as binder. Moreover, the application of these models should check the actual strain and stress conditions of elements to make the correct choice of damage patterns, especially as external loading and reinforcement are present in structural elements. Last point to be noted is the external sulfate environments: the models apply only as the sulfates dominate in the external aggressive agents; as the other aggressive ions, such as magnesium and chlorides, are present with important concentrations, other damage mechanisms intervene and these models lose their validity.

7.4 Conclusion

1. A spalling rate model is proposed for CBM exposed to the combined action of ESA and leaching. The pore transport considers the dissolution-diffusion of hydroxide ions and the binding-diffusion of external sulfate ions. The formation of AFt is dictated by the supersaturation degree, the effective stress from pore crystallization is evaluated through poromechanics using the Correns' law, and the fracture criterion is set as the effective tensile stress attaining the tensile strength. The spalling depth is defined as the position where the fracture criterion is satisfied. Two sub-models are developed with respect to two damage patterns: the surface layered spalling and the surface in-plane cracking. For these two cases, the semi-infinite space is divided into three zones: dissolved/cracked zone, crystallized/uncracked zone and the intact zone to leaching. On this basis, the dual moving boundary problems are established and solved for the sulfate and hydroxide profiles. The moving rates for dissolved/cracking front and leaching front are also solved as proportional to the square root of exposure time, so is the spalling depth. Such models incorporate the main knowledge of CBM damage by sulfate chemical reactions and provide analytical results for the damage rate.

2. The established models are validated against two sets of experiments on cement paste specimens exposed to external sulfate solution with pH value of solution controlled to neutral state. The sub-model for layered damage pattern, without cracking effect on diffusivity, is validated against uni-dimensional sulfate diffusion on disk specimens in PIII-2 condition, and the spalling depths measured are used to validate the sub-model. With the consideration of decreased diffusivity by ageing effect, the model gives conservative prediction for spalling rate but on the same order of magnitude as measured one. Then, the sub-model for in-plane cracking is employed to predict the sulfate attack on smaller cylinder specimens. With the help of coordinate transformation, the spalling rate is predicted using the usual range values for cracking magnification for diffusivity, and the model prediction gives conservative results but in good agreement with measured cracking depths. Through the validations, the spalling depth is first confirmed to scale linearly with the square root of exposure time, indicating the the sulfate damage is dominated by diffusion processes. Due to the conservative nature and correct prediction on magnitude order of spalling depth, these models have good potential for engineering use.

3. For the spalling rate model, four groups of parameters interplay: the diffusivities, the boundary ionic concentrations, the contents of reactive solid phases, and the mechani-

cal properties related to fracture. Through dimensionless quantity analysis, the normalized spalling rate drops rapidly as the normalized sulfate concentration and the relative sulfate diffusivity decrease. The single parameter analysis shows that the sulfate diffusivity, in physical aspect, and the aluminate content, in chemical aspect, are two foremost impact factors for spalling damage rate, which provides the basis for technical specification for CBM exposed in such environments. For the intensity classification of combined action of ESA and leaching, the gradation on logarithmic scale of external sulfate concentration is more appropriate. The portlandite content has less important impact on the spalling rate, so the CH content is not relevant to the spalling rate control.

4. Some strong assumptions are made in the modeling for the sake of simplified models and analytical results for spalling depth. Among these assumptions, the leaching of only CH phase, the constant aluminate concentration and complete/instantaneous AFt formation all leads to the overestimation of the effective stress and the spalling rate, and the activity coefficient has few impact on spalling rate. The models will be more reasonably applied to CBM using Portland cement as the main component of binder. As long as the prediction is on the correct order of magnitude for spalling depth, the conservative nature of prediction is favored by engineering use. The constant diffusivity assumption on time scale needs attention when the models are applied to real engineering cases, and the long-term diffusivity values should be used instead of laboratory short-term measurements or theoretically estimated value because ageing can occur for diffusivity. Moreover, as other aggressive ions (Mg^{2+}, Cl^{-}) are present along with sulfates in an important concentration, the models should not be used as the damage mechanism would be different from AFt formation.

CHAPTER 8 GENERAL CONCLUSIONS

8.1 Conclusions

1. The high sulfate concentration and the heating treatment accelerate the AFt formation, but the chlorides inhibit the AFt formation. The accelerating effects of these factors are ordered as: DEF > high sulfate concentration > chlorides(decelerating). The high sulfate concentration and the heating treatment lead to higher AFt supersaturation. The chlorides alter the multi-phase equilibria with the pore solution, resulting in a decrease in aluminate concentration and AFt supersaturation. The change in AFt supersaturation coincides with the change in AFt formation rate. Based on this point, a kinetic law is proposed to account for the important change on the AFt formation rate with the AFt supersaturation. The kinetic law is fitted from the measured AFt content with time in Part II experimental work. An exponential relation between the AFt formation rate and the AFt supersaturation is adopted, and the exponential order is fitted as 1.90.

2. For pure ESA, sulfate reacts with aluminum phases to form AFt, and the AFt crystallization occurs in the whole range of pore space of hardened cement paste. The AFt crystals, formed in the micropores of interposed outer CSH from different cement grains, fill up the neck pores and block the enclosed pore space in the ”ink-bottle” pores. In the range of 40-100nm, the AFt precipitation and AFm/CH dissolution interplay together to influence the pore volume. The continuous AFt formation in micropores the reopened “ink-bottle” pores and leads to microcracks. The pore crystallization of AFt leads to the corresponding change in transport property and mechanical behavior. The pore-filling by AFt crystals causes a decrease in apparent vapour diffusivity, and the subsequent AFt formation induces microcracks and augments the vapour diffusivity. The AFt crystallization in the pore-neck part of micropores would be the direct source for pore pressure generation and material expansion. The expansion of the specimen is closely related to the evolution of the measured AFt content. The linear expansion stage is well captured by classical poromechanics.

3. Chlorides obviously mitigate the ESA damage. Chlorides convert part of the AFm phases into TAH phase, reducing AFt formation, and a higher concentration of chlorides results in a slower AFt generation rate. The presence of chlorides also leads to a reduction in the supersaturation of AFt crystals, and this effect, as well as the reducing effect

on AFt formation, results in the mitigating effect on expansion damage. For the change in transport properties, the presence of chlorides offsets the pore-filling of AFt formation in early exposure and even increases the vapour diffusivity due to the synthetic effect from AFm/CH dissolution. Besides, chlorides mitigate the sulfate ingress, the sulfate binding rate, and the occurrence of cracking. Adding chlorides reduces the activity coefficients of calcium ions and the supersaturation of gypsum, leading to a smaller generation rate of gypsum and a less promotion effect on leaching damage of solid matrix of materials as well. The sulfates, in turn, reduce the bound chlorides significantly through the transformation of Friedel's salts. These aspects constitute the interaction mechanism between sulfates and chlorides during ESA.

4. Leaching significantly accelerates ESA damage. The leaching specimens show more rapid sulfate ingress and contain more bound sulfates compared to non-leaching specimens. The leaching specimens crack faster and show larger cracks, and the cracks parallel to the exposure surface display a spalling pattern of damage. Gypsum is found to be a special product in leaching condition from the mineral phase distribution by XRD. Through a simplified chemical model, we found that the absence of gypsum in the non-leaching specimens is due to the very low calcium activity in the highly alkaline pore solution whilst the formation of gypsum in the leaching specimens is due to the direct reaction between the portlandite and the low-pH sulfate-bearing solution (PIII-2) which penetrates into the cracks in the solid matrix. The formation of gypsum is the consequence of solid matrix fracture rather than its cause in the leaching specimens. Through a gypsum formation model in a cylindrical crack, the gypsum formation in cracks depends closely on, among other factors, the crack size and the external sulfate concentration, and the possible pressure during gypsum crystal growth in cracks is too low to be likely to contribute to the crack propagation.

5. DEF (heating treatment) aggravates the ESA damage. The heating treatment dissolves the formed AFt in the early curing period into the TAH phase, and initiates the microcracks during the later cooling storage. Under the combined ESA and DEF conditions, the sulfates come from both the external environment and the material itself, leading to a larger formation rate of AFt compared to the ESA condition alone. The rapid formation of ettringite accelerates the enclose and reopen of "ink-bottle" pores in MIP curves. In addition, the microcracks formed inside the materials in DEF conditions reduce the materials' resistance to deformation. Also, the heating treatment (DEF) accelerates the

sulfate ingress, ESA expansion, and cracking damage. Though DEF has little impact on chloride binding, it promotes the penetration of free chlorides into specimens due to the initiation of microcracks by heating treatment. In combined ESA, DEF and chlorides condition, the aggravating effect of DEF exceeds the mitigating effect of chlorides on ESA damage. The aggravating effects of the investigated coupling actions are ordered as: DEF > leaching > chlorides(mitigating).

6. A chemo-poromechanical model based on crystallization pressure and crystal growth kinetics is proposed to predict the expansion damage of CBM exposed to sulfate attack with and without chlorides. The proposed kinetic law is applied to the pore crystallization processes in two directions of crystal, the pore invasion process in the axial direction and the pore deformation process in the radial direction. And two corresponding rate constants, K_r and K_p, are proposed in this model. The crystallization pressure during the crystallization process is derived from the deformation assumption, isotropic deformation, incompressible solid matrix, and constitutive equations of linear elastic porous materials. Then the effective stress and the consequent damage are addressed in a poromechanical approach. The predicted expansions show good consistency with the experimental results in this study and in the literature.

7. A spalling rate model is established to estimate the damage of CBM subjected to the combined action of leaching and ESA. Two sub-models are developed to consider the different damage patterns. The profiles of sulfate and hydroxide ions are obtained from the solution of a dual moving boundary problem (MBP). The supersaturation of ettringite crystal is evaluated from these profiles, the effective stress is calculated through poromechanics for pore crystallization, and the spalling depth is determined using the fracture criterion. The experimental validation confirms the proportionality between the spalling depth and the square root of exposure time, and the models give conservative results but on the correct magnitude order for spalling depth. The parametric analysis shows the foremost impact of aluminate content and sulfate diffusivity on the damage rate. The main assumptions in models lead to conservative predictions, but yet the model results are meaningful for engineering use.

8.2 Perspectives

1. In Part I, the abnormal drop of AFt content at 28d immersion of powder samples makes it difficult to analyze. Although we have fitted a kinetic law based on the measured

AFt content with time on 2mm slice specimens in Part II, the explanation of the rate constant in the law still needs further support. Therefore, a further investigation on the kinetics of AFt formation in CBM, especially the rate constant, is required.

2. In Part II, the effects of the AFt formation, including pore filling effect and cracking effect, on vapour diffusivity are qualitatively investigated. It is useful to develop a quantitative model to account for the change of transport properties, especially sulfate diffusivity, in terms of AFt formation. It will help us predict the sulfate transport and the consequent damage of CBM subjected to ESA.

3. In the chemo-poromechanical model, the diffusion process is not yet developed. The diffusion process has an essential influence on the ion concentrations and AFt supersaturation. The AFt supersaturation impacts both the AFt formation and the AFt crystallization pressure. Therefore, it is necessary to take the diffusion process into consideration for the simulations to have more practical use.

REFERENCES

[1] National Minerals Information Center. Mineral commodity summaries 2022[R/OL]. 2022: 44-45. https://pubs.usgs.gov/periodicals/mcs2022/mcs2022-cement.pdf.

[2] Skalny J, Brown P. Sulfate attack on concrete[M]. Taylor & Francis, 2002.

[3] Mehta R K. Concrete technology for sustainable development – an overview of essential principles[C]//Concrete technology for sustainable development in the 21st century. New Delhi: Cement Manufactures' Association, 1999: 1-22.

[4] Lei M, Peng L, Shi C, et al. Experimental study on the damage mechanism of tunnel structure suffering from sulfate attack[J/OL]. Tunnelling and Underground Space Technology, 2013, 36: 5-13. DOI: https://doi.org/10.1016/j.tust.2013.01.007.

[5] Harboe E M. Longtime studies and field experiences with sulfate attack[J]. Special Publication, 1982, 77: 1-20.

[6] Al-Amoudi O S B. Sulfate attack and reinforcement corrosion in plain and blended cements exposed to sulfate environments[J/OL]. Building and Environment, 1998, 33(1): 53-61. DOI: https://doi.org/10.1016/S0360-1323(97)00022-X.

[7] WEI Q, LI B, LI X. Analysis on the characters of soil salinization in the turpan basin[J]. Journal of Arid Land Resources and Environment, 2014, 4: 163-167.

[8] Fengxian L, Hua W, Yongjian W. Corrosion evaluation of the groundwater and soils in tianjin area[J]. Soil Engineering and Foundation, 2015, 29(2): 100.

[9] Li K, Li Q, Zhou X, et al. Durability design of the hong kong-zhuhai-macau sea-link project: Principle and procedure[J]. J. Bridge Eng, 2015, 20: 04015001.

[10] Maes M, De Belie N. Resistance of concrete and mortar against combined attack of chloride and sodium sulphate[J/OL]. Cement and Concrete Composites, 2014, 53: 59-72. DOI: https://doi.org/10.1016/j.cemconcomp.2014.06.013.

[11] Irbe L, Beddoe R, Heinz D. The role of aluminium in c-a-s-h during sulfate attack on concrete [J/OL]. Cement and Concrete Research, 2019, 116: 71-80. DOI: https://doi.org/10.1016/j.cemconres.2018.11.012.

[12] Gu Y, Martin R P, Omikrine Metalssi O, et al. Pore size analyses of cement paste exposed to external sulfate attack and delayed ettringite formation[J/OL]. Cement and Concrete Research, 2019, 123: 105766. DOI: https://doi.org/10.1016/j.cemconres.2019.05.011.

[13] Zhang Z, Zhou J, Yang J, et al. Understanding of the deterioration characteristic of concrete exposed to external sulfate attack: Insight into mesoscopic pore structures[J/OL]. Construction and Building Materials, 2020, 260: 119932. DOI: https://doi.org/10.1016/j.conbuildmat.2020.119932.

[14] Ikumi T, Segura I, Cavalaro S H. Effects of biaxial confinement in mortars exposed to external sulfate attack[J/OL]. Cement and Concrete Composites, 2019, 95: 111-127. DOI: https://doi.org/10.1016/j.cemconcomp.2018.10.017.

[15] Haufe J, Vollpracht A. Tensile strength of concrete exposed to sulfate attack[J/OL]. Cement and Concrete Research, 2019, 116: 81-88. DOI: https://doi.org/10.1016/j.cemconres.2018.11.005.

[16] Taylor H F, et al. Cement chemistry: volume 2[M]. Thomas Telford London, 1997.

[17] Tixier R, Mobasher B. Modeling of damage in cement-based materials subjected to external sulfate attack. i: Formulation[J]. Journal of Materials in Civil Engineering, 2003, 15(4): 305-313.

[18] Idiart A E, López C M, Carol I. Chemo-mechanical analysis of concrete cracking and degradation due to external sulfate attack: A meso-scale model[J/OL]. Cement and Concrete Composites, 2011, 33(3): 411-423. DOI: https://doi.org/10.1016/j.cemconcomp.2010.12.001.

[19] Santhanam M, Cohen M, Olek J. Differentiating seawater and groundwater sulfate attack in portland cement mortars[J/OL]. Cement and Concrete Research, 2006, 36(12): 2132-2137. DOI: https://doi.org/10.1016/j.cemconres.2006.09.011.

[20] Santhanam M, Cohen M D, Olek J. Mechanism of sulfate attack: a fresh look: Part 2. proposed mechanisms[J/OL]. Cement and Concrete Research, 2003, 33(3): 341-346. DOI: https://doi.org/10.1016/S0008-8846(02)00958-4.

[21] Scrivener K, Snellings R, Lothenbach B, et al. A practical guide to microstructural analysis of cementitious materials: volume 540[M]. Crc Press Boca Raton, FL, USA:, 2016.

[22] Müllauer W, Beddoe R E, Heinz D. Sulfate attack expansion mechanisms[J/OL]. Cement and Concrete Research, 2013, 52: 208-215. DOI: https://doi.org/10.1016/j.cemconres.2013.07.005.

[23] Scrivener K, Füllmann T, Gallucci E, et al. Quantitative study of portland cement hydration by x-ray diffraction/rietveld analysis and independent methods[J/OL]. Cement and Concrete Research, 2004, 34(9): 1541-1547. DOI: https://doi.org/10.1016/j.cemconres.2004.04.014.

[24] Andersen M D, Jakobsen H J, Skibsted J. A new aluminium-hydrate species in hydrated portland cements characterized by 27al and 29si mas nmr spectroscopy[J]. Cement and Concrete Research, 2006, 36(1): 3-17.

[25] Ragoug R, Metalssi O O, Barberon F, et al. Durability of cement pastes exposed to external sulfate attack and leaching: Physical and chemical aspects[J/OL]. Cement and Concrete Research, 2019, 116: 134-145. DOI: https://doi.org/10.1016/j.cemconres.2018.11.006.

[26] Tixier R. Microstructural development and sulfate attack modeling in blended cement-based materials[D]. Arizona State University, 2000.

[27] Qin S, Zou D, Liu T, et al. A chemo-transport-damage model for concrete under external sulfate attack[J/OL]. Cement and Concrete Research, 2020, 132: 106048. DOI: https://doi.org/10.1016/j.cemconres.2020.106048.

[28] Zuo X B, Sun W, Yu C. Numerical investigation on expansive volume strain in concrete subjected to sulfate attack[J/OL]. Construction and Building Materials, 2012, 36: 404-410. DOI: https://doi.org/10.1016/j.conbuildmat.2012.05.020.

[29] Cefis N, Comi C. Chemo-mechanical modelling of the external sulfate attack in concrete[J/OL]. Cement and Concrete Research, 2017, 93: 57-70. DOI: https://doi.org/10.1016/j.cemconres.2016.12.003.

[30] Bary B, Leterrier N, Deville E, et al. Coupled chemo-transport-mechanical modelling and numerical simulation of external sulfate attack in mortar[J/OL]. Cement and Concrete Composites, 2014, 49: 70-83. DOI: https://doi.org/10.1016/j.cemconcomp.2013.12.010.

[31] Gu Y, Dangla P, Martin R P, et al. Modeling the sulfate attack induced expansion of cementitious materials based on interface-controlled crystal growth mechanisms[J/OL]. Cement and Concrete Research, 2022, 152: 106676. DOI: https://doi.org/10.1016/j.cemconres.2021.106676.

[32] Soive A, Tran V Q. External sulfate attack of cementitious materials: New insights gained through numerical modeling including dissolution/precipitation kinetics and surface complexation[J/OL]. Cement and Concrete Composites, 2017, 83: 263-272. DOI: https://doi.org/10.1016/j.cemconcomp.2017.07.024.

[33] Coussy O. Mechanics and physics of porous solids[M]. John Wiley & Sons, 2011.

[34] Baur I, Keller P, Mavrocordatos D, et al. Dissolution-precipitation behaviour of ettringite, monosulfate, and calcium silicate hydrate[J/OL]. Cement and Concrete Research, 2004, 34(2): 341-348. DOI: https://doi.org/10.1016/j.cemconres.2003.08.016.

[35] Tumidajski P J, Chan G, Philipose K E. An effective diffusivity for sulfate transport into concrete[J/OL]. Cement and Concrete Research, 1995, 25(6): 1159-1163. DOI: https://doi.org/10.1016/0008-8846(95)00108-O.

[36] Ragoug R. Attaque sulfatique externe des matériaux cimentaires : Impact de différents facteurs âge, composition du liant, présence de chlorures: 2016PESC1148[D/OL]. Université Paris-Est, 2016. https://tel.archives-ouvertes.fr/tel-01552785.

[37] Naik N N. Sulfate attack on portland cement-based materials: mechanisms of damage and long-term performance[M]. Georgia Institute of Technology, 2003.

[38] Schmidt T, Lothenbach B, Romer M, et al. Physical and microstructural aspects of sulfate attack on ordinary and limestone blended portland cements[J/OL]. Cement and Concrete Research, 2009, 39(12): 1111-1121. DOI: https://doi.org/10.1016/j.cemconres.2009.08.005.

[39] Brown P, Hooton R, Clark B. Microstructural changes in concretes with sulfate exposure[J/OL]. Cement and Concrete Composites, 2004, 26(8): 993-999. DOI: https://doi.org/10.1016/j.cemconcomp.2004.02.033.

[40] Tosun K, Baradan B. Effect of ettringite morphology on def-related expansion[J/OL]. Cement and Concrete Composites, 2010, 32(4): 271-280. DOI: https://doi.org/10.1016/j.cemconcomp.2010.01.002.

[41] Samson E, Marchand J. Modeling the transport of ions in unsaturated cement-based materials [J/OL]. Computers & Structures, 2007, 85(23): 1740-1756. DOI: https://doi.org/10.1016/j.compstruc.2007.04.008.

[42] Yu Y, Zhang Y, Khennane A. Numerical modelling of degradation of cement-based materials under leaching and external sulfate attack[J/OL]. Computers & Structures, 2015, 158: 1-14. DOI: https://doi.org/10.1016/j.compstruc.2015.05.030.

[43] Sarkar S, Mahadevan S, Meeussen J, et al. Numerical simulation of cementitious materials degradation under external sulfate attack[J/OL]. Cement and Concrete Composites, 2010, 32(3): 241-252. DOI: https://doi.org/10.1016/j.cemconcomp.2009.12.005.

[44] Krajcinovic D, Basista M, Mallick K, et al. Chemo-micromechanics of brittle solids[J/OL]. Journal of the Mechanics and Physics of Solids, 1992, 40(5): 965-990. DOI: https://doi.org/10.1016/0022-5096(92)90058-A.

[45] Karihaloo B L. Fracture mechanics & structural concrete[J/OL]. Longman Scientific and Technical, 1995. DOI: https://doi.org/10.1007/BF00035376.

[46] Tian B, Cohen M D. Does gypsum formation during sulfate attack on concrete lead to expansion?[J/OL]. Cement and Concrete Research, 2000, 30(1): 117-123. DOI: https://doi.org/10.1016/S0008-8846(99)00211-2.

[47] Kunther W, Lothenbach B, Scrivener K. Influence of bicarbonate ions on the deterioration of mortar bars in sulfate solutions[J/OL]. Cement and Concrete Research, 2013, 44: 77-86. DOI: https://doi.org/10.1016/j.cemconres.2012.10.016.

[48] Santhanam M, Cohen M D, Olek J. Mechanism of sulfate attack: A fresh look: Part 1: Summary of experimental results[J/OL]. Cement and Concrete Research, 2002, 32(6): 915-921. DOI: https://doi.org/10.1016/S0008-8846(02)00724-X.

[49] Lee S T, Park D W, Ann K Y. Mitigating effect of chloride ions on sulfate attack of cement mortars with or without silica fume[J]. Canadian Journal of Civil Engineering, 2008, 35(11): 1210-1220.

[50] Yu C, Sun W, Scrivener K. Mechanism of expansion of mortars immersed in sodium sulfate solutions[J/OL]. Cement and Concrete Research, 2013, 43: 105-111. DOI: https://doi.org/10.1016/j.cemconres.2012.10.001.

[51] Jirásek M, Patzák B. Consistent tangent stiffness for nonlocal damage models[J/OL]. Computers & Structures, 2002, 80(14): 1279-1293. DOI: https://doi.org/10.1016/S0045-7949(02)00078-0.

[52] Gollop R, Taylor H. Microstructural and microanalytical studies of sulfate attack. i. ordinary portland cement paste[J]. Cement and Concrete Research, 1992, 22(6): 1027-1038.

[53] Gollop R, Taylor H. Microstructural and microanalytical studies of sulfate attack. ii. sulfate-resisting portland cement: Ferrite composition and hydration chemistry[J]. Cement and Concrete Research, 1994, 24(7): 1347-1358.

[54] Gollop R, Taylor H. Microstructural and microanalytical studies of sulfate attack iii. sulfate-resisting portland cement: Reactions with sodium and magnesium sulfate solutions[J]. Cement and Concrete research, 1995, 25(7): 1581-1590.

[55] Gollop R, Taylor H. Microstructural and microanalytical studies of sulfate attack. iv. reactions of a slag cement paste with sodium and magnesium sulfate solutions[J]. Cement and Concrete Research, 1996, 26(7): 1013-1028.

[56] Lagerblad B. Long term test of concrete resistance against sulphate attack[C]//Seminar on Sulfate Attack Mechanisms. 1998: 325-336.

[57] Atkinson A, Hearne J A. Mechanistic model for the durability of concrete barriers exposed to sulphate-bearing groundwaters[J]. MRS Online Proceedings Library (OPL), 1989, 176.

[58] Þorvaldsson Þ, Larmour R. The action of sulphates on the components of portland cement[M]. 1927.

[59] Cohen M. Modeling of expansive cements[J]. Cement and Concrete Research, 1983, 13(4): 519-528.

[60] Mehta P. Mechanism of expansion associated with ettringite formation[J/OL]. Cement and Concrete Research, 1973, 3(1): 1-6. DOI: https://doi.org/10.1016/0008-8846(73)90056-2.

[61] Rasheeduzzafar. Influence of cement composition on concrete durability[J]. ACI Materials Journal, 1992, 89(6): 574-586.

[62] Taylor H. Sulfate reactions in concrete–microstructural and chemical aspects[J]. Ceramic Transactions, 40 pp., 1994, 61.

[63] Scherer G W. Crystallization in pores[J/OL]. Cement and Concrete Research, 1999, 29(8): 1347-1358. DOI: https://doi.org/10.1016/S0008-8846(99)00002-2.

[64] Scherer G W. Stress from crystallization of salt[J/OL]. Cement and Concrete Research, 2004, 34(9): 1613-1624. DOI: https://doi.org/10.1016/j.cemconres.2003.12.034.

[65] Mehta P. Scanning electron micrographic studies of ettringite formation[J/OL]. Cement and Concrete Research, 1976, 6(2): 169-182. DOI: https://doi.org/10.1016/0008-8846(76)90115-0.

[66] Correns C W. Growth and dissolution of crystals under linear pressure[J]. Discussions of the Faraday society, 1949, 5: 267-271.

[67] Ostwald W. Über die vermeintliche isomerie des roten und gelben quecksilberoxyds und die oberflächenspannung fester körper[J]. Zeitschrift für physikalische Chemie, 1900, 34(1): 495-503.

[68] Freundlich H. Kapillarchemie: eine darstellung der chemie der kolloide und verwandter gebiete [M]. akademische Verlagsgesellschaft, 1922.

[69] Hansen W. Attack on portland cement concrete by alkali soils and waters-a critical review[J]. Highway Research Record, 1966(113).

[70] Hansen W. Crystal growth as a source of expansion in portland cement concrete[C]//Proc. ASTM: volume 63. 1963: 932-945.

[71] Mather B. Discussion of “the process of sulfate attack on cement mortars” by shen yang, xu zhongzi, and tang mingshu[J]. Advanced Cement Based Materials, 1997, 5(3-4): 109-110.

[72] Tian B, Cohen M D. Does gypsum formation during sulfate attack on concrete lead to expansion?[J/OL]. Cement and Concrete Research, 2000, 30(1): 117-123. DOI: https://doi.org/10.1016/S0008-8846(99)00211-2.

[73] Mehta P. Sulfate attack on concrete–a critical review[J]. Mater. Sci. Concr., IIIpp., 1992, 105.

[74] Santhanam M, Cohen M D, Olek J. Effects of gypsum formation on the performance of cement mortars during external sulfate attack[J/OL]. Cement and Concrete Research, 2003, 33(3): 325-332. DOI: https://doi.org/10.1016/S0008-8846(02)00955-9.

[75] Taylor H F. A method for predicting alkazi ion concentrations in cement pore solutions[J]. Advances in Cement Research, 1987, 1(1): 5-17.

[76] Brouwers H, vanEijk R. Alkali concentrations of pore solution in hydrating opc[J/OL]. Cement and Concrete Research, 2003, 33(2): 191-196. DOI: https://doi.org/10.1016/S0008-8846(02)01022-0.

[77] Chen W, Brouwers H. Alkali binding in hydrated portland cement paste[J/OL]. Cement and Concrete Research, 2010, 40(5): 716-722. DOI: https://doi.org/10.1016/j.cemconres.2009.12.007.

[78] LY/T 1251. Analysis methods of water soluble salts of forest soil[S]. 1999.

[79] ASTM C1580. Standard test method for water-soluble sulfate in soil[S]. 2020.

[80] BS 1377-3. Methods of test for soils for civil engineering purposes. chemical and electrochemical tests[S]. 2018.

[81] El-Hachem R, Rozière E, Grondin F, et al. Multi-criteria analysis of the mechanism of degradation of portland cement based mortars exposed to external sulphate attack[J/OL]. Cement and Concrete Research, 2012, 42(10): 1327-1335. DOI: https://doi.org/10.1016/j.cemconres.2012.06.005.

[82] Naik N, Jupe A, Stock S, et al. Sulfate attack monitored by microct and edxrd: Influence of cement type, water-to-cement ratio, and aggregate[J/OL]. Cement and Concrete Research, 2006, 36(1): 144-159. DOI: https://doi.org/10.1016/j.cemconres.2005.06.004.

[83] Heller L, Ben-Yair M. Effect of sulphate solutions on normal and sulphate-resisting portland cement[J]. Journal of applied chemistry, 1964, 14(1): 20-30.

[84] Lothenbach B, Bary B, Le Bescop P, et al. Sulfate ingress in portland cement[J/OL]. Cement and Concrete Research, 2010, 40(8): 1211-1225. DOI: https://doi.org/10.1016/j.cemconres.2010.04.004.

[85] ASTM C150. Standard specification for portland cement[S]. 2022.

[86] Bogue R H. Calculation of the compounds in portland cement[J]. Industrial & Engineering Chemistry Analytical Edition, 1929, 1(4): 192-197.

[87] Gollop R, Taylor H. Microstructural and microanalytical studies of sulfate attack. ii. sulfate-resisting portland cement: Ferrite composition and hydration chemistry[J/OL]. Cement and Concrete Research, 1994, 24(7): 1347-1358. DOI: https://doi.org/10.1016/0008-8846(94)90120-1.

[88] Baghabra Al-Amoudi O S. Attack on plain and blended cements exposed to aggressive sulfate environments[J/OL]. Cement and Concrete Composites, 2002, 24(3): 305-316. DOI: https://doi.org/10.1016/S0958-9465(01)00082-8.

[89] Monteiro P J, Kurtis K E. Time to failure for concrete exposed to severe sulfate attack[J/OL]. Cement and Concrete Research, 2003, 33(7): 987-993. DOI: https://doi.org/10.1016/S0008-8846(02)01097-9.

[90] European Standard EN 206-1. Concrete-specification, performance, production and conformity [S]. 2000.

[91] GB/T 50476. Standard for design of concrete structure durability[S]. 2019.

[92] ACI-318. Building code requirements for structural concrete and commentary[S]. 2019.

[93] ASTM C1012. Standard test method for length change of hydraulic-cement mortars exposed to a sulfate solution[S]. 2018.

[94] GB/T 749. Test methods for determining capacity of resisting sulfate corrode of cement[S]. 2008.

[95] Cohen M D, Bentur A. Durability of portland cement-silica fume pastes in magnesium and sodium sulfate solutions[J]. Materials Journal, 1988, 85(3): 148-157.

[96] Tumidajski P J, Turc I. A rapid test for sulfate ingress into concrete[J/OL]. Cement and Concrete Research, 1995, 25(5): 924-928. DOI: https://doi.org/10.1016/0008-8846(95)00084-P.

[97] Fathima Suma M, Santhanam M, Rahul A. The effect of specimen size on deterioration due to external sodium sulphate attack in full immersion studies[J/OL]. Cement and Concrete Composites, 2020, 114: 103806. DOI: https://doi.org/10.1016/j.cemconcomp.2020.103806.

[98] Brunetaud X, Khelifa M R, Al-Mukhtar M. Size effect of concrete samples on the kinetics of external sulfate attack[J/OL]. Cement and Concrete Composites, 2012, 34(3): 370-376. DOI: https://doi.org/10.1016/j.cemconcomp.2011.08.014.

[99] Ukpata J O, Muhammed Basheer P, Black L. Expansion of cem i and slag-blended cement mortars exposed to combined chloride-sulphate environments[J/OL]. Cement and Concrete Research, 2019, 123: 105794. DOI: https://doi.org/10.1016/j.cemconres.2019.105794.

[100] Brown P W. An evaluation of the sulfate resistance of cements in a controlled environment[J]. Cement and Concrete Research, 1981, 11(5-6): 719-727.

[101] Xiong C, Jiang L, Xu Y, et al. Deterioration of pastes exposed to leaching, external sulfate attack and the dual actions[J/OL]. Construction and Building Materials, 2016, 116: 52-62. DOI: https://doi.org/10.1016/j.conbuildmat.2016.04.133.

[102] Taylor H, Famy C, Scrivener K. Delayed ettringite formation[J/OL]. Cement and Concrete Research, 2001, 31(5): 683-693. DOI: https://doi.org/10.1016/S0008-8846(01)00466-5.

[103] Day R L. The effect of secondary ettringite formation on the durability of concrete: a literature analysis: RD108T[M]. 1992.

[104] Scrivener K, Damidot D, Famy C. Possible mechanisms of expansion of concrete exposed to elevated temperatures during curing (also known as def) and implications for avoidance of field problems[J]. Cement, Concrete and Aggregates, 1999, 21(1): 93-101.

[105] Odler I. Interaction between gypsum and the csh phase formed in c3s hydration[C]//7th international Congress on Chemistry of Cement: volume 4. 1980: 439-495.

[106] Fu Y. Delayed ettringite formation in portland cement products.[M]. University of Ottawa (Canada), 1996.

[107] Barbarulo R. Comportement des matériaux cimentaires: actions des sulfates et de la température [J]. LMT-ENS de Cachan, France, Thèse de Doctorat, 2002.

[108] Divet L, Randriambololona R. Delayed ettringite formation: The effect of temperature and basicity on the interaction of sulphate and c-s-h phase 11communicated by m. moranville-regourd. [J/OL]. Cement and Concrete Research, 1998, 28(3): 357-363. DOI: https://doi.org/10.1016/S0008-8846(98)00006-4.

[109] Fu Y, Xie P, Gu P, et al. Effect of temperature on sulphate adsorption/desorption by tricalcium silicate hydrates[J/OL]. Cement and Concrete Research, 1994, 24(8): 1428-1432. DOI: https://doi.org/10.1016/0008-8846(94)90156-2.

[110] Barbarulo R, Peycelon H, Leclercq S. Chemical equilibria between c–s–h and ettringite, at 20 and 85 °c[J/OL]. Cement and Concrete Research, 2007, 37(8): 1176-1181. DOI: https://doi.org/10.1016/j.cemconres.2007.04.013.

[111] Leklou N, Aubert J E, Escadeillas G. Microscopic observations of samples affected by delayed ettringite formation (def)[J]. Materials and Structures, 2009, 42(10): 1369-1378.

[112] Zhang Z, Olek J, Diamond S. Studies on delayed ettringite formation in early-age, heat-cured mortars: I. expansion measurements, changes in dynamic modulus of elasticity, and weight gains[J/OL]. Cement and Concrete Research, 2002, 32(11): 1729-1736. DOI: https://doi.org/10.1016/S0008-8846(02)00862-1.

[113] Escadeillas G, Aubert J E, Segerer M, et al. Some factors affecting delayed ettringite formation in heat-cured mortars[J/OL]. Cement and Concrete Research, 2007, 37(10): 1445-1452. DOI: https://doi.org/10.1016/j.cemconres.2007.07.004.

[114] Lewis M C. Heat curing and delayed ettringite formation in concretes.[D]. Imperial College London (University of London), 1996.

[115] Yang R, Lawrence C D, Lynsdale C J, et al. Delayed ettringite formation in heat-cured portland cement mortars[J/OL]. Cement and Concrete Research, 1999, 29(1): 17-25. DOI: https://doi.org/10.1016/S0008-8846(98)00168-9.

[116] ACI 116R. Cement and concrete terminology[S]. 2000.

[117] Hobbs D. Expansion and cracking of concrete attributed to delayed ettringite formation[J]. Proceedings of a 'technical Session–Ettringite: The sometimes host of destruction, American Concrete Institute, Seattle, Washington, SP-177, 1999: 151-181.

[118] Divet L, Pavoine A. Delayed ettringite formation in massive concrete structures: an account of some studies of degraded bridges[J]. International RILEM TC, 2004: 98-126.

[119] Flatt R J, Scherer G W. Thermodynamics of crystallization stresses in def[J/OL]. Cement and Concrete Research, 2008, 38(3): 325-336. DOI: https://doi.org/10.1016/j.cemconres.2007.10.002.

[120] Brunetaud X. Étude de l'influence de différents paramètres et de leurs interactions sur la cinétique de l'amplitude de la réaction sulfatique interne au béton[D]. Châtenay-Malabry, Ecole centrale de Paris, 2005.

[121] Gu Y. Experimental pore scale analysis and mechanical modeling of cement-based materials submitted to delayed ettringite formation and external sulfate attacks[D]. Université Paris-Est, 2018.

[122] Mohammed T U, Hamada H. Corrosion of steel bars in concrete with various steel surface conditions[J]. ACI Materials Journal, 2006, 103(4): 233.

[123] Angst U, Elsener B, Larsen C K, et al. Critical chloride content in reinforced concrete — a review[J/OL]. Cement and Concrete Research, 2009, 39(12): 1122-1138. DOI: https://doi.org/10.1016/j.cemconres.2009.08.006.

[124] Ramachandran V S, Seeley R, Polomark G. Free and combined chloride in hydrating cement and cement components[J]. Matériaux et Construction, 1984, 17(4): 285-289.

[125] Theissing E, Hest-Wardenier P, De Wind G. The combining of sodium chloride and calcium chloride by a number of different hardened cement pastes[J]. Cement and Concrete Research, 1978, 8(6): 683-691.

[126] Stroh J, Meng B, Emmerling F. Deterioration of hardened cement paste under combined sulphate-chloride attack investigated by synchrotron xrd[J/OL]. Solid State Sciences, 2016, 56: 29-44. DOI: https://doi.org/10.1016/j.solidstatesciences.2016.04.002.

[127] Glasser F, Kindness A, Stronach S. Stability and solubility relationships in afm phases: Part i. chloride, sulfate and hydroxide[J]. Cement and Concrete Research, 1999, 29(6): 861-866.

[128] Balonis M, Lothenbach B, Le Saout G, et al. Impact of chloride on the mineralogy of hydrated portland cement systems[J/OL]. Cement and Concrete Research, 2010, 40(7): 1009-1022. DOI: https://doi.org/10.1016/j.cemconres.2010.03.002.

[129] Brown P, Badger S. The distributions of bound sulfates and chlorides in concrete subjected to mixed nacl, mgso4, na2so4 attack[J/OL]. Cement and Concrete Research, 2000, 30(10): 1535-1542. DOI: https://doi.org/10.1016/S0008-8846(00)00386-0.

[130] Geng J, Easterbrook D, yuan Li L, et al. The stability of bound chlorides in cement paste with sulfate attack[J/OL]. Cement and Concrete Research, 2015, 68: 211-222. DOI: https://doi.org/10.1016/j.cemconres.2014.11.010.

[131] Hossain K M A. Performance of volcanic ash and pumice-based blended cements in sulphate and sulphate–chloride environments[J/OL]. Advances in Cement Research, 2006, 18(2): 71-82. DOI: 10.1680/adcr.2006.18.2.71.

[132] Kind V. Effect of chlorides on the speed of sulfate corrosion of portland cement[J]. BRE Digest No. 346, 1956, 22(1): 3-6.

[133] Corner H, Rippstain D. Effect of aqueous sodium chloride solution on ettringite[J]. Touindustrie-Zeitung (TIZ) Fachberichte, 1985, 9: 680-683.

[134] Johnston J, Grove C. The solubility of calcium hydroxide in aqueous salt solutions[J/OL]. Journal of the American Chemical Society, 1931, 53(11): 3976-3991. DOI: 10.1021/ja01362a009.

[135] Robinson R, Stokes R. Electrolyte solutions[M]. London, Butterworth, 1968.

[136] Helgeson H C, Kirkham D H, Flowers G C. Theoretical prediction of the thermodynamic behavior of aqueous electrolytes by high pressures and temperatures; iv, calculation of activity coefficients, osmotic coefficients, and apparent molal and standard and relative partial molal properties to 600°*c* and 5kb[J/OL]. American Journal of Science, 1981, 281(10): 1249-1516. DOI: 10.2475/ajs.281.10.1249.

[137] Lothenbach B, Zajac M. Application of thermodynamic modelling to hydrated cements[J/OL]. Cement and Concrete Research, 2019, 123: 105779. DOI: https://doi.org/10.1016/j.cemconres.2019.105779.

[138] Biczok I. Concrete corrosion and concrete protection[M]. Chemical Publishing Company, 1967.

[139] Kulik D A, Wagner T, Dmytrieva S V, et al. Gem-selektor geochemical modeling package: revised algorithm and gems3k numerical kernel for coupled simulation codes[J/OL]. Computational Geosciences, 2013, 17(1): 1-24. DOI: 10.1007/s10596-012-9310-6.

[140] De Weerdt K, Orsáková D, Geiker M. The impact of sulphate and magnesium on chloride binding in portland cement paste[J/OL]. Cement and Concrete Research, 2014, 65: 30-40. DOI: https://doi.org/10.1016/j.cemconres.2014.07.007.

[141] Tran V Q, Soive A, Bonnet S, et al. A numerical model including thermodynamic equilibrium, kinetic control and surface complexation in order to explain cation type effect on chloride binding capability of concrete[J/OL]. Construction and Building Materials, 2018, 191: 608-618. DOI: https://doi.org/10.1016/j.conbuildmat.2018.10.058.

[142] Al-Amoudi O S B, Maslehuddin M, Abdul-Al Y A. Role of chloride ions on expansion and strength reduction in plain and blended cements in sulfate environments[J/OL]. Construction and Building Materials, 1995, 9(1): 25-33. DOI: https://doi.org/10.1016/0950-0618(95)92857-D.

[143] Zhang M, Chen J, Lv Y, et al. Study on the expansion of concrete under attack of sulfate and sulfate–chloride ions[J/OL]. Construction and Building Materials, 2013, 39: 26-32. DOI: https://doi.org/10.1016/j.conbuildmat.2012.05.003.

[144] Li G, Zhang A, Song Z, et al. Ground granulated blast furnace slag effect on the durability of ternary cementitious system exposed to combined attack of chloride and sulfate[J/OL]. Construction and Building Materials, 2018, 158: 640-648. DOI: https://doi.org/10.1016/j.conbuildmat.2017.10.062.

[145] Yu Y, Gao W, Feng Y, et al. On the competitive antagonism effect in combined chloride-sulfate attack: A numerical exploration[J/OL]. Cement and Concrete Research, 2021, 144: 106406. DOI: https://doi.org/10.1016/j.cemconres.2021.106406.

[146] Mindess S, Young J F, Darwin D. Concrete[M]. Prentice hall, 2003.

[147] Choi Y S, Yang E I. Effect of calcium leaching on the pore structure, strength, and chloride penetration resistance in concrete specimens[J/OL]. Nuclear Engineering and Design, 2013, 259: 126-136. DOI: https://doi.org/10.1016/j.nucengdes.2013.02.049.

[148] Kurumisawa K, Haga K, Hayashi D, et al. Effects of calcium leaching on diffusion properties of hardened and altered cement pastes[J/OL]. Physics and Chemistry of the Earth, Parts A/B/C, 2017, 99: 175-183. DOI: https://doi.org/10.1016/j.pce.2017.03.007.

[149] Carde C, François R. Modelling the loss of strength and porosity increase due to the leaching of cement pastes[J/OL]. Cement and Concrete Composites, 1999, 21(3): 181-188. DOI: https://doi.org/10.1016/S0958-9465(98)00046-8.

[150] Jebli M, Jamin F, Garcia-Diaz E, et al. Influence of leaching on the local mechanical properties of an aggregate-cement paste composite[J/OL]. Cement and Concrete Composites, 2016, 73: 241-250. https://www.sciencedirect.com/science/article/pii/S0958946516301263. DOI: https://doi.org/10.1016/j.cemconcomp.2016.05.001.

[151] Gabrisová A, Havlica J, Sahu S. Stability of calcium sulphoaluminate hydrates in water solutions with various ph values[J/OL]. Cement and Concrete Research, 1991, 21(6): 1023-1027. DOI: https://doi.org/10.1016/0008-8846(91)90062-M.

[152] Haynes H. Sulfate attack on concrete: Laboratory vs. field experience[J]. Concrete International, 2002, 22: 64-70.

[153] Bonen D, Cohen M D. Magnesium sulfate attack on portland cement paste — ii. chemical and mineralogical analyses[J/OL]. Cement and Concrete Research, 1992, 22(4): 707-718. DOI: https://doi.org/10.1016/0008-8846(92)90023-O.

[154] Ferraris C, Clifton J, Stutzman P, et al. Mechanisms of degradation of portland cement-based systems by sulfate attack[J]. Mechanisms of chemical degradation of cement-based systems, 1997, 1997: 185-192.

[155] Sarkar S, Mahadevan S, Meeussen J, et al. Sensitivity analysis of damage in cement materials under sulfate attack and calcium leaching[J]. Journal of materials in civil engineering, 2012, 24 (4): 430-440.

[156] Jain J, Neithalath N. Analysis of calcium leaching behavior of plain and modified cement pastes in pure water[J/OL]. Cement and Concrete Composites, 2009, 31(3): 176-185. DOI: https://doi.org/10.1016/j.cemconcomp.2009.01.003.

[157] Nakarai K, Ishida T, Maekawa K. Modeling of calcium leaching from cement hydrates coupled with micro-pore formation[J/OL]. Journal of Advanced Concrete Technology, 2006, 4(3): 395-407. DOI: 10.3151/jact.4.395.

[158] Xu A, Shayan A, Baburamani P. Test methods for sulfate resistance of concrete and mechanism of sulfate attack-state of the art review: number 5[M]. 1998.

[159] Mehta P K, Monteiro P J. Concrete: microstructure, properties, and materials[M]. McGraw-Hill Education, 2014.

[160] Bonen D, Cohen M D. Magnesium sulfate attack on portland cement paste-i. microstructural analysis[J/OL]. Cement and Concrete Research, 1992, 22(1): 169-180. DOI: https://doi.org/10.1016/0008-8846(92)90147-N.

[161] Bonen D, Cohen M D. Magnesium sulfate attack on portland cement paste — ii. chemical and mineralogical analyses[J/OL]. Cement and Concrete Research, 1992, 22(4): 707-718. DOI: https://doi.org/10.1016/0008-8846(92)90023-O.

[162] Bensted J. A discussion of the review paper “sulphate attack research—whither now?” by m. santhanam, m.d. cohen, and j. olek[J/OL]. Cement and Concrete Research, 2002, 32(6): 995-1000. DOI: https://doi.org/10.1016/S0008-8846(02)00731-7.

[163] Stumm W, Morgan J J. Aquatic chemistry: chemical equilibria and rates in natural waters[M]. John Wiley & Sons, 2012.

[164] Harrison W, Teychenné D C. Sulphate resistance of buried concrete; second interim report on long-term investigation at northwick park: Monograph[M]. 1981.

[165] Thomas M, Bleszynski R, Scott C. Sulfate attack in a marine environment[J]. Materials Science of Concrete Special Volume: Sulfate Attack, 1999.

[166] Mangat P, El-Khatib J. Influence of initial curing on sulphate resistance of blended cement concrete[J]. Cement and Concrete Research, 1992, 22(6): 1089-1100.

[167] Lea F. The mechanism of sulphate attack on portland cement[J]. Canadian Journal of Research, 1949, 27(4): 297-302.

[168] Bear J, Bachmat Y. Introduction to modeling of transport phenomena in porous media: volume 4 [M]. Springer Science & Business Media, 2012.

[169] Hill R. Elastic properties of reinforced solids: some theoretical principles[J]. Journal of the Mechanics and Physics of Solids, 1963, 11(5): 357-372.

[170] Neville A. The confused world of sulfate attack on concrete[J/OL]. Cement and Concrete Research, 2004, 34(8): 1275-1296. DOI: https://doi.org/10.1016/j.cemconres.2004.04.004.

[171] DePuy G. Chemical resistance of concrete[J]. ASTM SPECIAL TECHNICAL PUBLICATION, 1994, 169: 263-281.

[172] EN 197-1. Cement, composition, specifications and conformity criteria for common cements [S]. 2011.

[173] Martin R P. Analyse sur structures modèles des effets mécaniques de la réaction sulfatique interne du béton[D]. Université Paris-Est, 2010.

[174] Hema J. The effects of liquid nitrogen on concrete hydration, microstructure, and properties [M]. The University of Texas at Austin, 2007.

[175] Sakurai J, Napolitano J. Modern quantum mechanics. 2-nd edition[M]. Person Education, 2014.

[176] Skibsted J, Henderson E, Jakobsen H J. Characterization of calcium aluminate phases in cements by aluminum-27 mas nmr spectroscopy[J]. Inorganic chemistry, 1993, 32(6): 1013-1027.

[177] d'Espinose de Lacaillerie J B, Fretigny C, Massiot D. Mas nmr spectra of quadrupolar nuclei in disordered solids: The czjzek model[J/OL]. Journal of Magnetic Resonance, 2008, 192(2): 244-251. DOI: https://doi.org/10.1016/j.jmr.2008.03.001.

[178] Garbalińska H, Bochenek M, Malorny W, et al. Comparative analysis of the dynamic vapor sorption (dvs) technique and the traditional method for sorption isotherms determination — exemplified at autoclaved aerated concrete samples of four density classes[J/OL]. Cement and Concrete Research, 2017, 91: 97-105. DOI: https://doi.org/10.1016/j.cemconres.2016.11.001.

[179] Baroghel-Bouny V. Water vapour sorption experiments on hardened cementitious materials. part ii: Essential tool for assessment of transport properties and for durability prediction[J/OL]. Cement and Concrete Research, 2007, 37(3): 438-454. DOI: https://doi.org/10.1016/j.cemcon res.2006.11.017.

[180] Thomson W. On the equilibrium of vapour at a curved surface of liquid[J]. Proceedings of the Royal Society of Edinburgh, 1872, 7: 63-68.

[181] Li K. Durability design of concrete structures: Phenomena, modeling, and practice[M]. John Wiley & Sons, 2016.

[182] Washburn E W. Note on a method of determining the distribution of pore sizes in a porous material[J]. Proceedings of the National academy of Sciences of the United States of America, 1921, 7(4): 115.

[183] Winslow D N. The validity of high pressure mercury intrusion porosimetry[J]. Journal of Colloid and Interface Science, 1978, 67(1): 42-47.

[184] Adolphs J, Setzer M, Heine P. Changes in pore structure and mercury contact angle of hardened cement paste depending on relative humidity[J]. Materials and Structures, 2002, 35(8): 477-486.

[185] Giesche H. Mercury porosimetry: a general (practical) overview[J]. Particle & particle systems characterization, 2006, 23(1): 9-19.

[186] Zeng Q, Li K, Fen-chong T, et al. Pore structure characterization of cement pastes blended with high-volume fly-ash[J/OL]. Cement and Concrete Research, 2012, 42(1): 194-204. DOI: https://doi.org/10.1016/j.cemconres.2011.09.012.

[187] Bragg W H, Bragg W L. The reflection of x-rays by crystals[J]. Proceedings of the Royal Society of London. Series A, Containing Papers of a Mathematical and Physical Character, 1913, 88(605): 428-438.

[188] Touzet P, Druon M, Hantbout R, et al. Recueil des modes opératoires pour l'analyse des ciments, bétons, roches et sols[J]. Laboratoire Centrale des Ponts et Chaussées, 1993.

[189] BS EN 14629:2007. Products and systems for the protection and repair of concrete structures, test methods, determination of chloride content in hardened concrete[S]. British Standards Institute, London, 2007.

[190] BS EN 480-10:2009. Admixtures for concrete, mortar and grout test methods—part 10: Determination of water soluble chloride content[S]. British Standards Institute, London, 2009.

[191] Baquerizo L G, Matschei T, Scrivener K L, et al. Hydration states of afm cement phases[J/OL]. Cement and Concrete Research, 2015, 73: 143-157. DOI: https://doi.org/10.1016/j.cemconres.2015.02.011.

[192] Matschei T, Lothenbach B, Glasser F. The afm phase in portland cement[J]. Cement and concrete research, 2007, 37(2): 118-130.

[193] Birnin-Yauri U, Glasser F. Friedel's salt, ca2al(oh)6(cl,oh)·2h2o: its solid solutions and their role in chloride binding[J/OL]. Cement and Concrete Research, 1998, 28(12): 1713-1723. DOI: https://doi.org/10.1016/S0008-8846(98)00162-8.

[194] Cao Y, Guo L, Chen B. Influence of sulfate on the chloride diffusion mechanism in mortar [J/OL]. Construction and Building Materials, 2019, 197: 398-405. DOI: https://doi.org/10.1016/j.conbuildmat.2018.11.238.

[195] Lothenbach B, Kulik D A, Matschei T, et al. Cemdata18: A chemical thermodynamic database for hydrated portland cements and alkali-activated materials[J/OL]. Cement and Concrete Research, 2019, 115: 472-506. DOI: https://doi.org/10.1016/j.cemconres.2018.04.018.

[196] Vočka R, Gallé C, Dubois M, et al. Mercury intrusion porosimetry and hierarchical structure of cement pastes: Theory and experiment[J/OL]. Cement and Concrete Research, 2000, 30(4): 521-527. DOI: https://doi.org/10.1016/S0008-8846(99)00252-5.

[197] Gallé C. Effect of drying on cement-based materials pore structure as identified by mercury intrusion porosimetry: A comparative study between oven-, vacuum-, and freeze-drying[J/OL]. Cement and Concrete Research, 2001, 31(10): 1467-1477. DOI: https://doi.org/10.1016/S0008-8846(01)00594-4.

[198] Baroghel-Bouny V. Caractérisation des pâtes de ciment et des bétons: méthodes, analyses, interprétations[M]. Laboratoire Central des Ponts et Chausees, 1994.

[199] Cook R A, Hover K C. Mercury porosimetry of hardened cement pastes[J/OL]. Cement and Concrete Research, 1999, 29(6): 933-943. DOI: https://doi.org/10.1016/S0008-8846(99)00083-6.

[200] Rashidi M, Paul A, Kim J Y, et al. Insights into delayed ettringite formation damage through acoustic nonlinearity[J/OL]. Cement and Concrete Research, 2017, 95: 1-8. DOI: https://doi.org/10.1016/j.cemconres.2017.02.004.

[201] Chen J J, Thomas J J, Jennings H M. Decalcification shrinkage of cement paste[J/OL]. Cement and Concrete Research, 2006, 36(5): 801-809. DOI: https://doi.org/10.1016/j.cemconres.2005.11.003.

[202] Muller A C A. Characterization of porosity & csh in cement pastes by ^{1}h nmr[R]. EPFL, 2014.

[203] Diamond S. Microstructure of cement-based systems/bonding and interfaces in cementitious materials[C]//Mat. Res. Soc. Symp. Proc., MRS, Pittsburgh: volume 370. 1995: 217.

[204] Jooss M, Reinhardt H W. Permeability and diffusivity of concrete as function of temperature [J/OL]. Cement and Concrete Research, 2002, 32(9): 1497-1504. DOI: https://doi.org/10.1016/S0008-8846(02)00812-8.

[205] Baroghel-Bouny V. Water vapour sorption experiments on hardened cementitious materials. part ii: Essential tool for assessment of transport properties and for durability prediction[J/OL]. Cement and Concrete Research, 2007, 37(3): 438-454. DOI: https://doi.org/10.1016/j.cemconres.2006.11.017.

[206] Santhanam M, Cohen M D, Olek J. Effects of gypsum formation on the performance of cement mortars during external sulfate attack[J/OL]. Cement and Concrete Research, 2003, 33(3): 325-332. DOI: https://doi.org/10.1016/S0008-8846(02)00955-9.

[207] Zhang H, Šavija B, Luković M, et al. Experimentally informed micromechanical modelling of cement paste: An approach coupling x-ray computed tomography and statistical nanoindentation[J/OL]. Composites Part B: Engineering, 2019, 157: 109-122. DOI: https://doi.org/10.1016/j.compositesb.2018.08.102.

[208] Ikumi T, Cavalaro S H, Segura I, et al. Alternative methodology to consider damage and expansions in external sulfate attack modeling[J/OL]. Cement and Concrete Research, 2014, 63: 105-116. DOI: https://doi.org/10.1016/j.cemconres.2014.05.011.

[209] Ulm F, Constantinides G, Heukamp F. Is concrete a poromechanics material[J/OL]. A multiscale investigation of poroelastic properties, Materials, 2004, 420: 43-58. DOI: https://doi.org/10.1007/BF02481626.

[210] Xie M, Dangla P, Li K. Reactive transport modelling of concurrent chloride ingress and carbonation in concrete[J/OL]. Materials and Structures, 2021, 54(5): 1-19. DOI: https://doi.org/10.1617/s11527-021-01769-9.

[211] Yu C, Sun W, Scrivener K. Degradation mechanism of slag blended mortars immersed in sodium sulfate solution[J/OL]. Cement and Concrete Research, 2015, 72: 37-47. DOI: https://doi.org/10.1016/j.cemconres.2015.02.015.

[212] Jakobsen U H, De Weerdt K, Geiker M R. Elemental zonation in marine concrete[J/OL]. Cement and Concrete Research, 2016, 85: 12-27. DOI: https://doi.org/10.1016/j.cemconres.2016.02.006.

[213] Fjendbo S, Sørensen H E, De Weerdt K, et al. Correlating the development of chloride profiles and microstructural changes in marine concrete up to ten years[J/OL]. Cement and Concrete Composites, 2022, 131: 104590. DOI: https://doi.org/10.1016/j.cemconcomp.2022.104590.

[214] Boudache S, Rozière E, Loukili A, et al. Towards common specifications for low- and high-expansion cement-based materials exposed to external sulphate attacks[J/OL]. Construction and Building Materials, 2021, 294: 123586. DOI: https://doi.org/10.1016/j.conbuildmat.2021.123586.

[215] Lothenbach B, Winnefeld F. Thermodynamic modelling of the hydration of portland cement [J/OL]. Cement and Concrete Research, 2006, 36(2): 209-226. DOI: https://doi.org/10.1016/j.cemconres.2005.03.001.

[216] Taylor H F W. A method for predicting alkazi ion concentrations in cement pore solutions [J/OL]. Advances in Cement Research, 1987, 1(1): 5-17. DOI: 10.1680/adcr.1987.1.1.5.

[217] Rozière E, Loukili A, El Hachem R, et al. Durability of concrete exposed to leaching and external sulphate attacks[J/OL]. Cement and Concrete Research, 2009, 39(12): 1188-1198. DOI: https://doi.org/10.1016/j.cemconres.2009.07.021.

[218] Mehta P, Pirtz D, Polivka M. Properties of alite cements[J/OL]. Cement and Concrete Research, 1979, 9(4): 439-450. DOI: https://doi.org/10.1016/0008-8846(79)90041-3.

[219] Mickaël T. Modelling of atmospheric carbonation of cement based materials considering the kinetic effects and modifications of the microstructure and the hydric state[D/OL]. Ecole des Ponts ParisTech, 2005. https://pastel.archives-ouvertes.fr/pastel-00001517/document.

[220] Hina A, Nancollas G H. Precipitation and dissolution of alkaline earth sulfates: Kinetics and surface energy[J/OL]. Reviews in Mineralogy and Geochemistry, 2000, 40(1): 277-301. DOI: https://doi.org/10.2138/rmg.2000.40.5.

[221] Uibu M, Tamm K, Velts-Jänes O, et al. Utilization of oil shale combustion wastes for pcc production: Quantifying the kinetics of ca(oh)2 and caso4·2h2o dissolution in aqueous systems [J/OL]. Fuel Processing Technology, 2015, 140: 156-164. DOI: https://doi.org/10.1016/j.fuproc.2015.09.010.

[222] Coussy O. Deformation and stress from in-pore drying-induced crystallization of salt[J/OL]. Journal of the Mechanics and Physics of Solids, 2006, 54(8): 1517-1547. DOI: https://doi.org/10.1016/j.jmps.2006.03.002.

[223] Coussy O. Revisiting the constitutive equations of unsaturated porous solids using a lagrangian saturation concept[J]. International Journal for Numerical and Analytical Methods in Geomechanics, 2007, 31(15): 1675-1694.

[224] Van Genuchten M T. A closed-form equation for predicting the hydraulic conductivity of unsaturated soils[J]. Soil science society of America journal, 1980, 44(5): 892-898.

[225] Lasaga A C, Soler J M, Ganor J, et al. Chemical weathering rate laws and global geochemical cycles[J/OL]. Geochimica et Cosmochimica Acta, 1994, 58(10): 2361-2386. DOI: https://doi.org/10.1016/0016-7037(94)90016-7.

[226] Nancollas G. Mechanism of growth and dissolution of sparingly soluble salts[J]. Ceramic Powder Science II. Transactions Westerville, Oh., 1988,, 1988, 1: 8-22.

[227] Burton W K, Cabrera N, Frank F. The growth of crystals and the equilibrium structure of their surfaces[J]. Philosophical Transactions of the Royal Society of London. Series A, Mathematical and Physical Sciences, 1951, 243(866): 299-358.

[228] Nielsen A E. Rate laws and rate constants in crystal growth[J]. Croatica Chemica Acta, 1987, 60(3): 531-539.

[229] Nancollas G, LoRe M, Perez L, et al. Mineral phases of calcium phosphate[J]. The Anatomical Record, 1989, 224(2): 234-241.

[230] Kondo D, Welemane H, Cormery F. Basic concepts and models in continuum damage mechanics [J]. Revue européenne de génie civil, 2007, 11(7-8): 927-943.

[231] PIJAUDIER-CABOT G, MAZARS J. Section 6.13 - damage models for concrete[M/OL]// LEMAITRE J. Handbook of Materials Behavior Models. Burlington: Academic Press, 2001: 500-512. DOI: https://doi.org/10.1016/B978-012443341-0/50056-9.

[232] Jönsson B, Nonat A, Labbez C, et al. Controlling the cohesion of cement paste[J]. Langmuir, 2005, 21(20): 9211-9221.

[233] Petersson P E. Crack growth and development of fracture zones in plain concrete and similar materials[R]. Lund Inst. of Tech.(Sweden). Div. of Building Materials, 1981.

[234] Attiogbe E K, Darwin D. Submicroscopic cracking of cement paste and mortar in compression [R]. University of Kansas Center for Research, Inc., 1985.

[235] de Borst R. Numerical aspects of cohesive-zone models[J/OL]. Engineering Fracture Mechanics, 2003, 70(14): 1743-1757. DOI: https://doi.org/10.1016/S0013-7944(03)00122-X.

[236] Grandclerc A, Dangla P, Gueguen-Minerbe M, et al. Modelling of the sulfuric acid attack on different types of cementitious materials[J]. Cement and Concrete Research, 2018, 105: 126-133.

[237] Whittaker M J. The impact of slag composition on the microstructure of composite slag cements exposed to sulfate attack[D]. University of Leeds, 2014.

[238] Damidot D, Glasser F. Thermodynamic investigation of the cao□al2o3□caso4□h2o system at 25°c and the influence of na2o[J/OL]. Cement and Concrete Research, 1993, 23(1): 221-238. DOI: https://doi.org/10.1016/0008-8846(93)90153-Z.

[239] Mainguy M, Coussy O. Propagation fronts during calcium leaching and chloride penetration [J]. Journal of Engineering Mechanics, 2000, 126(3): 250-257.

[240] Gebhart B. Heat conduction and mass diffusion[M]. New York: McGraw-Hill, 1993.

[241] Li K, Zhao F, Zhang Y. Influence of carbonation on the chloride ingress into concrete: Theoretical analysis and application to durability design[J/OL]. Cement and Concrete Research, 2019, 123: 105788. DOI: https://doi.org/10.1016/j.cemconres.2019.105788.

[242] Yokozeki K, Watanabe K, Sakata N, et al. Modeling of leaching from cementitious materials used in underground environment[J]. Applied clay science, 2004, 26(1-4): 293-308.

[243] Dangla P. A modeling platform based on finite volume/element method[EB/OL]. 2022. https://github.com/ifsttar/bil.

[244] Gérard B, Marchand J. Influence of cracking on the diffusion properties of cement-based materials: Part i: Influence of continuous cracks on the steady-state regime[J/OL]. Cement and Concrete Research, 2000, 30(1): 37-43. DOI: https://doi.org/10.1016/S0008-8846(99)00201-X.

[245] Buckingham E. On physically similar systems; illustrations of the use of dimensional equations [J]. Physical review, 1914, 4(4): 345.

[246] Eurocode 2. Design of conrete structure[S]. 1992.

[247] Crank J. The mathematics of diffusion[M]. Oxford university press, 1979.

[248] Garboczi E, Bentz D. Computer simulation of the diffusivity of cement-based materials[J]. Journal of materials science, 1992, 27(8): 2083-2092.

APPENDIX A CLASSIFICATION OF EXPOSURE TO SULFATES

Table A.1 European standard EN206-1:2000[90,246].

Class of exposure	Concentration of sulfates as SO_4	
	In ground water (ppm)	In soil (ppm total)
Slightly aggressive	200 – 600	2000 – 3000
Moderately aggressive	600 – 3000	3000 – 12,000
Highly aggressive	3000 – 6000	12,000 – 24,000

Table A.2 ACI 318 Building Code[92].

Class of exposure	Concentration of sulfates as SO_4	
	In ground water (ppm)	Water soluble in soil (percent by weight)
Negligible	< 150	< 0.10
Moderate	150–1500	0.10–0.20
Severe	1500–10,000	0.20–2.00
Very severe	>10,000	>2.00

Table A.3 Chinese standard GB/T 50476[91].

Class of exposure	Concentration of sulfates as SO_4	
	In ground water (mg/L)	Water soluble in soil (mg/kg)
Moderate	200–1000	300-1500
Severe	1000–4000	1500-6000
Very severe	4000-10,000	6000-15,000

APPENDIX B DETERMINATION OF POROELASTIC PROPERTIES

Taking the spherical voids embedded in a homogeneously strained solid matrix, the bulk and shear modulus of porous materials, K and G, can be expressed in the form,

$$\begin{cases} K = (1-\phi_0)\dfrac{4k_S g_S}{4+g_S+3\phi_0 k_S} \\ G = (1-\phi_0)\dfrac{(9k_S+8g_S)g_S}{9k_S(1+\frac{2}{3}\phi_0)+8g_S(1+\frac{2}{3}\phi_0)} \end{cases} \tag{B.1}$$

where k_S and g_S are the bulk and shear modulus of a solid matrix, respectively. The Biot coefficients can be related to the bulk modulus of solid matrix and porous materials,

$$b = b_C + b_L = 1 - \frac{K}{k_S} \tag{B.2}$$

The deformation of the pore space is assumed to be isotropic in the porous materials. Thus the partial porosity variation of fluid phase, φ_J, is linearly related to its supersaturation degree S_J,

$$\varphi_J = S_J \varphi \tag{B.3}$$

When $p_C = p_L = 0$, the volume isodeformation assumption is still valid. Then Eq. $(1.52)_{II}$ and Eq. $(1.52)_{III}$,

$$b_J = S_J \frac{\phi}{\epsilon} \tag{B.4}$$

Substituting Eq. (B.4) into Eq. (B.2) gives the expression of Biot coefficients,

$$b_J = bS_J, \quad S_C + S_L = 1 \tag{B.5}$$

Providing $\sigma = -p_C = -p_L$, Eq. (1.40) can be restated as: $\sigma = \sigma_S$. With the homogeneous assumption of solid matrix, the volume dilation ϵ_S in solid matrix can be expressed as,

$$\epsilon_S = -\sigma/k_S \tag{B.6}$$

When $\sigma = -p_C = -p_L$, the solid matrix and porous space deform in the same way,

$$\epsilon = \epsilon_S = -\sigma/k_S \tag{B.7}$$

Combination of Eqs. $(1.52)_{\mathrm{II}}$, $((1.52)_{\mathrm{III}})$ and (B.7) provides,

$$\frac{1}{N_{\mathrm{JJ}}}+\frac{1}{N_{\mathrm{CJ}}}=\frac{b_{\mathrm{J}}-\phi_0 S_{\mathrm{J}}}{k_{\mathrm{S}}} \tag{B.8}$$

Besides, the pore space occupied by fluid phase J undergoes a volume dilation,

$$\frac{\varphi_{\mathrm{J}}}{\phi_0}S_{\mathrm{J}}=\left(1+\frac{3k_{\mathrm{S}}}{4g_{\mathrm{S}}}\right)\epsilon_{\mathrm{S}}+\frac{3}{4g_{\mathrm{S}}}p_{\mathrm{J}} \tag{B.9}$$

Substitution of Eq. (B.9) into Eq. (1.37) gives the expression of volume dilation of solid matrix ϵ_{S},

$$\epsilon_{\mathrm{S}}=\frac{4g_{\mathrm{S}}}{3\phi_0 k_{\mathrm{S}}+4g_{\mathrm{S}}}\left(\epsilon-\frac{3\phi_0\sigma_p}{4g_{\mathrm{S}}}\right) \tag{B.10}$$

with $\sigma_{\mathrm{p}}=S_{\mathrm{C}}p_{\mathrm{C}}+S_{\mathrm{L}}p_{\mathrm{L}}$. A combination of Eqs. $(1.52)_{\mathrm{II}}$, $(1.52)_{\mathrm{III}}$, (B.5), (B.8) and (B.10) provides separate expressions of N_{JJ} and N_{CL},

$$\begin{cases}\dfrac{1}{N_{\mathrm{JJ}}}=\dfrac{S_{\mathrm{J}}^2}{N}+\dfrac{3S_{\mathrm{C}}S_{\mathrm{L}}\phi_0}{4g_{\mathrm{S}}}\\[2ex] \dfrac{1}{N_{\mathrm{CL}}}=\dfrac{S_{\mathrm{C}}S_{\mathrm{L}}}{N}-\dfrac{3S_{\mathrm{C}}S_{\mathrm{L}}\phi_0}{4g_{\mathrm{S}}}\\[2ex] \dfrac{1}{N}=\dfrac{1}{N_{\mathrm{CC}}}+\dfrac{2}{N_{\mathrm{CL}}}+\dfrac{1}{N_{\mathrm{LL}}}\end{cases} \tag{B.11}$$

Solving the above equations gives the solution of modulus N_{JJ} and N_{CL}.

Form the above analysis, K, G, N and b only depend on geometry of porous space and mechanical properties of solid matrix, b_{J} N_{JJ} and N_{CL} are also dependent on saturation of fluid phase.

APPENDIX C EXPERIMENTAL RESULTS IN PART II

C.1 ^{27}Al NMR results

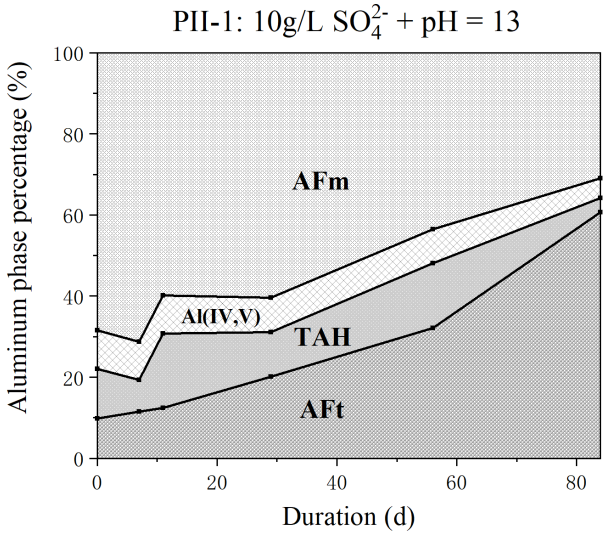

Figure C.1 Aluminum phase contents in cement paste layer specimens exposed to 10g/L SO_4^{2-} + pH = 13 condition (PII-1) at different exposure ages.

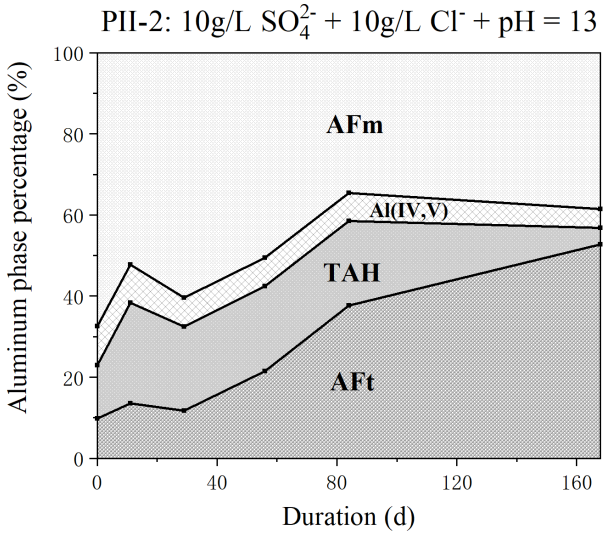

Figure C.2 Aluminum phase contents in cement paste layer specimens exposed to 10g/L SO_4^{2-} + 10g/L Cl^- + pH = 13 condition (PII-2) at different exposure ages. Al(IV,V) represents the sum of IV and V aluminum phases.

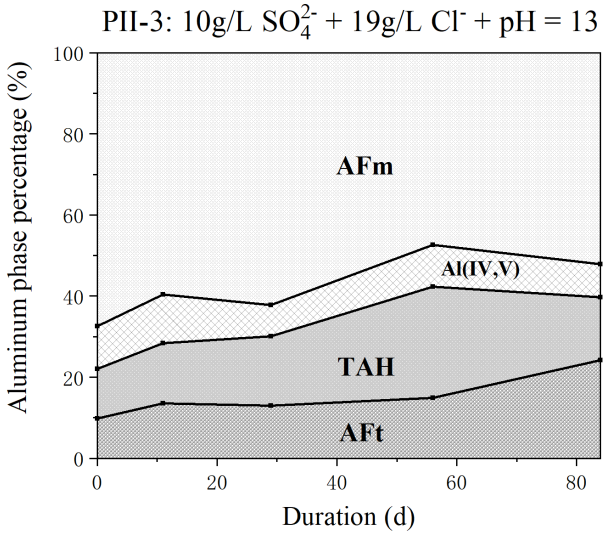

Figure C.3 Aluminum phase contents in cement paste layer specimens exposed to 10g/L SO_4^{2-} + 19g/L Cl^- + pH = 13 condition (PII-3) at different exposure ages. Al(IV,V) represents the sum of IV and V aluminum phases.

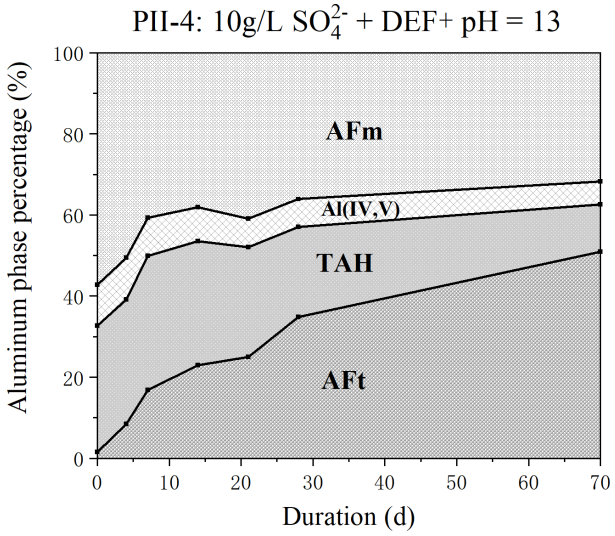

Figure C.4 Aluminum phase contents in cement paste layer specimens exposed to 10g/L SO_4^{2-} + + DEF + pH = 13 condition (PII-4) at different exposure ages. Al(IV,V) represents the sum of IV and V aluminum phases.

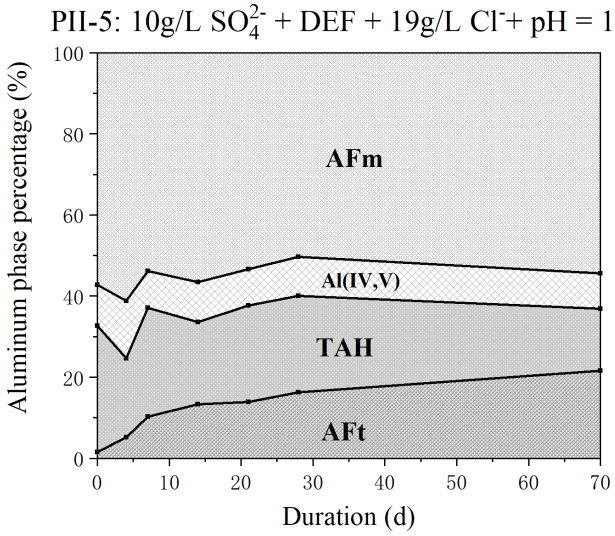

Figure C.5 Aluminum phase contents in cement paste layer specimens exposed to 10g/L SO_4^{2-} + 19g/L Cl^- + DEF + pH = 13 condition (PII-5) at different exposure ages. Al(IV,V) represents the sum of IV and V aluminum phases.

C.2 XRD results

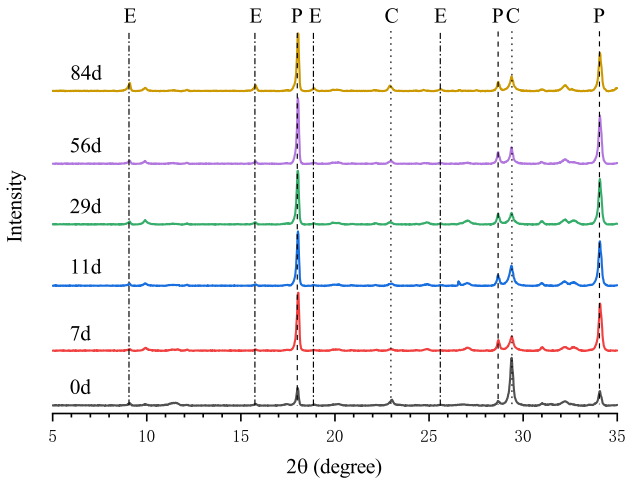

(a)

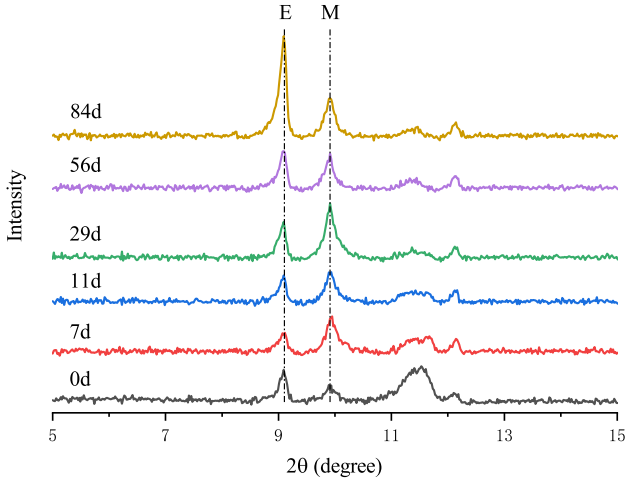

(b)

Figure C.6 XRD analysis of cement paste layer specimens exposed to PII-1 condition (a) and zoom (b). “E”, “P”, “C” and “M” stand for ettringite, portlandite, calcite and monosulfoaluminate.

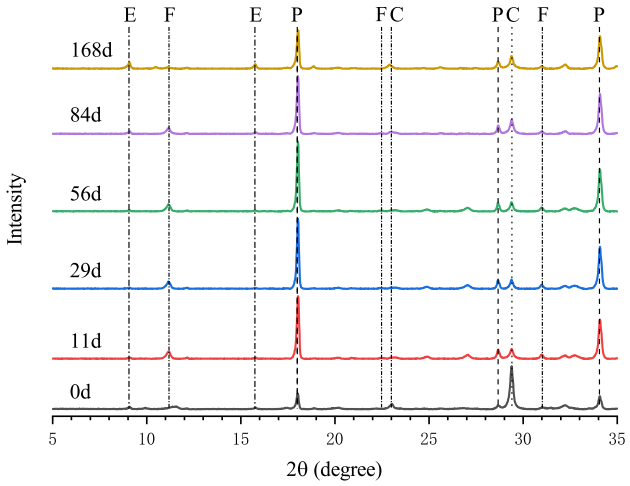

(a)

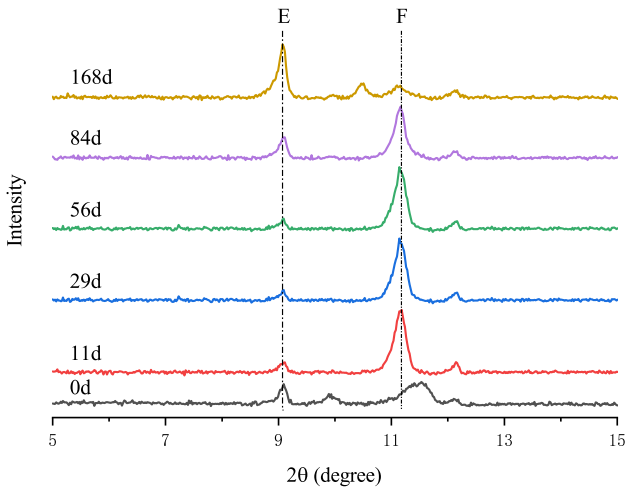

(b)

Figure C.7 XRD analysis of cement paste layer specimens exposed to PII-2 condition (a) and zoom (b). “E” , “P”, “C”, “M” and “F” stand for ettringite, portlandite, calcite, monosulfoaluminate and Friedel’s salt.

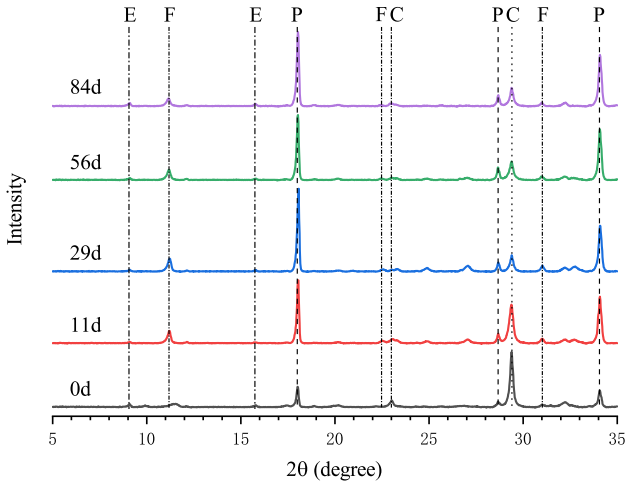

(a)

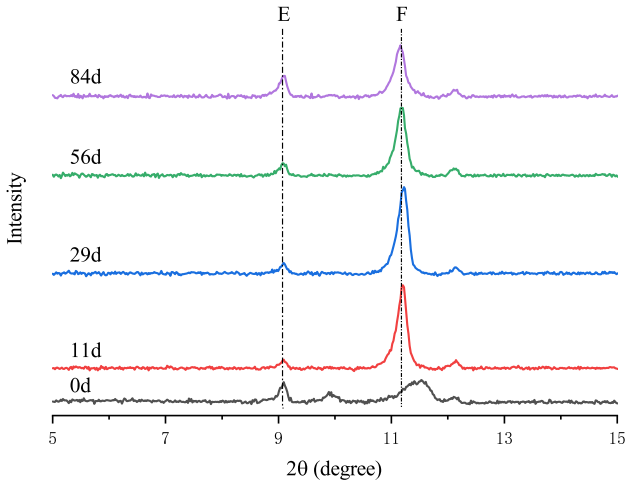

(b)

Figure C.8 XRD analysis of cement paste layer specimens exposed to PII-3 condition (a) and zoom (b). “E” , “P”, “C”, “M” and “F” stand for ettringite, portlandite, calcite, monosulfoaluminate and Friedel’s salt.

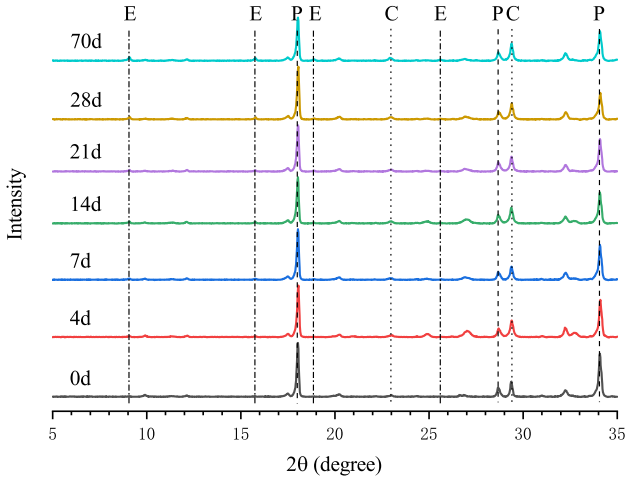

(a)

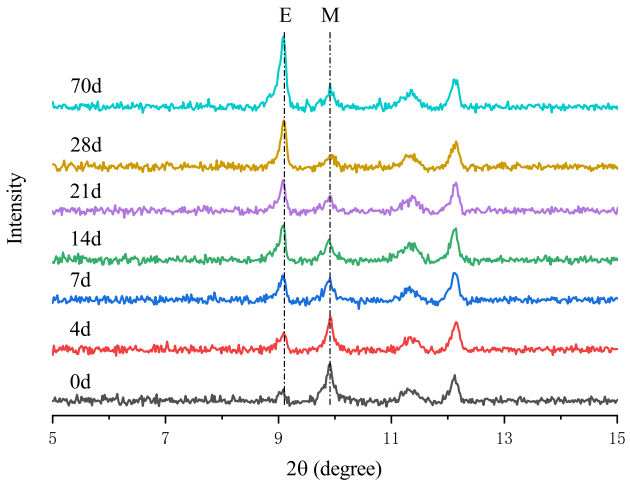

(b)

Figure C.9 XRD analysis of cement paste layer specimens exposed to PII-4 condition (a) and zoom (b). “E” , “P”, “C” and “M” stand for ettringite, portlandite, calcite and monosulfoaluminate.

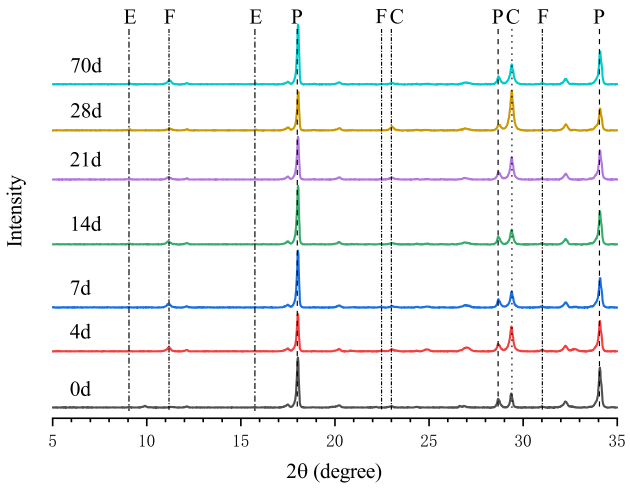

(a)

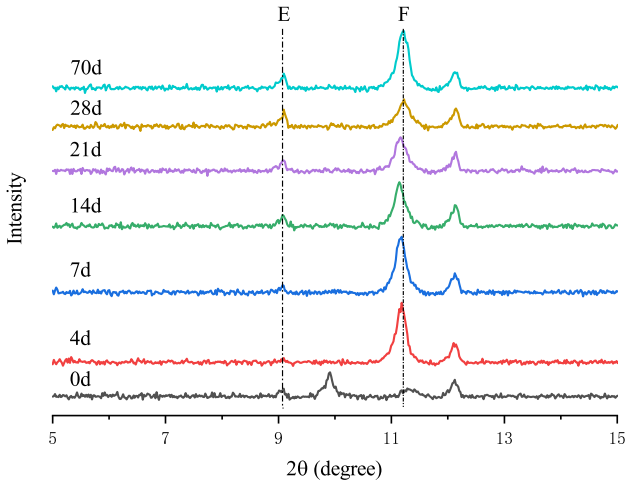

(b)

Figure C.10 XRD analysis of cement paste layer specimens exposed to PII-5 condition (a) and zoom (b). “E” , “P”, “C”, “M” and “F” stand for ettringite, portlandite, calcite, monosulfoaluminate and Friedel’s salt.

C.3 MIP results

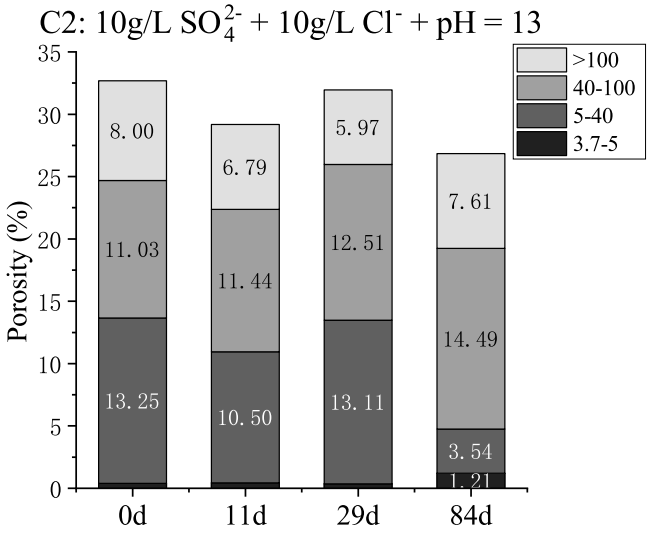

Figure C.11 Pore volume of cement paste specimens exposed to 10g/L SO_4^{2-} + 10g/L Cl^- + pH = 13 condition (PII-2) at different exposure ages.

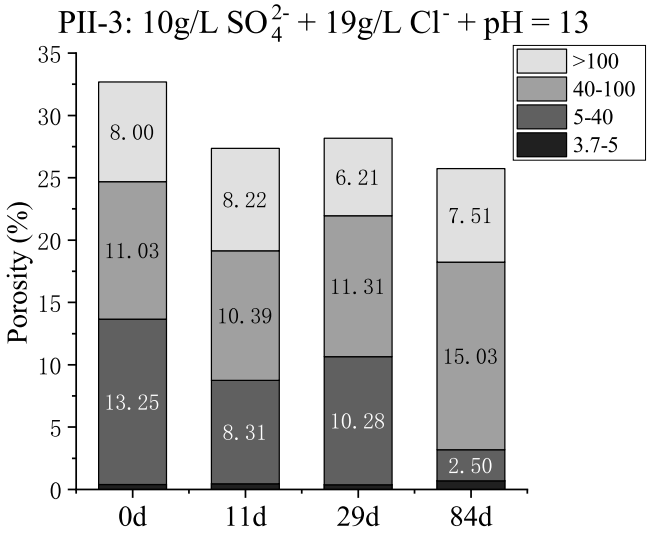

Figure C.12 Pore volume of cement paste specimens exposed to 10g/L SO_4^{2-} + 19g/L Cl^- + pH = 13 condition (PII-3) at different exposure ages.

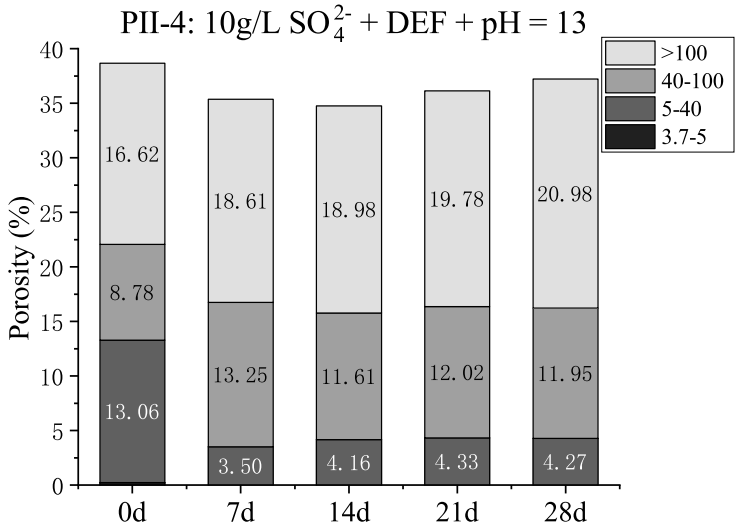

Figure C.13 Pore volume of cement paste specimens exposed to 10g/L SO_4^{2-} + DEF + pH = 13 condition (PII-4) at different exposure ages.

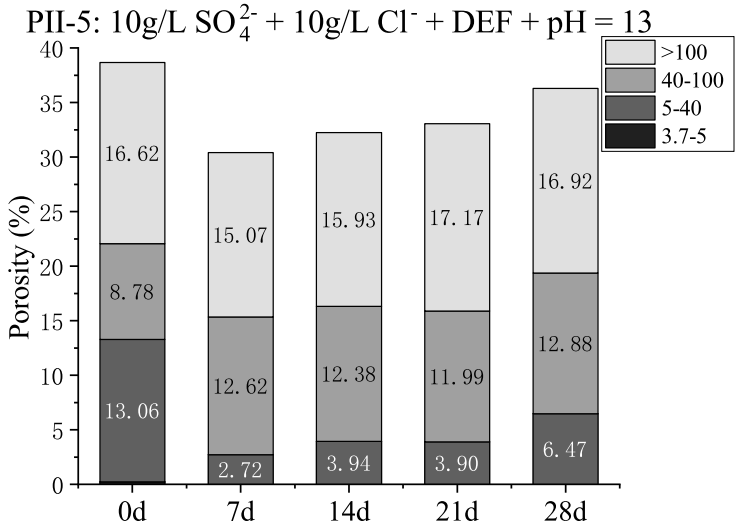

Figure C.14 Pore volume of cement paste specimens exposed to 10g/L SO_4^{2-} + 19g/L Cl^- + DEF + pH = 13 condition (PII-5) at different exposure ages.

APPENDIX D EXPERIMENTAL RESULTS IN PART III

D.1 Sulfate profiles

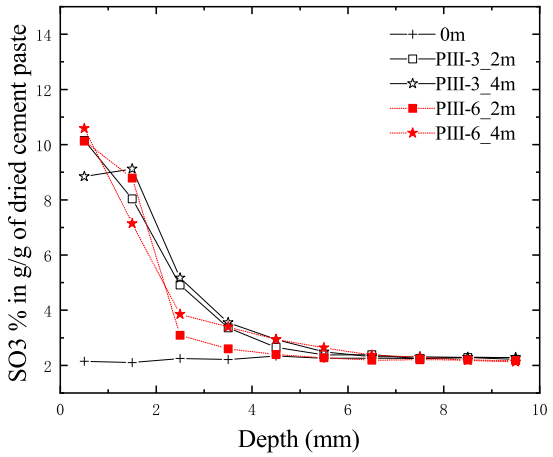

Figure D.1 Comparisons of sulfate profiles measured by ICP-AES for cement paste disks immersed into ESA with and without DEF conditions in the presence of leaching and chloride (PIII-3 and PIII-6) for different exposure ages. PIII-3 stands for 10g/L SO_4^{2-} + + 19 g/L Cl^- + pH = 7, and PIII-6 sfor 10g/L SO_4^{2-} + + 19 g/L Cl^- + pH = 7 + DEF.

D.2 Chloride profiles

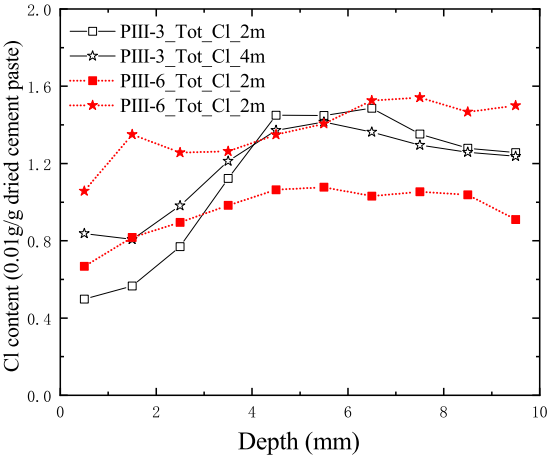

Figure D.2 Comparison of total chloride profiles of cement paste disks immersed into combined ESA and chlorides conditions with and without DEF (PIII-3 for no DEF and PIII-6 for DEF). PIII-3 stands for 10g/L SO_4^{2-} + + 19 g/L Cl^- + pH = 7, and PIII-6 sfor 10g/L SO_4^{2-} + + 19 g/L Cl^- + pH = 7 + DEF.

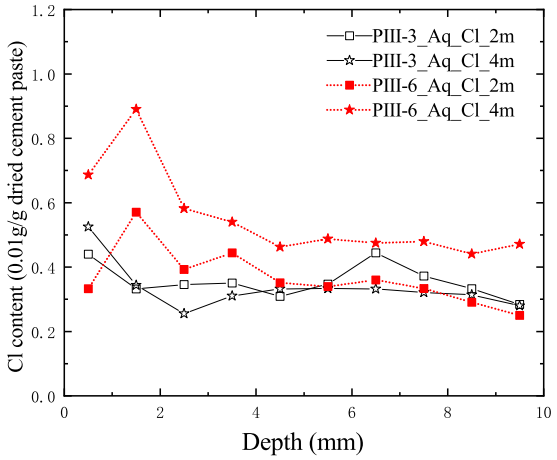

Figure D.3 Comparison of water-soluble chloride profiles of cement paste disks immersed into combined ESA and chlorides conditions with and without DEF (PIII-3 for no DEF and PIII-6 for DEF). PIII-3 stands for 10g/L SO_4^{2-} + + 19 g/L Cl^- + pH = 7, and PIII-6 sfor 10g/L SO_4^{2-} + + 19 g/L Cl^- + pH = 7 + DEF.

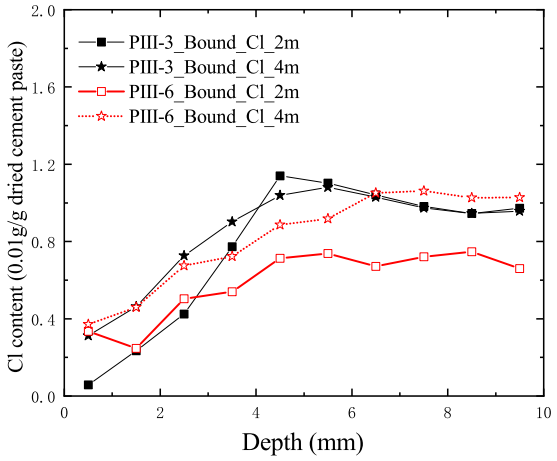

Figure D.4 Comparison of bound chloride profiles of cement paste disks immersed into combined ESA and chlorides conditions with and without DEF (PIII-3 for no DEF and PIII-6 for DEF). PIII-3 stands for 10g/L SO_4^{2-} + + 19 g/L Cl^- + pH = 7, and PIII-6 sfor 10g/L SO_4^{2-} + + 19 g/L Cl^- + pH = 7 + DEF.

D.3 EDS results

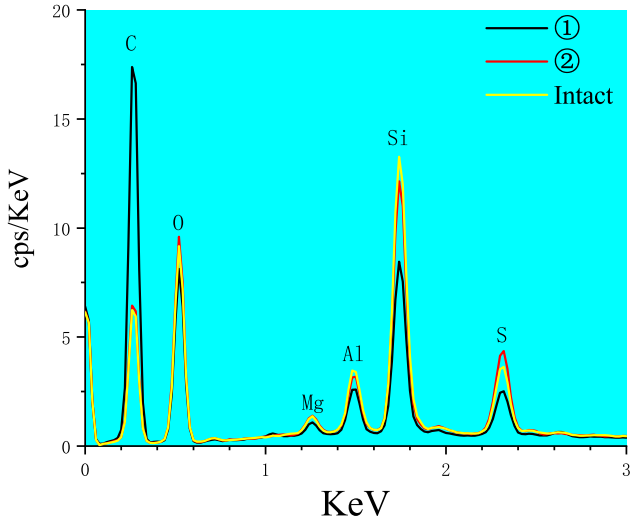

Figure D.5 EDS spectra of cement paste disks immersed into 10g/L SO_4^{2-} + pH of 13 condition (PIII-1).

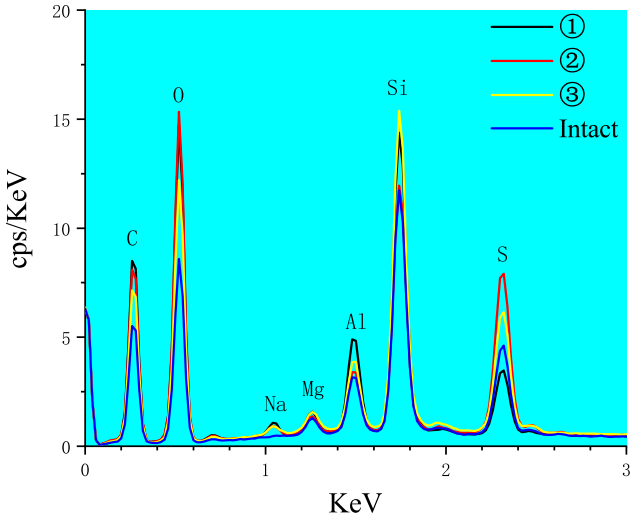

Figure D.6 EDS spectra of cement paste disks immersed into 10g/L SO_4^{2-} + pH of 7 condition (PIII-2).

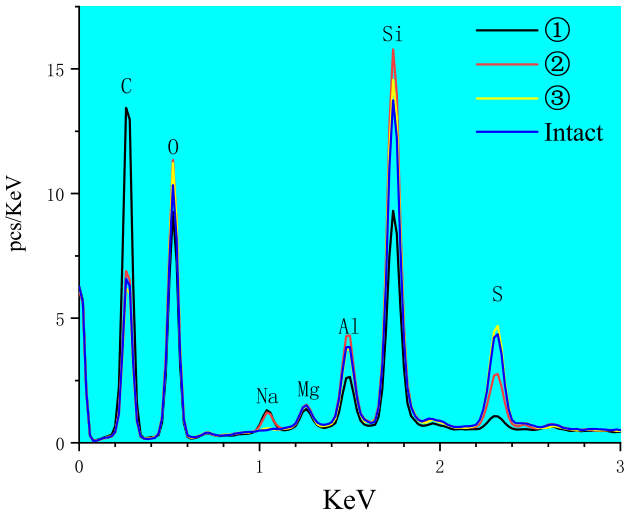

Figure D.7 EDS spectra of cement paste disks immersed into 10g/L SO_4^{2-} + 19g/L Cl^- + pH of 7 condition (PIII-3).

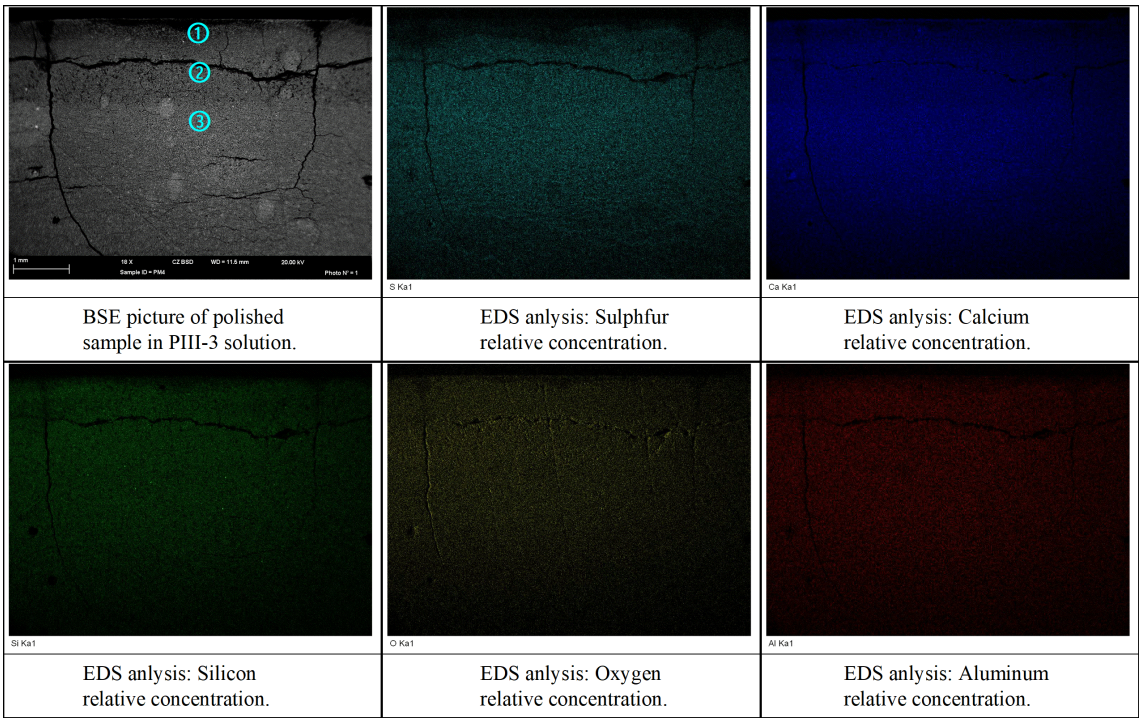

BSE picture of polished sample in PIII-3 solution.	EDS anlysis: Sulphfur relative concentration.	EDS anlysis: Calcium relative concentration.
EDS anlysis: Silicon relative concentration.	EDS anlysis: Oxygen relative concentration.	EDS anlysis: Aluminum relative concentration.

Figure D.8 BSE and EDS element maps on the cross section of cement paste disk immersed into PIII-3 condition (10g/L SO_4^{2-} + 19g/L Cl^- + pH of 7 condition) for 8 months. Top edge of each image is the exposure surface.

APPENDIX E DERIVATION OF CORRENS' EQUATION

The chemical potential equilibrium between crystal phase "C" and aqueous solute "sol" writes,

$$\mu_{\mathrm{C}}(P_{\mathrm{C}}, T) = \mu_{\mathrm{sol}}(P_{\mathrm{L}}, T, x) \tag{E.1}$$

Here the term x is the molar fraction of solute in aqueous solution. Under an isotherm process, the change in chemical potential of crystal phase due to the pressure change can be obtained through the Gibbs-Duhem equation,

$$\mathrm{d}\mu_{\mathrm{C}}(P_{\mathrm{C}}, T) = \overline{V}_{\mathrm{C}}\mathrm{d}P_{\mathrm{C}} \tag{E.2}$$

The chemical potential of solute in aqueous solution is contributed as the chemical potential of pure solute prior to mixing $\mu^{*}_{\mathrm{sol}}(P_{\mathrm{L}}, T)$ and the decreased part through mixing. For an ideal solution, the decreased part is simplified as $RT\ln x$. Thus, the chemical potential of solute writes,

$$\mu_{\mathrm{sol}}(P_{\mathrm{L}}, T, x) = \mu^{*}_{\mathrm{sol}}(P_{\mathrm{L}}, T) + RT\ln x \tag{E.3}$$

The differential of the chemical potential of solute under an isotherm condition can be stated as,

$$\mathrm{d}\mu_{\mathrm{sol}}(P_{\mathrm{L}}, T, x) = \mathrm{d}\mu^{*}_{\mathrm{sol}}(P_{\mathrm{L}}, T) + RT\mathrm{d}\ln x \tag{E.4}$$

Applying Gibbs-Duhem equation to the evolution of pure solute,

$$\mathrm{d}\mu^{*}_{\mathrm{sol}}(P_{\mathrm{L}}, T) = \overline{V}^{*}_{\mathrm{sol}}\mathrm{d}P_{\mathrm{L}} \tag{E.5}$$

where $\overline{V}^{*}_{\mathrm{sol}}$ is the molar volume of the pure solute prior to its mixing with the solvent. The equilibrium equation Eq. (E.1) after an isotherm process supplies a differential form,

$$\mathrm{d}\mu^{*}_{\mathrm{sol}}(P_{\mathrm{L}}, T) = \mathrm{d}\mu_{\mathrm{sol}}(P_{\mathrm{L}}, T, x) \tag{E.6}$$

Substituting Eqs. (E.2-E.5) into (E.6) gives the relation,

$$\overline{V}_{\mathrm{C}}\mathrm{d}P_{\mathrm{C}} = \overline{V}^{*}_{\mathrm{sol}}\mathrm{d}P_{\mathrm{L}} + RT\mathrm{d}\ln x \tag{E.7}$$

Let us consider a conventional reference state where the crystal and liquid pressure equals to atmospheric pressure $P_C = P_L = P_{atm}$, and the related molar fraction x is equal to the crystal solubility $x_{cry}(T)$ depending only on temperature. Then integrating Eq. (E.7) from the reference state to the current state provides the modified Correns' equation,

$$P_C - P_{atm} - \frac{\overline{V}^*_{sol}}{\overline{V}_C}\left(P_L - P_{atm}\right) = \frac{RT}{\overline{V}_C}\ln\left(\frac{x}{x_{cry}}\right) \tag{E.8}$$

The ratio $\overline{V}^*_{sol}/\overline{V}_C$ represents the volume dilation ($\overline{V}^*_{sol} > \overline{V}_C$) or shrinkage ($\overline{V}^*_{sol} < \overline{V}_C$) of phase transition from solid crystal phase to aqueous pure solute phase. Normally, this ratio is recognized as 1.

APPENDIX F SOLUTION OF DUAL MOVING BOUNDARY PROBLEM

The Fick's second law with constant diffusivity can be reduced to an ordinary differential equation using Boltzmann variables[247]. For the dual MBP defined through Eq.(7.7) to Eq.(7.11), the following Boltzmann variables are defined.

$$\eta = \frac{x}{\sqrt{t}} \quad \text{and} \quad k = \frac{X_{\mathrm{C}}}{\sqrt{t}},\ \kappa = \frac{X_{\mathrm{L}}}{\sqrt{t}} \tag{F.1}$$

F.1 Sulfate diffusion

The sulfate diffusion equations in Eq.(7.7) can be rewritten using the Boltzmann variables as,

$$-\eta\frac{\partial c_{\mathrm{S}}}{\partial \eta} = \begin{cases} 2D_{1,\mathrm{S}}\dfrac{\partial^2 c_{\mathrm{S}}}{\partial \eta^2}, & \eta < k \\ \\ 2D_{2,\mathrm{S}}\dfrac{\partial^2 c_{\mathrm{S}}}{\partial \eta^2}, & \eta \geqslant k \end{cases} \tag{F.2}$$

The initial condition, boundary condition and the moving boundary conditions can be expressed in terms of these Boltzmann variables by putting Eq.(F.1) into Eq.(7.9),

$$\begin{cases} c_{\mathrm{S}}(\eta \to \infty) = 0, \quad c_{\mathrm{S}}(\eta = 0) = c_{\mathrm{S}}^0 \\ c_{\mathrm{S}}|_{\eta=k^-} = c_{\mathrm{S}}|_{\eta=k^+}, D_{1,\mathrm{S}}\dfrac{\partial c_{\mathrm{S}}}{\partial \eta}\Big|_{\eta=k^-} = D_{2,\mathrm{S}}\dfrac{\partial c_{\mathrm{S}}}{\partial \eta}\Big|_{\eta=k^+} \end{cases} \tag{F.3}$$

It is readily to verify that the following solution satisfies both Eq.(F.2) and Eq.(F.3),

$$\frac{c_{\mathrm{S}}}{c_{\mathrm{S}}^0} = \begin{cases} A_1 \mathrm{erfc}\left(\dfrac{\eta}{2\sqrt{D_{1,\mathrm{S}}}}\right) + A_2, & \eta < k \\ \\ A_3 \mathrm{erfc}\left(\dfrac{\eta}{2\sqrt{D_{2,\mathrm{S}}}}\right), & \eta \geqslant k \end{cases} \tag{F.4}$$

And the integral constants $A_{1,2,3,4}$ are expressed as,

$$\begin{cases} A_1 = \dfrac{1}{1-\mathrm{erfc}\left(\dfrac{K_2}{K_1}\right)+K_1\mathrm{erfc}(K_2)\exp\left(K_2^2-\dfrac{K_2^2}{K_1^2}\right)} \\ A_2 = 1-A_1, \quad A_3 = K_1\exp\left(K_2^2-\dfrac{K_2^2}{K_1^2}\right)A_1 \end{cases} \tag{F.5}$$

with

$$K_1 = \sqrt{\frac{D_{1,\mathrm{S}}}{D_{2,\mathrm{S}}}},\ K_2 = \frac{k}{2\sqrt{D_{2,\mathrm{S}}}} \tag{F.6}$$

F.2 Hydroxide diffusion

The hydroxide diffusion equations in Eq.(7.10) can be rewritten using the Boltzmann variables as,

$$-\eta\frac{\partial c_{\mathrm{OH}}}{\partial\eta} = \begin{cases} 2D_{1,\mathrm{OH}}\dfrac{\partial^2 c_{\mathrm{OH}}}{\partial\eta^2}, & \eta < k \\ 2D_{2,\mathrm{OH}}\dfrac{\partial^2 c_{\mathrm{OH}}}{\partial\eta^2}, & k \leqslant \eta < \kappa \end{cases} \tag{F.7}$$

The initial condition, boundary condition and the moving boundary conditions can be expressed in terms of these Boltzmann variables by putting Eq.(F.1) into Eq.(7.11),

$$\begin{cases} c_{\mathrm{OH}}(\eta=0)=0, \ \ c_{\mathrm{S}}(\eta \geqslant \dfrac{X_{\mathrm{L}}}{\sqrt{t}}) = c_{\mathrm{OH}}^0 \\ c_{\mathrm{OH}}|_{\eta=k^-} = c_{\mathrm{OH}}|_{\eta=k^+},\ D_{1,\mathrm{OH}}\dfrac{\partial c_{\mathrm{OH}}}{\partial\eta}\Big|_{\eta=k^-} = D_{2,\mathrm{OH}}\dfrac{\partial c_{\mathrm{OH}}}{\partial\eta}\Big|_{\eta=k^+} \end{cases} \tag{F.8}$$

It is readily to verify that the following solution satisfies both Eq.(F.7) and Eq.(F.8),

$$\frac{c_{\mathrm{OH}}}{c_{\mathrm{OH}}^0} = \begin{cases} a_1\mathrm{erf}\left(\dfrac{\eta}{2\sqrt{D_{1,\mathrm{OH}}}}\right), & \eta < k \\ a_2\mathrm{erf}\left(\dfrac{\eta}{2\sqrt{D_{2,\mathrm{OH}}}}\right)+a_3, & k \leqslant \eta < \kappa \\ 1, & \eta \geqslant \kappa \end{cases} \tag{F.9}$$

And the integral constants $a_{1,2,3,4}$ are expressed as,

$$\begin{cases} a_2 = \dfrac{1}{\operatorname{erf}(\lambda) - \operatorname{erf}\left(\dfrac{k_2}{k_1}\right) + k_1 \operatorname{erf}(k_2) \exp\left(k_2^2 - \dfrac{k_2^2}{k_1^2}\right)} \\ a_1 = k_1 \exp\left(k_2^2 - \dfrac{k_2^2}{k_1^2}\right) a_2, \quad a_3 = 1 - \operatorname{erf}(\lambda) a_2 \end{cases} \tag{F.10}$$

with

$$k_1 = \sqrt{\frac{D_{2,\mathrm{OH}}}{D_{1,\mathrm{OH}}}},\ k_2 = \frac{k}{2\sqrt{D_{1,\mathrm{OH}}}};\quad \lambda = \frac{\kappa}{2\sqrt{D_{2,\mathrm{OH}}}} \tag{F.11}$$

APPENDIX G CALCULATION OF TRANSPORT PROPERTIES

A multi-scale model is adopted to estimate the effective ionic diffusivities for SO_4^{2-} and OH^- in this study[242]. According to [242], the effective ionic diffusivity is calculated through the following equations,

$$D_i^e = \frac{1-\lambda_{\mathrm{ca}} v_{\mathrm{ca}}}{1-\lambda_{\mathrm{fa}} v_{\mathrm{fa}}} v_{\mathrm{paste}} f(\phi_{\mathrm{p}}) D_0^i \tag{G.1}$$

$$f(\phi_{\mathrm{p}}) = 0.001 + 0.07\phi_{\mathrm{p}}^2 + 1.8 < \phi_{\mathrm{p}} - 0.18 > (\phi_{\mathrm{p}} - 0.18)^2 \tag{G.2}$$

with $< x >= x$ when $x \geqslant 0$ and $< x >= 0$ when $x < 0$. The terms in Eqs. (G.1)-(G.2) are listed in Table G.1.

Table G.1 Terms in the calculation equations (G.1)-(G.2) for the effective ionic diffusivity.

Term	Physical meaning
D_i^e	Effective diffusivity for ion species *i* through CBM
D_i^0	Diffusivity of ion *i* in pure water
$\lambda_{\mathrm{ca,fa}}$	Tortuosity parameters for the coarse and fine aggregates
$v_{\mathrm{ca,fa}}$	Volumetric fractions of coarse and fine aggregates in CBM
$f(\phi_{\mathrm{p}})$	Percolation function for ionic diffusion through pores[248]
ϕ_{p}	capillary porosity of cement paste in CBM

Without binding between the ions and the solid matrix, the apparent diffusivity writes,

$$D_i^a = \frac{D_i^e}{\phi} \tag{G.3}$$

For sulfate ions, there exists chemical binding between the ions and the solid matrix. The apparent sulfate diffusivity in the crystallized zone $D_{2,\mathrm{S}}$ takes into account the chemical binding by AFt formation through,

$$D_{2,\mathrm{S}} = \frac{D_{2,\mathrm{S}}^i}{\phi_2(1 + r_{\mathrm{S}} n_{\mathrm{C_3A}})} \tag{G.4}$$

The parameters and the apparent diffusivities in the dissolved and crystallized zones are

provided in TableG.2 for different usages.

Table G.2 Parameters and values for apparent diffusivity of SO_4^{2-} and OH^- ions

Parameter(unit)	Disk	Small cylinder[37]	Parameter analysis
Initial capillary porosity ϕ_0 (-)	0.33	0.25	0.11
Porosity change $\Delta\phi_1$ (-) by leaching	0.072	0.085	0.045
Porosity change $\Delta\phi_2$ (-) by sulfate attack	0.055	0.087	0.034
Porosity in dissolved zone ϕ_1 (-)	-0.402	-0.335	-0.155
Porosity in crystallized zone ϕ_2 (-)	0.347	0.248	0.121
Pore percolation function in Z_1 zone $f(\phi_1)$ (-)	0.0320	0.0155	0.0474
Pore percolation function in Z_2 zone $f(\phi_2)$ (-)	0.0178	0.0059	0.0175
Fine aggregate content v_{fa} (-)	0	0	0.26
Coarse aggregate content v_{ca} (-)	0	0	0.39
Cement paste content v_{paste} (-)	1	1	0.35
OH^- diffusivity in water D_{OH}^0 (10^{-9} m^2/s)	5.27		
SO_4^{2-} diffusivity in water D_S^0 (10^{-9} m^2/s)	1.07		
Effective OH^- diffusivity in Z_1 zone $D_{1,OH}^e$ (10^{-12} m^2/s)	16.86	8.20	1.91
Effective OH^- diffusivity in Z_2 zone $D_{2,OH}^e$ (10^{-12} m^2/s)	9.39	3.09	0.71
Effective SO_4^{2-} diffusivity in Z_1 zone $D_{1,S}^e$ (10^{-12} m^2/s)	3.42	1.67	0.39
Effective SO_4^{2-} diffusivity in Z_2 zone $D_{2,S}^e$ (10^{-12} m^2/s)	1.91	0.63	0.14
Apparent OH^- diffusivity in Z_1 zone $D_{1,OH}$ (10^{-11} m^2/s)	4.20	2.45	1.23
Apparent OH^- diffusivity in Z_2 zone $D_{2,OH}$ (10^{-11} m^2/s)	2.71	1.25	0.58
Apparent SO_4^{2-} diffusivity in Z_1 zone $D_{1,S}$ (10^{-12} m^2/s)	8.52	4.97	2.50
Chemical reaction coefficient r (m^3/mol)	0.035		
Aluminum phase content n_{C_3A} (mol/m^3)	320	520	198
Apparent SO_4^{2-} diffusivity in Z_2 zone $D_{2,S}$ (10^{-13} m^2/s)	4.50	1.35	1.49

APPENDIX H DIFFUSION IN 1D AXIS-SYMMETRY CASE

In the 1D axis-symmetry case, the Fick's second law with constant diffusivity is converted into a radical coordinate system as,

$$\frac{\partial c}{\partial t} = D(\frac{1}{r}\frac{\partial c}{\partial r} + \frac{\partial^2 c}{\partial r^2}) \tag{H.1}$$

Accordingly, the sulfate and hydroxide diffusion equations with a moving boundary R_{M} and leaching front R_{L} write,

$$\begin{cases} \dfrac{\partial c_{\mathrm{S}}}{\partial t} = D_{1,\mathrm{S}}(\dfrac{c_{\mathrm{S}}}{r} + r\dfrac{\partial^2 c_{\mathrm{S}}}{\partial r^2}), \quad \dfrac{\partial c_{\mathrm{OH}}}{\partial t} = D_{1,\mathrm{OH}}(\dfrac{c_{\mathrm{OH}}}{r} + r\dfrac{\partial^2 c_{\mathrm{OH}}}{\partial r^2}), & R_{\mathrm{M}} \leqslant r \leqslant R \\ \dfrac{\partial c_{\mathrm{S}}}{\partial t} = D_{2,\mathrm{S}}(\dfrac{c_{\mathrm{S}}}{r} + r\dfrac{\partial^2 c_{\mathrm{S}}}{\partial r^2}), \quad \dfrac{\partial c_{\mathrm{OH}}}{\partial t} = D_{2,\mathrm{OH}}(\dfrac{c_{\mathrm{OH}}}{r} + r\dfrac{\partial^2 c_{\mathrm{OH}}}{\partial r^2}), & R_{\mathrm{L}} \leqslant r < R_{\mathrm{M}} \\ \dfrac{\partial c_{\mathrm{S}}}{\partial t} = D_{2,\mathrm{S}}(\dfrac{c_{\mathrm{S}}}{r} + r\dfrac{\partial^2 c_{\mathrm{S}}}{\partial r^2}), \quad \dfrac{\partial c_{\mathrm{OH}}}{\partial t} = 0, & 0 \leqslant r < R_{\mathrm{L}} \end{cases} \tag{H.2}$$

where R represents the radius of cylinder specimen. For sulfate diffusion, the initial condition and boundary conditions, at the surface boundary and moving boundary in Eq.(7.9), write,

$$\begin{cases} c_{\mathrm{S}}(r < R, t = 0) = 0,\ c_{\mathrm{S}}(r = R, t > 0) = c_{\mathrm{S}}^0 \\ c_{\mathrm{S}}|_{r=R_{\mathrm{M}}^-} = c_{\mathrm{S}}|_{r=R_{\mathrm{M}}^+},\ rD_{1,\mathrm{S}}\dfrac{\partial c_{\mathrm{S}}}{\partial r}\Big|_{r=R_{\mathrm{M}}^-} = rD_{2,\mathrm{S}}\dfrac{\partial c_{\mathrm{S}}}{\partial r}\Big|_{r=R_{\mathrm{M}}^+} \end{cases} \tag{H.3}$$

For hydroxide diffusion, the initial and boundary conditions, at the surface and moving boundaries in Eq.(7.11), write,

$$\begin{cases} c_{\mathrm{OH}}(r = 0, t > 0) = 0, \quad c_{\mathrm{OH}}(r \leqslant R_{\mathrm{L}}) = c_{\mathrm{OH}}^0 \\ c_{\mathrm{OH}}|_{r=R_{\mathrm{M}}^-} = c_{\mathrm{OH}}|_{r=R_{\mathrm{M}}^+}, \quad rD_{1,\mathrm{OH}}\dfrac{\partial c_{\mathrm{OH}}}{\partial r}\Big|_{r=R_{\mathrm{M}}^-} = rD_{2,\mathrm{OH}}\dfrac{\partial c_{\mathrm{OH}}}{\partial x}\Big|_{r=R_{\mathrm{M}}^+} \\ n_{\mathrm{CH}}\dfrac{\mathrm{d}R_{\mathrm{L}}}{\mathrm{d}t} = -\phi_2 D_{2,\mathrm{OH}}\dfrac{\partial c_{\mathrm{OH}}}{\partial r}\Big|_{r=R_{\mathrm{L}}} \end{cases} \tag{H.4}$$

RESUME

RAN Bo was born on 11th October 1994 in Youyang County, Chongqing, China.

He began his bachelor's study in the Department of Civil Engineering, Tsinghua University in September 2013, majoring in Civil Engineering, and got a Bachelor of Science degree in July 2017.

He has started to pursue a doctor's degree in Civil Engineering in the Department of Civil Engineering, Tsinghua University since September 2017. He has started to pursue a doctor's degree in UMR MCD, Cerema, Université Gustave Eiffel since October 2018.

During this period, he has made academic achievements as follows.

Journal article

[1] Ran B, Omikrine-Metalssi O, Fen-Chong T, Dangla P, Li K. Sulfate diffusivity altered by pore crystallization due to chemical sulfate attack of cement-based materials [C]. The 4th international RELEM conference on Microstructure Related Durability of Cementitious composites Microdurability2021, webinar program, April –May 2021, Den Haag, Netherlands. Integrated Ferroelectrics, 2003, 52:229-235.

[2] Ran B, Li K, Fen-Chong T, Omikrine-Metalssi O, Dangla P. Spalling rate of concretes subject to combined leaching and external sulfate attack [J]. Cement and Concrete Research, 2022, 162: 106951.

[3] Ran B, Fen-Chong T, Omikrine-Metalssi O, Dangla P, Li K. Pore crystallization and expansion of cement pastes in sulfate solutions with and without chlorides. Submitted to Cement and Concrete Research. (revised)

[4] RAN B, Omikrine-Metalssi O, Fen-Chong T, Dangla P, Li K. Impact of leaching and chlorides on sulfarte attack for cement paste. Submitted to Construction and Building Materials. (under review)

COMMENTS FROM THESIS SUPERVISOR

This thesis addresses one of the main durability concerns of cement-based materials exposed in real environments bearing sulfates. Besides the conventional sulfate attack on cement-based materials, the influence of chlorides, leaching and delayed ettringite formation (DEF) is taken into account. The objectives of this thesis are to clarify the kinetics of ettringite formation, the pore crystallization and pressure accumulation, and the damage process of materials under these complex conditions. Also, scientific and engineering models are developed to help the prediction of service lives of cement-based materials used in civil engineering.

To this purpose, the thesis investigates the kinetics of AFt formation through immersion tests of ground powder samples of hardened cement pastes into different sulfate solutions, studies the alteration of pore structure and transport properties by AFt formation, and the resulted material expansion as well. The damage patterns and the transport of different ionic species are studied through immersion tests of disk specimens. On the basis of these experimental observation, a poromechanical model is established to simulate the expansion and damage of cement-based materials under complex sulfate attack. Moreover, to address the specific damage pattern of observed spalling under sulfate attack and leaching, a spalling rate model is developed to predict the damage rate.

The works in this thesis have been finished independently by the PhD candidate under the mutual supervision between Tsinghua and UGE. The results shed new light on the AFt crystallization process at pore level and quantify the AFt formation kinetics with presence of chlorides. The results and models obtained during the thesis work are original and innovative. The technical writing of thesis is clear and rigorous. The works presented in this thesis satisfy the requirements for PhD thesis of both Tsinghua and UGE, thus eligible for final dissertation defense.

RESOLUTION OF THESIS DEFENSE COMMITTEE

This thesis addresses one of the main durability concerns of cement-based materials exposed in real environments bearing sulfates. The research topic has both theoretical significance and application value. The main results obtained from the study include:

(1) High sulfate concentrations and DEF accelerate the AFt formation but the chlorides inhibit the formation. The AFt content was successfully quantified by NMR method. These effects are caused by the change in the AFt supersaturation. An exponential kinetics law is identified for AFt formation rate and the exponential order on the AFt supersaturation is fitted as 1.90.

(2) The AFt crystallization occurs in whole range of material pore space. The AFt crystals formed in micropores close the neck-part of "ink-bottle" pores, dramatically lowering the vapor diffusivity and detectable porosity by MIP. The AFt crystals formed in micropores leads to cracking and the reopening of the "ink-bottle" pores, resulting in the rapid expansion rate and the increase in vapor diffusivity.

(3) The damage of materials under the combined ESA and leaching is found to follow a spalling pattern. Leaching accelerates the sulfate ingress and cracking damage, and the gypsum is a product specific to the combined ESA and leaching condition. The chlorides mitigate the sulfate ingress, material expansion and cracking. DEF initiates the microcracks during curing and the microcracks aggravate the cracking damage and promote the penetration of sulfates and chlorides.

(4) The chemo-poromechanical model is developed for ESA expansion, considering the pore chemistry, the pore crystallization, the crystallization pressure, and the material damage. The model is validated by experimental data and can be applied to ESA expansion in complex environments. A spalling rate model is established to solve the spalling damage rate for engineering use. The spalling rate model can help the durability design for concrete structures exposed to sulfates.

The works in thesis show that the author has acquired sound theoretical base and deepened knowledge in the civil engineering discipline, and has independent research capacity. The author shows good capacity in both theoretical and experimental works. Both the writing of thesis and the oral presentation have a good structure for research contents. The author addresses clearly and correctly all the questions and comments during the de-

fense. Overall, the works presented constitute an excellent doctoral thesis.

The jury, after anonymous vote, unanimously agree that Mr. Ran Bo passes the thesis defense, and unanimously recommend to confer on him the Doctoral Degree of Engineering of Tsinghua University and le grade de Docteur de l'Université Gustave Eiffel.